8-0

FINAL REPORT

A STUDY OF IMPROVED BLOWOUT PREVENTION SYSTEMS FOR OFFSHORE DRILLING OPERATIONS

Contract No. 14-12-0001-21169, Mod. 4

Sponsored by

Minerals Management Service
United States Department of the Interior
Reston, VA 22091

Principal Investigators:

Adam T. Bourgoyne, Campanile Professor

William R. Holden, Professor

Robert R. Desbrandes, LSU Foundation Hopkins P. Breazeale Professor

Julius P. Langlinais, Associate Professor

Walter R. Whitehead, Associate Professor

February, 1986

ABSTRACT

A number of new blowout control problems are associated with extending the search for hydrocarbons beyond the continental shelf to the deeper water depths of the continental slope using floating drilling vessels. These problems become much more severe as the water depth increases, because of the increased length of the marine riser and subsea flowlines and the increased susceptibility of shallow formations to fracture. A six year research project has been undertaken which is concerned with the development of improved blowout prevention systems that are better suited to deep water drilling operations. The two main systems included in the study are (1) the diverter system which can be employed to divert an uncontrolled flow of formation fluids away from the drilling rig, and (2) the well control system used to circulate formation fluids from the well under pressure. The diverter system is normally used to handle kicks from shallow formations encountered prior to setting surface casing. After setting surface casing, the well control system can be used. This report is an interim report on results obtained during the first three years of the project.

The shallow gas kicks for which diverter systems are needed occur infrequently. However, when a situation calling for the use of a diverter does arise, past experience has shown that failures in the diverter system are common. This high failure rate indicates the need for studying diverters and developing improved design criteria for these systems. A review of past failures indicated that piping failures are common which could be related to (1) erosion caused by produced sand, (2) poor anchoring of piping, and (3) higher pressures than expected. The trend to larger

The second major aspect of this project dealt with potential improvements in the well control system. It was determined that significant improvements in kick control systems could be made by integration of the measurements while drilling (MWD) technology and process control technology into well control operations. Integration of these techniques should permit the development of computer driven chokes and pumps, which would be capable of more precise control of bottom hole pressure during well control operations, and would permit advanced well control techniques such as bubble chopping to be employed. However, large improvements in MWD data transmission rate must be achieved in order to realize the full potential benefit of the automated well control system envisioned. Two novel MWD concepts that were experimentally investigated include (1) the use of electrical telemetry through a partially insulated drill pipe containing a conductive drilling fluid, and (2) the use of a fluidic device suitable for high rate pressure pulse telemetry through the drilling fluid. Although the electrical telemetry system appeared to offer much higher data rates than possible with the improved pressure pulse technology, it was determined that the data rate requirements could be met with either system. However, the pressure pulse telemetry could be implemented with much fewer modifications of a conventional rotary drilling system, and was shown to be more cost effective.

Four different choke designs were tested for use in the automated well control system. Testing was done in a 6,000 ft. test well designed to represent the well geometry present during well control operations being conducted on a floating drilling vessel in 3,000 ft. of water. The choke designs were ranked according to their suitability for use in the automated well control system.

Work is now continuing on both major aspects of this project. The diverter experiments are being extended to study pressure peaks experienced during the initial unloading of the well. The computer program will be modified to permit simulation of the unsteady-state behavior during the unloading sequence. Also, erosion tests are being extended to include gas/sand mixtures.

Work is also continuing on the development of an integrated computer controlled well control system. A system for interfacing a microcomputer to the best of the four choke designs tested is almost in place.

1. INTRODUCTION

Some of the most costly events that have ever occurred in the history of the oil industry have been caused by a loss of well control, commonly called a "blowout". Serious losses to life, property, and the environment have often been directly related to "blowouts". In a continuing search for domestic hydrocarbon deposits, the oil industry has begun to embark onto another frontier, i.e., the slopes of the outer continental shelf and deep marine sedimentary basins. If blowout prevention theory and practice is to advance along with the technology now being developed for drilling in deeper waters, research must be done to determine the most effective blowout prevention systems for this new, more hostile environment.

The Petroleum Engineering Department at LSU has played an active role over the past decade in well control research and in training of industry personnel in present-day methods of well control. With the help of the International Association of Drilling Contractors (IADC), a modern training and research facility was centered around a 6,000 ft well equipped to model well control operations conducted on land or in the shallow water marine environment of the continental slope. The facility has been maintained with the most up-to-date well control equipment and has afforded over 8,000 industry personnel the "hands-on" training experience of controlling an impending blowout without risk to personnel or the environment.

In 1978, work began on expanding the LSU Blowout Prevention Center to include research and training activities for floating drilling vessels in deep water. The facilities were expanded to include a second 6,000

ft. well designed to model well control operations on a floating vessel in 3,000 ft. of water. A two million dollar facility expansion was constructed to enable LSU to perform the needed research and training objectives for deepwater offshore operations. Funding for this expansion was achieved through the combined support of a consortium of 53 companies in the petroleum industry and through a research grant funded by the U. S. Minerals Management Service (MMS).

In 1979, a four year research effort on the testing of various blowout prevention procedures for deep water drilling operations was funded by MMS. Additional equipment and grants have been also provided by the petroleum industry in support of this research. The four year MMS research contract was completed in December, 1982, and a final report was issued in May, 1983. In this project, emphasis was placed on basic research into the fluid mechanics of the well control process and on the development of optimal procedures for use with existing equipment and blowout prevention systems.

On March 24, 1982, a workshop was conducted at LSU to assist in the formulation of a long range plan for future well control research. Workshop participants included (1) members of an industry advisory panel to the LSU Blowout Prevention Research Center and (2) representatives of various MMS districts.

Twenty-one desirable projects were identified by this group. The top ten projects are listed in Table 1 along with a composite priority level assigned by the workshop panel. First, a composite priority rating was determined assuming only one project could be funded. Next, a composite priority rating was determined assuming two projects could be funded. This process was then repeated for groupings of three, four, and five projects.

Table 1 - Recommendations made at March 24, 1982 LSU Well Control Workshop

Priority Level	Research Area	Votes Received Assuming Funding For Following Number of Projects: One,	Two,	Three,	Four,	or Five
1	Feasibility Study on Use of MWD Technology in Well Control Operations on Floating Vessels	6	9	9	10	11
2	Study of Well Control Operations with Simultaneous Formation Fracture	3	10	12	16	17
3	Well Control Operations for Short Casing Strings (Diverter Systems)	3	5	8	12	14
4	Improved Procedures for Handling Upward Gas Migration during Stripping or Snubbing Operations	1	3	5	5	8
5	Improved System for Detecting Gas in Mud at Depth (as opposed to present surface detectors)	2	3	5	5	7
6	Study of Upward Gas Migration in Slant (Directional) Boreholes	1	2	3	5	7
7	Scale-up of Fluidic Pulse Telemetry System to Longer Systems with Varying Mud Properties	0	1	3	4	5
8	Determination of Minimum Number of Requisite Parameters via MWD for Safe Drilling Operations	1	1	1	3	5
9	Scale-up of Ongoing Fire Suppression System Development for Offshore Drilling	2	3	3	4	4
10	Study of Potential Problems due to Gas Hydrate Formation in Subsea Well Control Equipment in Deep Water	0	3	4	4	4

Using input from the workshop, a six year research plan was proposed for developing improved well control systems for deep water offshore drilling operations. This research differs in thrust from the previous research effort in that the primary emphasis is being placed on the development of improved well control systems. Both divert systems and well control systems are included in the current study. The previous study concentrated primarily on optimizing the use of existing well control systems through improved procedures.

The six year plan calls for simultaneous study of both the diverter system and the well control system. Advances in design concepts for these two systems is the goal of this research. In this report, progress made during the first three years of implementation of the research plan is discussed. Specific areas of research that have been completed include:

(1) An experimental study of sonic exit pressures and multi-phase flowing gradients in diverter systems.

(2) An experimental study of plugging and erosion in diverters caused by mud/sand slurries.

(3) Computer modeling of diverter operations for estimating steady state design loads.

(4) Modeling of marine riser during diverter operations.

(5) A study of methods for diverting or removing gas trapped in a subsea BOP stack.

(6) Design requirements for integration of measurements while drilling (MWD) and well control technologies.

(7) An experimental study of an electrical telemetry method for transmitting drilling data to the surface.

(8) An experimental study of a fluidic mud pulser.

Work is now continuing on both major aspects of this project. The diverter project is being extended to study pressure peaks experienced during the initial unloading of the well. The computer model for diverter operations is being modified to permit simulation of the unsteady-state behavior during the unloading sequence. Also erosion tests are being extended to include gas/sand mixtures. Work is also continuing on the design of a computer controlled well control system that is capable of using downhole data provided by a MWD system.

2. EXPERIMENTAL STUDY OF SONIC EXIT PRESSURE AND MULTIPHASE FLOWING GRADIENTS IN DIVERTERS

Well control is especially difficult when a threatened blowout situation unexpectedly occurs at a shallow depth, prior to setting surface casing. This situation is illustrated by the example shown in Figure 2.1. In this example, a well is being drilled at a depth of 3,500 ft., just prior to setting the next casing string. Conductor casing was set at only 300 ft. Thus, the well could not withstand any significant pressure without exceeding the fracture pressure of the shallow sediments exposed below the conductor casing. In this type of situation if formation fracture occurs, there is a high probability that formation fractures may broach to the surface. When the flow through the fractures is severe, a crater may develop and destroy the foundations of the drilling platform.

The example described above is the situation just prior to the widely publicized blowout in the Santa Barbara Channel which occurred in 1968. Just prior to the blowout, the drill pipe was being raised in the well to remove the bit. The well started to flow and the crew dropped the drill pipe into the well and closed the blind rams of the blowout preventer stack. Soon after, oil moved from the wellbore through a fracture to the surface. Oil was released to the sea at a high rate.

The best available procedure for handling a threatened blowout situation caused by a shallow hydrocarbon deposit involves the use of a diverter system. Basically, a diverter system is a large vent line which conducts flow away from the rig and rig personnel in a downwind direction. More than one vent line must be available to assure that a

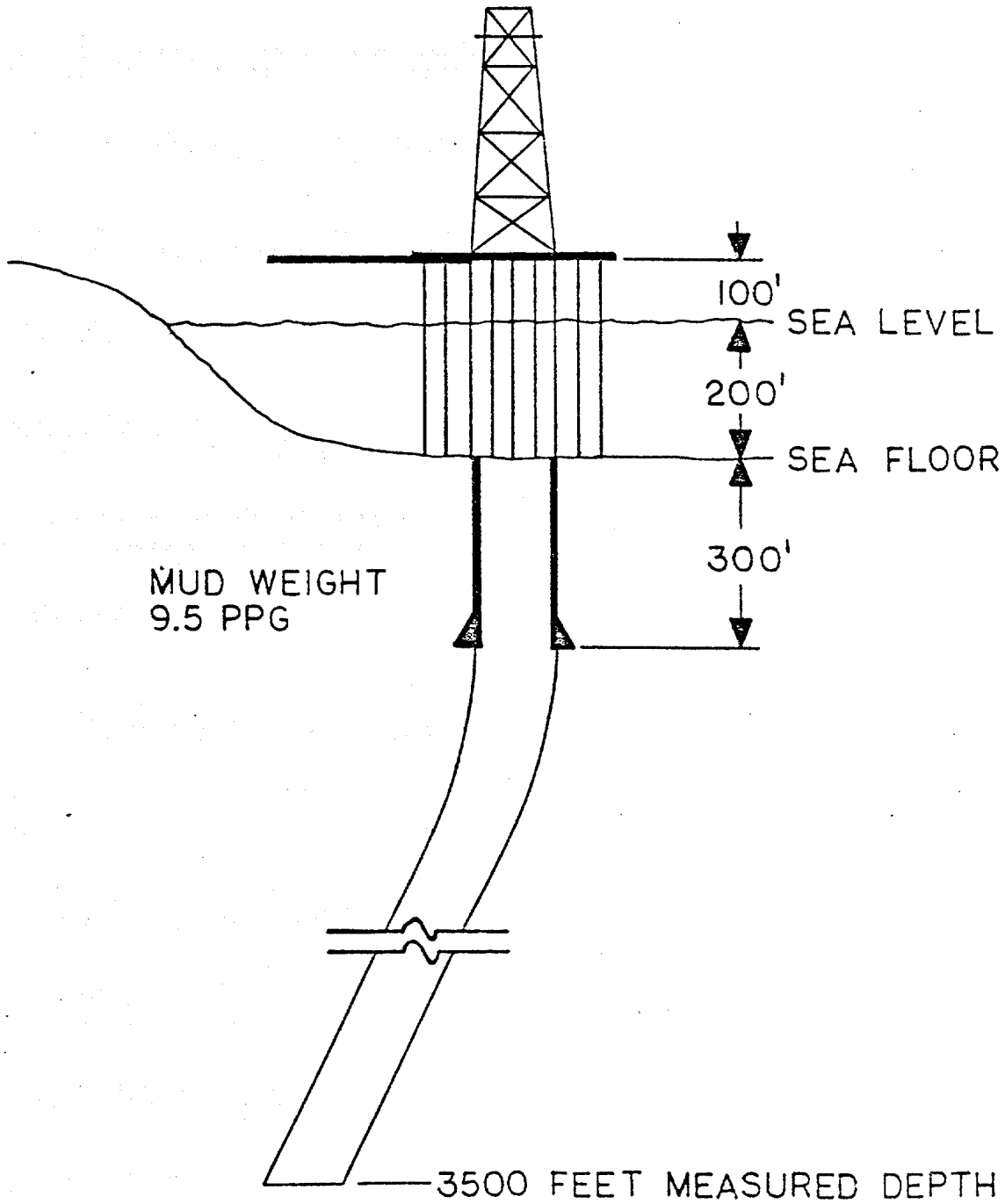

FIGURE 2.1 - DRILLING SITUATION ON SANTA BARBARA CHANNEL BLOWOUT

downwind diversion is possible. The vent line must be large enough to prevent a significant pressure build-up in the well. Proper flow diversion can maintain the integrity of the borehole and in some cases may permit a dynamic well kill procedure to be quickly employed, thus minimizing any environmental damage.

Although conceptually simple, the design, maintenance, and operation of an effective diverter system for the various types of drilling vessels is a deceptively difficult problem. On the great majority of wells, the diverter system is designed and added to the rig after the rig is built, complicating the routing of the vent lines. History has shown that average current industry practice is not adequate. Over the past 20 years, the diverter failure rate has been in excess of 50 percent.

Shown in Figure 2.2 is a photograph of a diverter failure on a drillship drilling off the Indonesian Coast in 1981. The diverter system failed soon after it was employed. The photograph shows that the pressure had pushed the inner barrel of the telescopic joint through the rig floor, breaking the diverter and lifting the rotary table, kelly bushings, rotary drive motor, and the kelly. Gas is exhausting on the rig floor. In addition, the hull was punctured by the expanding slip joint and the anchor mooring prevented the ship from moving out of the boil caused by a subsea leak. The vessel sank within 24 hours.

A diverter system consists of four components. They are the annular preventer, the vent or diverter line, associated valving and controls, and the conductor casing (Figure 2.3). The purpose of the annular preventer is to stop the upward flow of fluids and divert the flow into the vent line. The diverter vent line is a large diameter steel pipe connected to a spool below the annular preventer. This line carries

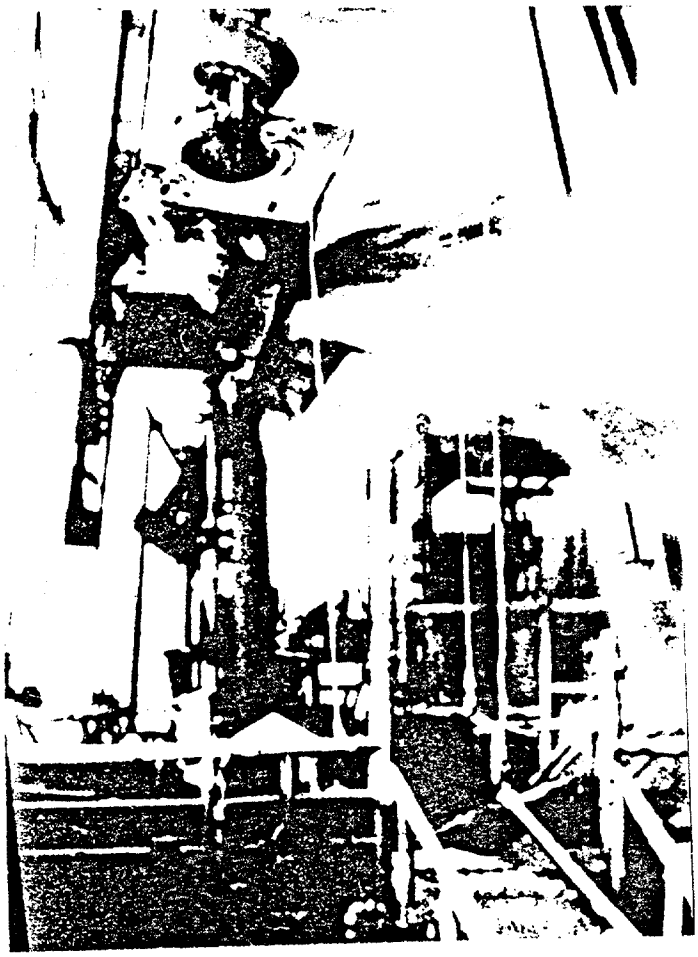

FIGURE 2.2 - PHOTOGRAPH OF DIVERTER FAILURE

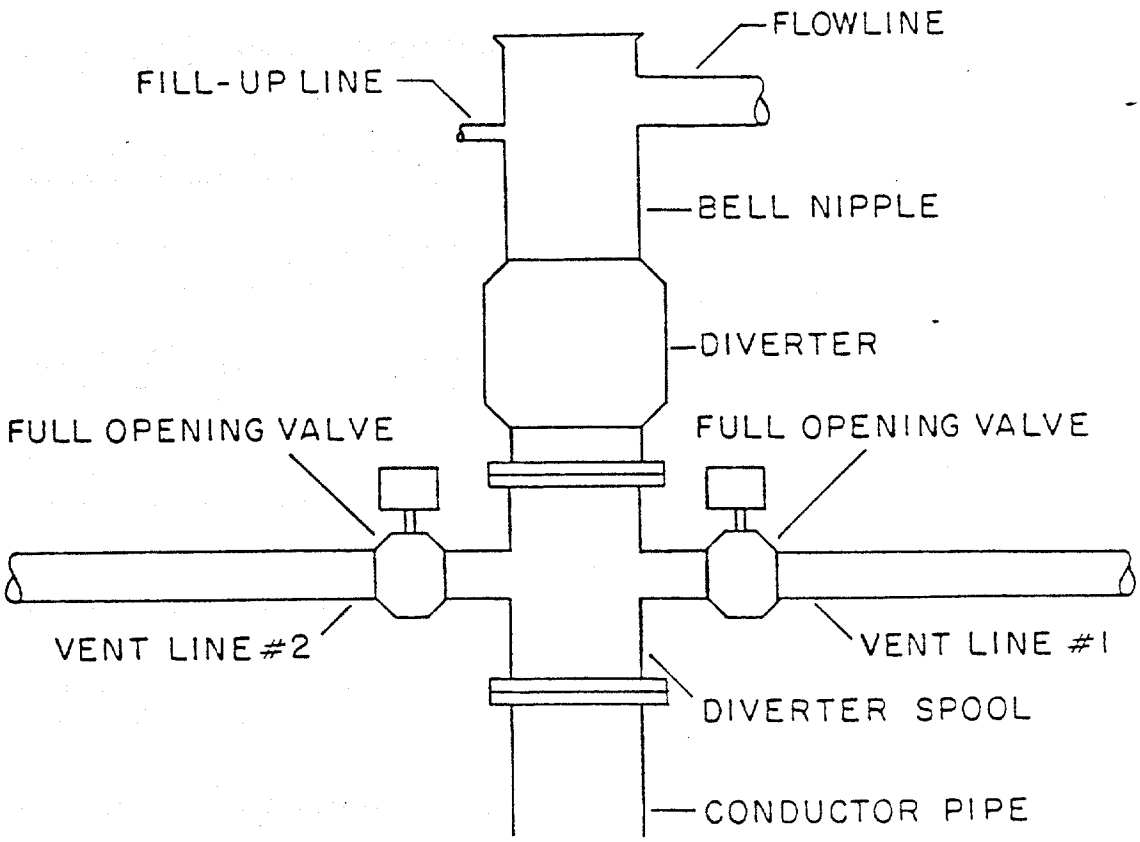

FIGURE 2.3 - A TYPICAL DIVERTER SYSTEM

fluids away from the rig. The line is normally sloped to prevent plugging. Diameters usually range in size from 4-in. to 16-in. Two lines are generally installed and oriented so that the flow can be directed downwind. The lengths of the lines are determined by the dimensions of the rig.

Valves are located on the diverter line to close the system during normal drilling operations. The minimum diameter of the valves should be no less than the diameter of the vent line to prevent the valve from acting as a choke during diverter operations. Valves are usually remote controlled, and must open before the annular preventer is closed.

The conductor pipe determines the size of the annular preventer that can be used. It should be set deep enough to protect shallow sediments from any backpressure associated with diverter operations.

Diverter systems have been used since the early 1970's as a means of well control in areas where shallow gas sands are likely to be encountered. The Minerals Management Service (formerly USGS) has required diverter systems to be installed on offshore rigs since 1975. During the history of their use diverter systems have a failure rate greater than 50 percent. Types of failures include mechanical failure of the valve system, erosion of vent lines, and mechanical failure of the annular preventer. In some failures the diverter system maintained its integrity, but caused enough backpressure on the well to fracture the formations and eventually crater the well. In many instances in which the diverter operations were considered successful gas bubbles appeared in the water around the rig, indicating at least some flow through the formations or around the conductor pipe to the sea floor. Many cases of diverter system failure can be traced to improperly designed, improperly sized, or poorly maintained equipment.

The basic function of a diverter system is to safely conduct the flow from the well to a point a safe distance from the rig. The system should place as little backpressure on the well as possible to avoid fracturing the formation. Calculations must include losses due to acceleration as well as to friction and elevation. The single most important factor in contributing backpressure to the well is the diameter of the diverter line.

In the past, backpressure estimates were made by assuming flow in the diverter line to be subcritical (pressure at the diverter exit is atmospheric), and acceleration effects were neglected. This allowed standard procedures of calculating pressure loss to be applied. However, these assumptions can result in large errors. When flow is critical, any increase in flow rate increases the pressure at the diverter exit, thus raising the overall pressure of the well.

In this study, experiments were performed to measure pressure traverses of flow at or near critical conditions and to measure the critical velocities of dry gas and gas-liquid mixtures. The measured traverses were used to test new methods used to predict pressure losses in both two-phase flow and dry gas flow.

EXPERIMENTAL APPARATUS AND PROCEDURE

Model diverters were constructed from 40 ft. sections of 1 in. and 2 in. steel line pipe. These models were equipped with pressure transducers accurate to 1 psi. Temperature probes were also mounted on the models to measure flowing temperatures. Experiments were run for both dry gas flow and for two-phase flow of gas and water. Methane was

supplied by high pressure gas storage tanks for the experiments in the 1 in. line. Gas flow rate was measured by a standard orifice meter accurate to approximately 5 percent of total rate. Water was supplied by mud pumps, and water rates were measured by accurately recording pump strokes. A schematic of the apparatus is shown in Figure 2.4.

The experiments were conducted by increasing gas flow into the system until flow became critical. The criteria for critical flow is that the pressure at the diverter exit be greater than atmospheric pressure. Once critical flow is attained any increase in flow rate results in an increase in exit pressure. The experiments were run over a wide range of exit pressures and flow rates.

EXPERIMENTAL RESULTS

The experiments resulted in the collection of data for 35 dry gas traverses and 56 two-phase traverses. Flow rates ranged up to 21 MMSCFD gas and 4000 BBL/MMSCF water. The traverses are tabulated in tables 1, 2, 3, and 4. Critical flow occurred in nearly all of the runs. In several runs flow was held below critical to measure traverses at atmospheric exit pressure.

Friction factors were calculated from the dry gas data and from water flow tests. From the friction factors, pipe roughness was calculated to be 0.0003 in. for the 1 in. line, and 0.0006 in for the 2 in. line. These values are well within the range expected for the line pipe used.

The recorded exit pressures (Tables 2.1-2.4, col. 2) show that the increase in exit pressure associated with critical flow can be significant.

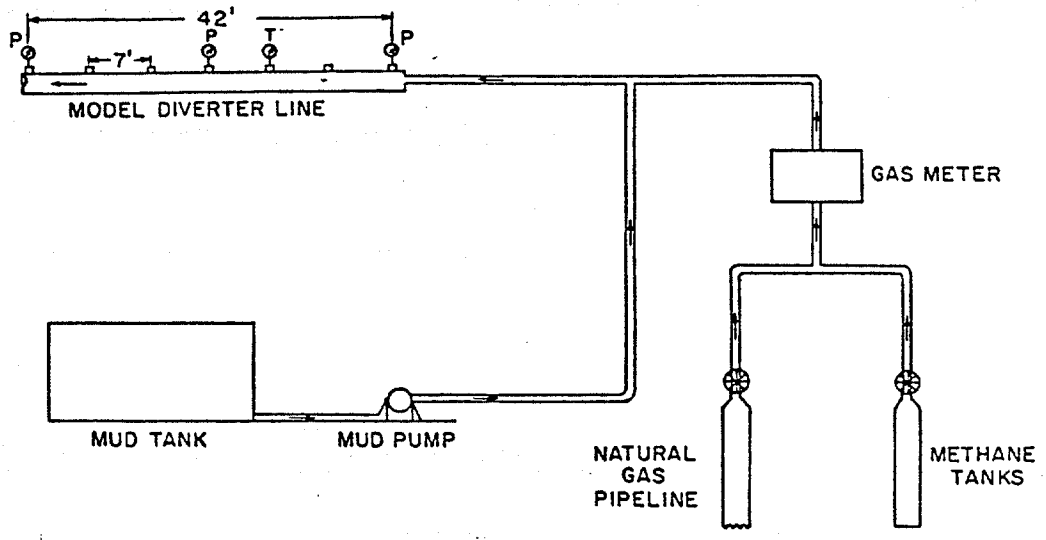

FIGURE 2.4 - SCHEMATIC OF EXPERIMENTAL APPARATUS

TABLE 2.1 - DRY GAS DATA FOR 1 IN. DIVERTER LINE
(I.D. 0.918 IN.).

	PRESSURE (PSIA) (AT DISTANCE (FT.) FROM EXIT)				
	DISTANCE			PRESSURE PREDICTED	GAS RATE
RUN #	0.198	13.78	41.82	@ 41.82	MMSCFPD
1	24	53	82	80	0.72
2	44	104	157	151	1.44
3	21	53	77	75	0.72
4	39	93	138	135	1.344
5	54	128	193	187	1.872
6	69	161	241	233	2.352
7	56	133	200	193	1.92
8	97	221	340	327	3.024
9	115	258	395	380	3.696
10	139	311	474	456	4.600
11	15	46	69	64	0.48
12	50	130	202	189	1.728
13	72	157	247	237	2.376
14	45	98	149	142	1.422
15	189	397	598	576	6.372
16	135	343	538	509	4.788
17	167	359	536	513	5.652
18	89	195	304	291	2.916

TABLE 2.2 - DRY GAS DATA FOR 2 IN. DIVERTER LINE (I.D. 1.937 IN.).

	PRESSURE (PSIA) AT DISTANCE (FT.) FROM EXIT)							
	DISTANCE						PRESSURE PREDICTED	GAS RATE
RUN #	0.198	6.79	13.79	20.79	28.02	41.82	@ 41.82	MMSCFPD
1	128	220	272	---	335	379	332	20.9
2	97	---	215	243	268	301	275	17.28
3	96	172	215	---	265	297	258	16.2
4	67	---	149	168	183	203	177	11.04
5	44	76	96	---	118	130	122	7.63
6	28	---	65	75	83	91	79	4.92
7	27	---	59	66	73	79	73	4.56
8	26	48	57	---	72	79	73	4.51
9	24	---	51	---	60	68	75	4.03
10	22	39	49	---	58	68	60	3.72
11	22	---	44	---	53	60	58	3.6
12	18	---	40	---	47	53	51	3.19
13	17	---	35	---	42	47	47	2.88
14	16	---	35	---	42	46	46	2.86
15	16	22	29	---	34	37	34	2.06
16	15	---	22	---	25	28	26	1.44
17	15	16	17	---	18	19	15	0.08

TABLE 2.3 - TWO-PHASE (GAS/WATER) DATA FOR 1 IN. DIVERTER LINE (I.D. 0.918 IN.).

	PRESSURE (PSIA) (AT DISTANCE (FT.) FROM EXIT)					
	DISTANCE			PRESSURE PREDICTED	GAS RATE	WATER RATE
RUN #	0.198	13.78	41.82	@ 41.82	MMSCFPD	BBL/MMSCF
1	129	279	428	521	2.952	392.6
2	177	370	590	624	3.84	325
3	172	472	586	612	2.976	554
4	134	355	603	599	1.728	1496
5	119	250	412	433	2.556	348.8
6	123	302	512	519	1.728	1134.9
7	85	206	340	361	1.386	900.1
8	182	396	595	613	3.946	278.9
9	153	383	619	610	1.836	1383.8
10	147	378	583	567	2.268	825.4
11	133	358	605	601	1.584	1744.6
12	145	359	605	599	2.304	890
13	173	374	574	607	3.564	362.7

TABLE 2.4 - TWO-PHASE (GAS/WATER) DATA FOR 2 IN. DIVERTER LINE (I.D. 1.937 IN.).

	PRESSURE (PSIA) AT DISTANCE (FT.) FROM EXIT)							
	DISTANCE					PRESSURE PREDICTED	GAS RATE	WATER RATE
RUN #	0.198	6.79	13.79	28.02	41.82	@ 41.82	MMSCFPD	BBL/MMSCF
1	35	62	78	---	124	118	3.36	689.8
2	44	---	126	174	196	182	1.92	4457.1
3	21	41	58	72	89	103	2.64	793.5
4	56	102	131	165	197	193	4.80.7	
5	49	83	133	165	201	185	2.04	4151.3
6	54	91	111	130	160	134	7.08	138.5
7	58	95	115	143	172	166	6.79	282.3
8	59	96	118	149	183	180	6.58	379.3
9	62	103	125	162	197	200	6.43	512.9
10	132	219	265	328	369	318	18.96	79.9
11	134	214	259	313	356	330	17.16	137.7
12	135	214	254	311	357	352	15.6	228.6
13	132	207	250	307	359	356	14.4	294
14	70	---	138	170	200	194	8.64	221.8
15	67	---	134	165	200	199	7.97	299.2
16	65	---	127	159	191	191	7.44	320.5
17	67	---	135	173	207	211	6.89	498.1
18	65	---	142	186	220	216	5.9	732.8
19	89	---	173	212	242	208	11.64	103.4
20	76	---	156	195	221	185	10.8	92.9
21	74	---	149	185	206	177	10.1	99.5
22	62	---	131	164	185	140	9.5	46.9
23	59	---	124	156	178	134	9.07	49.1
24	92	155	191	234	262	217	13.44	71.3
25	59	99	120	146	169	148	7.8	137.1
26	51	87	108	134	151	115	7.61	58.6
27	60	98	118	145	170	164	7.68	191.5
28	60	97	118	145	174	167	7.08	255
29	48	83	100	124	140	120	6.98	73.4
30	69	122	147	192	228	221	6.24	685.7

31	84	152	189	239	289	270	6.24	1028.6
32	96	175	214	271	323	301	6	1366.8
33	38	62	76	102	126	118	3.96	467.1
34	46	88	110	143	172	167	3.72	1114.3
35	54	105	139	178	215	208	3.55	1858.2
36	64	127	159	206	247	233	3.36	2520.4
37	28	---	60	73	86	65	3.72	131.8
38	31	---	65	83	101	91	3.41	366
39	32	---	68	90	111	100	3.17	534.3
40	25	---	51	64	77	60	3.12	178.6
41	26	---	54	70	85	79	3	364
42	23	---	47	59	71	56	2.88	193.4
43	33	---	76	98	121	111	2.98	777.8

The results of the experiments were used to test the accuracy of the empirical models used to predict pressure losses in both dry gas and two-phase flow. Available correlations, especially two-phase flow correlations, are not intended for use under critical flow conditions.

CALCULATION PROCEDURES

In addition to the experimental work, several calculation procedures for estimating the pressures in a diverter under a design load were investigated. The procedures recommended for use are presented below for both dry gas and gas-liquid mixtures.

Dry Gas

Dry gas flow was modeled using the pressure gradient equation for horizontal flow

$$\left(\frac{\Delta P}{\Delta L}\right)_{TOTAL} = \left(\frac{\Delta P}{\Delta L}\right)_{friction} + \left(\frac{\Delta P}{\Delta L}\right)_{acceleration} \quad (2.1)$$

The friction gradient is calculated by

$$\left(\frac{\Delta P}{\Delta L}\right)_{friction} = \frac{f\rho f^2}{2g_c d} \quad (2.2)$$

The acceleration gradient is calculated by

$$\left(\frac{\Delta P}{\Delta L}\right)_{acceleration} = \frac{\Delta(\rho f^2)}{2g_c \Delta L} \quad (2.3)$$

Theoretical pressure traverses were computed by the iterative method presented by Brill and Beggs (1978, p. 1-23). The experimental

values of flow rate and exit pressure were used to initiate the traverses. Pressures at the upstream end of the diverter model were predicted by this method with 4 percent average error in the 1 in. data and 8.5 percent average error in the 2 in. data.

Gas-Liquid Mixtures

Two-phase flow was modeled by the Dukler correlation for horizontal flow (Dukler, 1964). The subroutine for the correlation presented by Brill and Beggs (1978, p. A-18) was used. An acceleration term was added to the program to account for the rapid expansion of the gas at the diverter exit. The acceleration gradient was calculated by equation 2.3 with two-phase density and velocity substituted for gas density and velocity. The average two-phase density is given by

$$\rho = \lambda_g \rho_g + \lambda_w \rho_w \quad \ldots\ldots\ldots\ldots\ldots\ldots\ldots\ldots \quad (2.4)$$

and $\Delta(\rho v^2)$ is the change in the product of two-phase density and velocity over the finite element of the pressure traverse. This method predicted upstream pressures with a 5 percent average error in the 1 in. data and a 9 percent average error in the 2 in. data.

Critical Felocity

Dry gas

The critical velocity of dry gas was calculated by the following equation

$$V^*_{gas} = 41.4 \sqrt{\frac{KzT}{\gamma_g}} \quad \ldots\ldots\ldots\ldots\ldots\ldots\ldots\ldots \quad (2.5)$$

Flow rate is calculated by

$$Q^*_{gas} = \frac{V^*_{gas}\ D^2\ P_e\ T_{STD}}{2122\ z\ T_e\ P_{STD}} \quad \ldots\ldots\ldots\ldots\ldots\ldots\ (2.6)$$

Equations 2.5 and 2.6 were used to calculate the critical flow rate expected at the exit conditions of the experiments. Figure 2.5 shows calculated critical flow rate against measured critical flow rate. Use of equations 2.5 and 2.6 result in estimates of critical flow rate within 5 percent of those measured. Equation 2.5 is, therefore, appropriate for modeling the critical velocity of dry gas.

Gas-Liquid Mixtures

The literature presents two equations for calculating the critical velocity of a two-phase mixture. Fortunati (1972) defined two-phase critical velocity as

$$V^* = 68.1 \sqrt{\frac{m\ P_e}{\lambda_g \rho}} \quad \ldots\ldots\ldots\ldots\ldots\ldots\ (2.7)$$

where m is defined as

$$m = \frac{(1-x)C_{V_l} + xC_{P_g}}{(1-x)C_{V_l} + xC_{V_g}} \quad \ldots\ldots\ldots\ldots\ldots\ldots\ (2.8)$$

$$x = \frac{\text{gas mass rate}}{\text{total mass rate}} \quad \ldots\ldots\ldots\ldots\ldots\ldots\ (2.9)$$

and ρ is defined by equation 4.

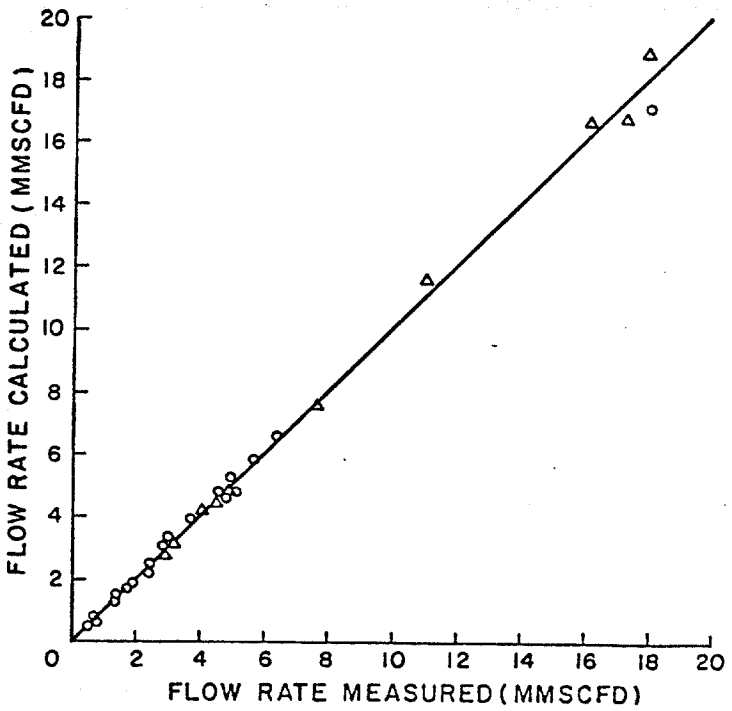

FIGURE 2.5. A Comparison of Predicted Critical Flow Rate and Measured Critical Flow Rate for Dry Gas in 1-in. (Circles) and 2-in. (Triangles) Model Diverters

Wallis (1969, p. 143) defined two-phase critical velocity as

$$V^* = (\lambda_g \rho_g + \lambda_w \rho_w)\left[\frac{\lambda_g}{\rho_g (V^*_{gas})^2} + \frac{\lambda_w}{\rho_w (V^*_w)^2} \right]^{-1/2} \quad \ldots\ldots (2.10)$$

where

$$V^*_w = 68.1 \sqrt{\frac{1}{\rho_w C_w}} \quad \ldots\ldots\ldots\ldots\ldots\ldots\ldots\ldots (2.11)$$

Both equations predict critical velocity to be a minimum at a liquid holdup of 0.5 and give similar estimates of critical velocity. Figure 2.6 is a plot of equation 7 and shows that two-phase critical velocities can be considerably less than the critical velocity in either phase. The critical velocities measured in the experiments confirm this behavior, but do not agree with the velocities predicted by either equation 7 or 10. Figure 2.7 compares critical flow rates calculated from equation 7 with the measured values. Calculated critical velocities and flow rates are somewhat lower than those measured in the experiments. Equations 7 and 10 predict critical velocities with average errors of 17 and 20 percent, respectively. However, either equation can be used for engineering purposes with acceptable accuracy.

DESIGN APPLICATION

The effect of critical flow calculations on actual diverter lines can be predicted by the theory presented. According to current Minerals Management Service regulations, 6 in. is the minimum allowable diverter line diameter. Table 2.5 presents critical flow rate, exit pressure, and the resulting increase in equivalent density due to the increase in

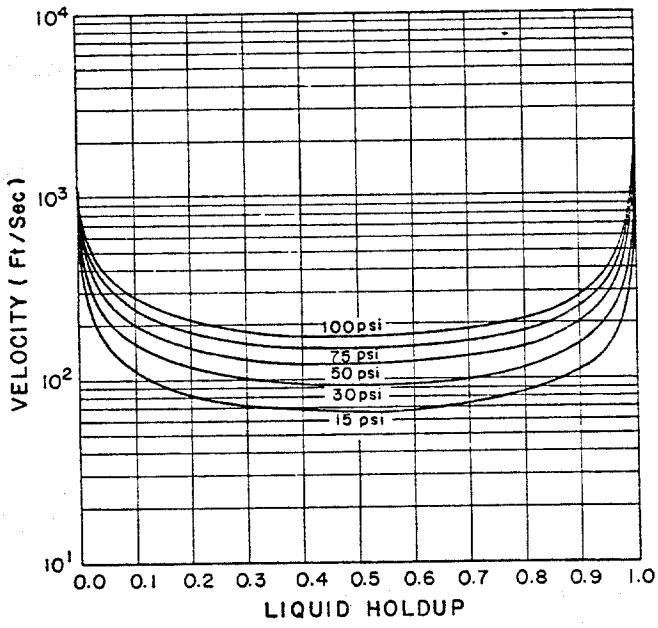

FIGURE 2.6. A Typical Critical Velocity Function

TABLE 2.5 - EQUIVALENT DENSITIES CAUSED BY THE PRESSURES ASSOCIATED WITH CRITICAL FLOW.
Dry Gas 500 bbl/mmscf

Gas Flow Rate (mmscfd)	Exit Pressure (psia)	ED (ppg)	Exit Pressure (psia)	ED (ppg)
20	15	0	43	1.8
40	30	1	85	4.5
60	45	1.9	127	7.2
80	60	2.9	170	9.9
100	75	3.8	---	---
150	112	6.2	---	---

ED - equivalent density @ 300 ft. casing shoe

exit pressure associated with critical flow in a 6 in. diverter line. As can be seen, equivalent densities can be significantly increased by critical flow.

A computer program developed in this study was used to generate diverter performance curves, which relate backpressure to flow rate. These curves assume critical flow at the diverter exit, and can be used in diverter design calculations. Figures 2.8-2.11 present diverter performance curves for dry gas and two-phase flow in various diameter diverters. The effect of diameter on backpressure is evident. Substantial differences can be found when comparing the results of Figure 5-8 to conventional calculations such as those given in Table 2.6.

CONCLUSIONS

(1) Experimental data and mathematical modeling suggests that critical flow and fluid acceleration effects should be considered when performing backpressure calculations on diverter lines.

(2) Equations 2.5 and 2.6 can be used to estimate critical velocity and critical flow rate for dry gas flow with good accuracy. The average error experienced using these equations was 5 percent.

(3) Equations 2.7 and 2.10 describe the critical velocity of a two-phase mixture with sufficient accuracy for engineering calculations. Average error experienced using these equations was under 20 percent.

(4) Estimates of the backpressure associated with critical flow in diverter lines can be made using the theory presented.

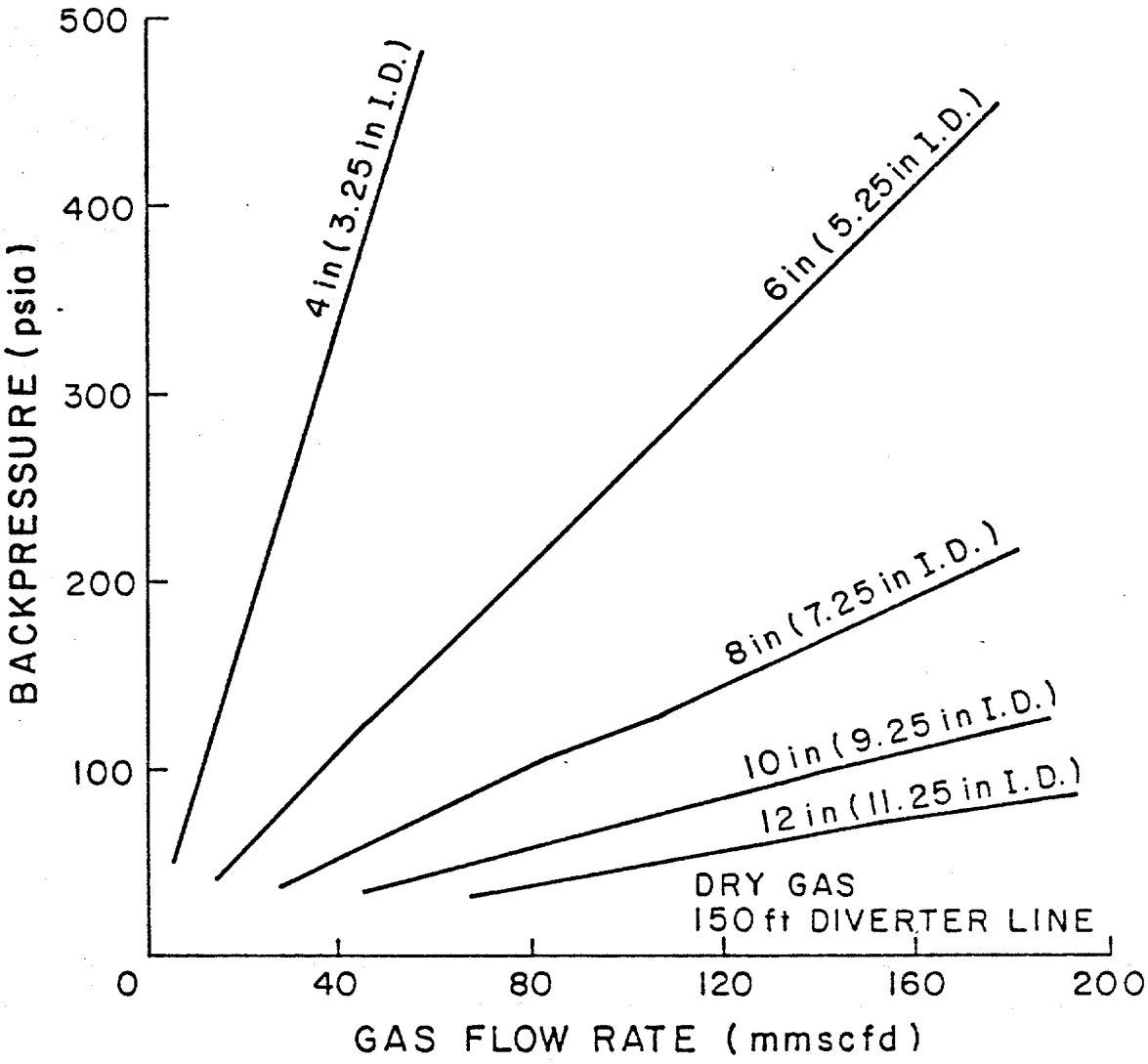

FIGURE 2.8. Diverter Backpressure Estimates for Critical Flow of Dry Gas (150 ft Equivalent Length)

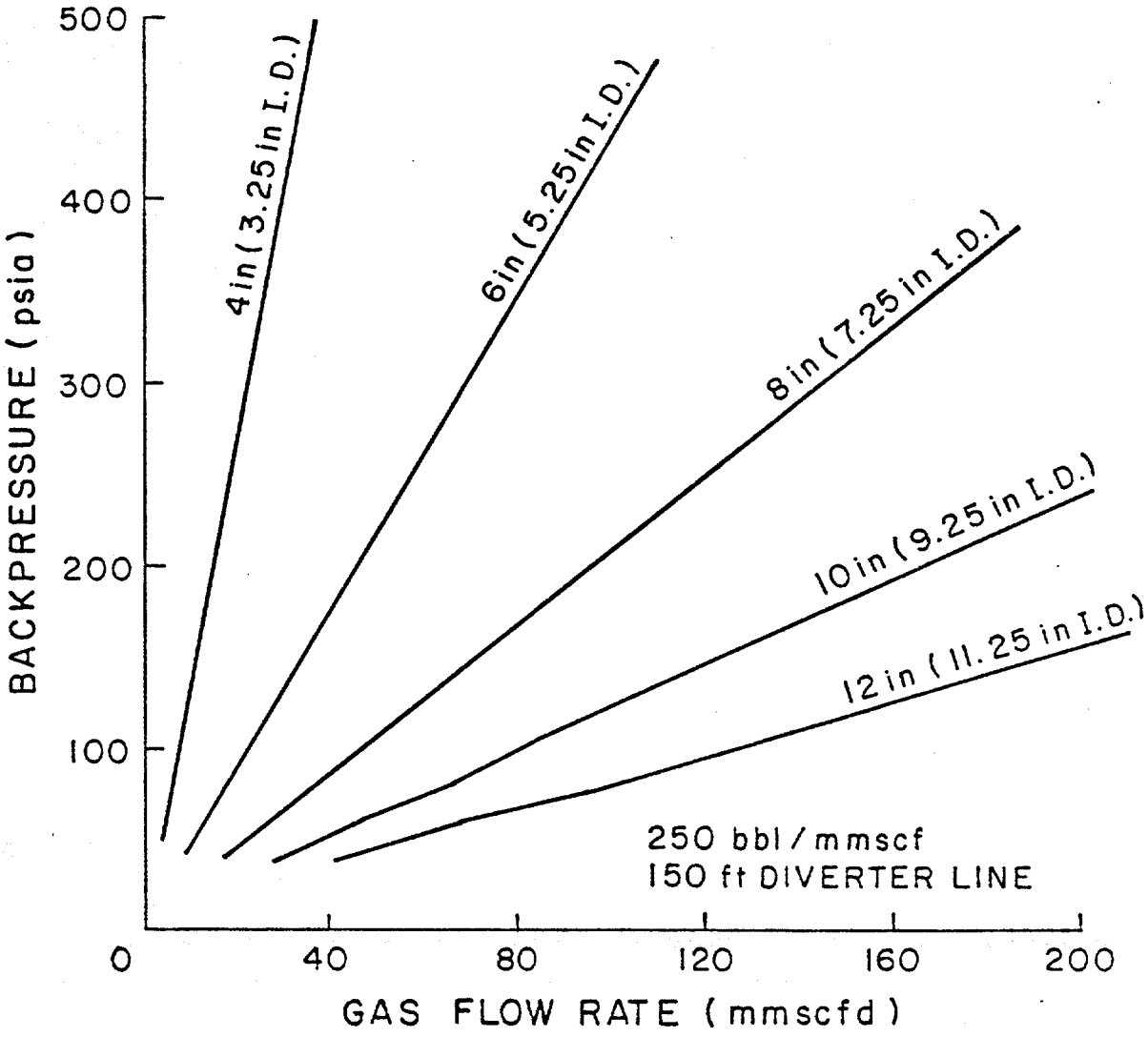

FIGURE 2.9. Diverter Backpressure Estimates for Critical Flow of Gas Containing 250 bbl/MMSCF (150 ft Equivalent Length)

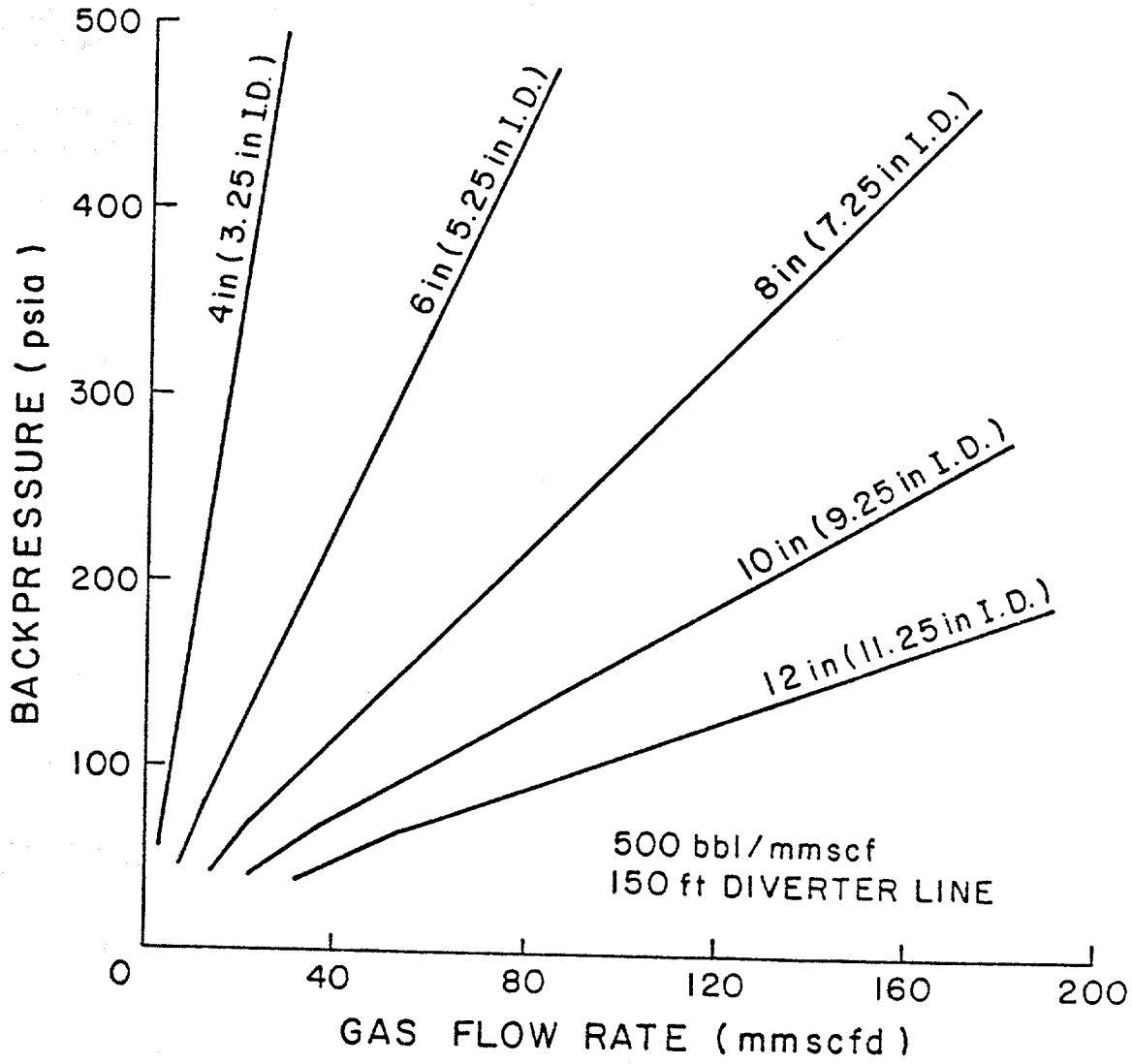

FIGURE 2.10. Diverter Backpressure Estimates for Critical Flow of Gas Containing 500 bbl/MMSCF (150 ft Equivalent length)

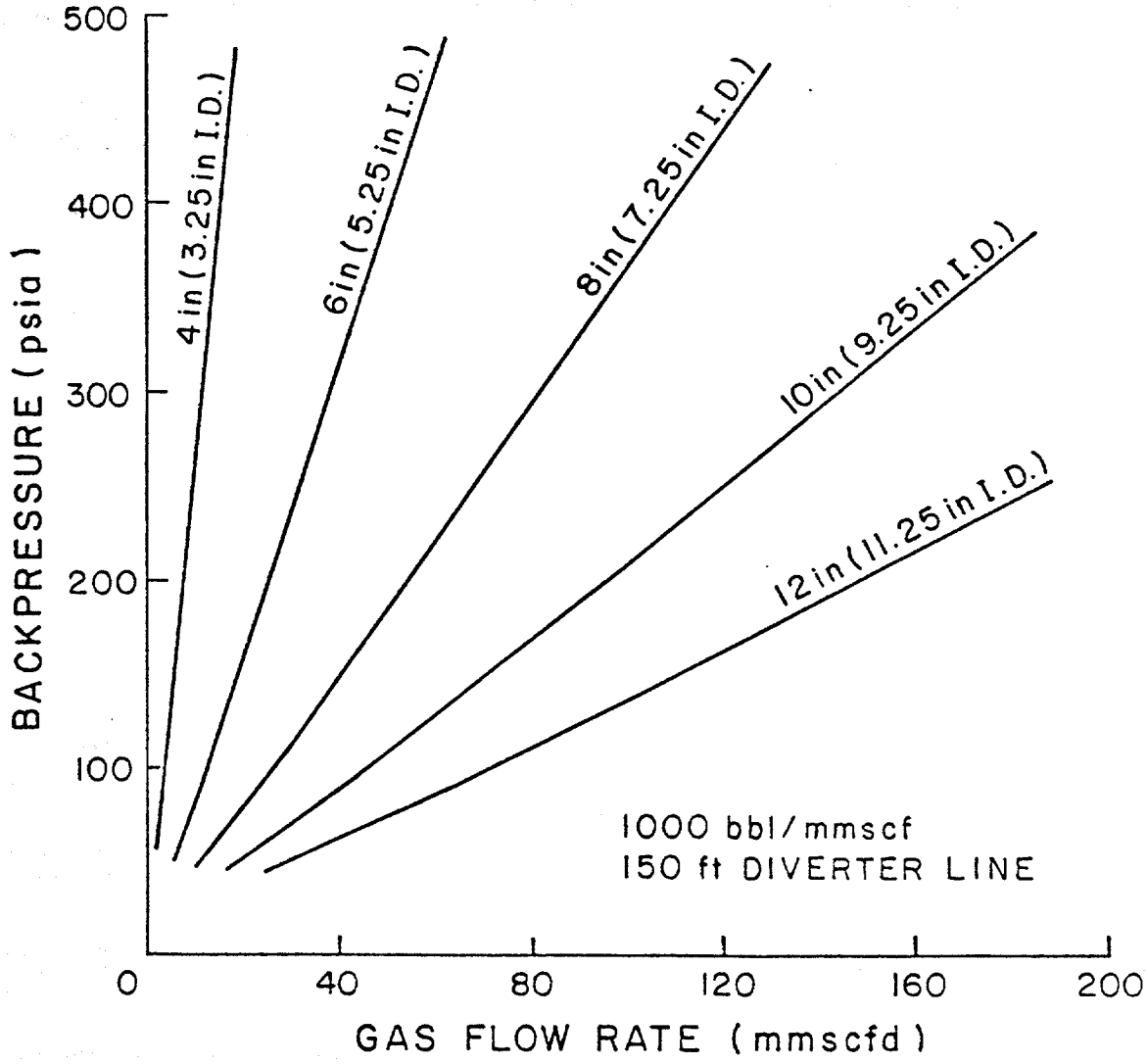

FIGURE 2.11. Diverter Backpressure Estimates for Critical Flow of Gas Containing 1000 bbl/MMSCF (150 ft Equivalent Length)

TABLE 2.6 - STEADY STATE PRESSURE DROPS FOR VARIOUS GAS AND LIQUID FLOW RATES AND PIPE DIAMETERS

4-IN NOMINAL (3.25-IN. ID)

MMSCF/D	GPM 0	GPM 100	GPM 200	GPM 300	GPM 500	GPM 1000
0	0	1.82	6.13	12.6	31.2	108
5	20.9	108	155	203	297	551
10	49.5	179	251	327	474	860
50	343	1086	1367	1655	2230	3692

6-IN NOMINAL (5.25-IN. ID)

MMSCF/D	GPM 0	GPM 100	GPM 200	GPM 300	GPM 500	GPM 1000
0	0	0.19	0.63	1.28	3.15	10.8
10	9.36	38.3	54.1	67.5	88.9	138
50	74.5	161	194	226	286	419
100	167	377	429	481	583	826

8-IN NOMINAL (7.25-IN. ID)

MMSCF/D	GPM 0	GPM 100	GPM 200	GPM 300	GPM 500	GPM 1000
0	0	0.04	0.14	0.27	0.68	2.31
10	2.36	11.9	17.8	22.8	31.5	48.1
50	27.0	57.9	68.8	78.8	96.9	136
100	62.6	119	133	147	173	232

10-IN NOMINAL (9.25-IN. ID)

MMSCF/D	GPM 0	GPM 100	GPM 200	GPM 300	GPM 500	GPM 1000
0	0	0.01	0.04	0.09	0.21	0.72
10	0.76	4.27	6.69	8.87	12.8	21.0
50	11.2	26.2	31.4	36.1	44.7	62.8
100	29.0	56.0	62.0	67.9	79.0	104

12-IN NOMINAL (11.25-IN. ID)

MMSCF/D	GPM 0	GPM 100	GPM 200	GPM 300	GPM 500	GPM 1000
0	0	0.005	0.02	0.03	0.08	0.28
10	0.30	1.73	2.79	3.80	5.67	9.83
50	5.06	12.9	15.6	18.2	23.0	33.1
100	14.6	30.0	33.2	36.4	42.5	55.9

OTHER DATA: Line Length = 150 ft; Outlet Pressure = 0 psig; Gas Specific Gravity = 0.7; Mud Density - 9.6 lb/gal; Plastic Vis. = 8 cp; Temperature = 80 F

Based on Beggs and Brill correlation; sonic velocity restrictions are ignored.

* Reprinted courtesy of Exxon Corp. from "Blowout Prevention and Well Control Manual, Floating Drilling Supplement," copyrighted February 1984.

NOMENCLATURE

Q = gas flow rate, mmscfd

P = pressure. psia

L = length, ft.

$\frac{\Delta P}{\Delta L}$ = pressure gradient, psi/ft

f = Moody friction factor

ρ = density, lbm/ft^3

d = diameter, ft.

D = diameter, inches

v = velocity, ft/sec

K = polytropic expansion coefficient, d'less

z = gas compressibility factor, d'less

γ_g = gas specific gravity (air = 1.0)

T = temperature, $^\circ$R

m = two-phase polytropic expansion coefficient, d'less

λ = holdup, d'less

x = defined by equation 9

C_{v_l} = specific heat of liquid at constant volume

C_{p_g} = specific heat of gas at constant pressure

C_{v_g} = specific heat of gas at constant volume

C = fluid compressibility, psi^{-1}

g_c = 32.172 lbm-ft/lbf-sec^2

SUBSCRIPTS AND SUPERSCRIPTS

*	-	critical conditions
g	-	gas
w	-	water
l	-	liquid
e	-	exit
std	-	standard conditions

BIBLIOGRAPHY

Brill, J. P. and Beggs, H. D.: Two-Phase Flow in Pipes, U. Tulsa, (March, 1978).

Dukler, A. E., Wicks, M., and Cleveland, R. G.: "Frictional Pressure Drop in Two-Phase Flow: B.: An Approach Through Similarity Analysis", AIChE Jour., (Jan., 1964) 44-51.

Fortunati, F.: "Two-Phase Flow Through Wellhead Chokes", AIME c1972, paper SPE 3742.

Wallis, G. B.: One-Dimensional Two-Phase Flow, McGraw-Hill Book Co., Inc., New York, 1969.

3. EXPERIMENTAL STUDY OF EROSION IN DIVERTERS BY SAND/MUD SLURRIES

One of the most common modes of diverter failure is through erosion of its component parts. The material flowing through the diverter contains a high concentration of erosive material (formation sand) traveling at very high speeds. Erosion occurs predominately where the flow changes directions. If every part of the diverter system were maintained well and functioned properly, the erosive nature of the flow stream alone can severely limit the life of the vent line.

The purpose of this study was to evaluate different pipe ells for their ability to withstand an erosive stream and recommend one fitting for use when the vent line must change directions. Six fitting designs were tested; the 1) cast short radius ell, 2) cast long radius ell, 3) cast plugged tee, 4) cast Vortice-Ell, 5) welded short radius ell, and 6) welded plugged tee. The 4 cast fittings are shown in figures 3.1, 3.2, 3.3, and 3.4 The first 3 fitting types are commonly found in the oil field whereas the Vortice-Ell is the trade name of a commercially available fitting made by the HammerTek Corporation. It is generally used in pneumatically conveyed materials-handling systems. The plugged tee is simply a pipe tee that is blanked off with a blind flange and positioned in the flow path so that the blind flange becomes a target, as shown in figure 3.5. The fittings were placed in an experimental flow loop that subjected them to an erosive stream of drilling mud and blasting sand. They were evaluated for their resistance to erosion based on 3 experimental criteria: 1) erosion pattern, 2) percent weight loss, and 3) weight loss divided by exposed surface area.

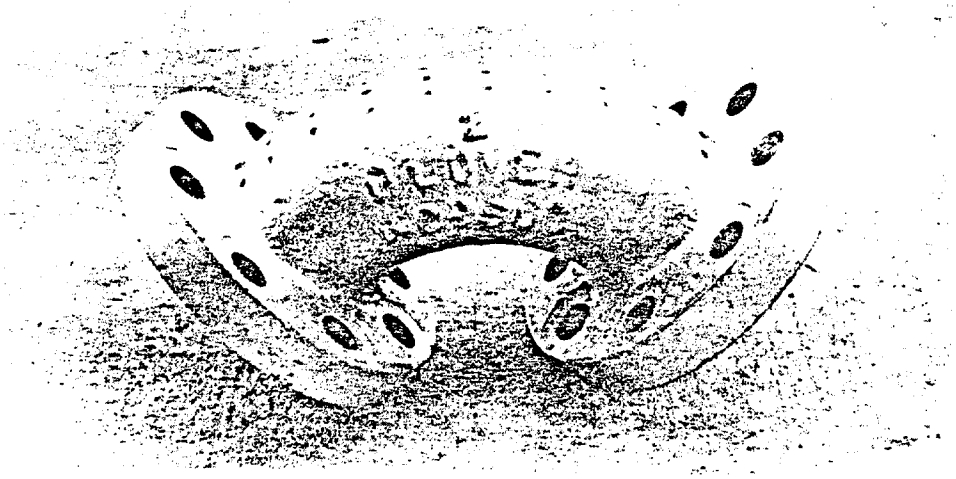

FIGURE 3.1 - SHORT RADIUS ELL

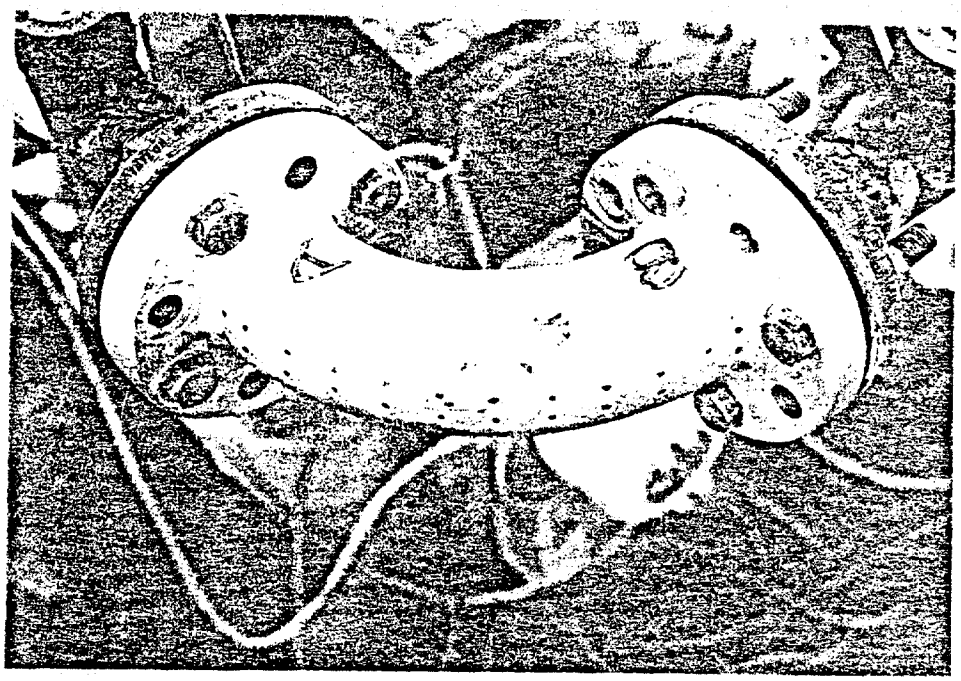

FIGURE 3.2 - LONG RADIUS ELL

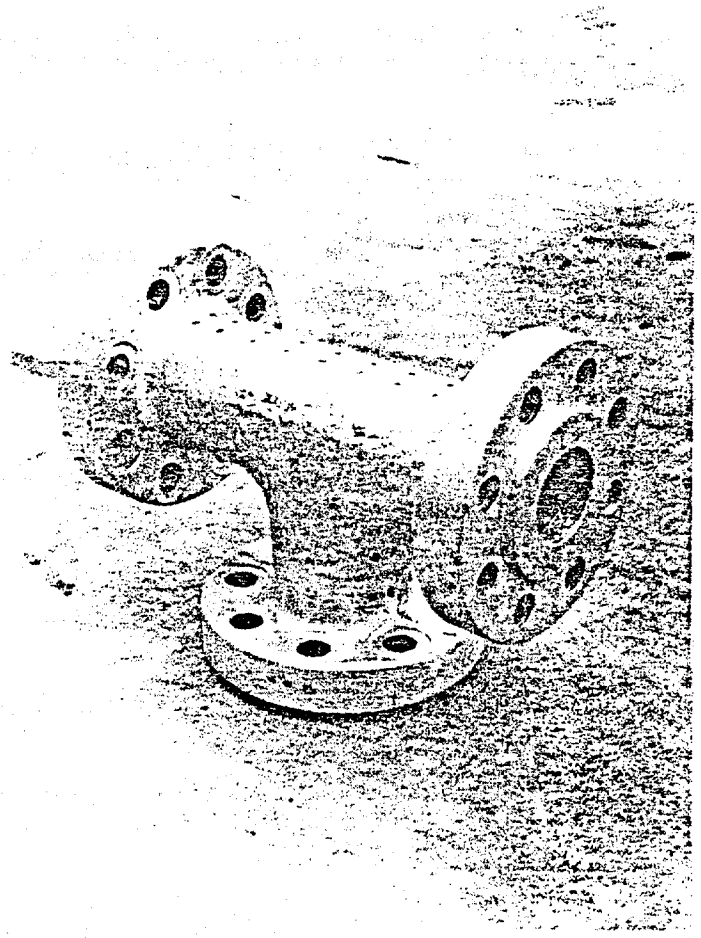

FIGURE 3.3 - PLUGGED TEE

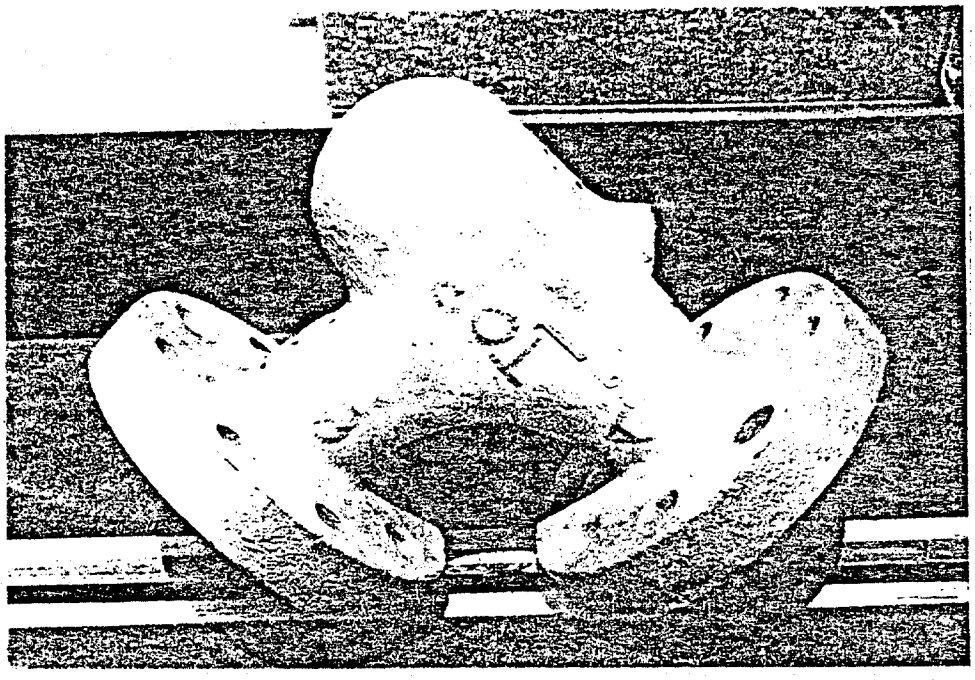

FIGURE 3.4 - VORTICE-ELL

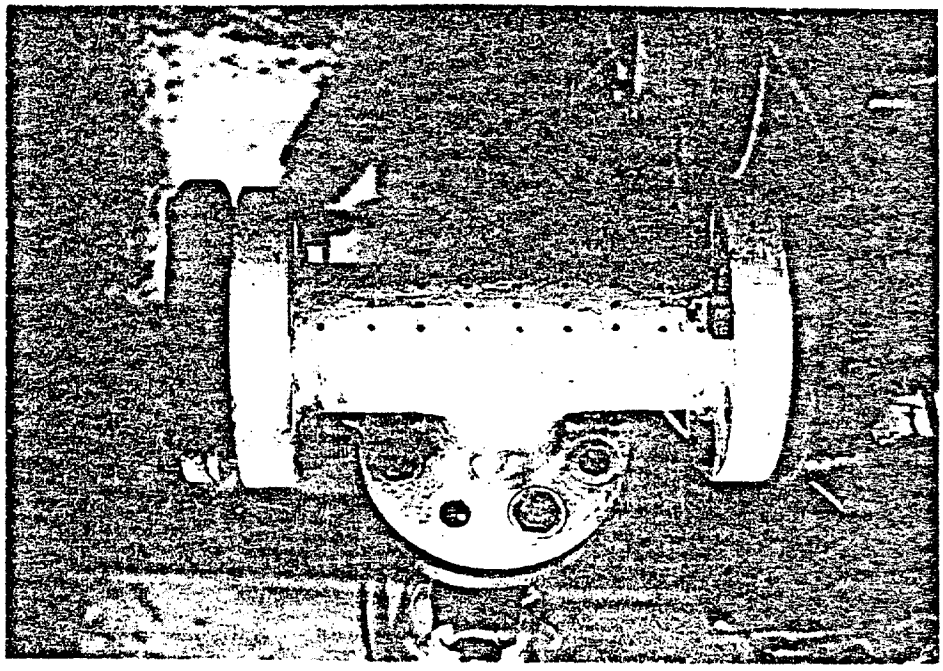

FIGURE 3.5 - PLUGGED TEE MOUNT IN THE FLOW LOOP

The aim of this project was to evaluate several different pipe bends for their relative erosion resistances. This project examined a whole system from an erosional standpoint and did not look into the mechanisms of erosion. Experiments done by the other investigators could not be used to test the pipe bends. Their experiments tested small pieces of metal for targets, not pipe ells with flanges attached. It was obvious that a new test setup was needed.

Available published erosion models also proved inapplicable to this study. Some of the input variables, such as impact angle, particle velocity, and strike efficiency, could only be obtained with blast tube and whirling arm type equipment. Angle of attack was undefined in this work because the erosive stream underwent a sweeping 90 degree change in direction. Typical laboratory experiments use high speed photography to measure particle velocity. With a slurry flow, the particle velocity could only be calculated. All of the models were developed with the abrasive traveling through air or a vacuum, but this study used liquid as the carrying fluid. This experiment used a particle size that varied over a much wider range than the laboratory experiments. Also, published mathematical models often require experimental values obtained from calibration test runs. These calibration values can only be obtained from laboratory type experiments.

For these reasons, the pipe ells were tested with an entirely different experimental setup. The ells were mounted in a flow loop and an abrasive fluid was pumped through the system. Erosion was evaluated by 3 means: 1) erosion pattern, 2) weight loss divided by exposed surface area, and 3) percent weight loss. Since abrasive concentration controls the width of the eroded channel, erosion pattern became the

primary evaluation criterion. Percent weight loss was used because the standard definition of erosion could not be applied. And weight lost per exposed surface area accounted for material loss at the flanges.

Experimental Setup

An experimental flow loop was constructed to simulate formation fluids blowing out through a diverter system. Figure 3.6 is a sketch of the experimental setup. Drilling mud flowed from the right side of the tank to the pump, through 20 feet of 2 inch inside diameter pipe, through the pipe ell, and back into the tank. The pipe ell was the erosional target of this whole experiment. Blasting sand was added to the mud to simulate formation sand being carried through the diverter. A Harrisburg 178, 5x6 inch centrifugal pump was used to move the slurry through the flow loop.

Abrasive Slurry

The mud was a simple mixture of bentonite clay, caustic soda, and water. The clay raised the viscosity of the mud and held the sand in a suspension. Number 2 blasting sand was chosen as the abrasive because it is well graded and more closely simulates formation sand than #1 blasting sand. Two propeller type mud agitators were installed in the tank in order to keep the sand from settling. In a further effort to keep the sand suspended, only the right side of the tank was filled with mud. By sucking and discharging from just the right side of the tank and leaving the left side empty, the mud was subjected to much more

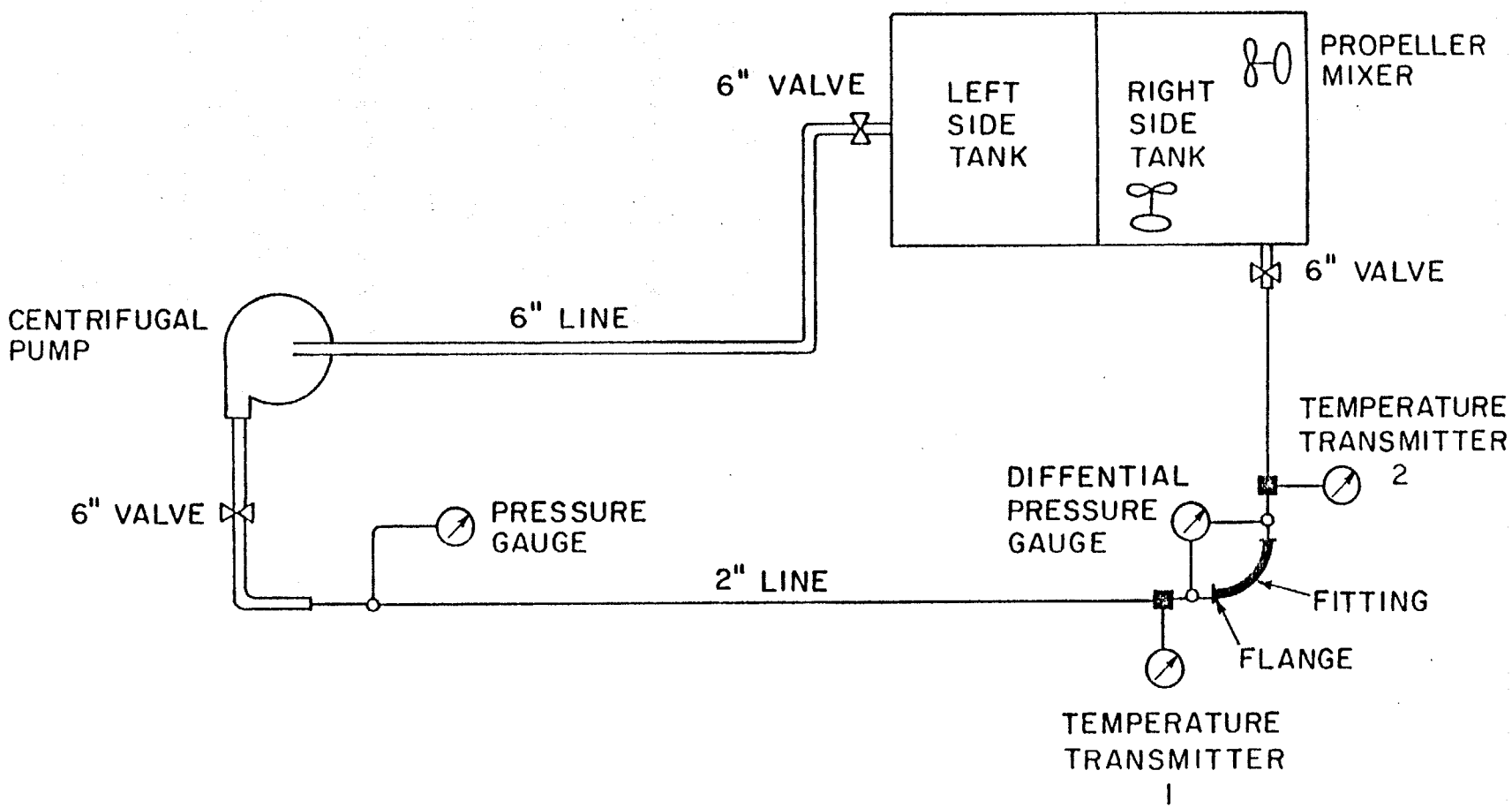

FIGURE 3.6 - SCHEMATIC OF THE FLOW LOOP EXPERIMENTAL SETUP

turbulence. All attempts were made to insure that the slurry had a smooth flow pattern as it reached the fitting. The 20 feet of flowline helped reduce the pump effects. All weldment burrs in the flowline were ground smooth. And raised face flanges provided smooth connections between the flowline and the fittings.

Measurements of Erosion

The pipe fitting was weighed once before and once after running through the flow loop. The scale, an Accu-Weigh III, model 301 TDX, had a rated sensitivity of 0.01 pounds. The wall thickness of the pipe fittings were measured using an ultrasonic thickness device. Comparison of wall thicknesses before and after the test gave insights into the wear pattern of each fitting.

Flow Loop Data

Several measurements were taken while the experiment was being run. These include flow rate, flowline pressure, differential pressure across the fitting, temperatures upstream and downstream of the fitting, sand content, and mud properties.

Flow rate was measured by recording the change in height of the mud level in the tank after a certain amount of pumping time. Under normal running operations, the left tank was left empty and the right tank was always full of mud. Certain valves were opened that allowed the mud to flow from the right tank to the left tank until their levels equilibrated. The suction line from the right tank was then closed causing the pump to

draw from the left side only. Since the flow loop discharged into the right tank only, the mud level in the left tank dropped and that in the right tank rose. By measuring the change in fluid level, the time elapsed, and the tank dimensions, the pump flow rate was easily calculated. The whole process was repeated 3 times and an average value taken.

Mud/sand slurry samples were taken from a 1 inch valve located on the suction line to the centrifugal pump. Samples were taken at least once a day and were used to measure the sand concentration and the mud properties. Measurements made on the slurry itself included sand concentration, sand sieve analysis, mud density, viscosity, and yield point determinations.

A large graduated cylinder was used to measure the sand concentration (volume percent) of the slurry sample. The sample was poured into the cylinder, a known volume of water added, mixed by shaking, and the sand settled to the bottom of the cylinder. The volume of sand and volume of mud were read off the graduations on the bottom of the cylinder. To measure changes in the initial grain size distribution, the sand from the mud samples was washed and dry sieved. The grain size distributions are plotted along with the initial sand and presented in the Appendix. To measure the mud properties, the samples were put in a centrifuge until the sand separated from the mud. The mud density was measured with a Magobar mud balance, and viscosity and yield point were measured with a Fann viscometer.

Smaller mud samples were taken daily in order to monitor the slurry's sand content. Over a period of 24 hours some of the sand had a tendency to settle out and the water tended to "boil" out of the slurry. A small sample was collected in a special sand content tube which gave sand

content from graduations on the bottom of the tube. After monitoring the mud, corrective measures could be taken to return the slurry properties to their desired values. These small samples were not used to find the slurry's true sand content because, it was felt, the larger samples were more representative.

Flowline pressure was measured using a Gould, series PG 3000 pressure transducer. The transducer was located just downstream of the pump on the 2 inch flowline. Differential pressure across the pipe fitting was measured with a Rosemount, type 1151 DP differential pressure cell. Fluid ports were drilled in the flow loop 4 inches upstream and downstream of the fitting flanges. Two RdF Corporation, series 2600 temperature transmitters were placed 1 foot upstream and downstream of the fitting flanges. The temperature sensors were strapped to the outside of the flowpipe and wrapped with insulation material.

All of the electronic sensors were calibrated in the lab to a zero response of 4 milliamps and a high range response of 20 milliamps. An operating voltage of twenty volts DC was applied to the instruments, their measuring signal channeled through a 4 channel switch, and the return current signal measured with a Fluke ammeter. The ammeter readings were entered into a handheld calculator that was programmed to convert the milliamp responses into pressure and temperature values. The program used the linear responses of the instruments as defined by the zero and range readings.

Choice of Materials Used

The types of steel, sand, and mud chosen for this experiment were selected on the basis of their availability to both the industry and the experiment. All fittings were made of steel with ASTM specification A216, grade WCB. This is a common grade of steel and is frequently used for oil field tubulars. Using a soft steel allows the experiment to examine a worst-case diverter system. The soft steel also eroded faster, making the results more dramatic. The sand was commercially available #2 blasting sand and had a large range of grain sizes. The simple drilling mud provided the fluid viscosity necessary for keeping the sand in suspension.

The entire experimental method proceeded as follows. The outside of the fittings were painted with a rust proofer and the thickness measurement locations painted on. The fitting was then weighed, ultrasonically tested, and flanged up to the flow loop. A premixed volume of mud was pumped from a mud storage tank to the flow loop tank and a known volume of #2 blasting sand was added to the mud. The centrifugal pump was turned on and pressure, differential pressure, temperatures, flow rate, sand content, and mud properties were measured. Every 24 hours these measurements were taken again and any mud conditioning was done. Each fitting was run for a total of 90 hours circulation time. The fitting was then removed from the flow loop, washed, re-weighed, and re-thickness tested. With each new fitting, the mud and sand were replaced to insure that each fitting was subjected to the same erosive stream.

Several changes were made to the original equipment setup. Each change was made in response to a particular problem that arose. Fortunately, most of the changes were made while testing the welded short radius ell, test Run #1. This was considered a trial run expressly for ironing out any experimental problems.

Run #1 was a test of a short radius fitting with the flanges welded on. The original set up included 1 centrifugal pump with a 9 inch impeller. The flow rate over a run time of 62 hours run time was 7.24 gallons per minute. The fitting weight loss was low and the ultrasonic thickness test showed a maximum of 0.03 inches of pipe wall material removed. The results of Run #1 were discouraging, to say the least. This small amount of erosion demanded that changes be made to the original setup.

The first change was to add a second centrifugal pump in parallel with the first pump. This pump also had a 9 inch impeller. Table 3.1 lists the pressures and flow rates delivered by the pumps.

TABLE 3.1

NINE INCH IMPELLER OUTPUTS

	flowline pressure (psi)	flowrate (bbl/min)
pump #1	27.8	7.22
pump #2	28.7	7.58
combo	28.7	7.67

The above data indicates that the flow rate was not raised significantly by adding a second pump in parallel with the first.

The next change was to swap-out the 9 inch impellers for two 12 inch impellers. Table 3.2 lists the pressures and flow rates of each pump run alone and in combination.

TABLE 3.2

TWELVE INCH IMPELLER OUTPUTS

	flowline pressure (psi)	flowrate (bbl/min)
pump #1	48.0	10.96
pump #2	46.5	10.48
combo	47.2	11.20

A significant increase in flow rate was realized by changing from a 9 inch to a 12 inch impeller. The benefits gained from using the 12 inch impeller were immediately realized. The welded short radius ell was mounted back in the flow loop. After only 67 hours, the ell eroded and a hole developed.

The 2 pumps were run alternately for 24 hour periods. When not in use, the idle pump was isolated from the flow loop by closing a butterfly valve at the discharge line. Run #2, the welded plugged tee, was terminated early when one of the pump housings developed a hole and all the mud/sand slurry was pumped out of the system. The exact time that this happened was not known, but did develop some time after the system was checked that night. So the elapsed time for this run was known to only plus or minus 4 hours. After this problem, the flow loop was converted back to a 1 pump system with one 12 inch impeller.

During Run #1, the pumps were only run during the day. Pressure and temperature measurements and mud samples were taken all throughout

the day. Since these parameters changed very little in a day's time, the move to one suite of measurements per day was justified. Also, by running the pump continuously, some variations in the data were eliminated. The mud did not cool off overnight as it did whenever the pump was turned off. With a constant temperature, the mud maintained a more constant viscosity. Viscosity affected both the mud's carrying capacity and the pump's discharge pressure.

By switching from an 8 hour run period to around the clock experimentation, the fitting would be expected to erode in one third the number of days. But if the fitting were to wear out during the middle of the night, all the mud would be lost from the system and the exact end of the run time would not be known. To eliminate this uncertainty, it was decided to run all the fittings on a predetermined length of time rather than running until the fitting wore through. This normalized the run times so that all the individual wear patterns and weight changes could be compared to each other. A run time of 90 hours was chosen because that was the elapsed time when the pump motor burned out on the cast short radius ell.

One other noteworthy change was made on the flow loop system. A butterfly valve, located in the return leg, was replaced with a 2 inch ball valve. This proved to be a futile effort since this valve eroded worse than the butterfly valve. The ball valve was left fully open throughout the entire experiment but the brass housing eroded and the stainless steel ball remained intact.

Three criteria were used in evaluating the erosion resistance of the pipe ells: 1) erosion pattern, 2) weight loss divided by exposed surface area, and 3) percent weight loss. Erosion pattern was illustrated

with plots of the ultrasonic thickness test data before and after running in the flow loop. Weight loss per surface area is the change in fitting weight divided by the inside surface area of the fitting, expressed in pounds per square inch. And percent weight loss is simply the calculated percent change in fitting weight.

Table 3.3 is a summary of the test results and the experimental flow loop data for all the fittings. The Appendix contains a detailed listing of all the experimental data.

The "BEFORE" and "AFTER" thicknesses were plotted against the distance along the fitting (from the upstream to the downstream positions). BEFORE thicknesses appear as a bold line while AFTER thicknesses appear as a thin line and have symbols at each data point. The different symbols correspond to 3 different rows of ultrasonic thickness measurements: top, middle, and bottom. The 3 rows give a good picture of the erosion pattern and indicate whether the erosion was uniform over the fitting surface or if channeling erosion predominated. All fittings were mounted in the flow loop in such a way that the fluid flowed in a horizontal plane. They were all thickness tested along their center lines as well as along lines 1/2 inch above and 1/2 inch below their center lines. The words "TOP" signify the row that was above the center line and "BOTTOM" signifies the row below the center line. The symbol for the top row is a "Y", the center row is a "X", and the bottom row is a "+".

Each fitting was ultrasonically tested on both the outside and inside radii of curvature. Correspondingly, there are 6 plots for each fitting; 1 plot for each row and 3 rows per side. One exception to this was the short radius ell. Only the center line was tested on the inside radius. This fitting was run early in the experimental process and, at that time, it was felt that 3 rows per side were unnecessary.

Table 3.3

SUMMARY OF EXPERIMENTAL DATA

Fitting Type	Change In Weight (lb)	Weight Change / Exposed Area (lb/in^2)	Percent Change In Weight (%)	Maximum Change In Thickness (in.)	Pump Flow Rate (bpm)	Percent Sand Content (Vol %)	Flowline Pressure (psi)	Differential Pressure (psi)	Upstream Temp. (°F)	Downstream Temp. (°F)
Short Radius Ell	0.64	0.0136	2.45	0.056	8.8	6	55.7	2.59	160	158
Plugged Tee	1.57	0.0222	3.66	0.308	9.8	8	51.5	6.78	149	147
Long Radius Ell	1.46	0.0258	6.46	0.338	11.2	3	43.1	1.17	151	150
Vortice Ell	1.89	0.0222	3.06	0.360	10.7	11	49.7	7.93	181	180

On a few plots the AFTER line appears above the BEFORE line. This does not mean that the wall thickness increased as a result of running the flow test. It was actually caused by one of the routines used by the Benson computer plotter. The computer tries to draw as smooth a curve as possible through all of the data points. Sometimes the smoothest AFTER curve lies above the smoothest BEFORE curve. Since each thickness test point was marked with a symbol, it is easy to see that these overlaps do not occur at an actual data point.

The BEFORE and AFTER curves illustrate the erosion patterns of each fitting. The plots from one fitting can be compared with those of another since each plot uses the same ordinate scale (thickness axis).

When evaluating a certain erosion pattern it is important to keep in mind the distance along the fitting where the erosion occurred. The fitting sketches indicate the locations of the measurement points. The Vortice-Ell has an unusual shape and, thus, has several distinct erosion patterns. Again, refer to the fitting sketches for the exact location of the data points.

Erosion pattern could not be determined over the entire eroded surface. The ultrasonic thickness readings could not be made closer than 1/2 inch to any flange face. Any erosion near the flanges are not accounted for in the plots. Weight change per exposed surface area and percent weight change take into account erosion over the fitting's entire inside surface. Dividing weight change by inside surface area normalizes the losses of each fitting so they can be compared directly.

It is important to realize that the smallest percent weight loss does not necessarily indicate the highest erosion resistance. If erosion occurs in only a small, concentrated area, the fitting will experience a

small weight loss. If this concentrated erosion were allowed to continue until a hole developed, the fitting would fail, yet only a small amount of material would have been lost.

Fitting weight that is not subjected to the erosive stream (flange weight) has the effect of artificially holding percent weight change low. If a fitting loses a considerable amount of material and its weight change is divided by a large initial weight, the percent change in weight will remain small. Thus, to get a true indication of a fitting's erosion resistance, percent weight change must be used in conjunction with erosion pattern and weight loss per surface area.

Not one section of straight pipe failed throughout the entire experiment. In fact, the straight pipe and the mud tank were the only 2 pieces of equipment that did not fail at some time during the investigation. The straight portions of the flow loop withstood a total of 547 hours of mud circulation. These sections were not ultrasonically thickness tested, but there was no indication that appreciable amounts of erosion took place. The 2 inch line held up equally as well as the 6 inch line. Even the reduction and expansion swages showed no visible signs of wear. The straight section of the plugged tee further supports this finding. Minimal erosion is evidenced by its thickness plots. Thus it was confirmed that the most reliable means of preventing vent line erosion failure is by designing the diverter with no bends.

One line failure did occur, but it happened just downstream of a welded connection. The 2 inch return leg failed just downstream of where a flange was welded on. After closer inspection, it was apparent that the weldment material stuck out into the slurry flow and altered the flow pattern. The swirling flow eroded the pipe in a small, concen-

trated area. Further downstream, the pipe wall thickness appeared uniform. As will be mentioned in the next section, smooth welded connections are recommended to prevent this type of point erosion. It is interesting to note that the weldment material was not worn smooth by the erosive slurry.

Several valves failed during this experiment. The butterfly valves eroded very quickly as did a 2 inch ball valve. The ball valve did not have an opening as large as the inside diameter of the pipe. In the butterfly valve, the pipe wall eroded right at the junction where the valve pivot and the pipe wall met. The only valve that remained intact was the 6 inch butterfly located at the bottom of the mud tank where the fluid velocity was low and flow path was undisturbed. These findings indicate that restrictions and disturbances in the flow path tend to promote erosion at or near the disturbance. It appears important that all valves be full opening and of the same size as the vent line. The valve's passage way should be as smooth as possible so as not to alter the flow path. The valve housing should be made of a material as hard or harder than the line pipe.

Welded Fitting Performances

The welded fittings were tested in the flow loop the same way as the cast fittings. But, because of the many problems encountered with initially setting up the equipment, the experimental variables could never be held constant. Several data were not recorded correctly or were not recorded at all. The welded fitting runs were used mainly for working out problems in the experimental procedure.

The results of the welded short radius ell and the welded plugged tee are given in the back of the Appendix. If the plots are compared with those of the cast fitting counterparts, no correlations can be drawn. Wide variations in erosion pattern are expected because the weldment material alters the flow pattern. Even between 1 of the same type of welded members, erosion patterns are expected to vary widely. For these reasons, the welded fittings were not considered in the evaluations. To reduce the effects of an altered flow path, it is suggested that all welded connections be made as smooth as possible.

Cast Fitting Performances

Based on the 3 erosion criteria, fittings were analysed and ranked for their resistance to erosion, from most resistant to least resistant.

1st - short radius ell

2nd - plugged tee

3rd - long radius ell

4th - Vortice-Ell

Plots of the erosion patterns are presented in this chapter and are followed by analyses of the fitting's overall performance.

The flow loop data shows that the long radius ell had the lowest pressure drop of all the fittings. Pressure drop in the vent line is an important consideration because the pressure is transferred to the formation in the form of backpressure. The short radius ell also created a small pressure drop. The plugged tee and the Vortice-Ell both caused substantially higher pressure drops. The fittings were evaluated on the basis of erosion resistance and not on pressure drop, so the short radius ell is still the preferred fitting.

From careful examination of the data summary table and erosion patterns, it is apparent that there is no direct correlation between the amount of erosion and sand content. The grain size distribution plots did not correlate with erosion either. This finding suggests that complex relationships are at work and further supports the use of erosion pattern and weight loss as the evaluation criteria.

Erosion patterns for the short radius ell is shown in Figure 3.7. The short radius ell showed the smallest percent weight loss, 2.45%, and the smallest weight loss per exposed area, 0.0136 psi. Its value of maximum pipe wall thickness change, 0.056 inches, was also the lowest of the fittings. All of these figures and the erosion pattern suggest that a very small amount of material was removed.

The small amount of erosion that did occur was all uniform in pattern. This suggests that the whole fitting would uniformly wear thin and fail only after a long flow time. The lack of any concentrated erosion was the primary reason for ranking the short radius ell number 1 in erosion resistance.

The inside radius plot indicates the minimal amount of erosion that took place. The first point (at the inlet) corresponds to a thickness change equal to 0.02 inches and the other points represents about the same amount. Ultrasonic tests were run only at the centerline on the inside radius. Based on the erosion pattern of the long radius ell, it was assumed that top and bottom rows would have exhibited the same erosion patterns as the center row.

The outside radius plots also indicate small amounts of material loss. The pattern shows no areas of concentrated erosion. A minimum amount of erosion occurred at the inlet and increased continuously from

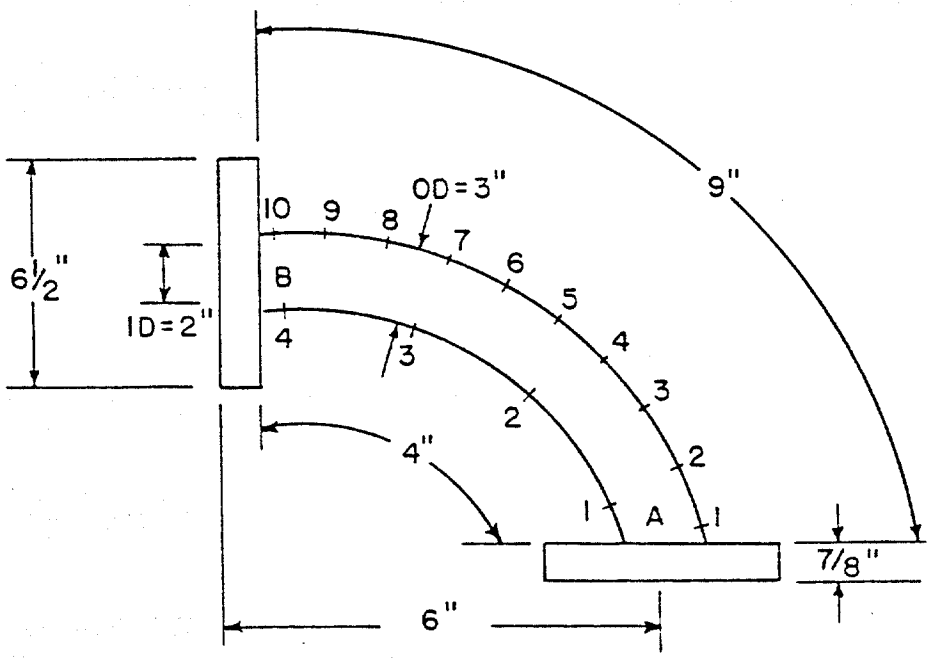

FIGURE 3.7a - SHORT RADIUS ELL GEOMETRY

OUTSIDE RADIUS

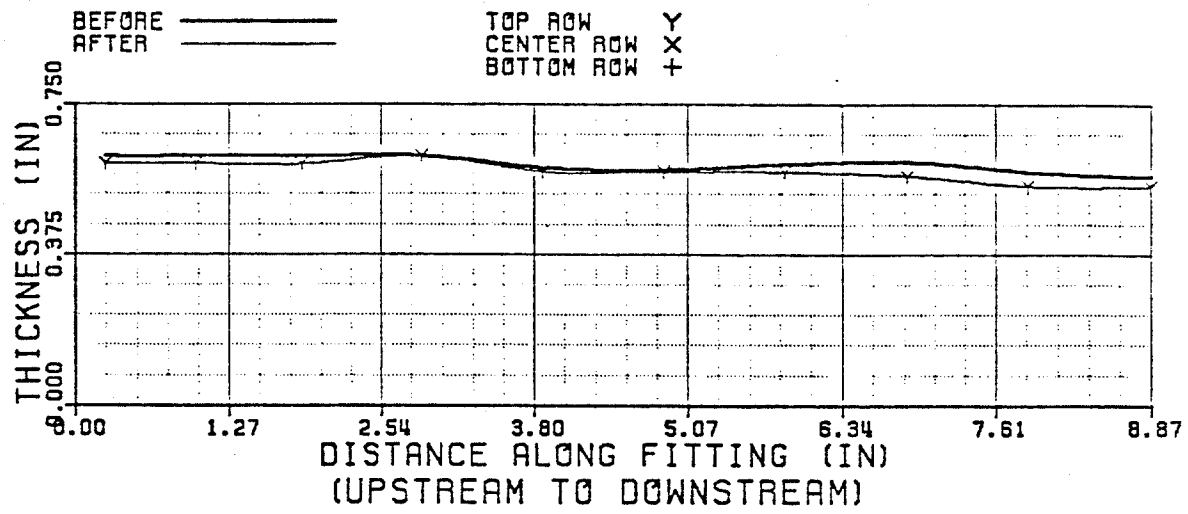

CAST SHORT RADIUS ELL
OUTSIDE (A TO B)

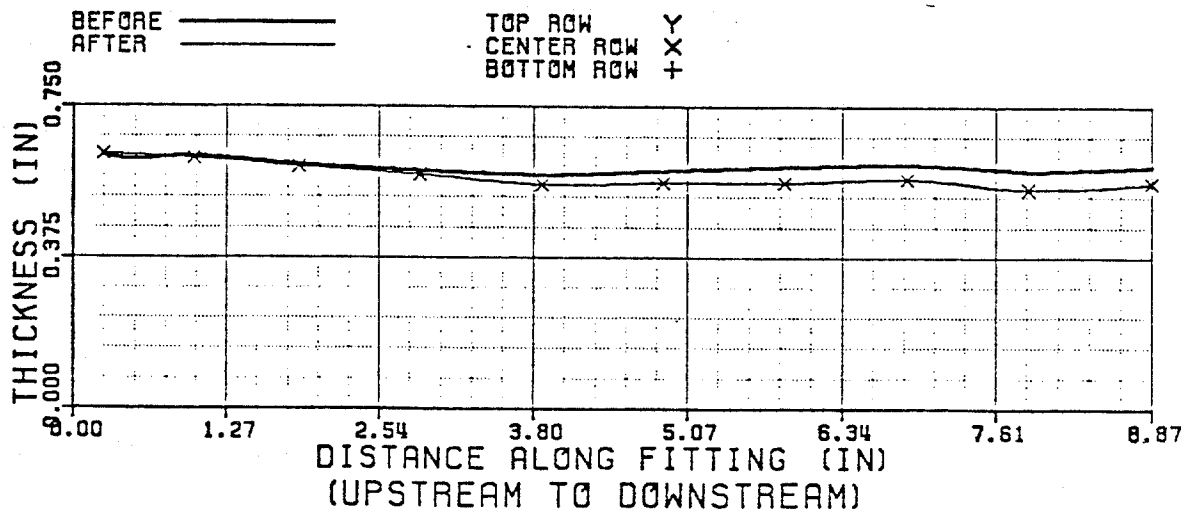

CAST SHORT RADIUS ELL
OUTSIDE (A TO B)

FIGURE 3.7b - Short Radius Ell Erosion Patterns

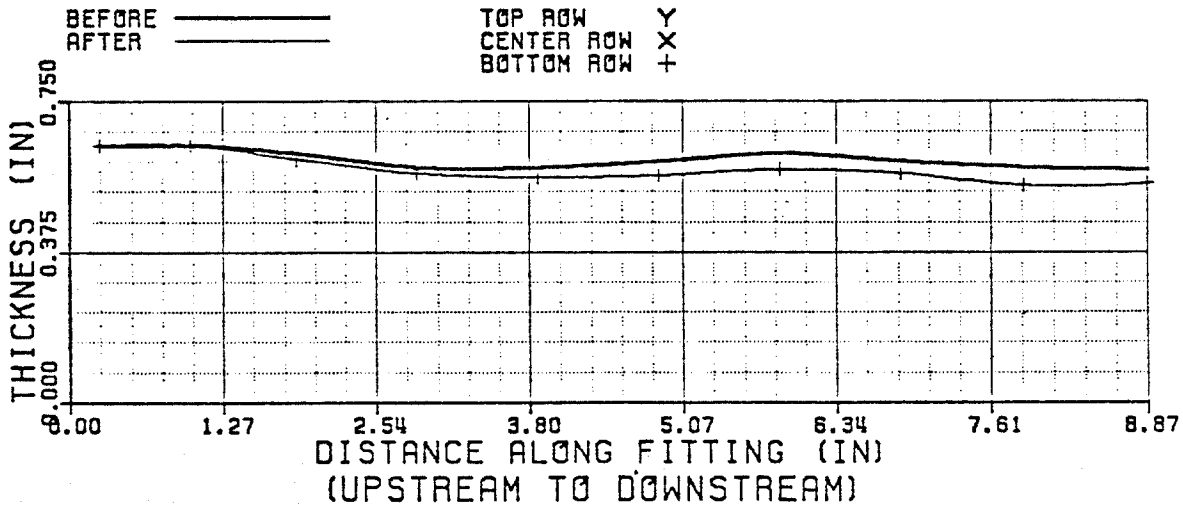

CAST SHORT RADIUS ELL
OUTSIDE (A TO B)

FIGURE 3.7b - (Continued)

INSIDE RADIUS

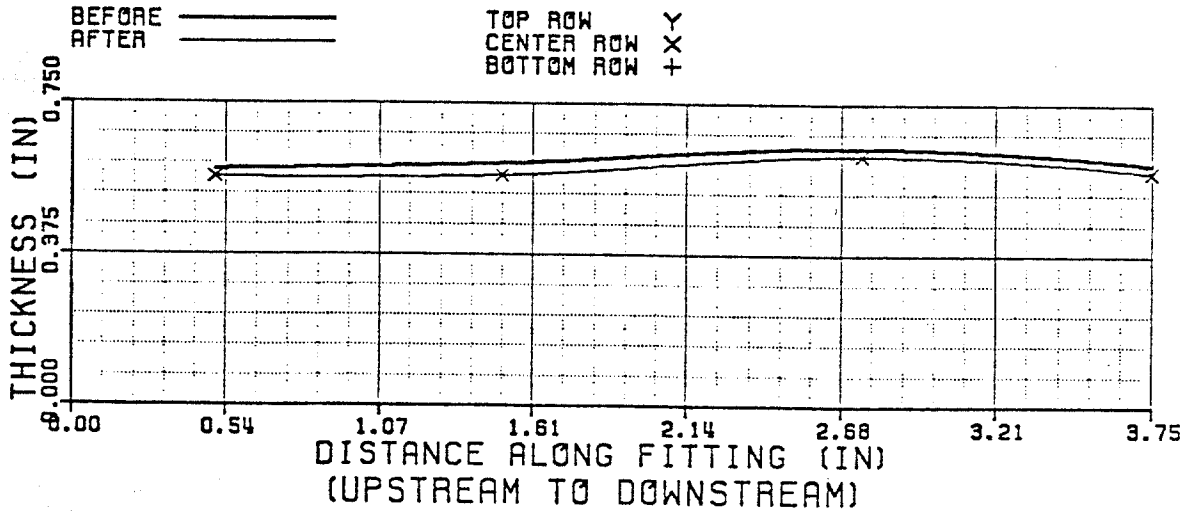

CAST SHORT RADIUS ELL
INSIDE (A TO B)

FIGURE 3.7b - (Continued)

the inlet to the outlet. The maximum thickness change at the exit, 0.056 inches, was still very small in magnitude.

The short radius ell received the highest ranking for erosion resistance to a sand/mud slurry because it was not limited by any criteria.

The erosion pattern for the plugged tee fitting is shown in Figure 3.8. This fitting lost a considerable amount of material, as evidenced by the weight loss per surface area figure. The plugged tee has 3 flanges, 1 more than the other fittings, so the percent change in weight was artifically held low by the third flange. The plugged tee lost 0.0222 pounds per square inch, yet only showed a 3.66 percent change in weight. This is a relatively large amount of material loss when compared with the weight losses of the other fittings.

The plugged tee has 2 inside surfaces and 1 outside surface, as shown in the drawing. The straight section from A to B underwent only a slight amount of uniform erosion. Since there were no areas of concentrated erosion, this portion of the plugged tee is not expected to be a limitation in the useful life of this fitting.

The A to C inside radius, from the inlet to the exit, displays considerable erosion at the exit. Almost no erosion occurred at the inlet, but thickness change at the exit was as large as 0.31 inches. This is a very large amount of material loss and was the main reason for ranking the plugged tee below the short radius ell.

The dead-end section, B to C, shows a similar wear pattern as that of section A to C. Very little erosion occurred at the inlet and a great deal of material was lost at the exit. This data also suggests that the plugged tee is limited by erosion at its exit. Combined with the plots from A to C, this data shows that erosion occurs uniformly around the exit and not preferentially to one side.

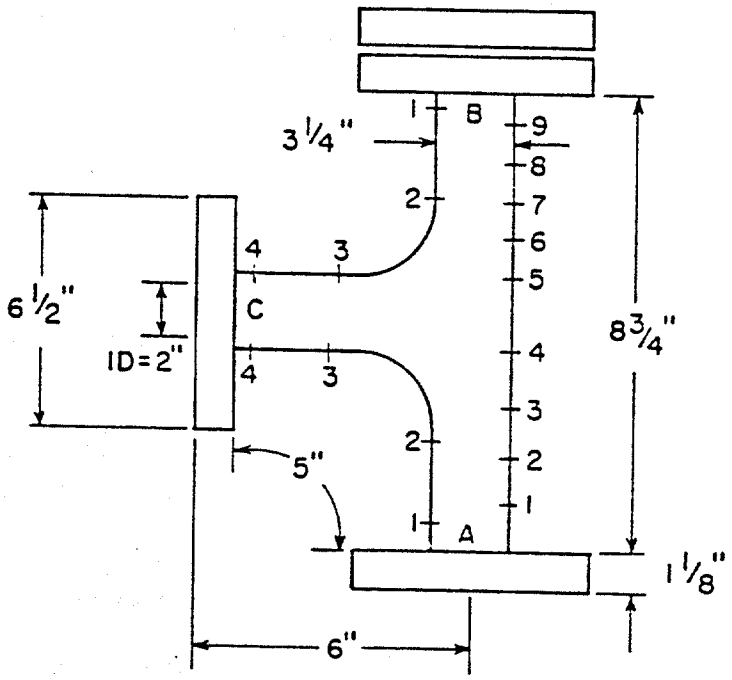

FIGURE 3.8a - Plugged tee geometry

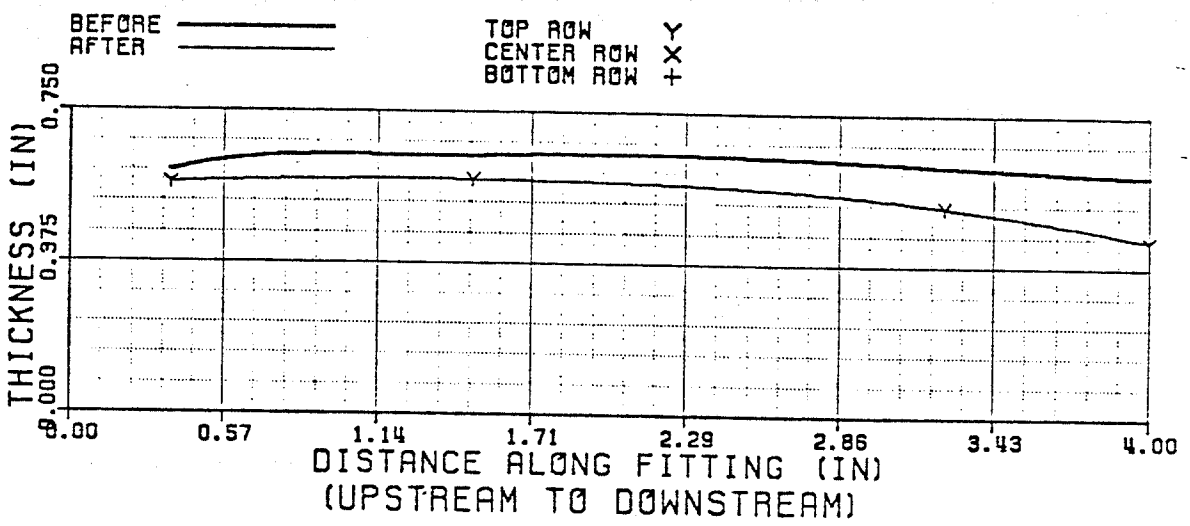

FIGURE 3.8b - Plugged Tee Erosion Patterns

INSIDE RADIUS

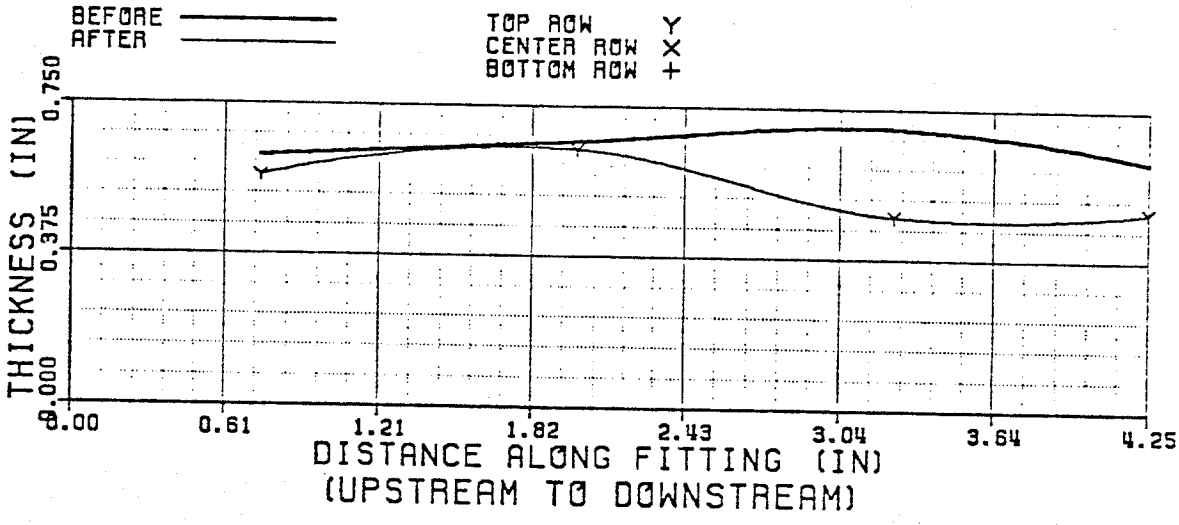

CAST PLUGGED TEE
INSIDE (B TO C)

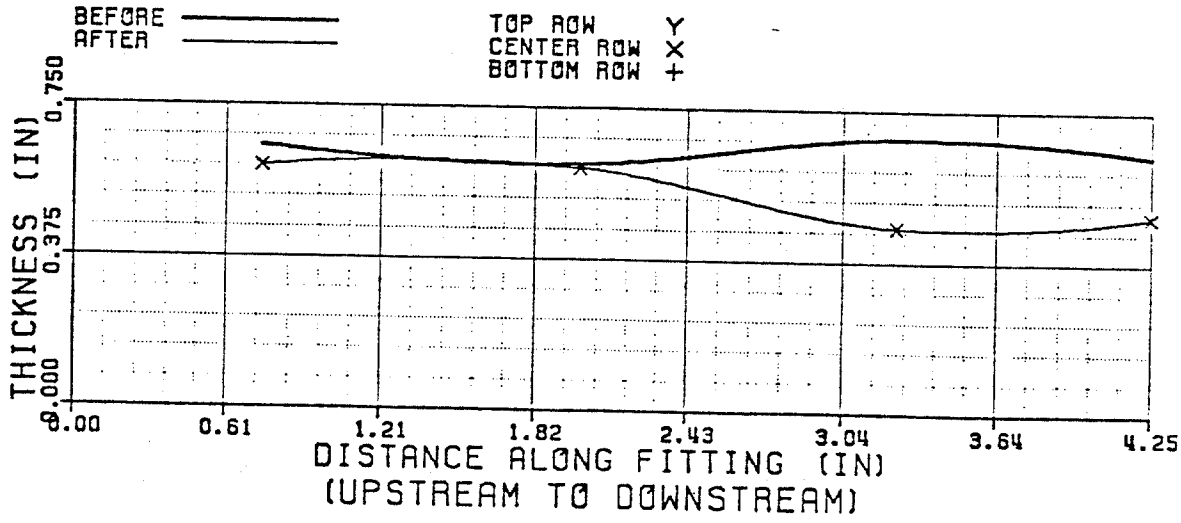

CAST PLUGGED TEE
INSIDE (B TO C)

FIGURE 3.8b - (Continued)

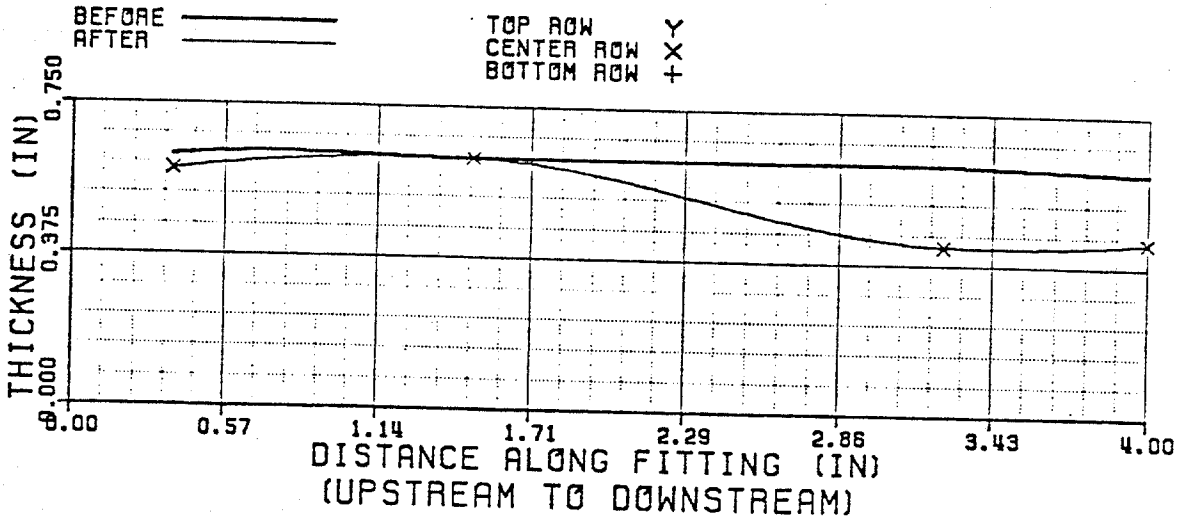

CAST PLUGGED TEE
INSIDE (A TO C)

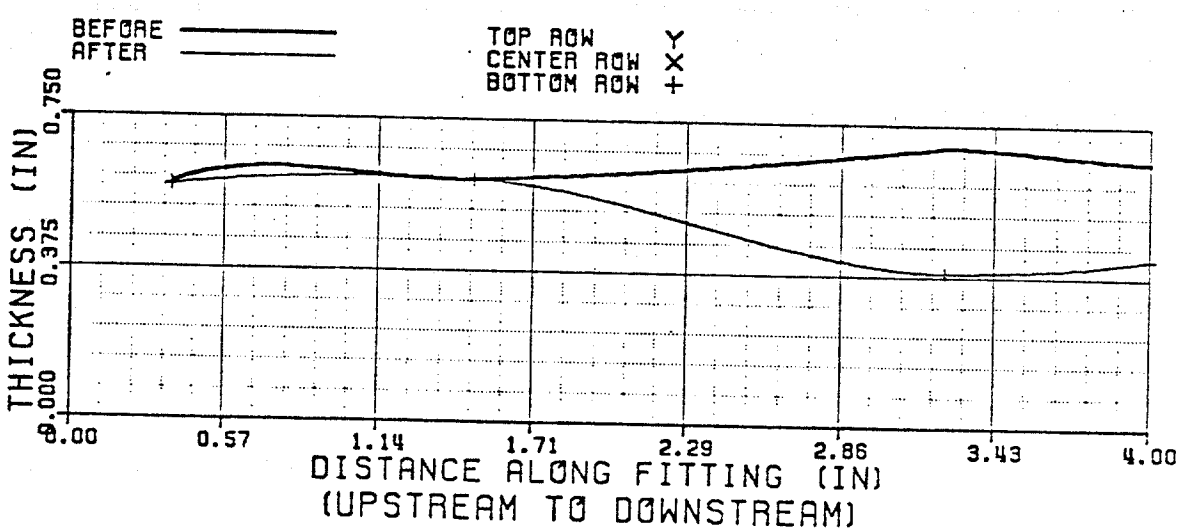

CAST PLUGGED TEE
INSIDE (A TO C)

FIGURE 3.8b - (Continued)

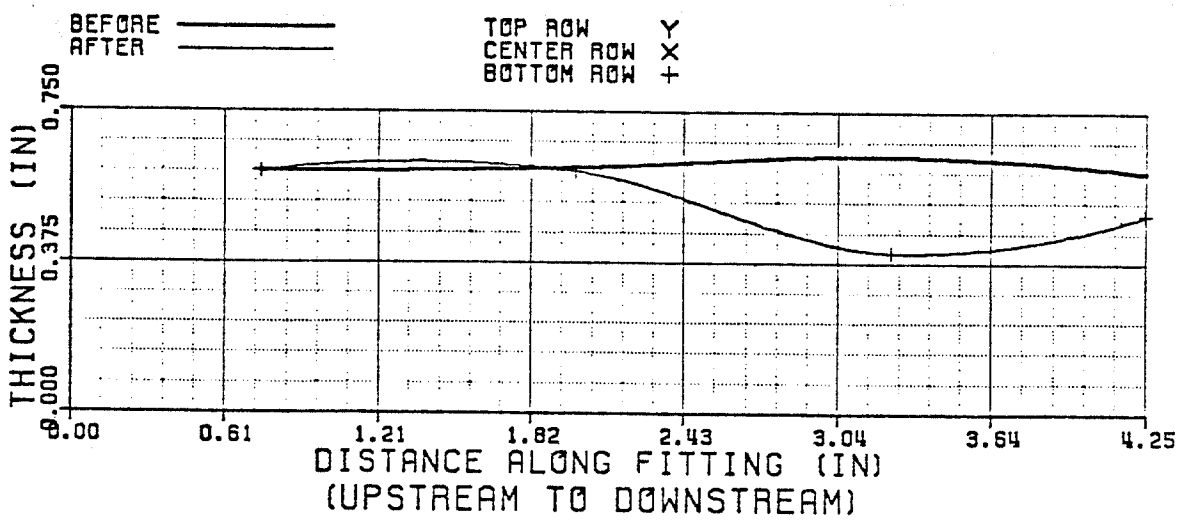

CAST PLUGGED TEE
INSIDE (B TO C)

FIGURE 3.8b - (Continued)

OUTSIDE RADIUS

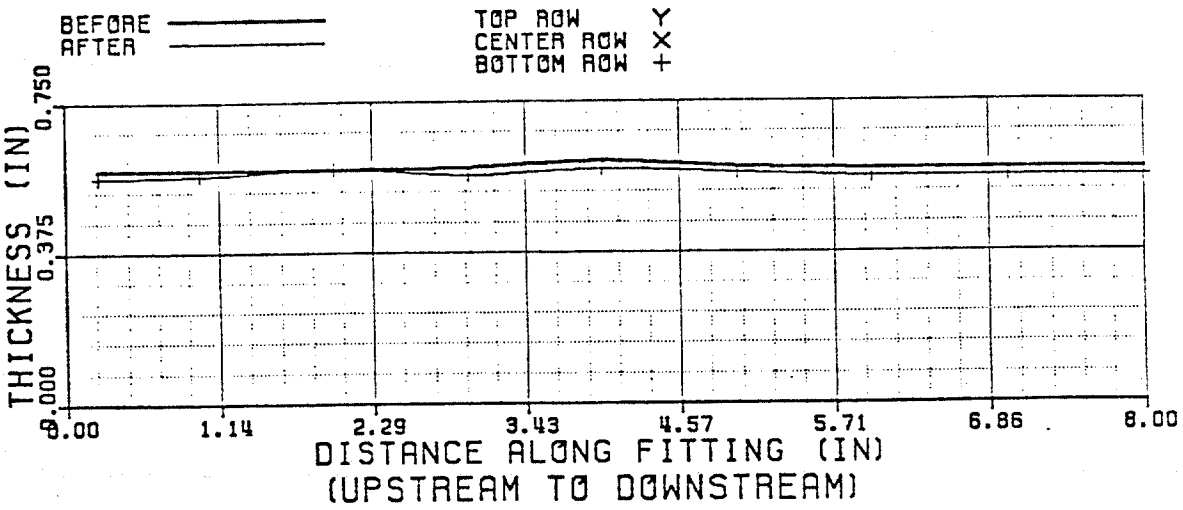

CAST PLUGGED TEE
OUTSIDE (A TO B)

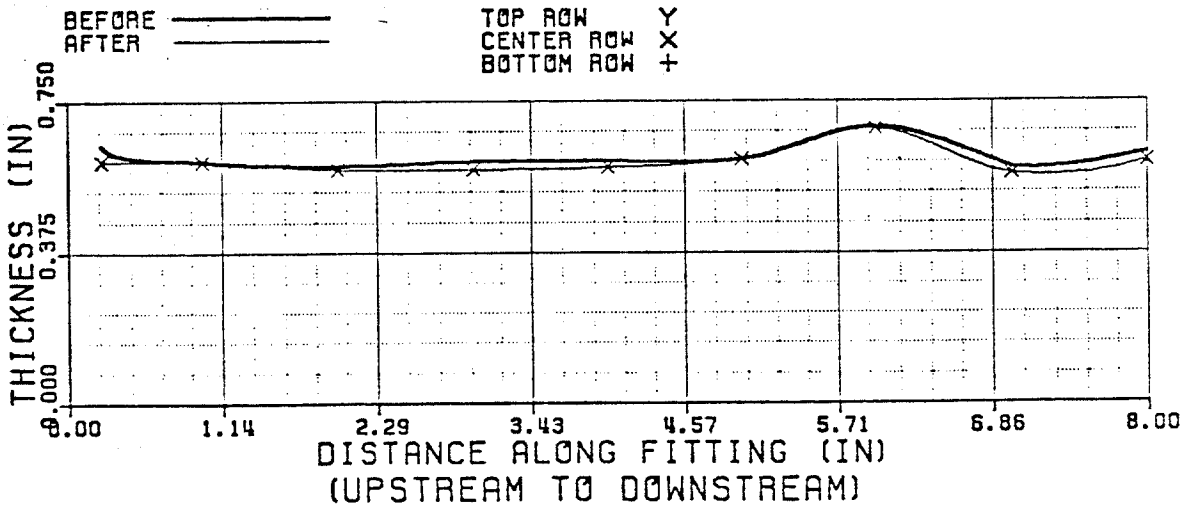

CAST PLUGGED TEE
OUTSIDE (A TO B)

FIGURE 3.8b - (Continued)

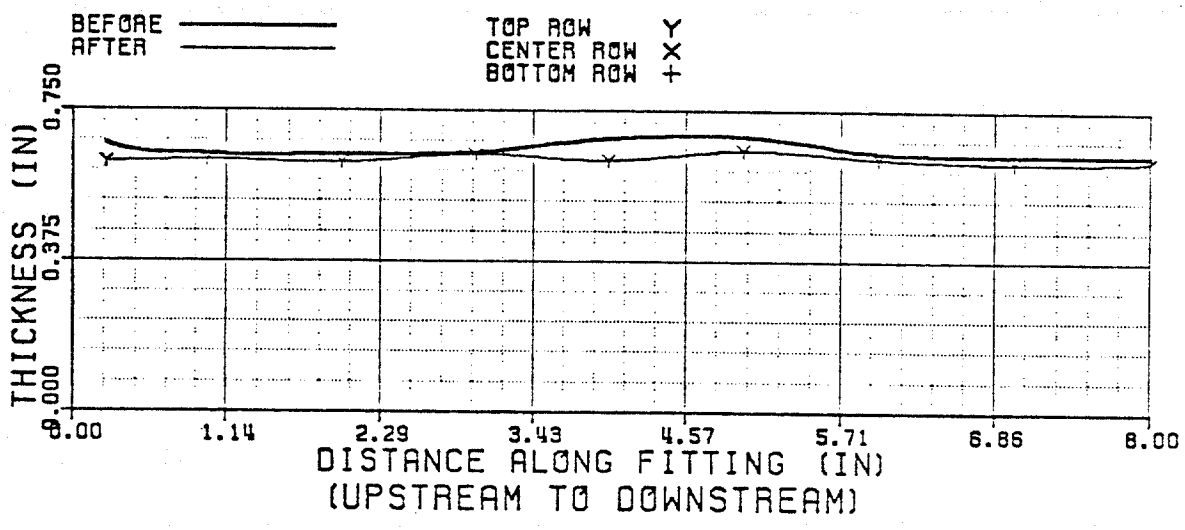

CAST PLUGGED TEE
OUTSIDE (A TO B)

FIGURE 3.8b - (Continued)

The erosion patterns of sections A-C and B-C are very similar yet there is a major difference between the curves. The first 2 data points on the A to C curve lie at the inlet of the plugged tee. The first 2 points on the B to C curve lie in the dead-end portion of the plugged tee. The B to C curve shows that some erosion did occur in the dead-end segment. This was a surprising result since the fluid inside the dead-end section was thought to be "stagnant". That is often the reasoning given for running plugged tees: that the dead-ended area catches some of the fluid, holds it in place, and allows the incoming fluid to strike the stagnant fluid. This theory cannot be accurate since erosion occurred in the dead-end area. The erosive stream entered the dead-end section and was forced to turn around after striking the blind flange. It also appears that erosion was greatest near the blind flange and decreased in the downstream direction. This suggests that a swirling type of fluid flow causes erosion in the dead-end.

The erosion pattern of this fitting can be called concentrated because only a small portion of the fitting eroded to an appreciable extent. The uniform erosion in other areas of the fitting was negligible compared with the erosion at the exit. The concentrated erosion pattern was the limiting factor for the plugged tee.

The erosion pattern for the long radius ell is shown in Figure 3.9. This fitting had the highest value of percent weight loss, 6.46%, and the highest value of weight loss per exposed surface area, 0.0258 pounds per square inch. It also had the second largest thickness change value, 0.338 inches. These figures indicate that a large amount of material was removed.

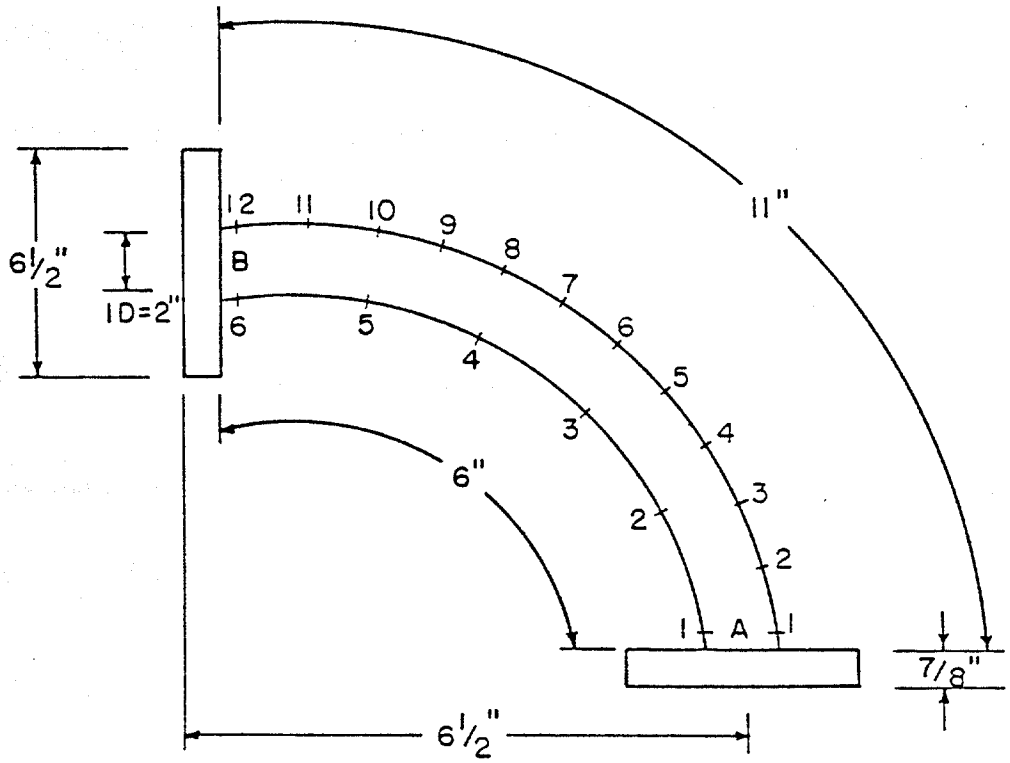

FIGURE 3.9a - Long radius ell geometry

LONG RADIUS ELL

Erosion Patterns

INSIDE RADIUS

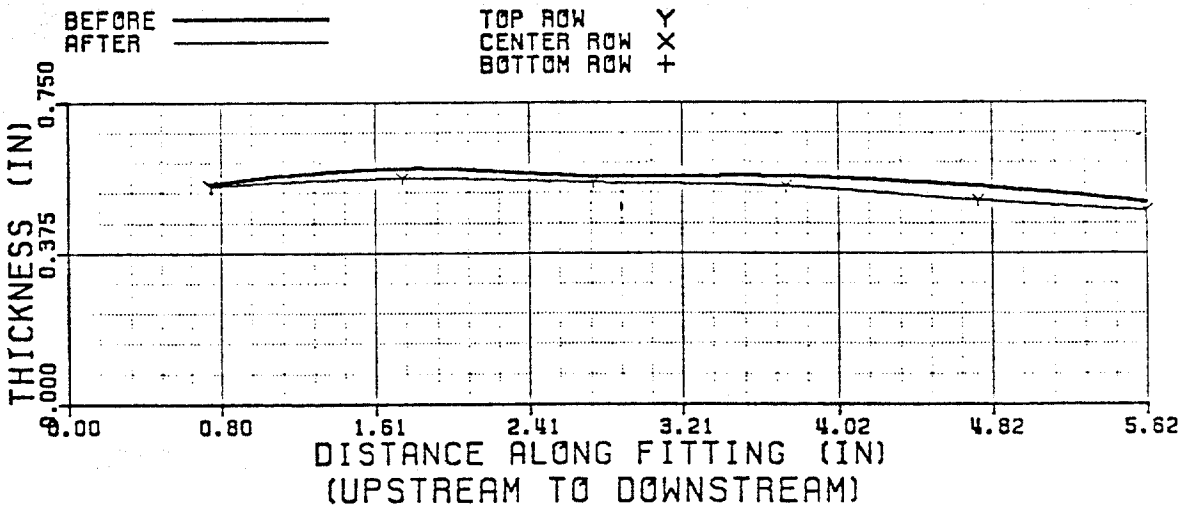

CAST LONG RADIUS ELL
INSIDE (A TO B)

FIGURE 3.9b - Long Radius Ell Erosion Patterns

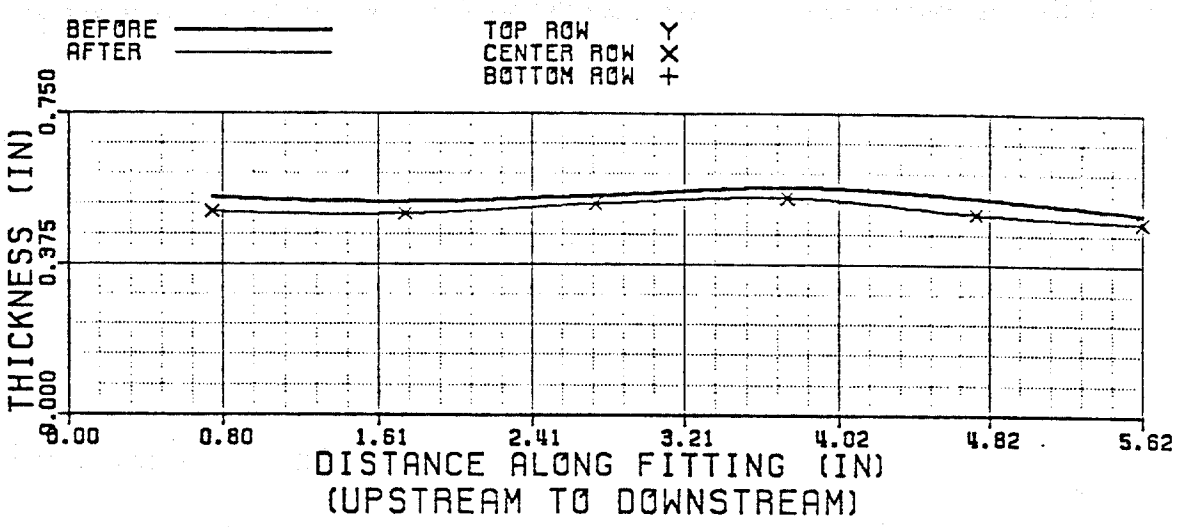

CAST LONG RADIUS ELL
INSIDE (A TO B)

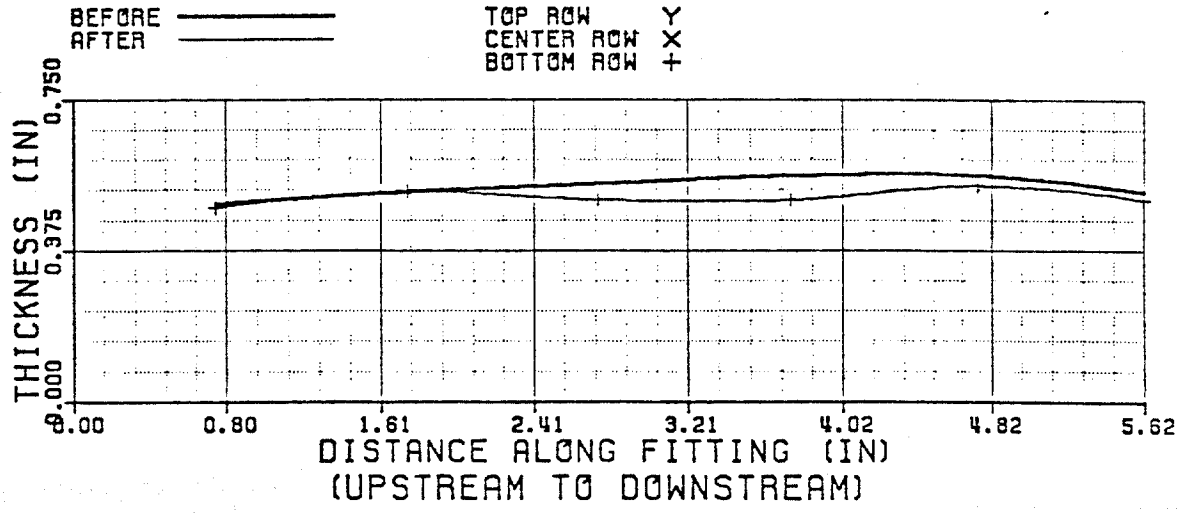

CAST LONG RADIUS ELL
INSIDE (A TO B)

FIGURE 3.9b - (Continued)

OUTSIDE RADIUS

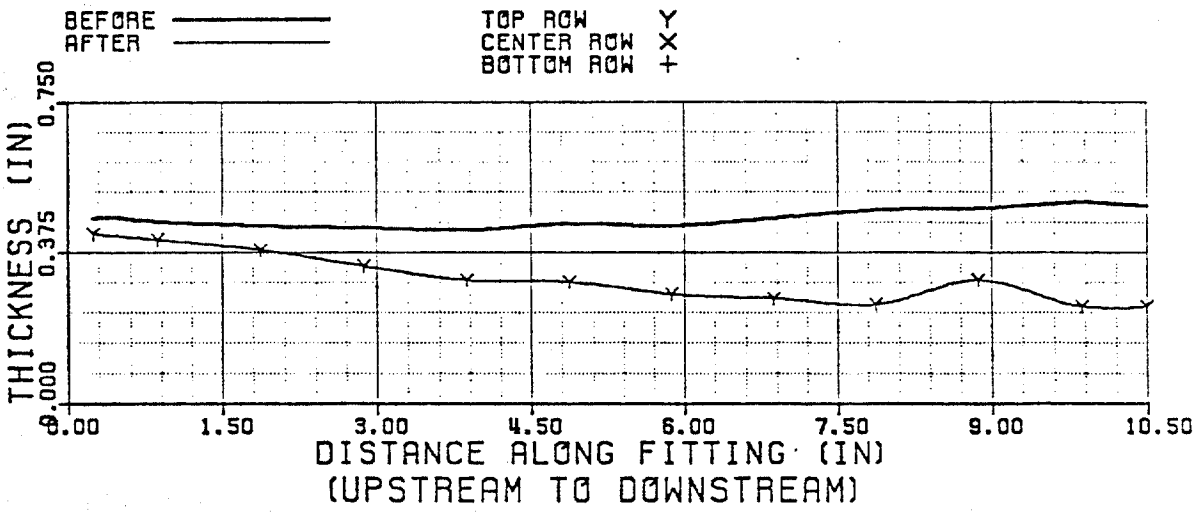

CAST LONG RADIUS ELL
OUTSIDE (A TO B)

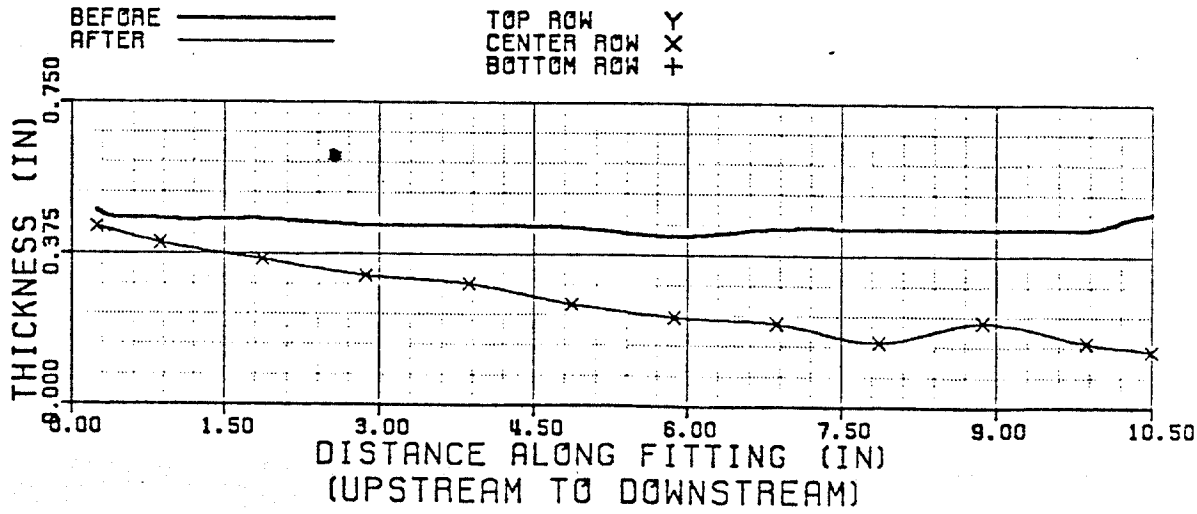

CAST LONG RADIUS ELL
OUTSIDE (A TO B)

FIGURE 3.9b - (Continued)

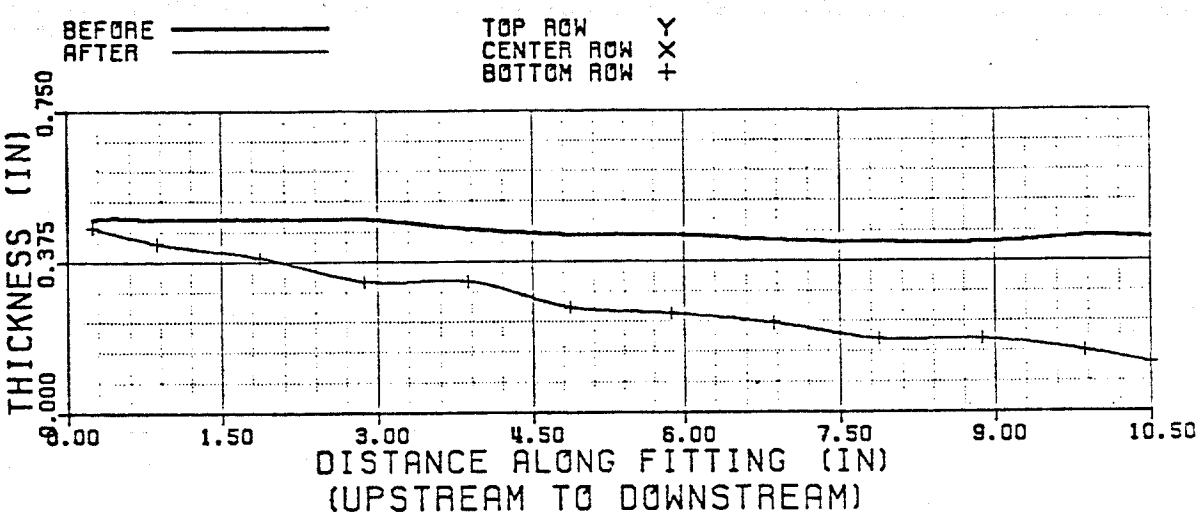

CAST LONG RADIUS ELL
OUTSIDE (A TO B)

FIGURE 3.9b - (Continued)

The erosion patterns of both the inside and outside surfaces were very similar to those of the short radius ell. The inside radius showed a very small amount of uniform erosion from the inlet to the exit with no trend of increasing erosion and no areas of concentrated erosion.

The outside radius showed a small amount of erosion at the inlet which gradually increased from the upstream to the downstream positions. Since the long radius ell has a greater curvilinear length than the short radius ell, it experienced a greater total thickness change. The large amount of material loss is illustrated by the BEFORE and AFTER curves, especially near the exit.

This fitting received such a low ranking (third) primarily because of the large amount material loss. Erosion pattern was not considered the limiting criterion because it was so similar to that of the short radius ell.

The erosion wear pattern observed in the Vortice-Ell is shown in Figure 3.10. The Vortice-Ell had the second largest weight loss per surface area, 0.0222 pounds per square inch. The percent change in weight calculated to be a small number, 3.06, but this value was influenced by the large flange weight. The Vortice-Ell has only 2 flanges but each were rated at 1500 psi and measured 1 5/8 inches in thickness and 8 1/2 inches in diameter. The flanges for all the other fittings were rated at only 300 psi and measured 5/8 inches in thickness and 6 1/2 inches in diameter. The initial weight of the Vortice-Ell was 61.85 pounds whereas the next heaviest member, the plugged tee, only weighed 42.86 pounds. The Vortice-Ell flanges added much more weight than the other flanges and, thus, held the percent weight change low.

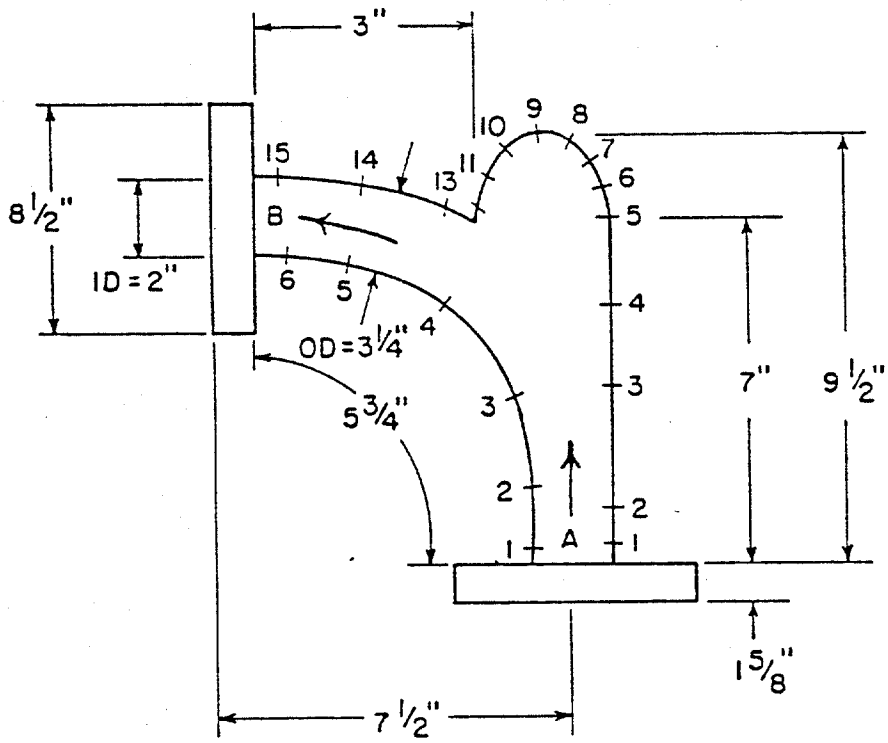

FIGURE 3.10a - Vortice-Ell geometry

INSIDE RADIUS

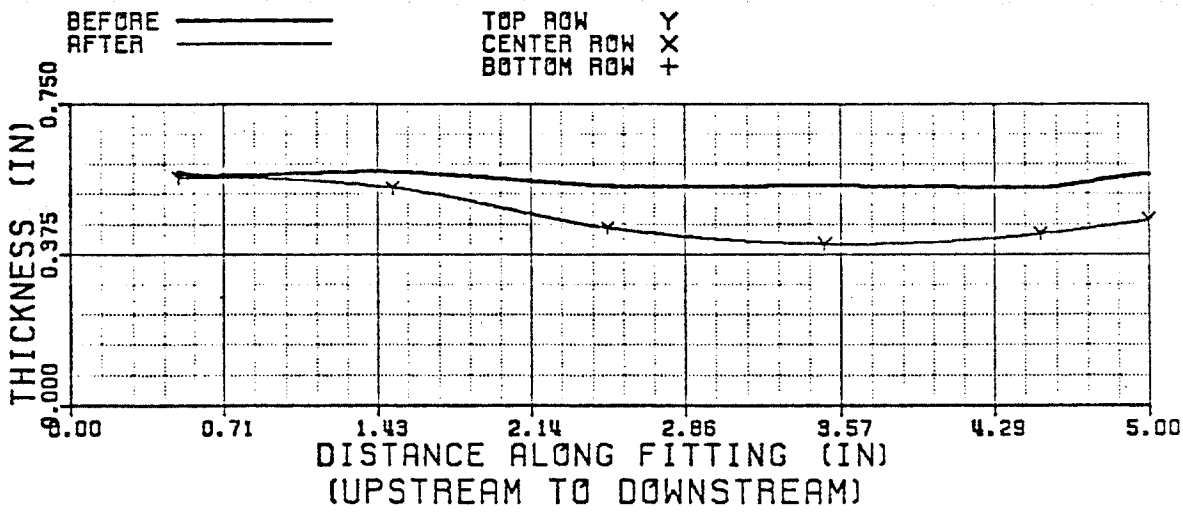

CAST VORTICE ELL
INSIDE (A TO B)

FIGURE 3.10b - Vortice-Ell erosion pattern

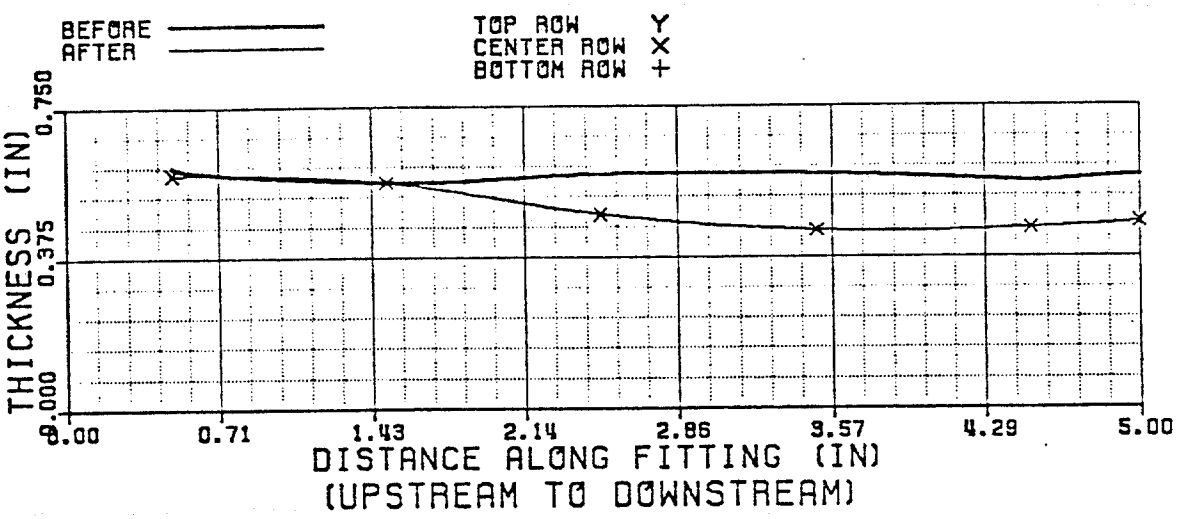

CAST VORTICE ELL
INSIDE (A TO B)

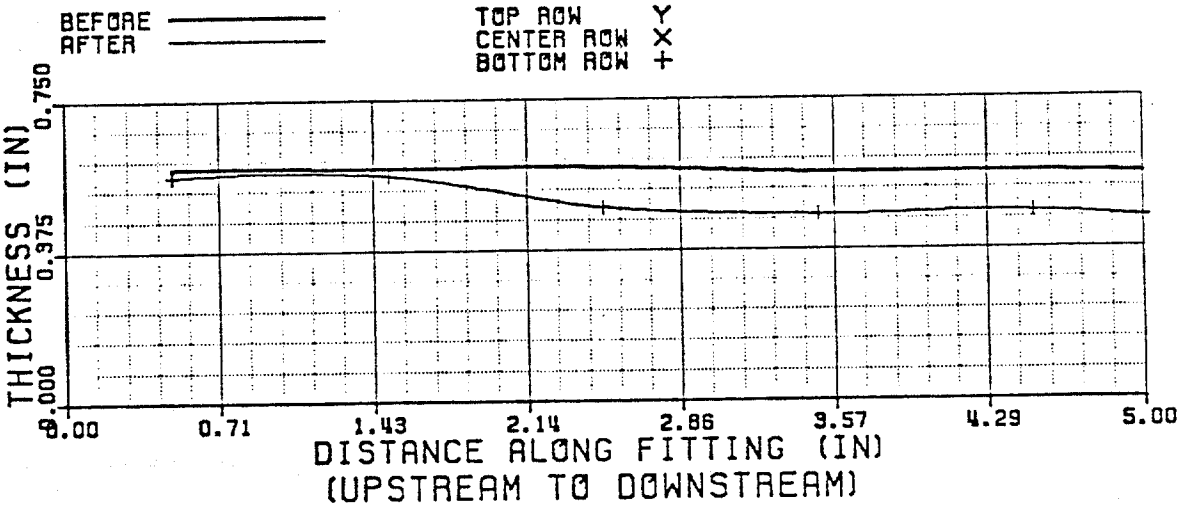

CAST VORTICE ELL
INSIDE (A TO B)

FIGURE 3.10b - (Continued)

OUTSIDE RADIUS

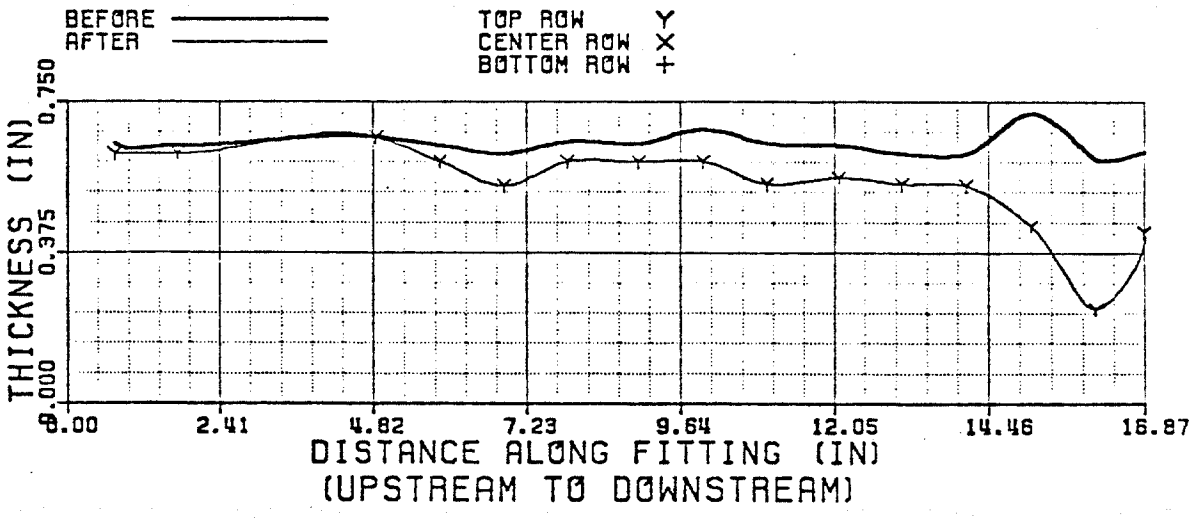

CAST VORTICE ELL
OUTSIDE (A TO B)

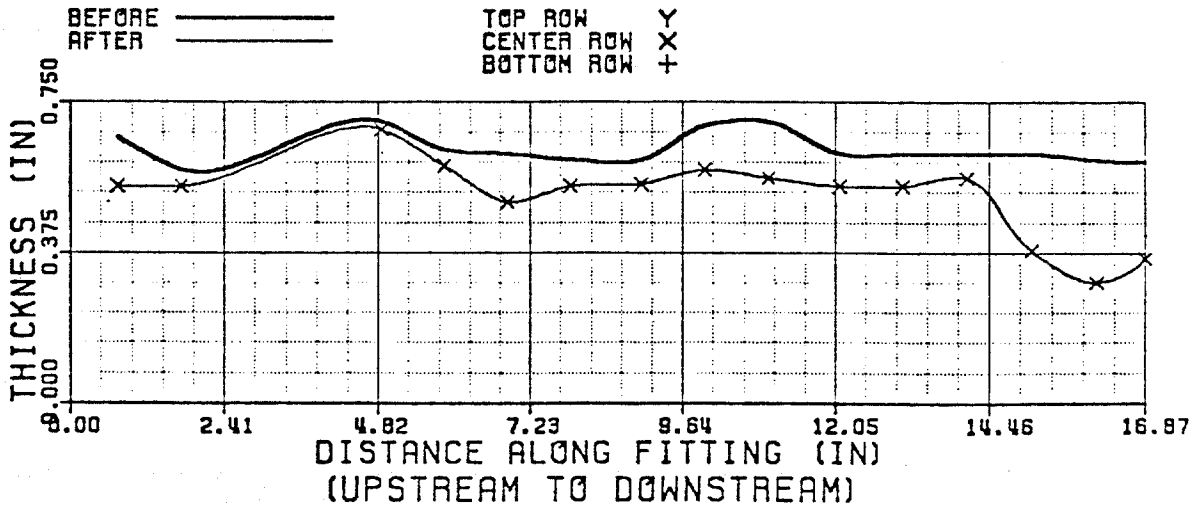

CAST VORTICE ELL
OUTSIDE (A TO B)

FIGURE 3.10b - (Continued)

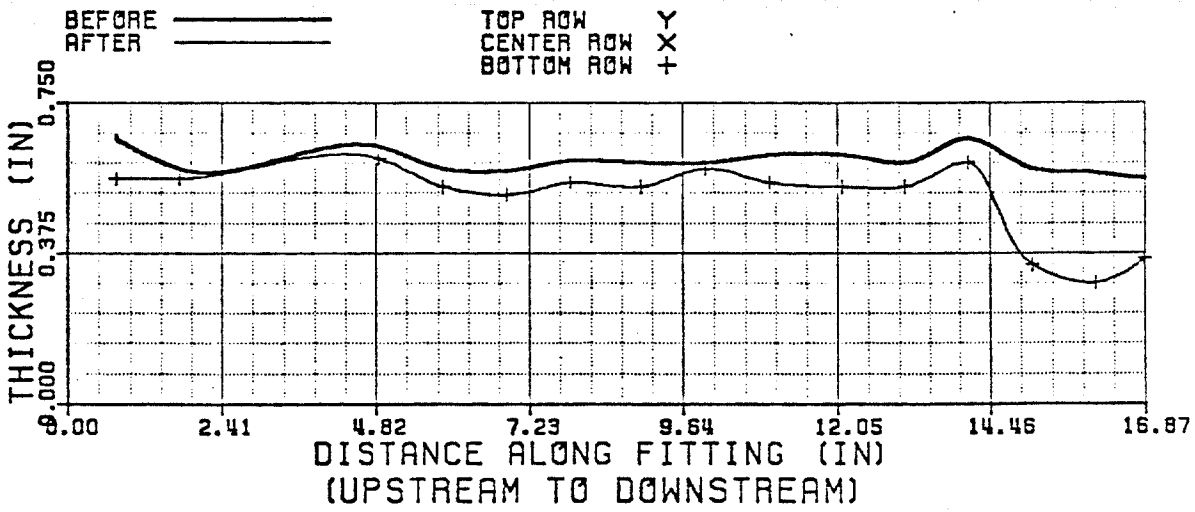

CAST VORTICE ELL
OUTSIDE (A TO B)

FIGURE 3.10b - (Continued)

All 3 plots of the inside radius showed the same erosion pattern: little erosion near the inlet and a considerable amount of erosion further downstream. By examining the Vortice-Ell drawing, it can be seen that the major area of erosion occurred opposite the "vortex chamber" (the bulb) and at points downstream. The plots indicate a uniform erosion pattern downstream of the vortex chamber and negligible erosion upstream.

The sketch of the Vortice-Ell illustrates how the outside radius has 3 distinct sections: the straight section going from the inlet to where the vortex chamber starts to curve, the vortex chamber, and the curved section just downstream of the bulb. Each of these sections had its own distinct erosion pattern.

The straight section includes all data points up to and including point number 4. This surface exhibited a small amount of uniform erosion. There appeared to be come concentrated erosion at the inlet, but this was not supported by measurements on the inside radius. Erosion was minimal along the straight section and increased to a considerable magnitude at the vortex chamber.

The erosion pattern was uniform throughout the vortex chamber. The magnitude of erosion and the lack of concentrated erosion agreed well with the pattern from the short radius ell where the target surface also curved sharply. The vortex chamber erosion pattern differed from that of the long radius ell in that erosion did not increase in a steady fashion from upstream to downstream. Neither the straight section nor the vortex chamber limited the usefulness of this fitting.

The last section, from the end of the bulb to the flange face, proved to be the limiting section on the Vortice-Ell. Each plot showed

a large amount of concentrated erosion just after the vortex chamber. One point had the largest thickness change among all the fittings: 0.36 inches. It appears that the middle point along this curved section, point number 14, always exhibited the maximum amount of erosion. This was possibly due to a swirling flow pattern similar to that in the plugged tee. It is believed that this concentrated erosion would continue until the fitting failed. For this reason, and the large amount of material loss, the Vortice-Ell received the lowest ranking of all the fittings.

It was learned, only after the experiments were completed, that the Vortice-Ell was designed to change the flow stream direction from horizontal to vertical. Unfortunately, it was not tested in this arrangement. One of the representatives of the HammerTek Corporation explained that the force of gravity on the abrasive had an important affect on the performance of the Vortice-Ell. In commercial applications, it has proven very effective in reducing erosion failures of pheumatic-transportation systems. This study was the first time the fitting was tested with a liquid for the carrying fluid.

CONCLUSIONS AND RECOMMENDATIONS

The conclusions drawn from this study are:

1. The laboratory type erosion experiments used by previous investigators were not useful in testing pipe bends.

2. Previously published erosion models could not be applied to the flow loop experiment used in this study.

3. The straight sections of pipe in the flow loop used in this study showed no appreciable amounts of erosion.

4. Valves that created the least amount of disturbance in the flow path gave the longest service lives. Butterfly valves and non-full open ball valves are quickly eroded.

5. The welded fittings eroded in erratic patterns and showed no correlation with the cast fittings.

6. Based on an analysis of the experimental data, the fittings were given the following ranking for erosion resistance (from most resistive to least resistive):

a) short radius ell,

b) plugged tee,

c) long radius ell,

d) Vortice-Ell.

7. The magnitude and pattern or erosion showed no direct correlations with sand concentration and grain size distribution.

8. In relation to imparting backpressure on the formation, the long radius ell produced the lowest pressure drop, followed closely by the short radius ell, then the plugged tee, and, finally, the Vortice-Ell.

LIST OF REFERENCES

Behrendt, A. 1970. Proc. Int. Conf. Rain Eros. Assoc. Phenomena, 3rd, RAE, England II, 797-820.

Bitter, J. G. A. 1963a. A study of erosion phenomena, Part I. Wear. 6:5-21.

Bitter, J. G. A. 1963b. A study of erosion phenomena, Part II. Wear. 6:5-21.

Eyre, T. S. and Dutta, K. 1975. Int. Mech. Engr. Conf. Piston Ring Scuffing. Paper C 74/75.

Eyre, T. S. 1979. Wear resistance of metals. Treatise On Material Science and Technology. 13:363-442.

Finnie, I. 1960. Erosion of surfaces by solid particles. Wear. 3:87-103.

Finnie, I., Wolak, J., and Y. Kabil. 1967. Erosion of metals by solid particles. Journal of Materials. 2:682-700.

Kruschov, M. N. 1957. Inst. Mech. Engr. Conf. Lub. Wear. 655.

Mason, J. S. and Mills, D. 1977. Int. Powder and Bulk Solids Handling and Proc. Conf., 2nd, Chicago, Illinois.

Neilson, J. H. and A. Gilchrist. 1968a. Erosion by a stream of solid particles. Wear. 2:111-22.

Neilson, J. H. and A. Gilchrist. 1968b. An experimental investigation into aspects of erosion in rocket motor tail nozzles. Wear. 2:123-43.

Paulson, J. 1985. Private communication.

Richardson, R. C. 1968. The wear of metals by relatively soft abrasives. Wear. 2:245-275.

Sage, W. and G. P. Tilly. 1969. The significance of particle size in sand erosion of small gas turbines. Aero J. 73:427-28.

Serpik, N. M. and M. M. Kantor. 1965. Frict. Wear Mach. 19:28.

Sheldon, G. L. and I. Finnie. 1966. The mechanism of material removal in the erosive cutting of brittle materials. Transactions of the ASME. 393-400.

Tilly, G. P. 1969. Erosion caused by airborne particles. Wear. 14:63-79.

Tilly, G. P. 1973. A two stage mechanism of ductile erosion. Wear. 23:87-96.

Tilly, G. P. 1979. Erosion caused by impact of solid particles. Treatise on Materials Science and Technology. 13:287-319.

Systems Analysis of Diverter Operations

As can be seen from Figure 4.1, flowing bottom hole pressure can be written as

$$FBHP(Q) = P_e(Q) + \Delta P_d(Q) + \Delta P_{wB}(Q) \quad \ldots\ldots\ldots\ldots\ldots (4.1)$$

or as

$$FBHP(Q) = \overline{P}_r - \Delta P_r(Q) \quad \ldots\ldots\ldots\ldots\ldots\ldots\ldots (4.2)$$

Solving these two equations simultaneously results in a unique flow rate, flowing bottom hole pressure, and pressure profile in the well for steady-state flow and forms the basis of the systems analysis. If equations 4.1 and 4.2 are evaluated at various flow rates, "performance" curves are generated that relate flow rate to flowing bottom hole pressure. The intersection of the two performance curves yields the simultaneous solution of these curves. i.e. the equilibrium flow rate and flowing bottom hole pressure of the specified system (See Figure 4.2). The performance curves are usually generated by a computer, and require the calculation of pressure traverses. Single phase or two-phase flow may be considered, and various methods of calculating the pressure losses in the reservoir can be applied. Critical flow can be considered by accounting for the P_e term in equation 4.1.

Beck, et. al. (1986), showed that accurate diverter line pressure loss calculations can be made for both single and two-phase (gas/water) flow by calculating both frictional pressure losses and pressure losses due to fluid acceleration. The frictional pressure loss gradient is given as

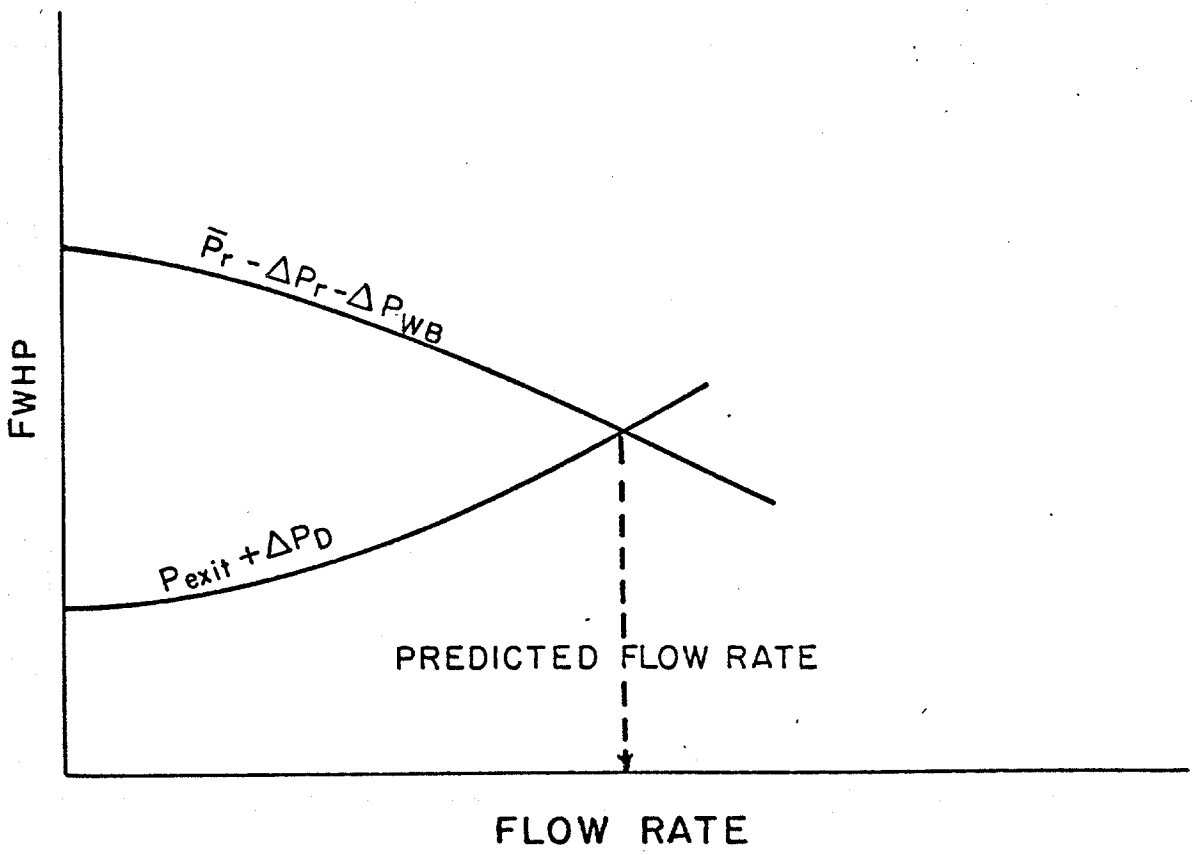

FIGURE 4.2 - Graphical presentation of equations 1 and 2

$$\left(\frac{\Delta P}{\Delta L}\right)_{Friction} = \frac{f\rho v^2}{2g_c d} \quad \ldots\ldots\ldots\ldots\ldots\ldots\ldots\ldots \quad (4.3)$$

and the acceleration gradient as

$$\left(\frac{\Delta P}{\Delta L}\right)_{Acceleration} = \frac{\Delta(\rho v^2)}{2g_c \Delta L} \quad \ldots\ldots\ldots\ldots\ldots\ldots\ldots\ldots \quad (4.4)$$

These methods were used to model pressure traverses measured in 1 in. and 2 in. model diverter lines and result in estimations of pressure loss with an average error of less than 10 percent.

The pressure gradient equation for vertical flow is given as

$$\left(\frac{\Delta P}{\Delta L}\right)_{Total} = \left(\frac{\Delta P}{\Delta L}\right)_{Elevation} + \left(\frac{\Delta P}{\Delta L}\right)_{Friction} + \left(\frac{\Delta P}{\Delta L}\right)_{Acceleration} \quad (4.5)$$

where $\left(\frac{\Delta P}{\Delta L}\right)_{Friction}$ and $\left(\frac{\Delta P}{\Delta L}\right)_{Acceleration}$ are identical to (4.3) and (4.4) above and the elevation gradient is given as

$$\left(\frac{\Delta P}{\Delta L}\right)_{elevation} = \frac{g}{g_c} \rho \sin\theta \quad \ldots\ldots\ldots\ldots\ldots\ldots\ldots\ldots \quad (4.6)$$

In gas/water flow the elevation and friction gradients can be calculated from empirical correlations such as the Hagedorn and Brown (1965) correlation. The acceleration gradient can be calculated from equation 4.4 by using a density defined as

$$\rho = \lambda_w \rho_w + \lambda_g \rho_g \quad \ldots\ldots\ldots\ldots\ldots\ldots\ldots\ldots\ldots\ldots \quad (4.7)$$

and a mixture velocity defined as

$$V = \frac{q_g + q_w}{A} \quad \ldots\ldots\ldots\ldots\ldots\ldots\ldots\ldots\ldots\ldots \quad (4.8)$$

It is suspected that two-phase correlations grossly under-predict pressure losses at high flow rates and high GLR's. An alternate method of computing pressure losses for gas/water flow is to assume that slippage between the phases is negligible, allowing the same procedures used for gas flow to be applied to gas/water flow. The following definitions can be used to calculate gas/water pressure gradients.

$$\rho = \lambda_w \rho_w + \lambda_g \rho_g \quad \ldots\ldots\ldots\ldots\ldots\ldots\ldots\ldots\ldots\ldots \quad (4.9)$$

$$\mu = \lambda_w \mu_w + \lambda_{g\mu g} \quad \ldots\ldots\ldots\ldots\ldots\ldots\ldots\ldots\ldots\ldots \quad (4.10)$$

$$V = \frac{q_g + q_w}{A} \quad \ldots\ldots\ldots\ldots\ldots\ldots\ldots\ldots\ldots\ldots \quad (4.11)$$

Using these terms in equations 4.3, 4.4, and 4.6, as well as in calculating Reynold's number and the Moody friction factor, provides an appropriate means of calculating pressure losses for high flow rates and high gas/liquid ratios.

The wellbore/reservoir performance curve requires calculation of pressure losses in both the reservoir and the wellbore. Reservoir pressure losses are calculated by the Jones equation (Jones, et al., 1976).

$$\Delta(P^2) = AQ + DQ^2 \quad \ldots\ldots\ldots\ldots\ldots\ldots\ldots\ldots\ldots\ldots \quad (4.3)$$

where

$$A = \frac{1.424\mu_g\, ZT}{kH}\ \ell n(.472\ \frac{r_e}{r_w}) + S \quad \ldots\ldots\ldots\ldots\ldots\ldots\ (4.4)$$

$$D = \frac{3.16 \times 10^{-18}\beta\gamma_g\, ZT}{H^2}\ (\frac{1}{r_w} - \frac{1}{r_e}) \quad \ldots\ldots\ldots\ldots\ldots\ (4.5$$

High flow rates are expected during diverter operations, so the non-darcy flow term is necessary to correctly predict the pressure losses in the reservoir.

CRITICAL FLOW CALCULATIONS

The exit pressure term in equation 4.1 is atmospheric for subcritical flow, but can be significantly greater than atmospheric pressure if flow is critical. P_e can be calculated as a function of flow rate by the following equation:

$$Q = \frac{V^*_{gas}\ D^2\ P_e\ T_{STD}}{2122\ ZT_e P_{STD}} \quad \ldots\ldots\ldots\ldots\ldots\ldots\ (4.13)$$

The critical velocity of dry gas is given as:

$$V_{gas} = 41.4\ \sqrt{\frac{KZT}{\gamma_g}} \quad \ldots\ldots\ldots\ldots\ldots\ldots\ (4.14)$$

Use of these equations resulted in errors of under 5 percent in 1 in. and 2 in. model diverters (Beck, et. al., 1986).

Exit pressure as a function of gas flow rate and water yield (bbl/mmcf) is given as:

$$Q_g^* = \frac{P_e\ T_{STD}}{Z_e T_e P_{STD}} \left[\frac{V^* d^2}{2122.1} - \frac{(3.062 \times 10^{-8}) V^* d^2 (Yield)_w\ P_e\ T_{STD}}{11.574\ Z_e\ T_e\ P_{STD}}\right] . \quad (4.15)$$

Critical velosity of a gas/water mixture is defined by Wallis (1969) as

$$V^* = (\lambda_g \rho_g + \lambda_w \rho_w) \left[\frac{\lambda_g}{\rho_g (V^*_{gas})^2} + \frac{\lambda_w}{\rho_w (V^*_w)^2}\right]^{-1/2} \quad . . . . . (4.16)$$

Calculations are simplified if pressure and water yield are assumed and a corresponding gas flow rate calculated. Beck (1986) reported errors of under 20 percent in using these equations to estimate critical flow rates in 1 in. and 2 in. model diverter lines.

Systems Analysis of Complex Geometries

In more complex geometries the possibility of critical flow occurring at some point other than the diverter exit must be considered. Critical flow may occur at any point where geometry changes, and is most likely to occur near the surface. Figure 4.3 shows a well with a more complex wellbore geometry. To investigate the possibility of critical flow at a point in the well, that point must be taken as the "node" point. (In the previous derivation the node point was the bottom of the well.) Using Figure 4.3 as an example, with the node point as shown, two equations can be written for the pressure at the node

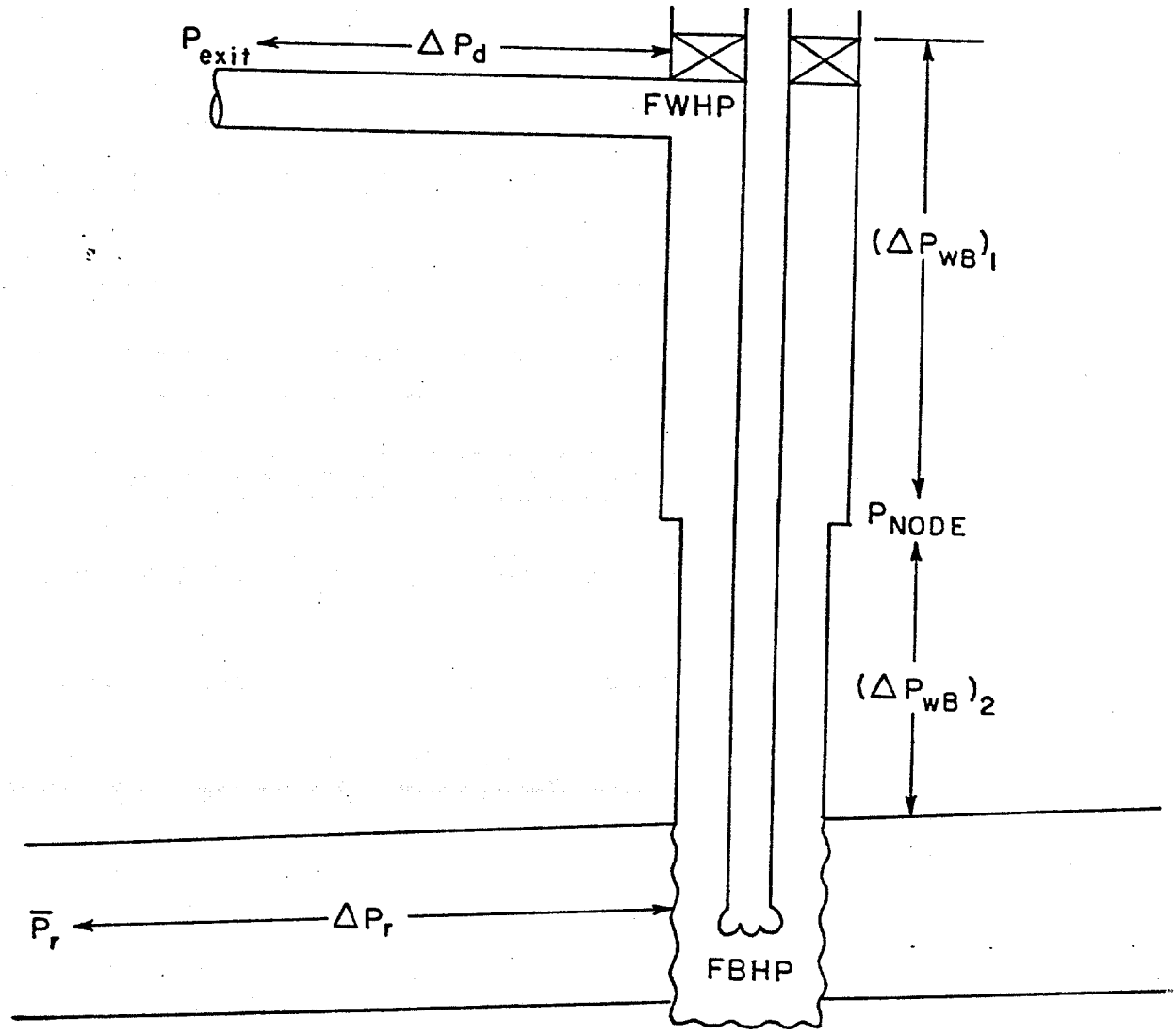

FIGURE 4.3 - Pressure losses in a well being diverted with critical flow possible within well

$$P_{NODE} - P_e(Q) + \Delta P_d(Q) + \Delta P_{wB_1}(Q) \quad \ldots \quad (4.17)$$

$$P_{NODE} = \bar{P}_r - \Delta P_r(Q) - \Delta P_{wB_2}(Q) \quad \ldots \quad (4.18)$$

If flow is critical at the node, a third equation can be written.

$$P_{NODE} = P^* \quad \ldots \quad (4.19)$$

where P* is defined by either equation 4.13 or 4.15. All three equations can be presented graphically, as in Figure 4.4. The simultaneous solution of two of the three equations will yield the equilibrium flow rate and pressure at the node. Two combinations of the equations are possible. The combination that yields the lowest flow rate is the correct solution. If equations 4.17 and 4.18 result in the lowest flow rate (i.e. $P_{NODE} = P_1^*$ in Figure 4.4), flow is critical at the node. The difference between pressure at this intersection and the pressure at the corresponding flow rate of Equation 4.17 will define a pressure drop at the node point. Flow may also be critical at the diverter exit. If Equations 4.17 and 4.18 result in the lowest flow rate (i.e. $P_{NODE} = P_2^*$ in Figure 4.4), flow is subcritical at the node and the method becomes identical to the method previously described. As before, once an equilibrium flow rate and pressure at a point are established, the pressure profile in the well can be determined.

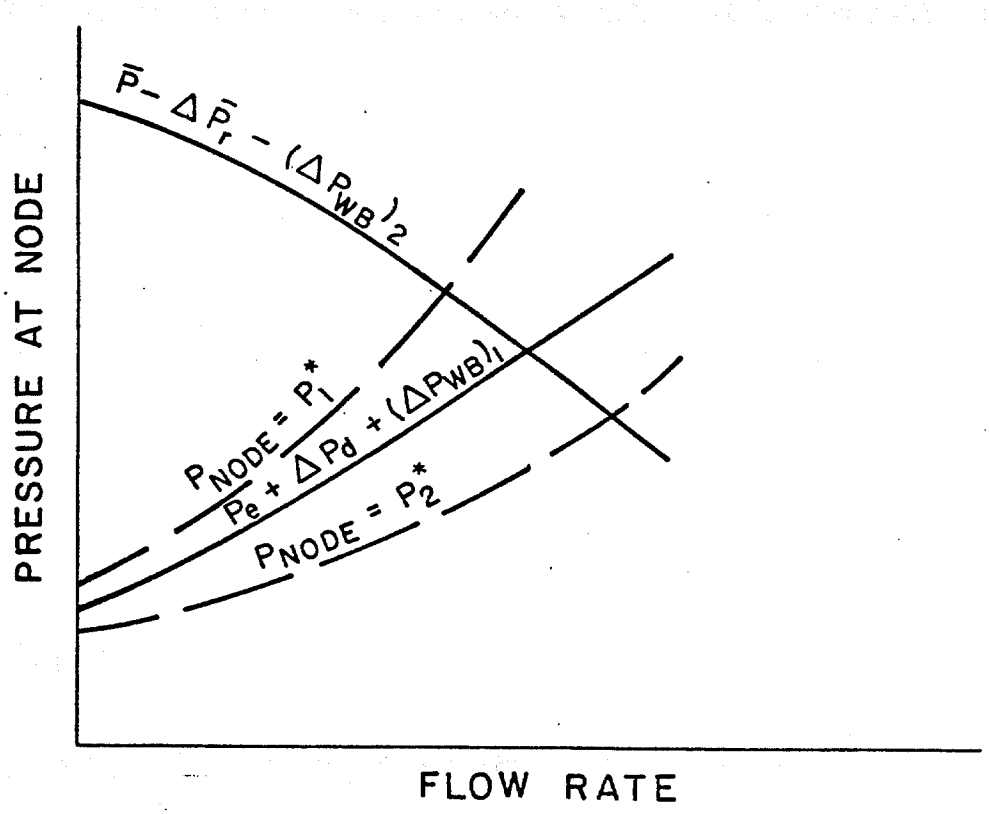

FIGURE 4.4 - Systems Analysis Considering Possibility of Critical Flow at Node Point

DESIGN APPLICATIONS

A computer program has been written to perform the systems analysis for a wide range of geometries and reservoir characteristics. The effects of various parameters on the pressure profile of the well can be determined. Parameters that have been studied thus far include:

1) diverter line diameter
2) diverter line length
3) pressure required to divert the well

Other parameters that remain to be studied are:

1) wellbore geometry
2) well depth
3) pore pressure gradients
4) sensitivity to reservoir parameters
5) water depth

Results of the systems analysis can be presented graphically to demonstrate the effects of these various parameters on a typical well. Figure 4.15 presents diverter diameter as a function of wellhead pressure, diverter exit pressure, and flow rate and is useful in determining surface conditions at which a specific diverter system will operate.

Figure 4.6 presents diverter line length as a function of wellhead pressure and diverter line diameter. Diverter line length has a much smaller effect on the operating conditions of the diverter than does diameter, and becomes even less significant in the larger diameter

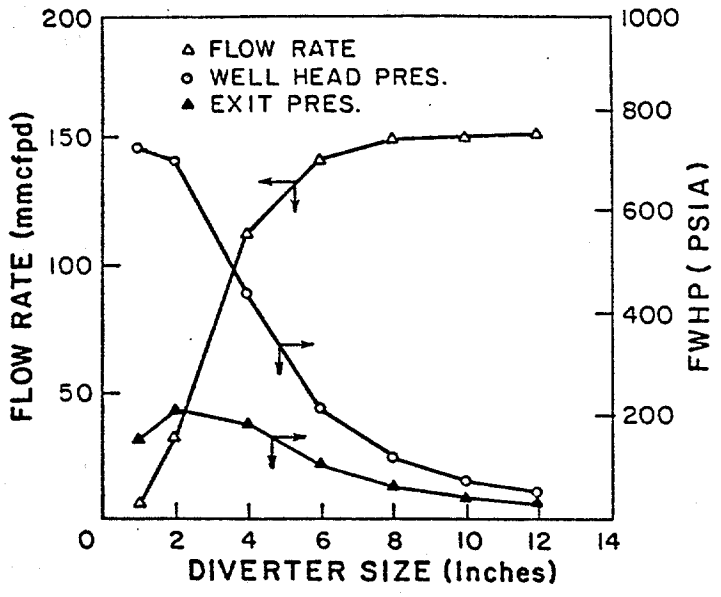

FIGURE 4.5 - Pressure and Flow Rates Expected For Example Well with 28-in. by 5 in. Annulus

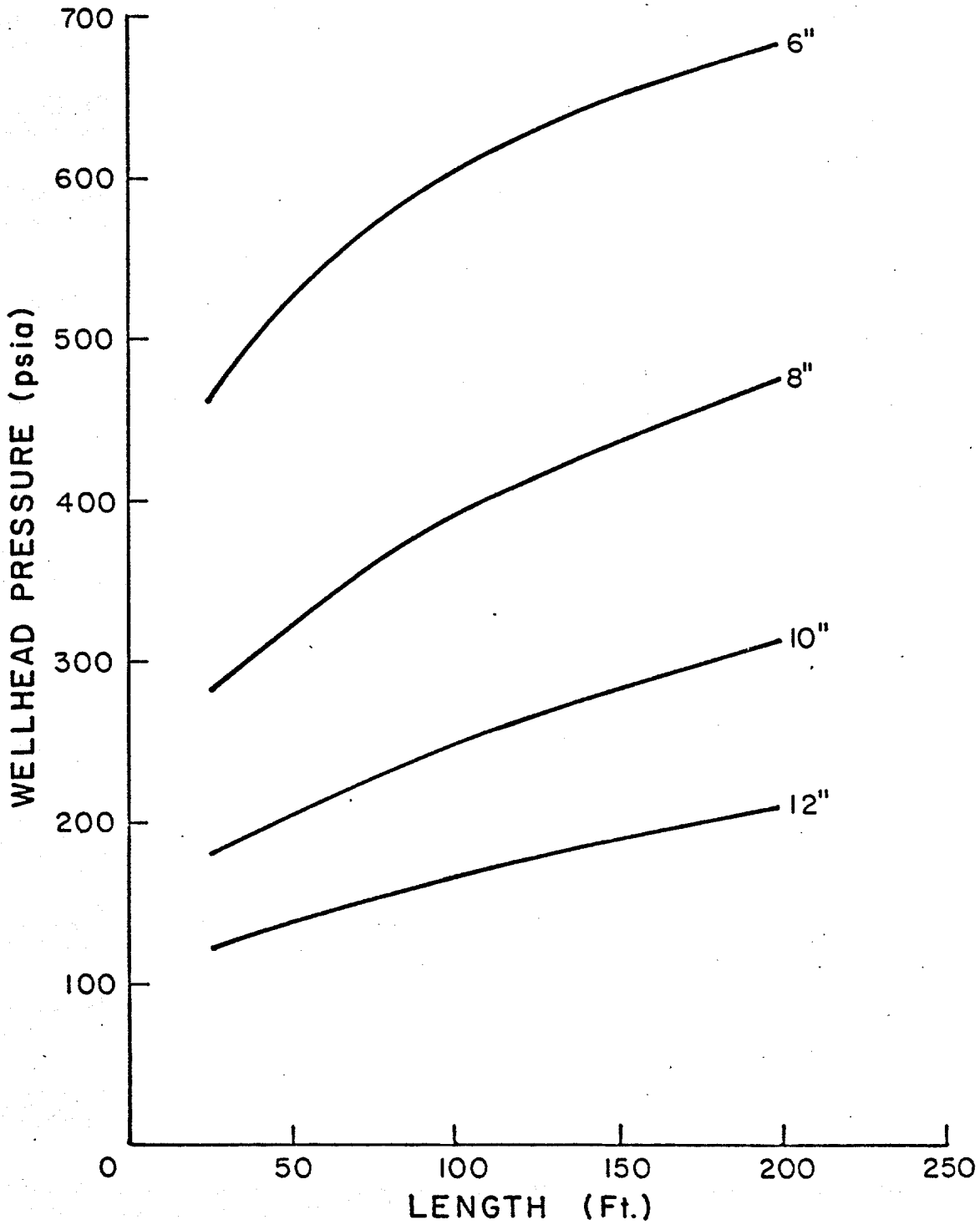

FIGURE 4.6 - Effect of Diverter Length on Wellhead Pressure for Example Well Situation

lines. Length changes on the scale of 10's of feet cause very small changes in flowing wellhead pressure.

Pressure profiles, in terms of equivalent densities, are shown in Figure 4.7. Smaller diameter lines create the largest loads on the well, and increasing line diameter can greatly decrease the load placed on a well. However, increasing the line diameter past 12 in. seems to have little or no effect of decreasing the load on the well. Pressure profiles, when combined with fracture pressure estimates, can be used to provide criteria for setting sufficient conductor casing to protect a well from the backpressure caused by its diverter system.

Figure 4.8 shows the pressure profiles resulting from various diameter diverters placed on a well with 20 in. conductor set to 785 ft. (385 ft BML) that has been drilled an additional 1000 ft. with a 17.5 in. bit. Fracture pressures are also shown on the figure to use in determining the load placed on the exposed formation. This figure shows that excessive backpressures are placed on the well at the conductor shoe for 4 in. and 6 in. diverter lines, indicating that either a larger diameter diverter line or deeper conductor pipe is required.

CONCLUSIONS

1) Systems analysis has been developed to estimate the flow rate and flowing pressures in a well that is being diverted. The corresponding pressure profile in the well represents the load placed on the well by the diverter system.

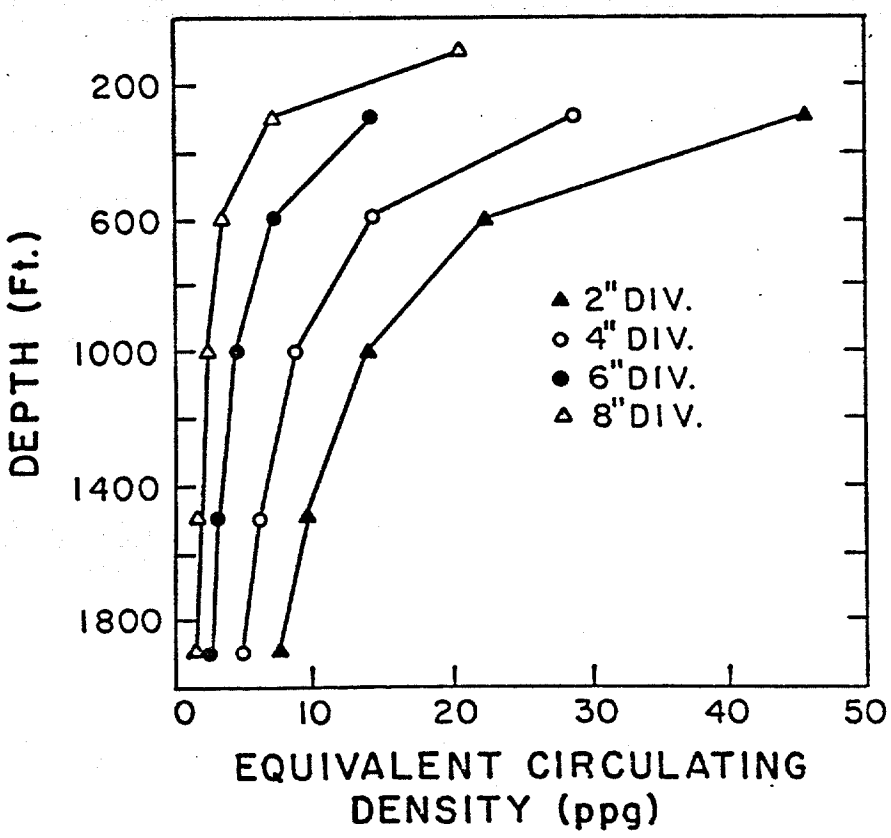

FIGURE 4.7 - Equivalent Density as a Function of 30-in. Drive Pipe, Setting Depth for Various Diverter Sizes.

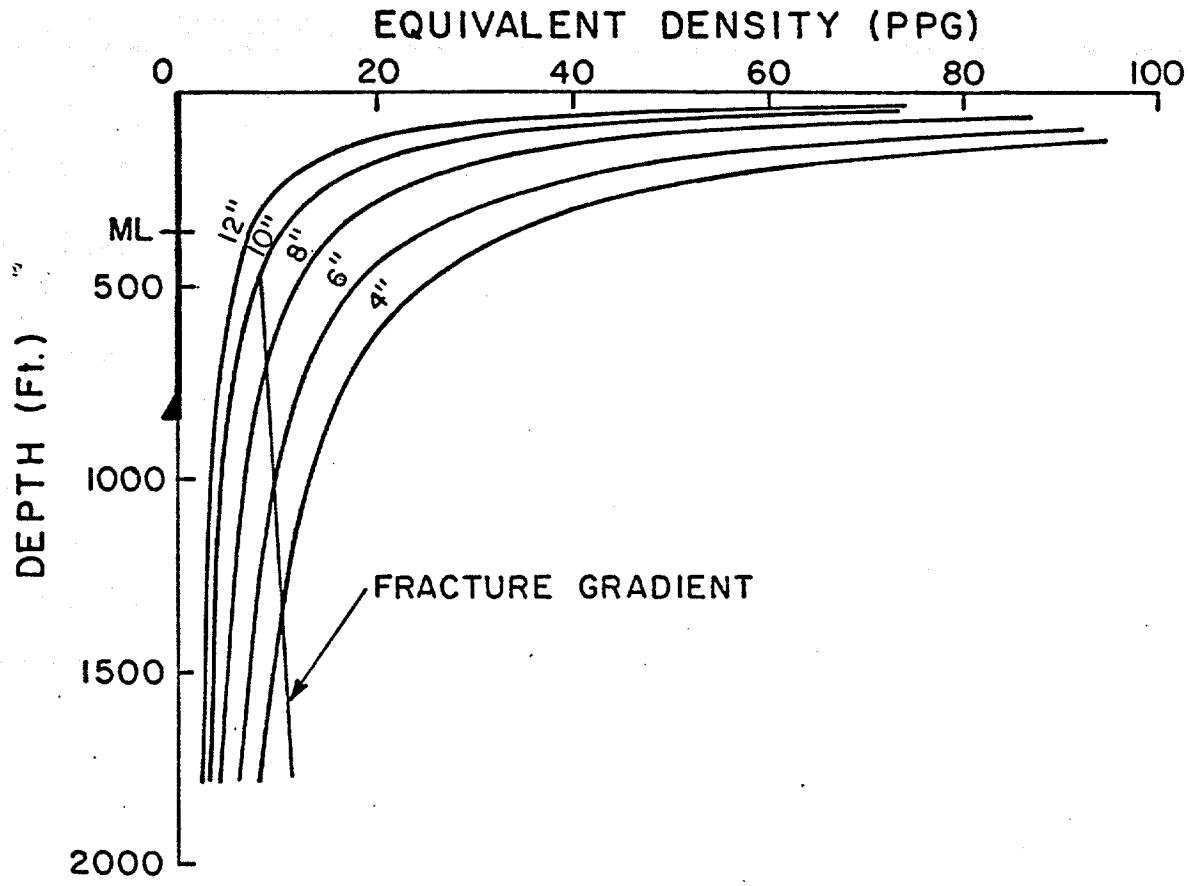

Figure 4.8 - Comparison of Equivalent Density During Diverter Operations to Formation Fracture Gradient for Example Well conditions

2) Diverter line diameter is very important in minimizing backpressure, but larger diameter lines cannot always sufficiently decrease backpressure to avoid fracturing the formation.

3) Diverter line length is of only minimal importance in designing the diverter system.

4) Calculated pressure profiles show that a specific diverter system determines the proper setting depth of the conductor pipe.

SUMMARY

Because diverters have such a high failure rate, it is necessary to develop a method of design that corresponds to general well plans and expected drilling conditions. The method of systems analysis provides a means of integrating the design of the diverter system with the design of the well. Diverter lines can be sized to minimize flowing pressures and, thus, maximize flow rate. Working pressures required to divert the well can be estimated and the proper annular preventor chosen. Flowing pressures within the well can also be estimated to facilitate the selection of the setting depths of the conductor casing string so that a successful diverter operation is possible for the existing diverter equipment. Experimental data from previous work supports the mathematical models used to carry out the systems analysis.

SELECTED BIBLIOGRAPHY

Beck, F., Langlinais, J., and Bourgoyne, A. T., Jr.: "Experimental and Theoretical Considerations for Diverter Evaluation and Design", SPE paper 15111, (preprint, 1986).

Brill, J. P., and Beggs, H. D.: Two-Phase Flow in Pipes, U. Tulsa, (March 1978).

Clark, A. R., and Perkins, T. K.: "Wellbore and Near-Surface Hydraulics of a Blown-Out Oil Well," SPE Paper 9257, (1980).

Crouch, E. C., and Pack, K. J.: "'Systems Analysis' Use for the Design and Evaluation of High Rate Gas Wells," SPE Paper 9424, (1980).

Dukler, A. E., Wicks, Moye III, and Cleveland, R. G.: "Frictional Pressure Drop in Two-Phase Flow: B: An Approach Through Similarity Analysis," AIChE Jour, (Jan. 1964), 44-51.

Fortunati, F., "Two-phase Flow Through Wellhead Chokes," AIME SPE Paper 3741, (1972).

Jones, L. G., and Blount, E. M.: "Use of Short Term Multiple Flow Tests to Predict Performance of Wells Having Turbulence," SPE Paper 6133, (1976).

Hagedorn, A. R., and Brown, K. W.: "Experimental Study of Pressure Gradients Occurring During Continuous Two-Phase Flow in Small-Diameter Conduits," J. Pet. Tech., (April 1965) 475-483.

Mach, J., Proano, E. A., and Brown, K. W.: "Application of Production Systems Analysis to Determine Completion Sensitivity on Gas Well Production," Journal of Energy Resources Technology, 104, (June 1982) 162-69.

Thomas, L. K.: "Determination of Acoustic Velocities for Natural Gas," AIME, SPE Paper 2579, (1970).

Wallis, G. B.: One Dimensional Two-Phase Flow, McGraw-Hill Book Co., Inc., New York (1969).

5. STUDY OF METHODS FOR DIVERTING GAS TRAPPED IN SUBSEA BOP STACK

When drilling in deep water, with a subsea BOP stack, it is possible under certain conditions to trap dangerous volumes of gas in the upper portion of the BOP stack. This can occur for certain BOP stack configurations and shut in procedures during the circulation of a kick. An example BOP stack configuation and shut-in procedure that can lead to trapped gas is shown in Figure 5.1. In this example, only the upper annular preventer was closed during the shut-in sequence. The location of the exit ports for the choke line was a significant distance below the upper annular preventer.

The amount of gas that can be trapped in this manner can be estimated by considering the dimensions of a typical subsea BOP stack (Figure 5.2). Shown in Table 5.1 are the calculated trapped gas volumes between the top annular preventer and the various flowline ports. Note that the volume varies from 6 to 9.6 bbl, depending on which flowline ports are used during the kick circulation.

The total standard volume of trapped gas depends on the pressure and temperature of the gas as well as the volume of the trap. In shallow water, the pressure is low, and thus the trapped gas standard volume will not be large enough to present a significant hazard. However, as the water depth is increased, the hazard rapidly becomes more significant. For example, in 200 ft. of water with a 13 lb/gal mud, the maximum gas volume is no more than 500 scf. In 1500 ft. of water this maximum volume increases to about 3,700 scf and in 7,000 ft. of water, it increases to 17,400 scf.

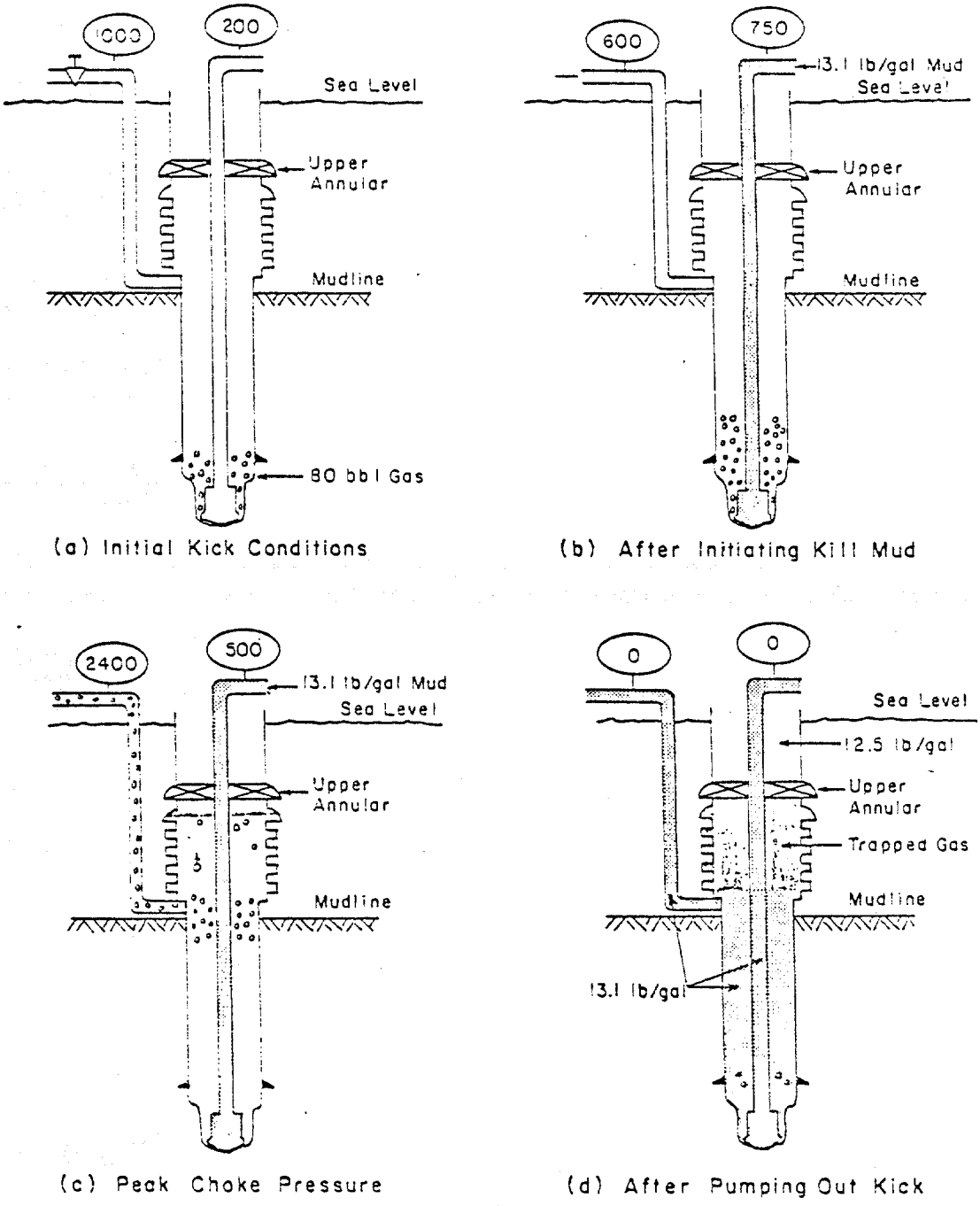

FIGURE 5.1. Trapped Gas Forming Under an Annular BOP in a Subsea Stack

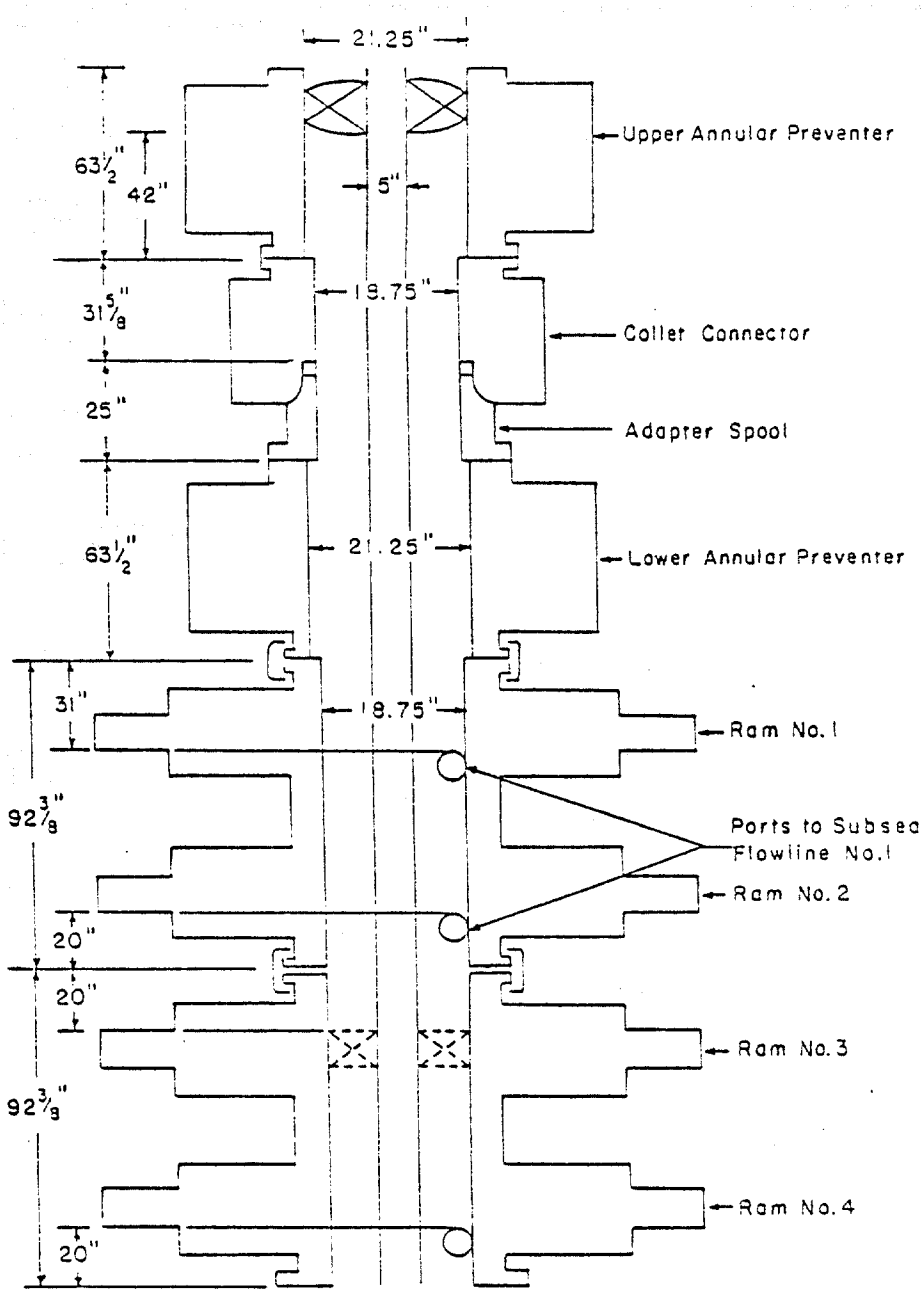

FIGURE 5.2. Dimensions of Typical BOP Stack Cavity

Description	O.D. (in.)	I.D. (in.)	Length (in.)	Trapped Gas Volume ($in.^3$)	(gal)	(bbl)
Closed Upper Annular	21.25	5.0	42	14,071	60.9	1.45
Collet & Adapter	18.75	5.0	57	14,619	63.3	1.51
Open Lower Annular	21.25	5.0	64	21,441	92.8	2.21
Subtotal				50,131	217.0	5.17
Ram Volume						
To Top Flowline Port	18.75	5.0	31	7,951	34.4	0.82
To Middle Flowline Port	18.75	5.0	73	18,723	81.1	1.93
To Bottom Flowline	18.75	5.0	166	42,576	184.3	4.39
To top of Ram 3	18.75	5.0	113	28,131	125.5	2.99
Total Trapped Gas						
To Top Flowline Port				58,082	251.4	5.99
To Middle Flowline Port				68,854	298.1	7.10
To Bottom Flowline				92,707	401.3	9.56
To top of Ram 3				79,113	342.5	8.16

Table 5.1. Calculation of Trapped Gas Volume

Numerous individuals attending the LSU BOP school have reported violent gas expansions when opening the annular BOP after circulating out a kick and starting the riser kill operation. Recently, an accident occurred in which gas that was being circulated from a marine riser caught fire, resulting in a loss of 4 lives.

The industry has developed several procedures for removing gas trapped in a subsea BOP stack. One method that has been proposed is illustrated in Figure 5.3. Seawater is first pumped down one of the subsea flowlines to the BOP stack. After filling the flowline with seawater, the trapped gas is isolated from the wellbase by closing one of the lower rams. The flowline containing seawater is then opened to the choke manifold to allow the trapped gas to expand, expelling as much gas as possible to the separator. The annular preventer is then opened (Figure 5.4), allowing the mud in the riser to sweep more of the gas down through the BOP stack and up the subsea flowline. However, the efficiency of gas removal by this process is not known. Some of the gas bubbles may rise through the mud due to the density difference between the gas and the mud, and thus enter the marine riser. When this gas is circulated to the surface while killing the riser, some gas expansion may occur.

Objective of Study

In this study, experiments were undertaken to experimentally measure gas removal efficiency using the procedures described above. These experiments should permit validation of a computer model of the gas removal process. In this way, the efficiency of the process could be predicted for a variety of field conditions.

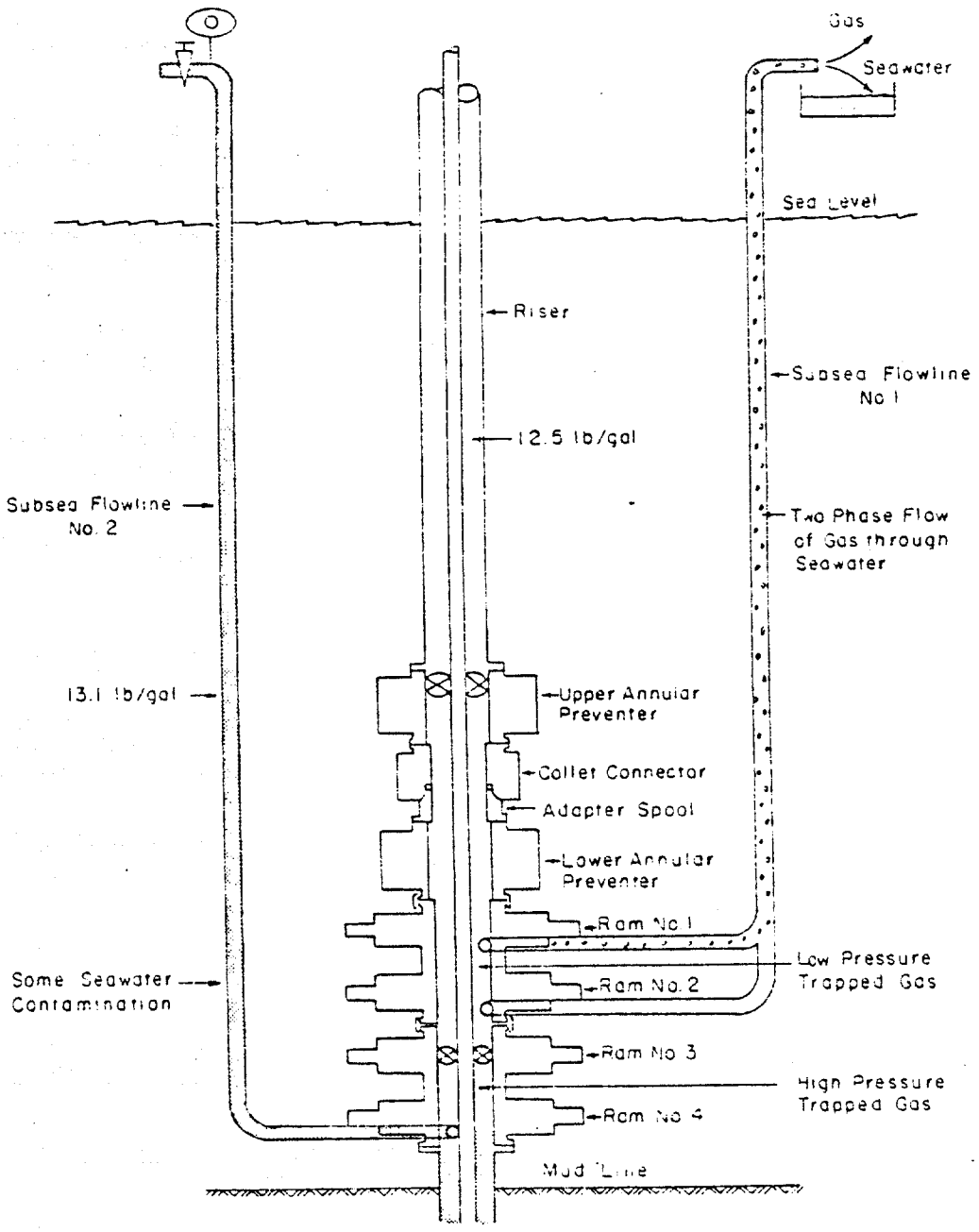

FIGURE 5.3. Release of Pressure on Trapped Gas - Version 1

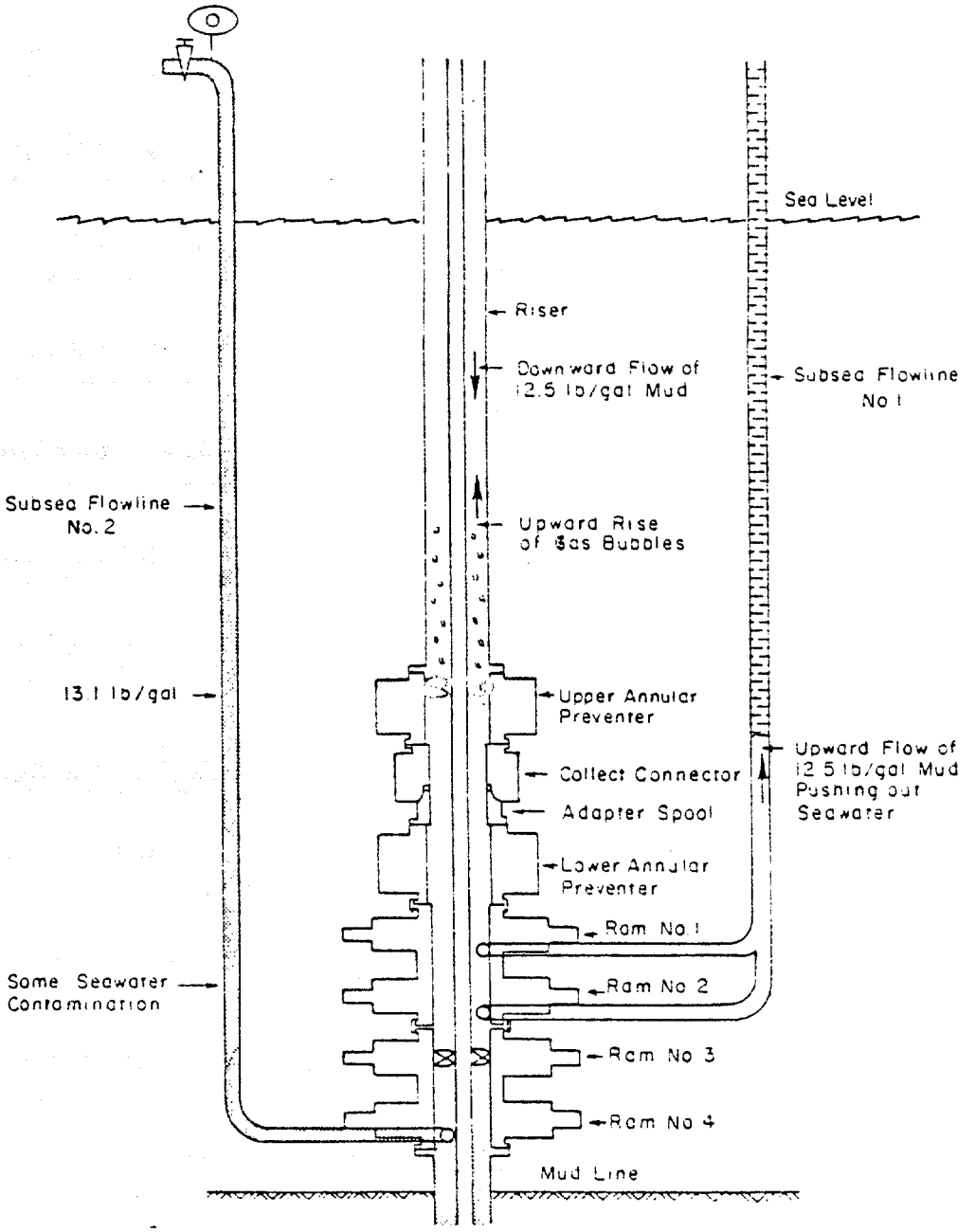

FIGURE 5.4. Release of Pressure on Trapped Gas - Version 2

The experimental apparatus consisted of a simplified subsea BOP stack equipped with several pressure and temperature transmitters (Figure 5.5). The lower section which includes the shaffer annular and the pipe below it simulated the BOP stack and the upper spool and centrifugal pump acted as the marine riser. The side outlet and choke acted as our chokeline and changes made in the choke position would represent increased chokeline friction due to increased water depth. The pressure transmitters were located at the "fluid in" level and at the fluid out level with a differential pressure cell reading across the hydril. The temperature transmitters were located below the hydril and at the top of the column and were used primarily for measurement of gas temperature for volume calculations. A wet test meter was installed at the top of the column to record the total amount of gas collected in the riser. The transducers were connected to a remote 6-pen chart recorder which kept a permanent record for later interpretation.

The experimental procedure went as follows: First the entire system was completely flushed of any gas. This is done by opening both the choke and the bleed valve at the top of the column with the pump running. Next, the BOP was closed and 3 gallons of water were displaced with low pressure air which was injected under the BOP. To increase the differential pressure the choke was opened slightly which allowed the trapped gas to expand to some lower pressure. The next step was to open the BOP and try to sweep the gas downward out of the system. After the BOP opened, the flow rate was measured using the trip tank. The gas that was not swept downward was given time to collect at the top of the column and was then measured using the wet-test meter. This procedure was repeated for the entire range of the available choke positions and then the entire set of runs were repeated for each fluid type tested.

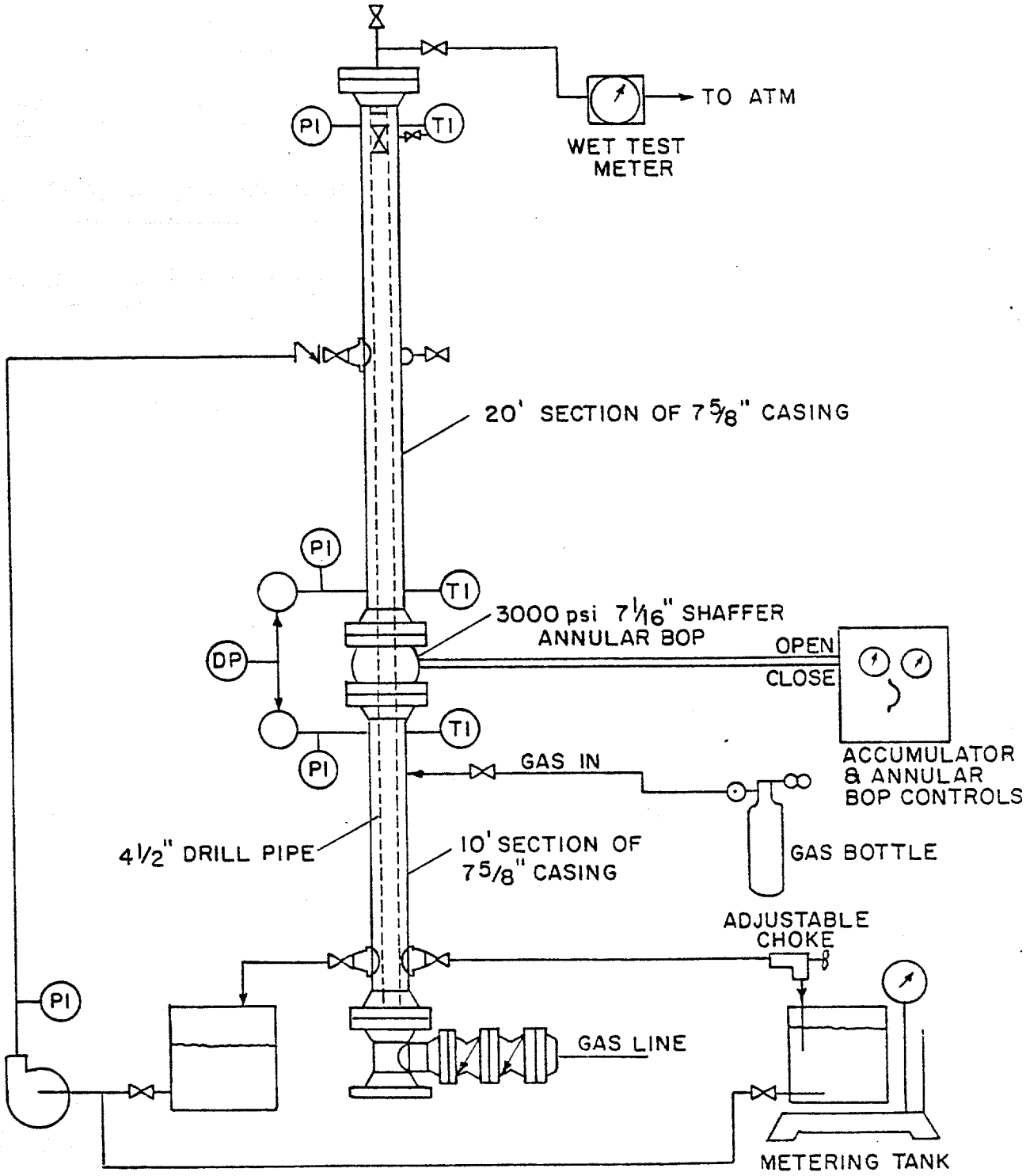

FIGURE 5.5. Schematic of Experimental Apparatus

The data obtained from each run was converted into convenient units for comparison. The flowrate through the BOP was converted to fluid velocity using the area of the annulus. The trapped gas volume and the gas volume not swept out were both converted to SCF for comparison.

The efficiency of the process was then calculated as percent of initial gas that was swept out. This efficiency was plotted against the corresponding fluid velocity to obtain the characteristic curve for each fluid.

EXPERIMENTAL RESULTS

The results obtained with fresh water with a 70 psi downward pressure differential across the preventer when it was opened is shown in Figure 5.6. Essentially 95% of the gas was successfully swept downward and out of the BOP stack for a choke line resistance that would limit the downward velocity to no less than 75 ft/min. For higher values of choke line resistance, the gas removal efficiency decreased. Only about 20% of the gas was recovered for equilibrium liquid velocities below 20 ft/min.

The results obtained with salt water are given in Figure 5.7. Note that salt water gives a more efficient recovery because the salt assists in maintaining more of the smaller bubble sizes. A gas removal efficiency of 95% can be achieved with a 50 ft/min equilibrium liquid velocity.

The results obtained with an 8.8 lb/gal gel-water mud are given in Figure 5.8. The mud had a plastic viscosity of 11 cp and a yield point of 3 lb/100 ft^2. Note that the results were very similar to those achieved with fresh water.

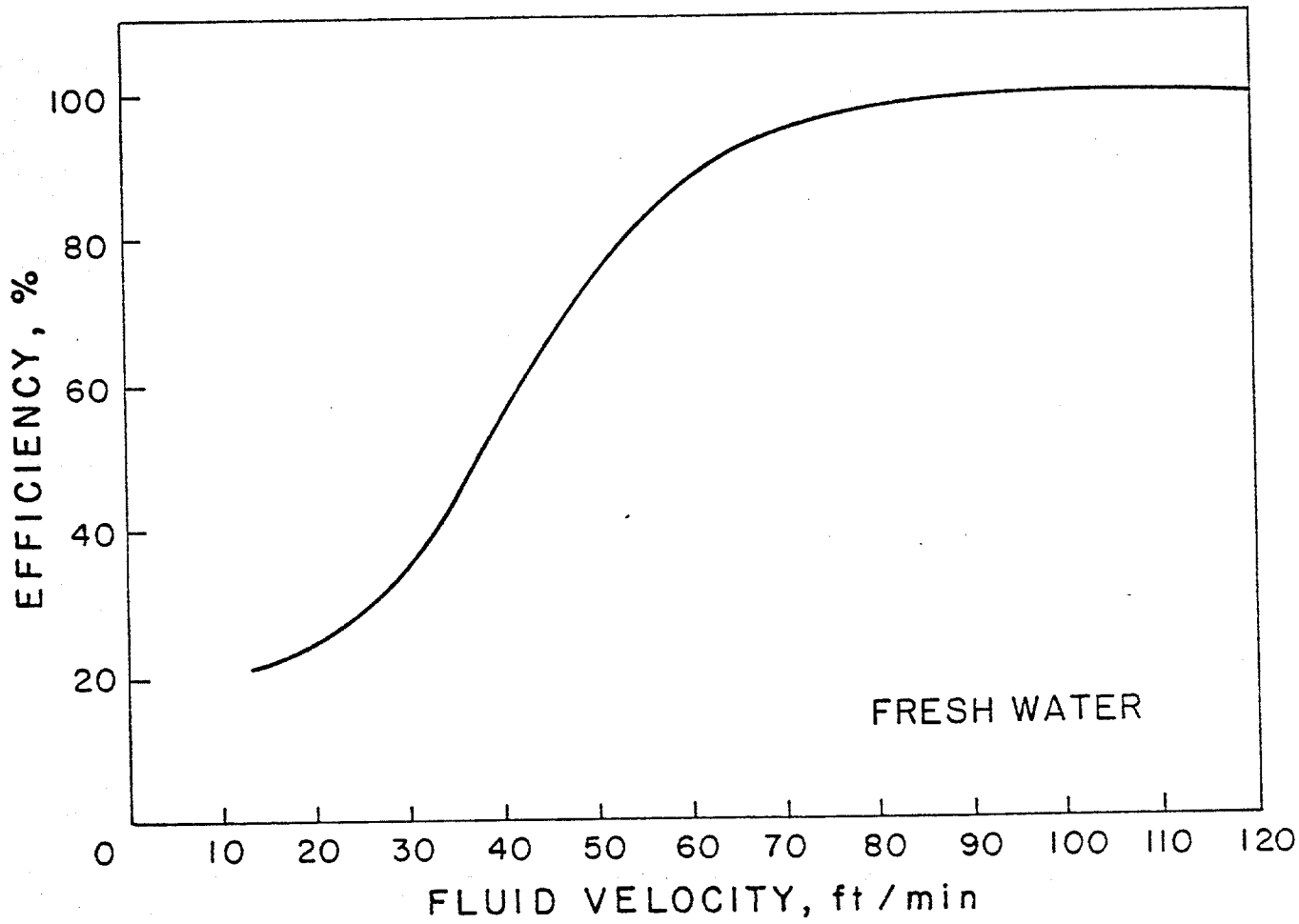

FIGURE 5.6. Gas Removal Efficiency as a Function of Equilibrium Downward Flow Velocity for Water and a 70 psi Initial Pressure Differential Across the Blowout Preventer

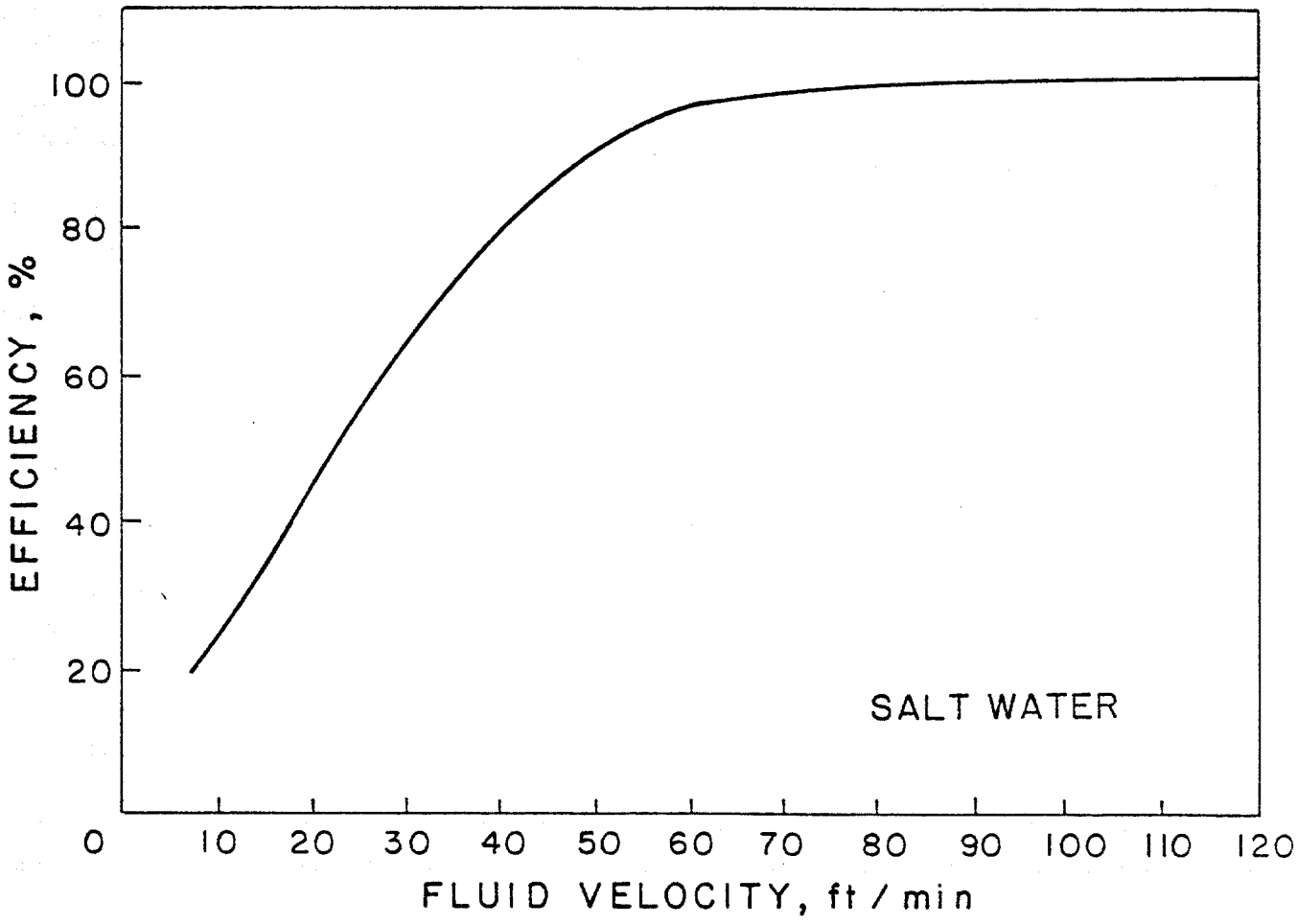

FIGURE 5.7. Gas Removal Efficiency as a Function of Equilibrium Downward Flow Velocity for 20,000 ppm Salt Water and 70 psi Initial Pressure Differential Across the Blowout Preventer

The effect of increasing the mud viscosity and gel strength is shown in Figure 5.9. The mud used had a plastic viscosity of 34 cp and a yield point of 30 lb/100 ft^2. Note that much higher equilibrium downward velocities are required to achieve a high gas recovery efficiency. This is caused by a slower initial mud entry rate through the preventer, and the formation of larger gas bubbles in the trapped gas chamber.

The effect of increasing the differential pressure across the blowout preventer from 70 psi to 100 psi for water is shown in Figure 5.10. Note that high efficiency is achieved at much lower equilibrium downward flow velocities at the higher differential pressure. This is thought to be due to the more rapid entry of liquid into the trapped gas chamber and the formation of smaller bubbles due to increased turbulence.

Application to Field Conditions

The experimental data obtained in this study should permit verification of a computer model of the U-tube method of removing gas trapped in a subsea BOP stack. This will be accomplished in a future phase of the research. However, an approximate estimate of results under field conditions can be obtained as follows:

1. Determine the pressure differential across the annular BOP by subtracting choke line hydrostatic pressure from the marine riser hydrostatic pressure.

2. Estimate choke line friction as a function of flow rate for the fluid present in the choke line.

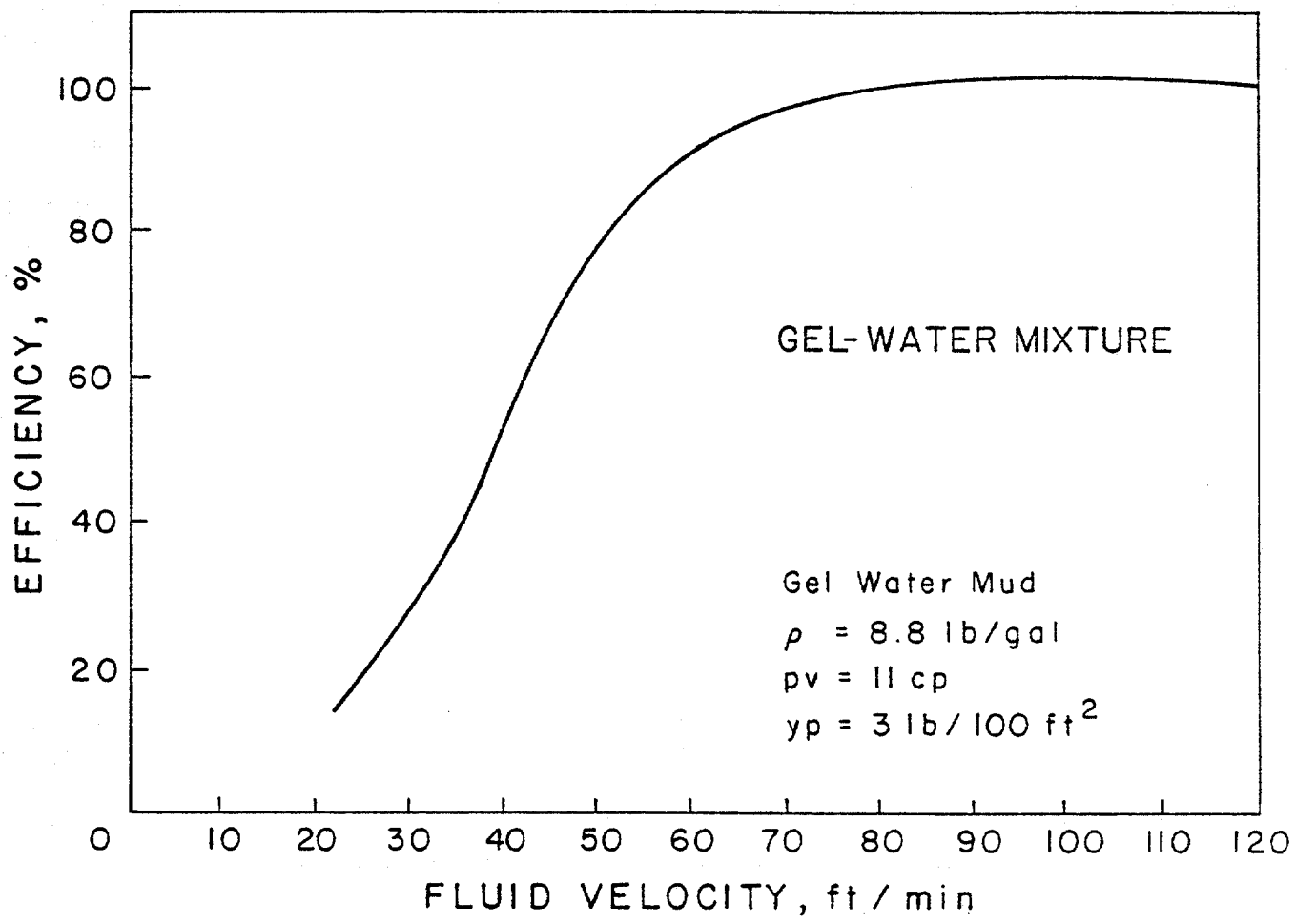

FIGURE 5.8. Gas Removal Efficiency as a Function of Equilibrium Downward Flow Velocity for Unweighted Water Base Mud and a 70 psi Initial Pressure Differential Across the Blowout Preventer

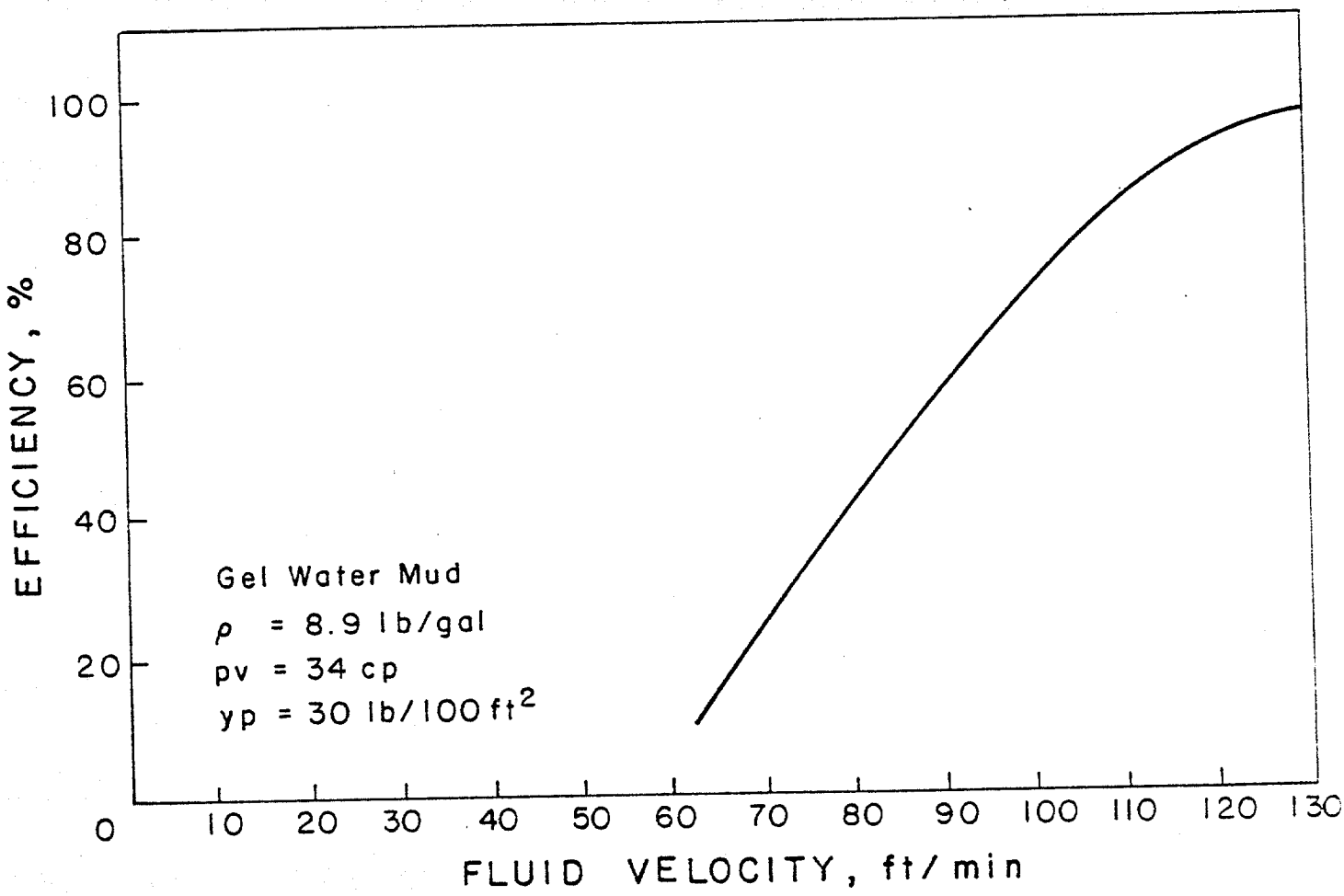

FIGURE 5.9. Gas Removal Efficiency as a Function of Equilibrium Downward Flow Velocity for Viscous Water-Base Mud and a 70 psi Initial Pressure Differential Across the Blowout Preventer

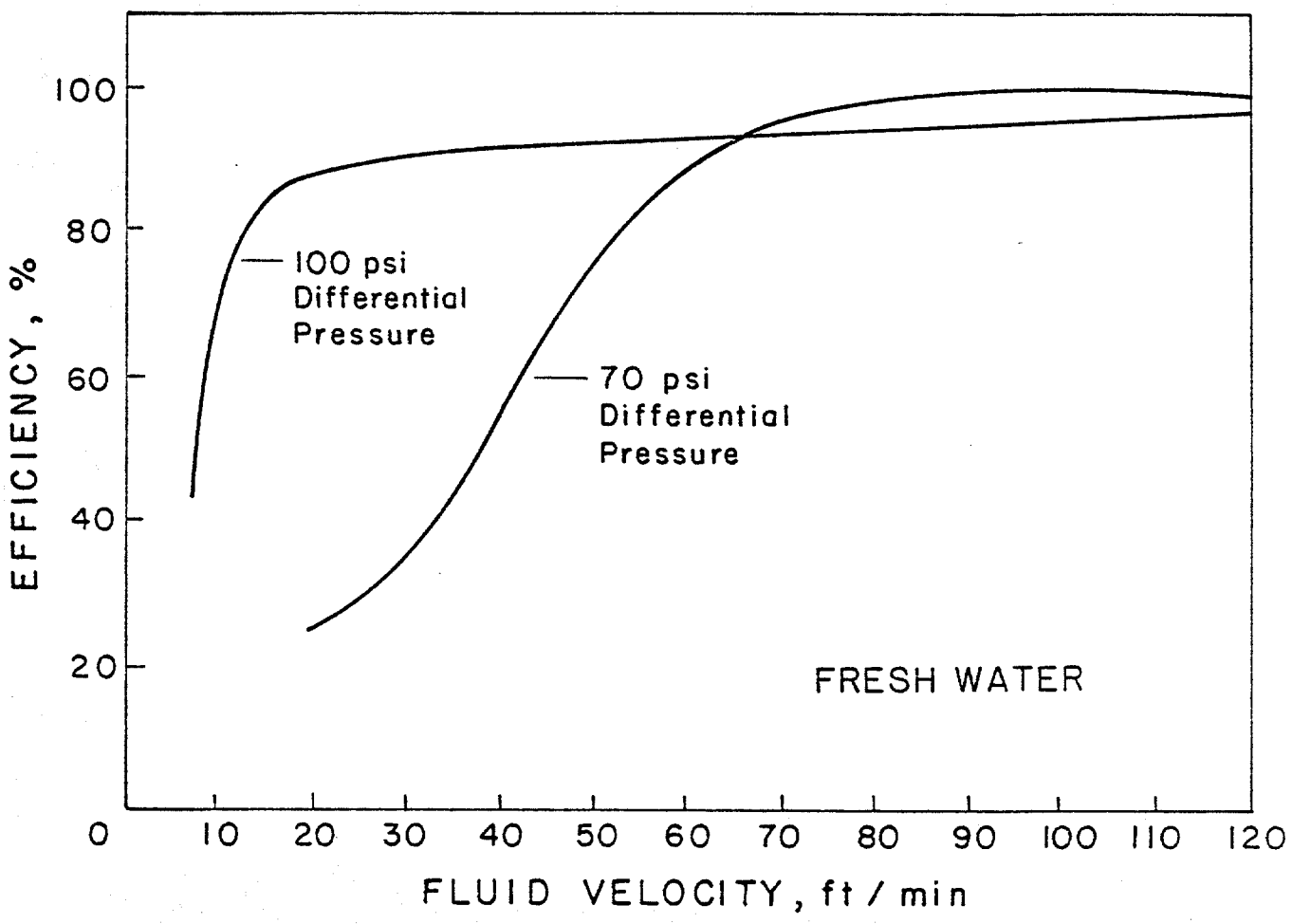

FIGURE 5.10. Effect of Differential pressure on Gas Removal Efficiency as a Function of Equilibrium Downward Flow Velocity

3. Determine downward flow rate as the rate required to make choke line friction equal to the pressure differential.

4. Compute a downward velocity in the BOP stack using the flow rate from Step 3 and the cross sectional area of the BOP stack.

5. Estimate gas removal efficiency based on the empirical data of this study.

Use of this approximate procedure for drilling fluids maintained in good condition for typical field conditions indicates that gas removal efficiencies in excess of 80% should be achieved. Thus, the U-tube method of removing gas trapped from a subsea BOP stack is usually a viable alternative.

CONCLUSIONS

As a result of this experimental study, the following conclusions have been drawn:

1. The percent of trapped gas being successfully removed depends primarily on the differential pressure and the fluid velocity.

2. Efficiency curves for the different fluids using the U-tube method have been developed for the range of conditions studied.

3. The efficiency curves developed in this study can be used to estimate field performance of the U-tube method.

4. The U-tube method is an effective well control procedure for most field conditions if proper precautions are taken.

RECOMMENDATIONS

In order to prevent future accidents in handling gas trapped in a subsea wellhead, the following steps could be taken:

1. Reduce the trapped gas volume as much as possible when selecting choke/kill line arrangement and shut-in procedures. Trapped gas volume can be greatly reduced by
   (a) Hanging-off drill string on rams just above choke-line outlet.
   (b) Modifying lower marine riser package to include a choke-line outlet just below the upper annular BOP.

2. Select surface gas handling equipment suitable for use with low pressure mud return line from riser.

3. Use of Automatic Diverter Sequence when operating limit of gas handling equipment is reached.

4. Use of low pump rate when killing marine riser to avoid over loading gas handling equipment.

5. Use of trapped gas removal procedure and riser killing procedure which will permit detection of leak across lower BOP during these procedures.

6. INTEGRATION OF MEASUREMENTS WHILE DRILLING (MWD) AND WELL CONTROL TECHNOLOGIES

In the late 1940's, the search for oil and gas accumulations first moved offshore to the shallow marine environment. Since that time, drilling operations have been extended steadily across the continental shelf. More recently, developments in the technology for drilling from floating drilling vessels have allowed exploratory drilling beyond the limits of the continental shelf and into the relatively deep water of the continental slopes. In 1974, the first well was drilled in a water depth in excess of 2000 feet [610 m].[1] By 1979, the water depth record was extended to 4876 feet [1486 m] on a well drilled offshore from Newfoundland[2]. More recent exploration off the east coast of the U.S. extended the water depth record to 6848 feet [2087 m].[3] Future plans in the Ocean Margin Drilling Program of the National Science Foundation call for scientific ocean drilling during the next decade in water depths of 13,000 feet [3962 m].[4]

Like many other aspects of drilling operations, the problem of blowout prevention increases in complexity for floating drilling vessels operating in deep water. Several special well control problems stem from greatly reduced fracture gradients and the use of long subsea choke and kill lines. Shown in Figure 6.1 is the approximate effect of water depth on fracture gradients, expressed in terms of the maximum mud density which can be sustained during normal drilling operations.[4] Note that the maximum mud density which can be used with casing penetrating 3500 feet [1067 m] into the sediments decreases from about 13.9 ppg [1666 kg/m^3] on land to about 10.7 ppg [1282 kg/m^3] in 4500 feet [1372

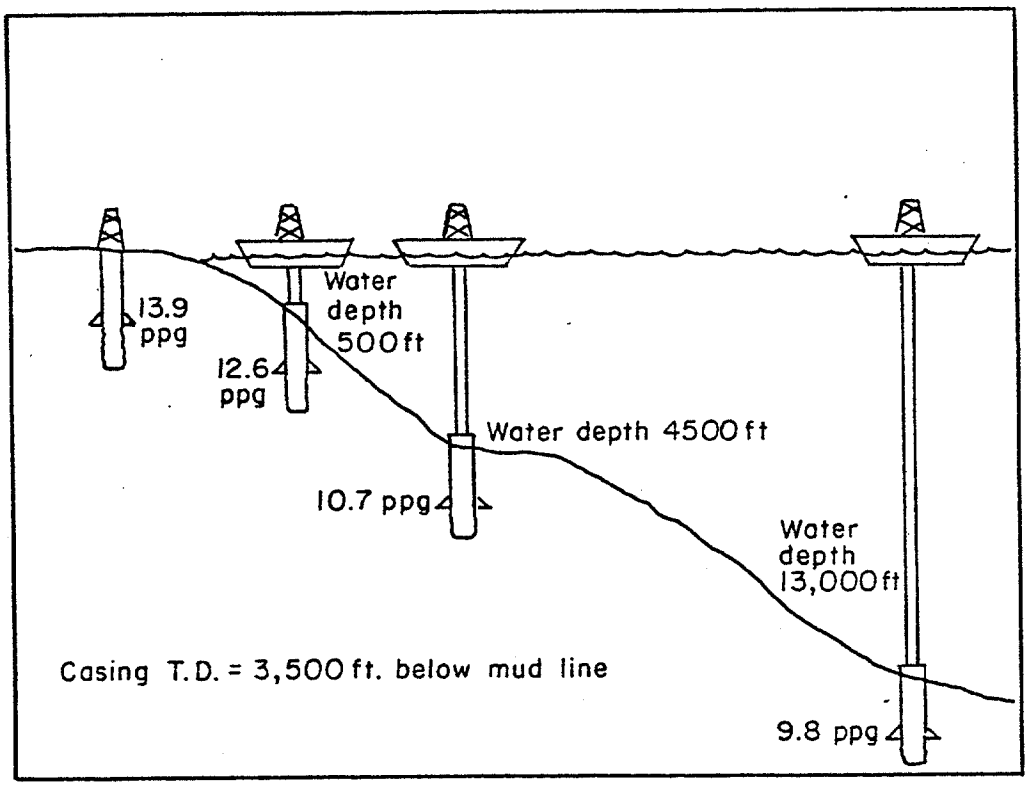

FIGURE 6.1. Approximate Effect of Water Depth on Fracture Gradient

m] of water, and to about 9.8 ppg [1174 kg/m^3] in 13,000 feet [3962 m] of water. These lower fracture gradients result primarily because the open hole must support a column of drilling fluid which extends far above the mudline to the rig floor. This additional column weight is only partially offset by the seawater. An additional contributing factor is the relatively low bulk density of unconsolidated shallow marine sediments.

The required vertical subsea choke and kill lines extending from the BOP stack at the sea floor have two detrimental aspects. One difficulty arises because of the increased circulating frictional pressure loss caused by the long length of these lines. This frictional pressure loss can cause a significant increase in the pressures occurring in the well bore. The combination of high circulating pressure losses in the choke line and low well-bore fracture gradients reduces the tolerance for error by the choke operator.

A second difficulty arises due to rapid changes in hydrostatic pressure in the vertical choke lines when circulating a gas kick. Hydrostatic pressure falls quickly when gas exits the large casing and proceeds to displace mud from the relatively small diameter choke line. In order to maintain the bottom hole pressure constant, there must be a corresponding increase in surface choke pressure to make up for this decrease in hydrostatic pressure. Choke operation becomes much more difficult during this period, as rapid changes in control pressure are required. This difficulty tends to increase with well depth because choke manipulation is based on surface drill-pipe pressure whose unsteady-state readjustment time increases with well depth and gas kick volume.

These problems require that the casing programs for wells drilled in deep water be far more complex and expensive than for a comparable land well. Shown in Figure 6.2 is an example casing program used to explore to a depth 7500 ft [2950 m] below the seafloor in 1465 ft of water in the offshore Louisiana area. Such casing programs are extremely expensive, but is the only way to maintain a significant differential between formation pore pressure and fracture gradient. Thus, it is important in well control operations conducted in this environment to make the best possible use of the available differential.

Tests were conducted at LSU's research well facility that is designed to model the geometry present on a deepwater offshore well (Figure 6.3). A simulated water depth of 3000 feet [914 m] was selected and the simulated subsea choke and kill lines (2.375-in. [0.0603-m] tubing) were run inside 10.75-in. [0.2731-m] casing to this depth. The effect of the BOP stack located on the sea floor is modeled in the well using a packer and triple parallel flow tube. A subsea kill line valve at 3000 feet [914 m] is modeled by using a surface-controlled subsurface safety valve. This control allows experiments to be conducted using only the choke line, the kill line being isolated from the system as is often the case in well-control operations on floating drilling vessels. The drill string is simulated using 6000 feet [1829 m] of 2.875-in. [0.0730-m] tubing. Gas is injected into the bottom of the well at 6,100 feet [1859 m] through 1.315-in. [0.0334-m] tubing placed in the drill string. A pressure sensor is located at the bottom of the gas injection line to allow continuous surface monitoring of bottom hole pressure during simulated well-control operations. The pressure signal is transmitted to the surface through 0.125-in. [.003175-m] capillary

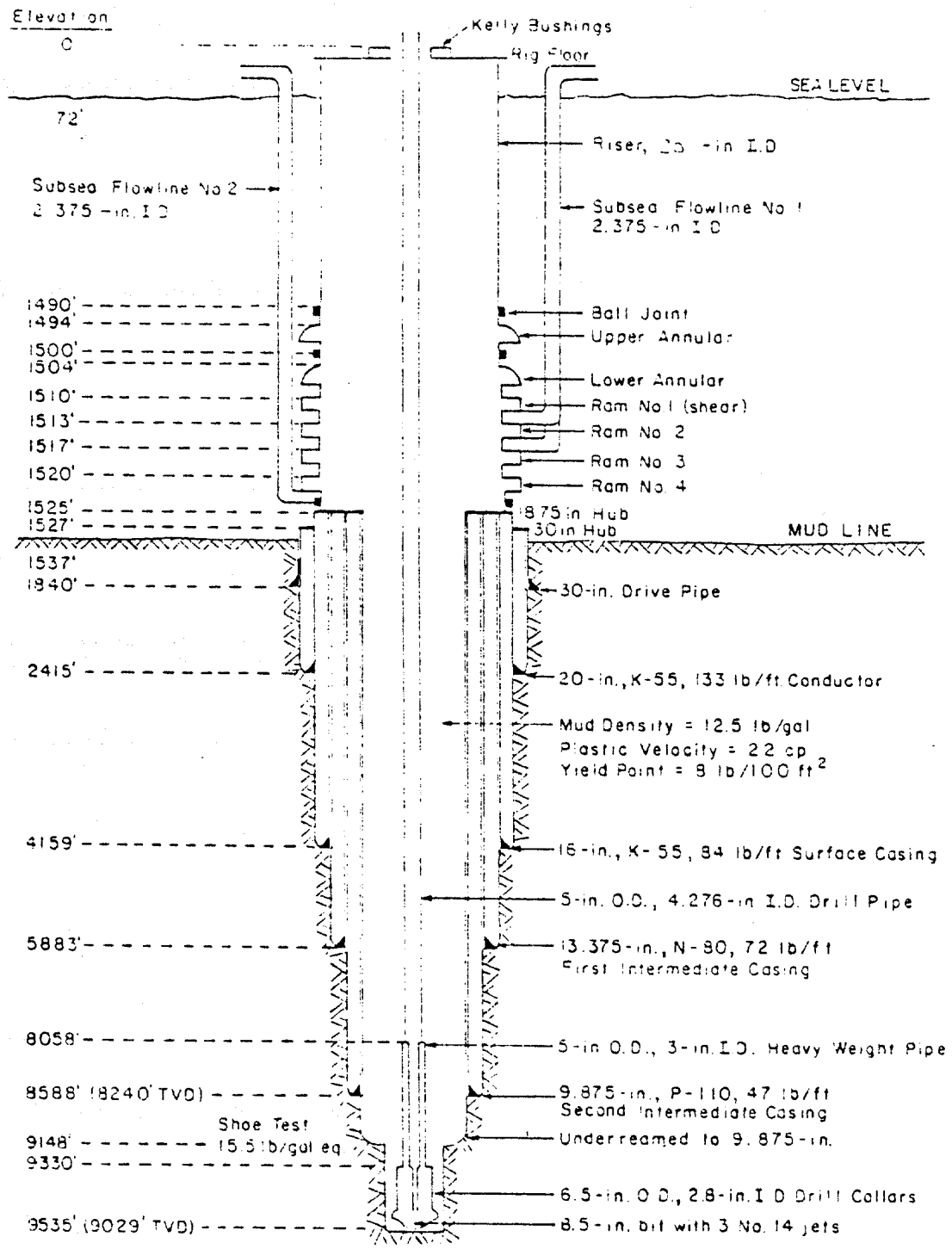

FIGURE 6.2. Example Casing Program for Deep Water Green Canyon Well

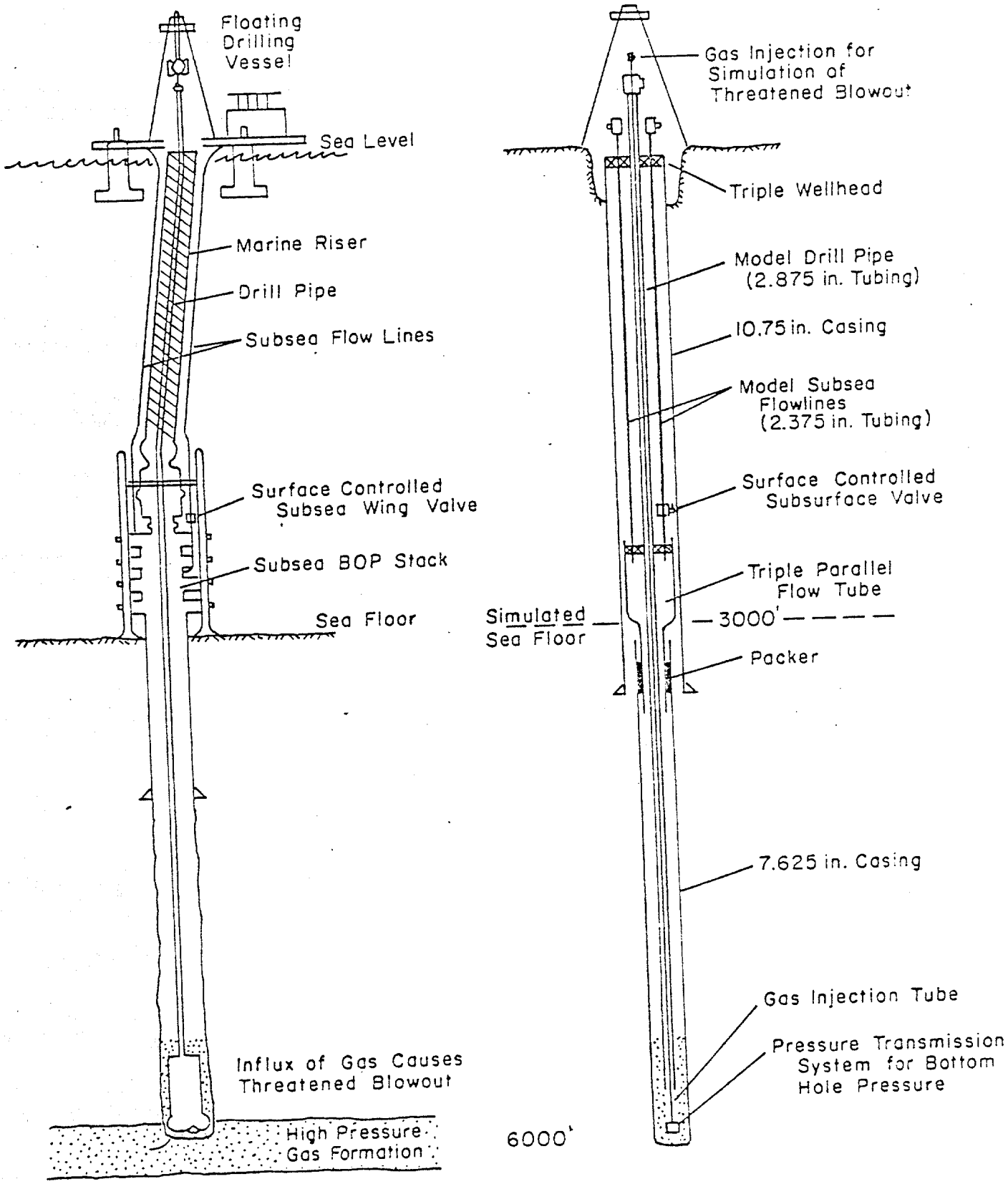

FIGURE 6.3. Well Design Selected to Model Well-Control Operations on a Deepwater Offshore Well

tubing which is strapped to the 1.315-in. [0.0334-m] tubing. A check value, located at the bottom of the nitrogen injection line, allows the line to be isolated from the system after injecting the gas kick in the well.

A photograph of the associated surface equipment for the experimental well facility is shown in Figure 6.4. The main components of this equipment include: (1) a choke manifold containing four 15,000 psi [103,400 k Pa] adjustable drilling chokes of varying design, (2) a 250 hp [186 kW] triplex mud pump, (3) two mud tanks having a total capacity of 540 bbl [85.9 m^3], (4) two 15 bbl [2.38 m] metering tanks, (5) a mud gas separator, (6) three mud degassers of varying designs, (7) a mud mixing system, and (8) an instrumentation and control house. Photographs taken inside the instrumentation and control house are shown in Figure 6.5.

Many drilling crews responsible for deepwater well control operations have trained at the LSU/MMS facility just prior to starting the deep water wells. Special schools have been conducted at the LSU/MMS facility for Shell Oil and Sonat prior to their drilling the wells off the East Coast of the U.S. which now hold the worldwide record depth for deep water drilling. Special schools have also been conducted for Odeco, for Zapata, for Amoco, for Sun, and for Tenneco prior to deep water work in the Green Canyon area of offshore Louisiana. These training exercises have provided an opportunity to measure crew performance in well control operations on a highly instrumented well.

Shown in Figure 6.6 is the most successful gas kick circulation that has been achieved to date at the experimental well facility. This exercise was conducted by J. A. Grant and J. W. Goodwin, Jr. of Shell

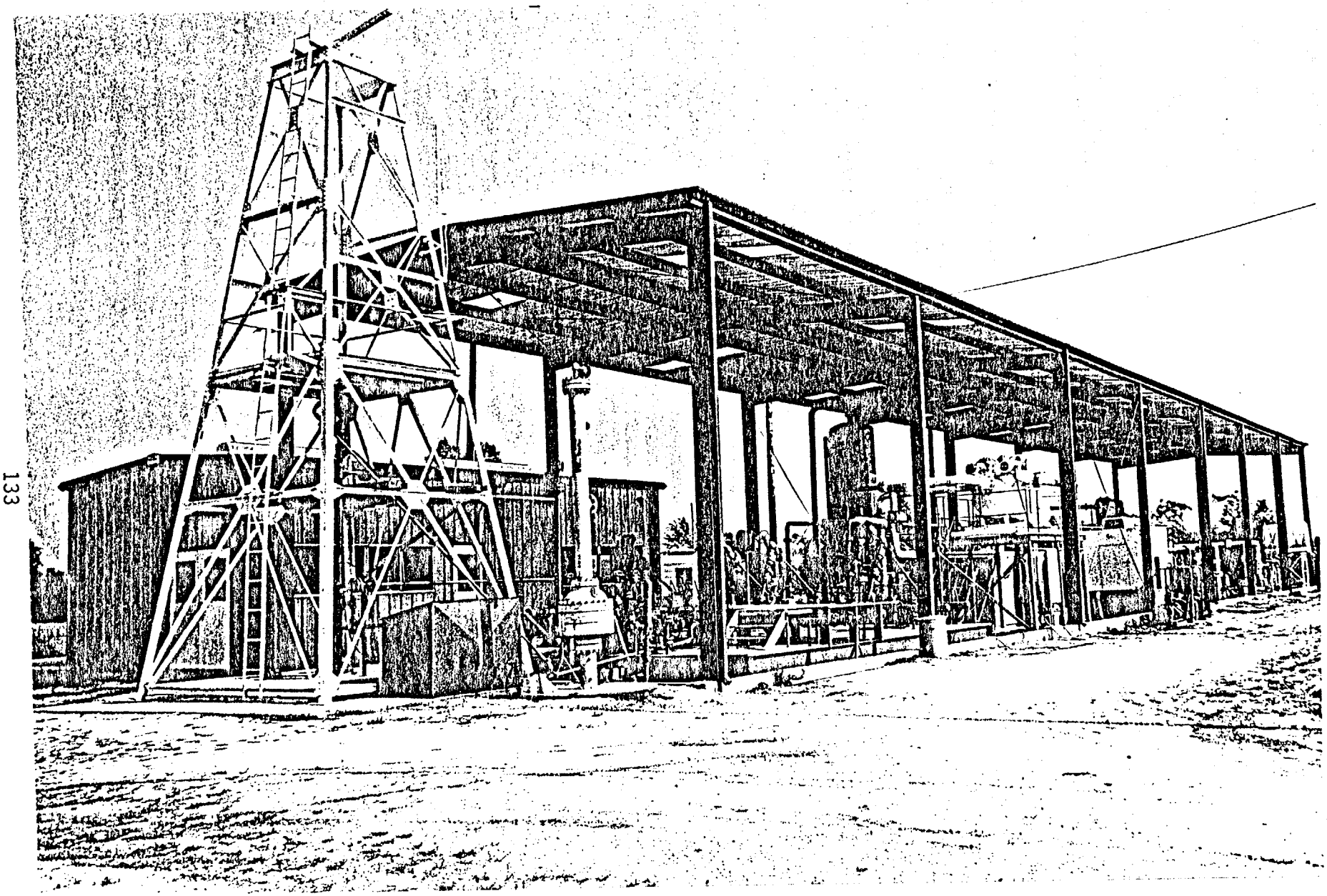

FIGURE 6.4. Associated Surface Equipment for Experimental Well Facility

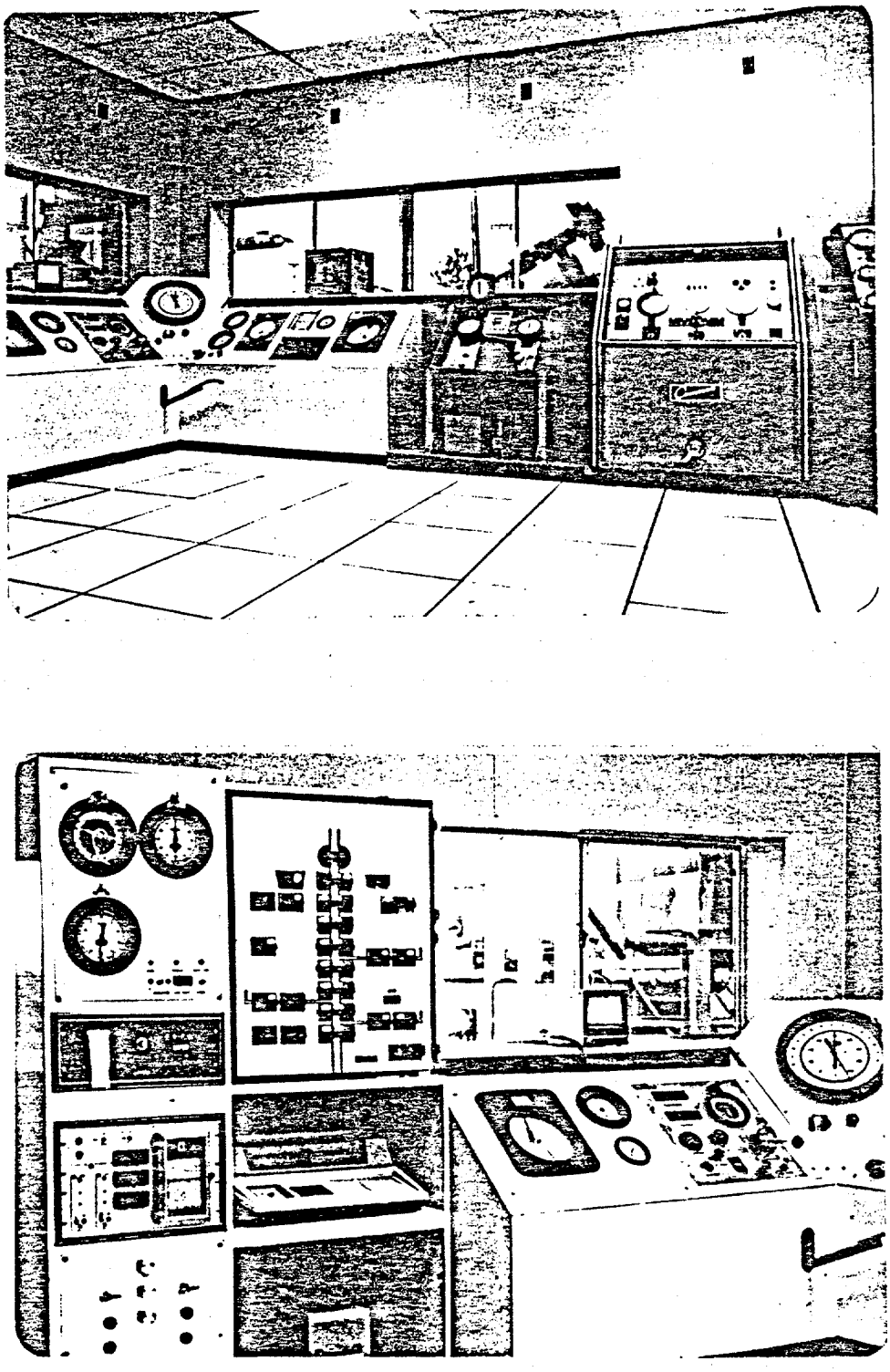

FIGURE 6.5. Instrumentation Panels in Control Room

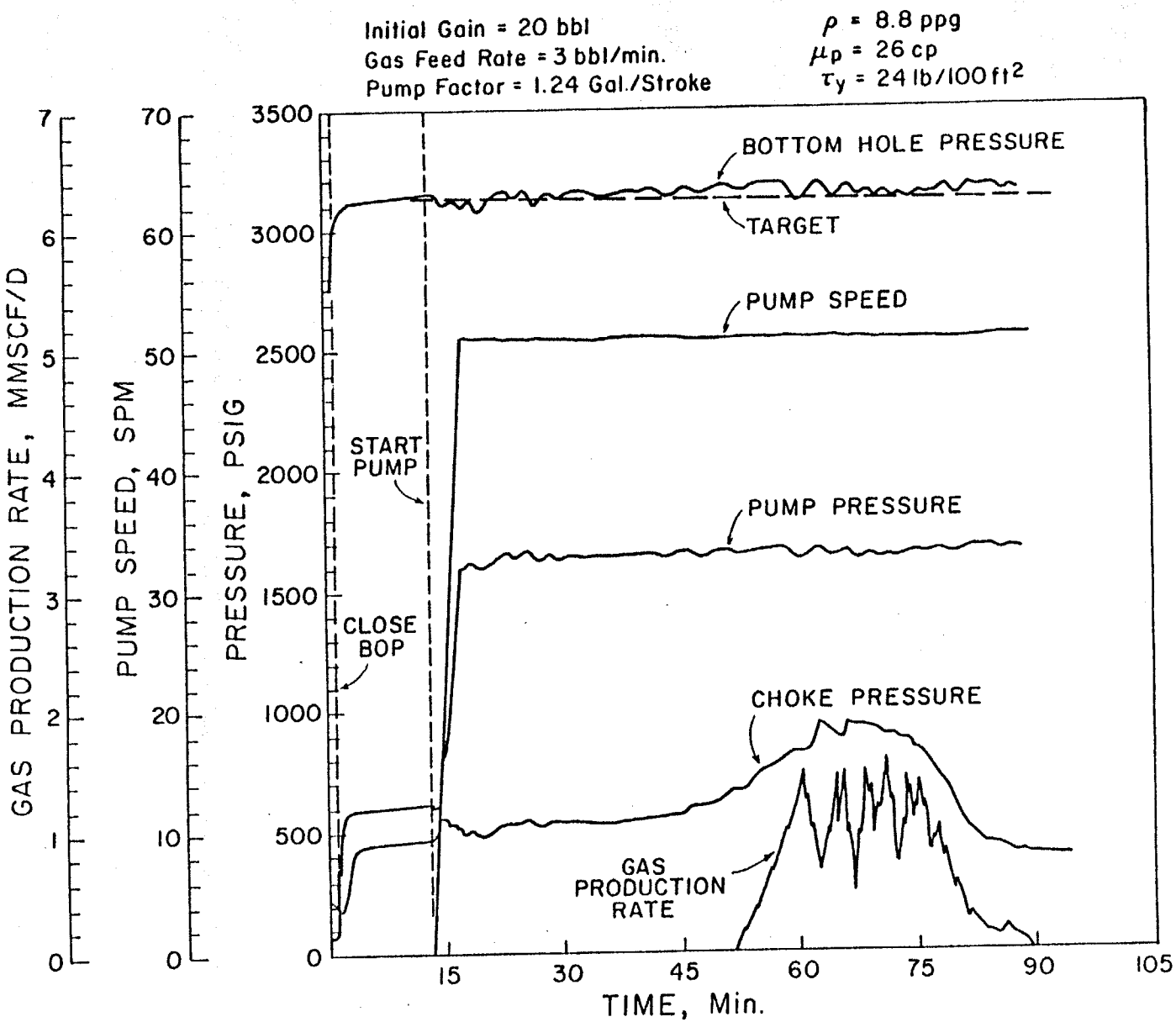

FIGURE 6.6. Successful Gas Kick Circulation Using Two Choke Lines

Offshore, Inc., using two choke lines in parallel. The kick size was 20 bbl [3.18 m^3], which was slightly less than the 23 bbl [3.66 m^3] volume of the two 2.0-in. [0.0508-m] I.D. choke lines. A kill speed of 51 spm (1.58 bbl/min) [0.00419 m^3/s] was used which corresponded to an average mud velocity in the choke lines of 203 ft/min [1.03 m/s]. The maximum error in bottom-hole pressure during pump start-up was -40 psig [-276 k Pa]. The maximum error in bottom-hole pressure while gas was in the subsea choke lines was +50 psig [+345 k Pa]. The maximum error occurred when the gas flow rate at the surface was rapidly increasing as maximum gas concentration reached the surface.

Shown in Figure 6.7 is the most successful gas kick circulation that has been achieved to date using a single choke line. This exercise was conducted by L. F. Eaton and J. W. Goodwin, Jr. of Shell Offshore, Inc. Maximum error of +75 psig [517 k Pa] occurred twice, once when the leading edge of the gas kick entered the choke line and once when the trailing edge of the gas kick exited the choke line.

A more average performance of subsea well control operations is shown in Figure 6.8. In this example, bottom hole pressure was maintained within 220 psi of the target pressure.

While the above examples illustrate that use of highly trained crews with existing equipment is adequate for current drilling practice, it also points out safety and economic advantages to be gained by the development of improved well control systems. If all kicks could be pumped out at peak efficiencies by use of computer aided choke and pump control systems, there would be significantly less risk of experiencing the complication of formation fracture during well control operations.

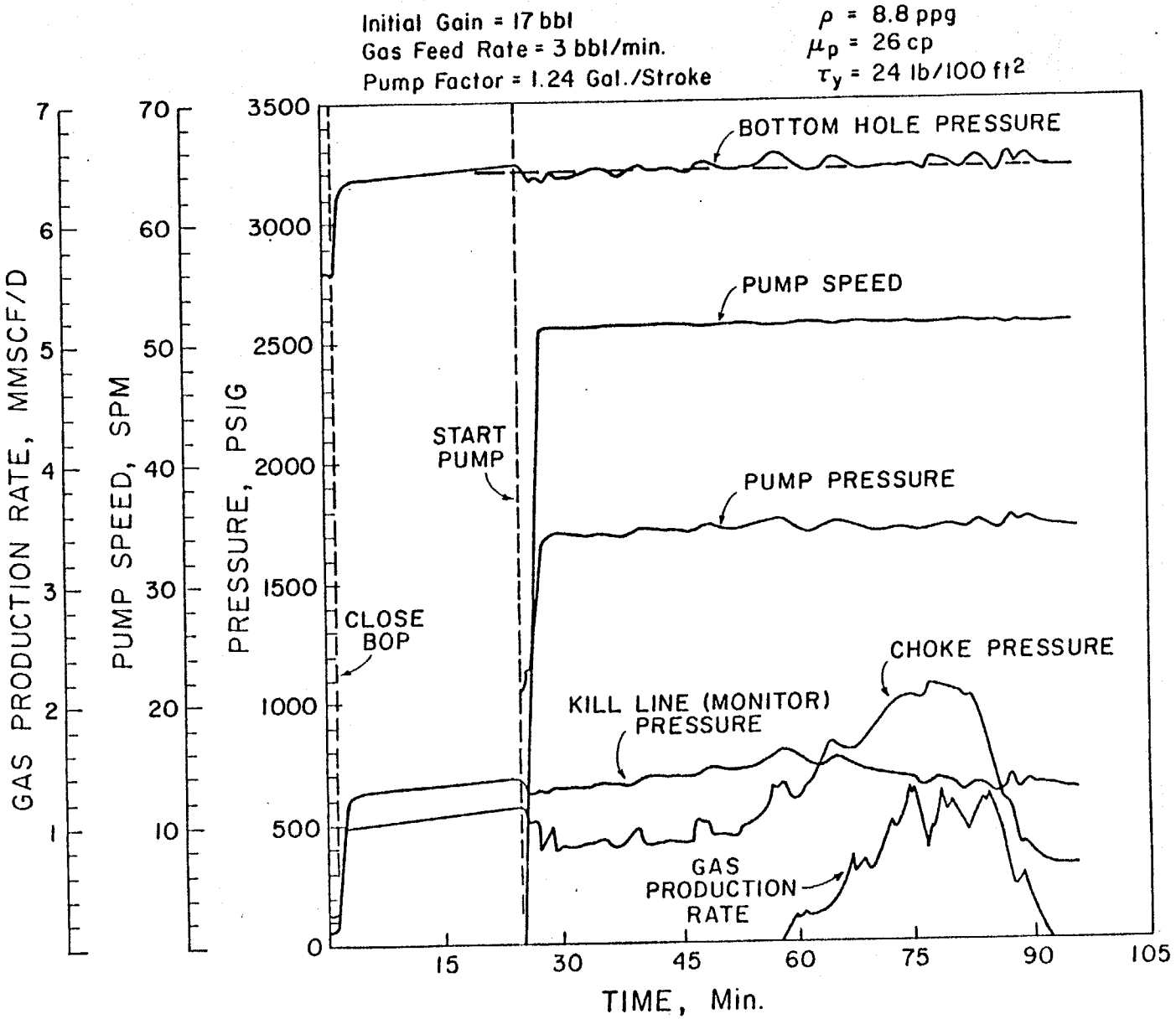

FIGURE 6.7. Successful Gas Kick Circulation Using a Single Choke Line

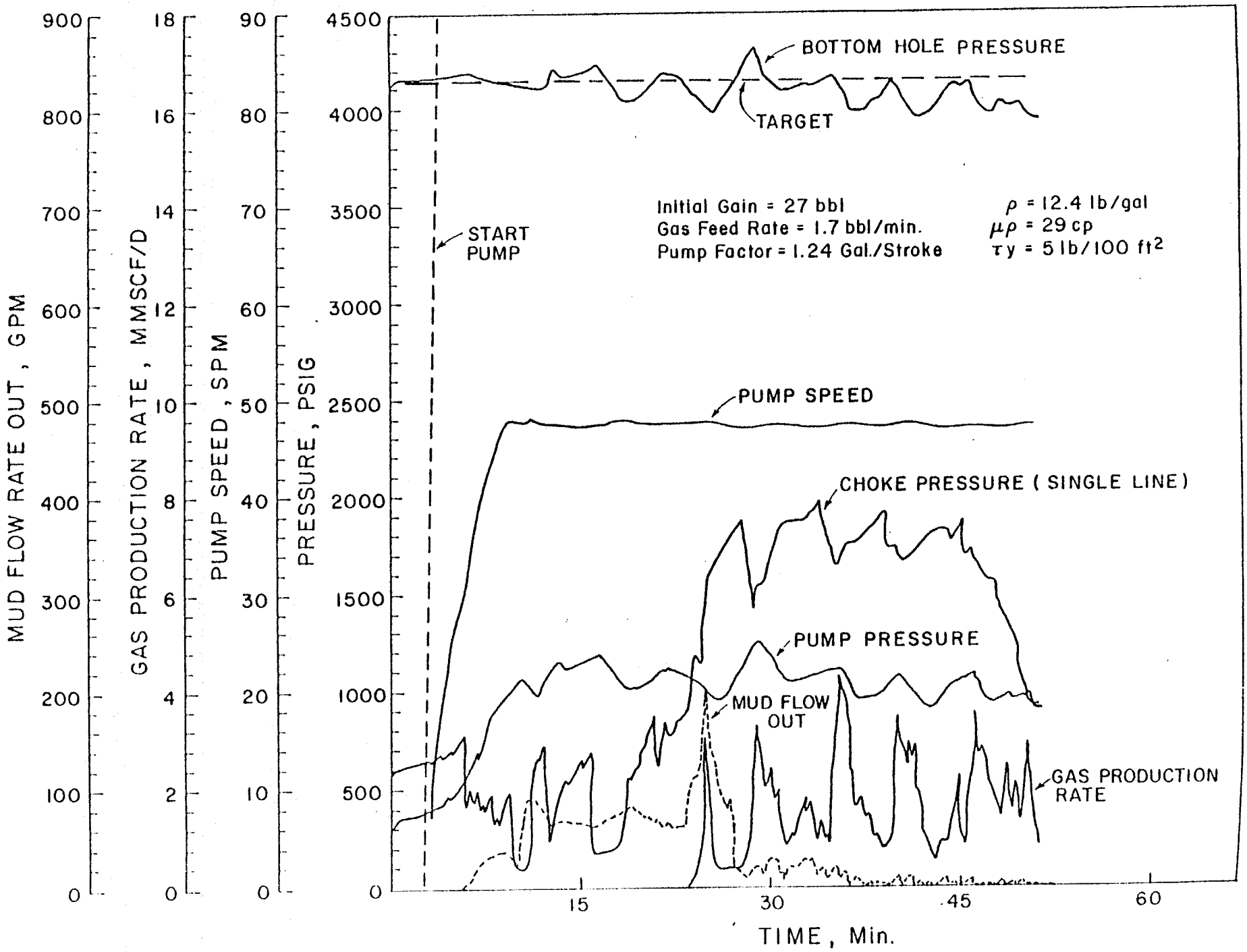

FIGURE 6.8. Example Gas Kick Circulation Showing Mud Flow Rate Out of Mud-Gas Separator

Another major factor influencing the risk of formation fracture during well control operations is the size of the kick that is taken before a well is shut-in. The risk of fracture increases greatly with kick size. Conventional kick detection on floaters is made much more difficult by vessel motion and marine riser slip-joint action. In many cases, it is difficult to detect a kick with less than a 20 bbl pit gain. Computer simulations have shown that well control operations would be greatly simplified if kicks could routinely be caught with less than a 10 bbl gain.

The amount of gas that enters the well prior to kick detection is also greatly influenced by the type of mud being used. Thomas, Lea, and Turik (1982) have shown that for an oil base mud, more than twice as much gas would enter a well before being detected by a 20 bbl gain at the surface.

All of the above kick detection problems could be eliminated by quick kick detection at the hole bottom through integration of MWD technology and well control technology. This is felt to be an area where major improvements in deepwater and drilling costs and rig safety could be made.

In the event a large gas kick is taken, integration of MWD and well control technology would also permit a novel technique to be used to reduce the risks associated with handling the kick. The novel approach is based on the observation that annular pressures experienced during well control operations are often less than anticipated when the gas is mixed with a significant volume of mud. The new process is directed at providing an additional alternative to the well operator faced with one of the problems discussed above.

BUBBLE CHOPPING CONCEPT

Experimental studies of annular two phase flow patterns under simulated well control situations have shown that formation gas entering a well mixes with the mud to form a bubble flow, churn flow, or slug flow pattern, depending on the well conditions present. The new well control process described in this paper is designed to enhance the mixing of gas and mud which normally takes place to reduce the concentration of gas in the mud to a much lower level by dispersing the gas into a much larger volume of mud. As the mud-gas mixture is circulated to the surface, less gas expansion will occur if the gas is dispersed over a large mud volume. Less gas expansion occurs because the top portion of the gas is removed from the well while the bottom portion of the gas is still compressed by considerable hydrostatic pressure. The gas is thus brought to the surface gradually, rather than as a unit.

Bubble chopping could be accomplished using various techniques. One possible approach is illustrated in Figure 6.9. A bubble chopper device could be installed in the drill string a few stands above the top of the drill collars. The exact location for maximum benefit would depend upon the well geometry under consideration. To be effective, the device should be located just above the top of the gaseous kick fluids when the blowout preventers are closed and the well stabilizes under shut-in conditions. Based on the pit gain, drill pipe pressure, and casing pressure observed for initial stabilized shut-in conditions, the operator would make a decision concerning the necessity of activating the new device. If the shut-in conditions indicate that the formation fluid is predominantly gas and the amount is too great to safely circulate

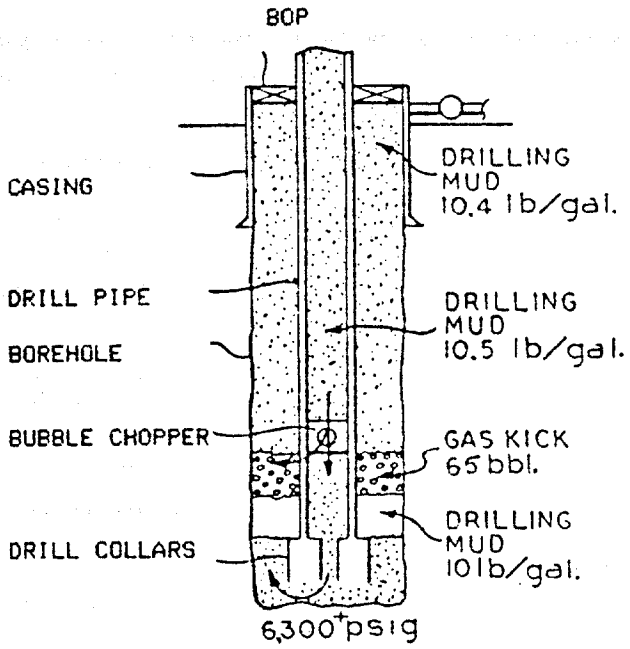

FIGURE 6.9. Bubble Chopping Concept

in the conventional manner, the bubble-chopper device could be actuated by dropping an actuator and applying pump pressure. Once actuated, the device would divert a portion of the mud flow stream to the annulus when circulation is initiated. The side port of the device would remain closed until circulation was initiated. A sufficient pressure drop through the device is needed to overcome a spring holding the side port closed. Included in the actuator mechanism is a constant flow regulation device to maintain an essentially constant-flow rate through the side port once a kill pump speed is achieved.

Bubble chopping is achieved as the gas moves past the device by the mud flowing from the side port of the device. The greater the fraction of the mud flow which is diverted out the side port, the greater the volume of mud mixed with the gas kick. Of course, the minimum possible annular pressure at points in the well above the bubble chopping point will occur when essentially all of the fluid is diverted through the side port. Unfortunately, the pumping time required to complete the well control operation increases as the flow rate fraction through the side port is increased. Thus, a decrease in maximum annular pressure can be achieved only through an increase in kick circulation time.

Whenever well circulation is stopped, the side port automatically closes by spring action. It is also desirable to deactivate the device without pulling the drill string once well-control operations are complete. This could be accomplished by dropping a ball which would form a seal in the top portion of the actuator. Pump pressure applied to the closed system would cause shear pins to fail, allowing the actuator to be pumped through the body of the device and be caught in a bypass assembly.

A comparison of the sequences involved in using the bubble chopping technique is shown in Figure 6.10. Note that dispersion of the gas with more mud would prevent formation fracture for this example.

Before the bubble chopping method can be made practical, equipment and techniques must be perfected which will insure that the bottom-hole pressure is maintained constant during well control operations. If choke operation is to be based on an observed surface drill pipe pressure, then a bubble chopper in the drill stem must contain a flow regulator to keep the flow rate through the side-port constant. This is true because the pressure drop across the side port varies as a gas kick moves up the annulus past the device. Engineering work in this area have provided several preliminary designs but none of these have proved feasible.

Other design factors which must be worked out are the prevention of leaks, erosion of the fluid passages, and the potential for plugging. The last thing an operator will want to do in an already critical situation is to activate a device in the drill stem which has a significant probability of plugging or malfunctioning due to leaks. An additional area of future study are problems related to unexpected large volumes of formation brine mixed with the gas kick.

The best promise for practical bubble chopping equipment is through integration of MWD and well control technologies. If advances in MWD technology would make it feasible to routinely monitor bottom-hole pressure during well-control operations. This would greatly simplify the problems associated with the development of a reliable bubble chopper for use in the drill stem. Choke operation could then be based on an observed bottom-hole pressure rather than surface drill pipe pressure.

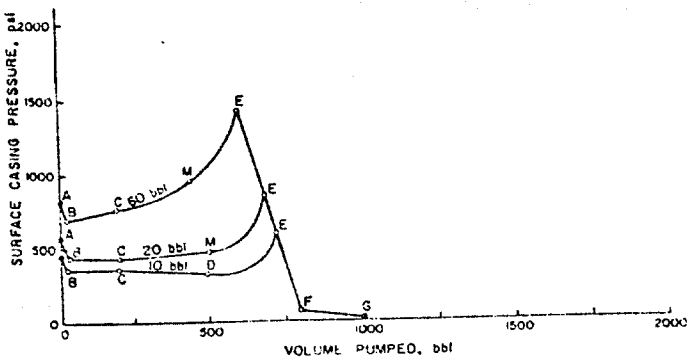

- COMPUTED CASING PRESSURE PROFILES FOR CONVENTIONAL WELL-CONTROL PROCEDURE AND SURFACE BOP STACK EXAMPLE

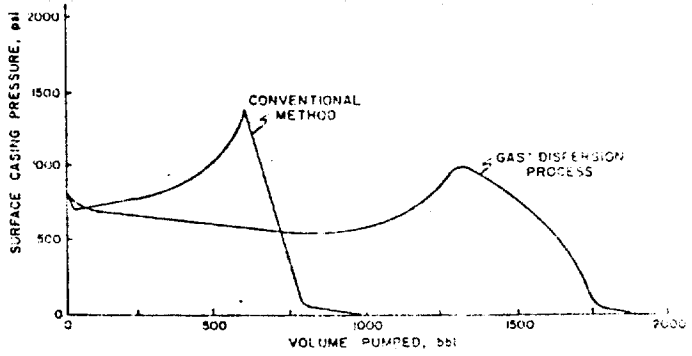

- COMPARISON OF CASING PRESSURE PROFILES FOR CONVENTIONAL AND BUBBLE CHOPPING WELL-CONTROL PROCEDURES FOR SURFACE BOP STACK EXAMPLE

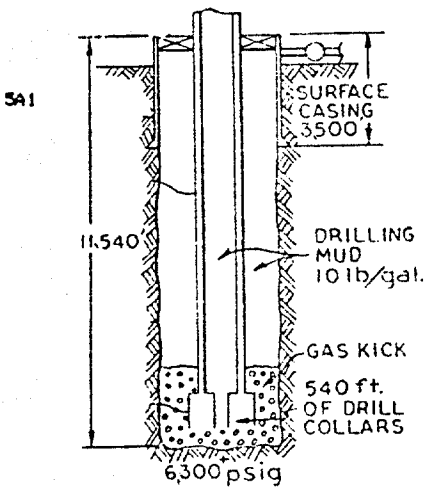

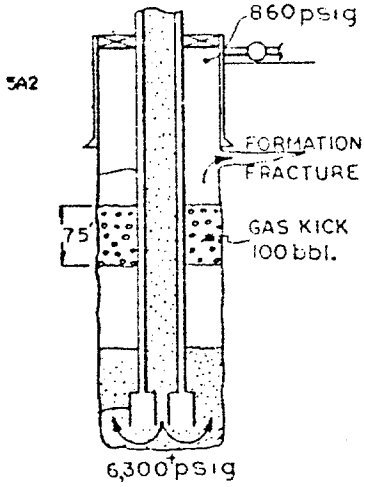

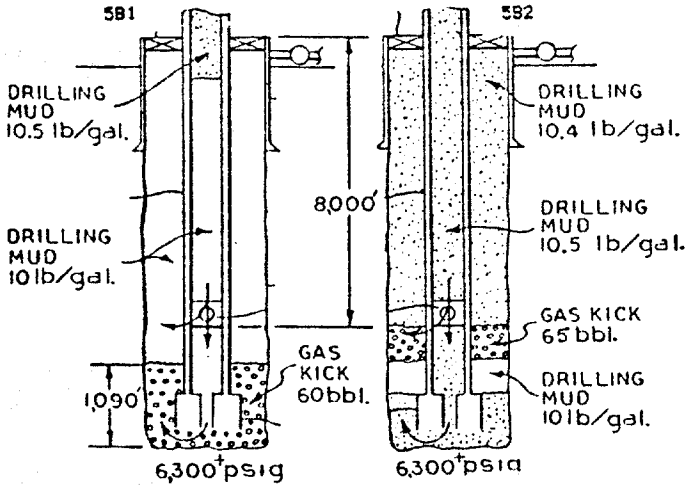

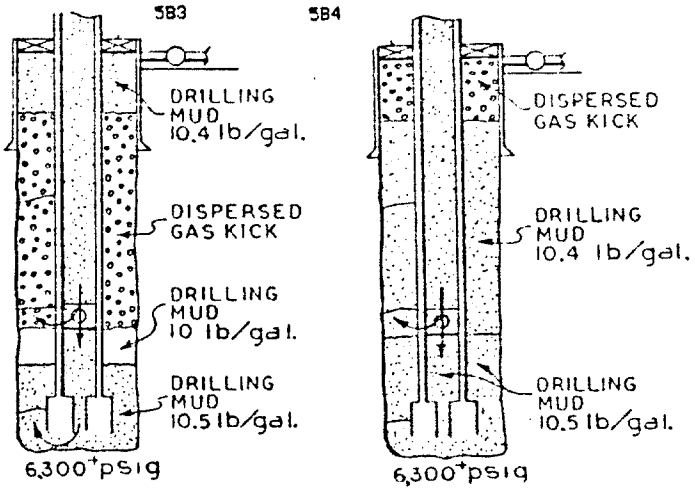

FIGURE 6.10. Comparison of Conventional Well Control to Bubble Chopping for Example 60 bbl gas kick.

OBJECTIVE OF STUDY

The objective of this study was to determine the design parameters required for the integration of MWD and well control technologies. Of major concern was (1) the determination of the best available choke design for use in an integrated system, (2) the minimum number of safety related MWD parameters needed for data transmission, and (3) the minimum data transmission rates needed for effective process control. In order to accomplish these objectives, some modifications of the existing research well facility were required.

RESEARCH WELL MODIFICATIONS

A functional schematic of the modifications of the research well facility made to permit evaluation of computer aided choke control equipment is shown in Figure 6.11. Three gas storage and compression wells were drilled to permit simulation of a natural gas formation being in constant communication with the bottom of the well. Prior to completion of this modification, gas injection was accomplished using a truck mounted high pressure cryogenic pumps. However, this arrangement was not realistic with respect to interaction between bottom hole pressure and gas injection rate after the kick was taken and well control operations were started. The construction work needed to accomplish this modification was a considerable undertaking, requiring about two years to plan and implement. A major portion of this modification was funded through industry grants.

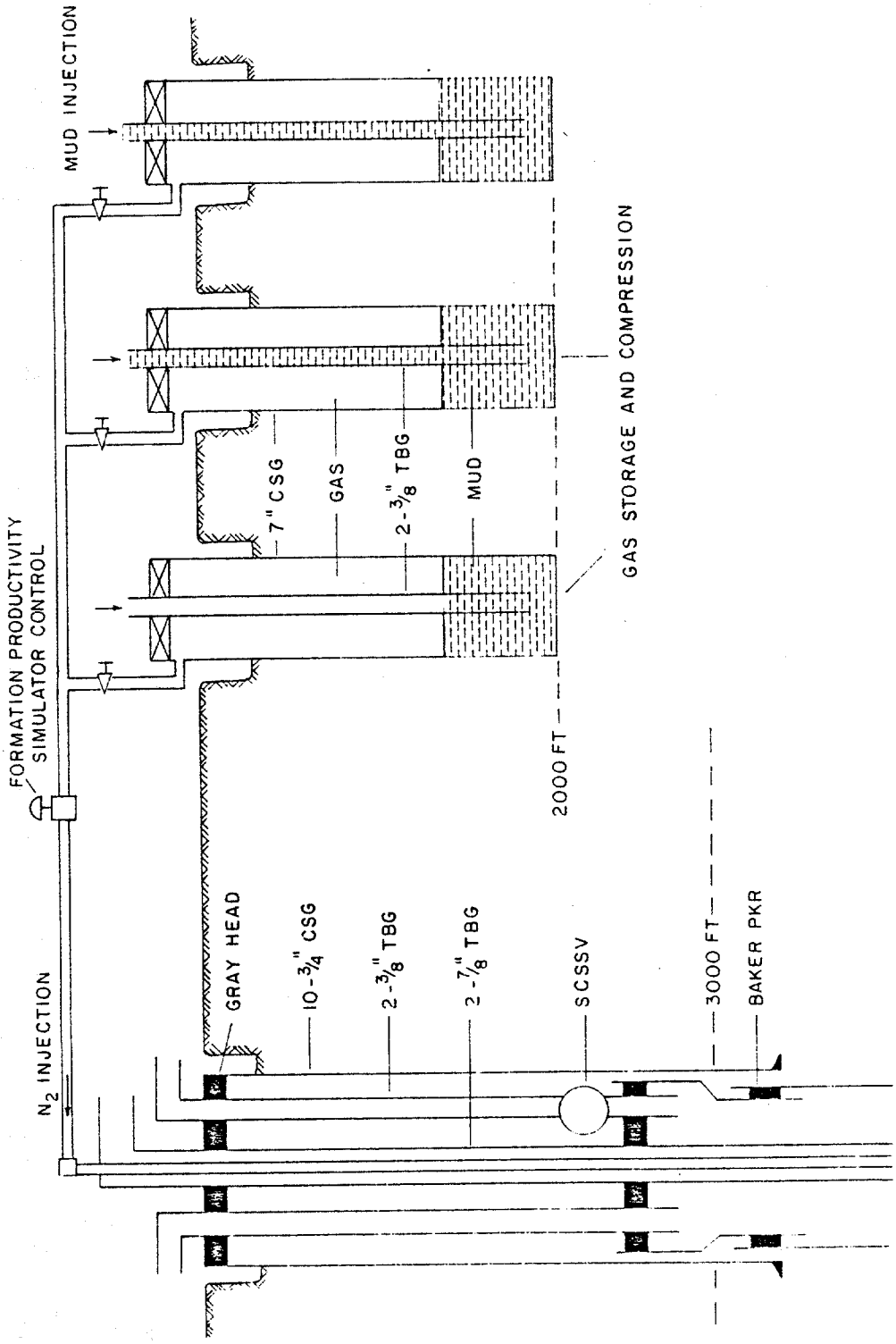

FIGURE 6.11. Schematic of Modified Research Well

EVALUATION OF ALTERNATIVE CHOKE DESIGNS

Extensive testing was done using the research well facility to evaluate four proprietary choke designs for use with an improved, integrated well control system. The choke designs used were selected because the manufacturer of these chokes had all expended a considerable research and development effort on the design of automatic or semi-automatic controls to use with these chokes. The results of these tests showed that none of the currently automatic chokes would consistently produce results for the deep water well control geometry that were better than could be accomplished with a manual system and an average level of crew training. Errors in bottom hole pressure in excess of 250 psi were generally observed when during the period gas was being produced at the surface. However, one of the four choke designs proved to have clearly superior control capabilities that could be interfaced much more easily for computer control. This choke design has been selected for use in the final development of an improved well control system.

MWD Kick Detection

Data transmission rates that can be achieved without extensive and expensive modifications to conventional rotary drilling equipment will be limited to less than 50 Hz. This will severely limit the number of parameters that can be continuously monitored. The minimum requirements for a safety system would include:

1. A formation lithology indicator such as spontaneous potential.

2. A formation porosity indicator that will also provide pore pressure prediction, such as formation conductivity, density, or sonic velocity.

3. A kick detection parameter.

4. Bottom hole well pressure.

If a high enough data rate could be achieved, then other variables such as borehole direction, inclination angle, bit weight, and torque which are useful for drilling optimization would also be highly desirable and would make the system more cost effective.

The approximate rates of data transmission presently available according to company representatives with mud pulse systems in a 10,000 ft drill hole are:

- Anadril	1.25 bits/sec
- Christensen	0.2 bit/sec
- Exlog	0.5 bit/sec
- Gearhart	0.33 bit/sec
- NL Industries	0.66 bit/sec
- Teleco	0.4 bit/sec

The MMS fluidic pulser could probably transmit 5 to 10 bits/sec at 10 to 20 Hz.

Figure 6.12 shows the various types of downhole gas detection principles which could be implemented. They are:

- Mud Acoustic Velocity,
- Mud Acoustic Attenuation,
- Mud Weight,
- Mud Resistivity,
- Mud Temperature,
- Annulus Noise Level,
- Annulus Particle Impact.

Figure 6.13 shows the acoustic velocity variation with the gas content in percent by volume. A decrease in excess of 500 ft/s is noticed for 1% gas by volume. No data on acoustic attenuation in gas cut mud has been located.

Figure 6.14 shows the mud weight variation with the gas content in percent by volume. 5 to 10% of gas are necessary for inducing an appreciable variation. Figure 6.15 shows the variation of mud resistivity. Again 5 to 10% of gas are necessary for noticing an appreciable variation. A calculation of the temperature variation of the annulus mud due to the gas expansion shows a very small effect. This can be related to the high heat capacity of the mud.

Thus the information most sensitive to gas or needed for kick control which could be transmitted with a gas kick alert system are:

- Mud sound velocity — 10 bits minimum
- Annulus mud pressure — 10 bits minimum

Since 10 bits = 1024, with a 20,000 psi pressure gauge the resolution would be 20 psi, it would be 5 psi for 12 bits and 0.3 for 16 bits. With a maximum mud sound velocity of 10,000 ft/sec the resolution would

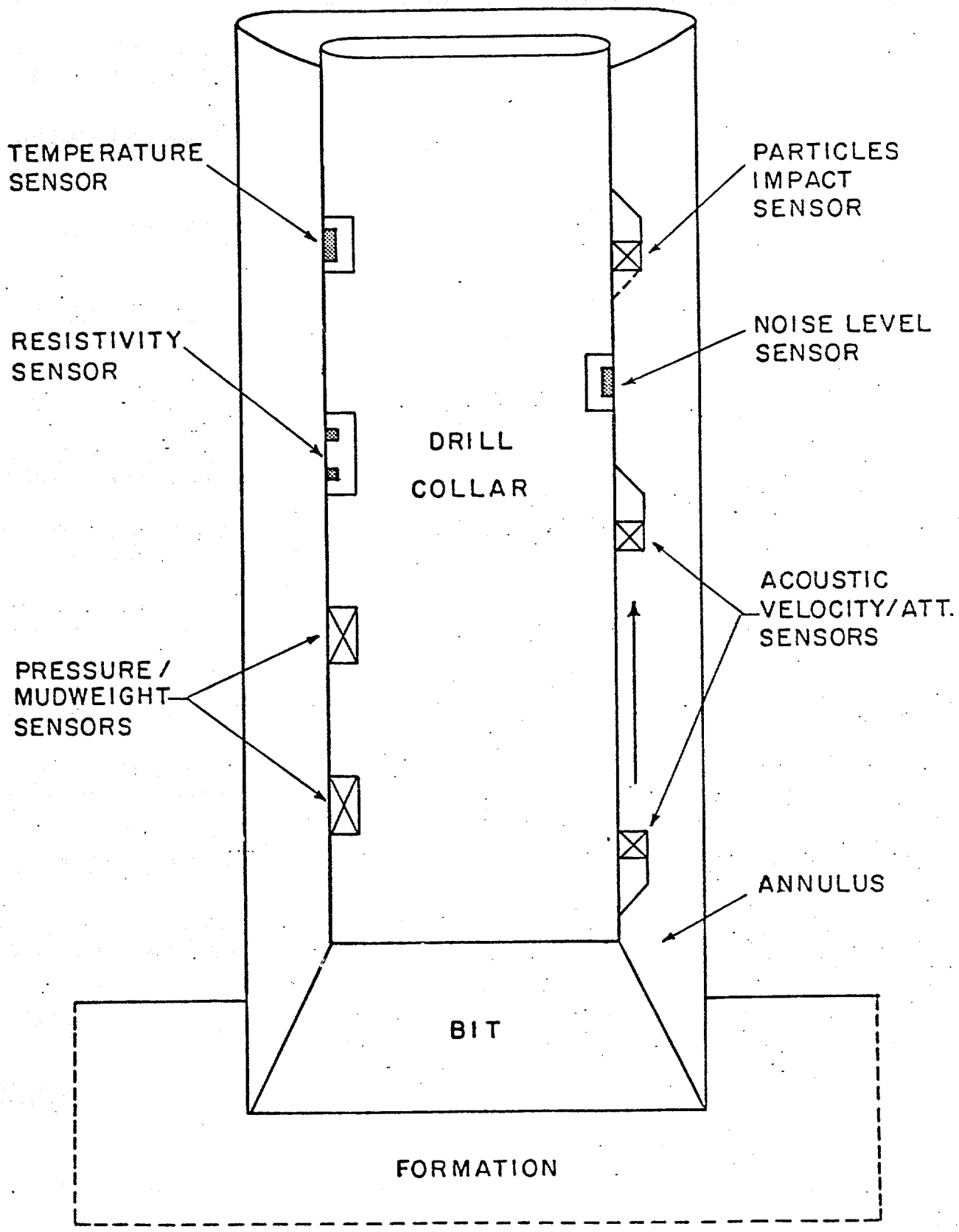

FIGURE 6.12. Downhole Gas Detection Principles

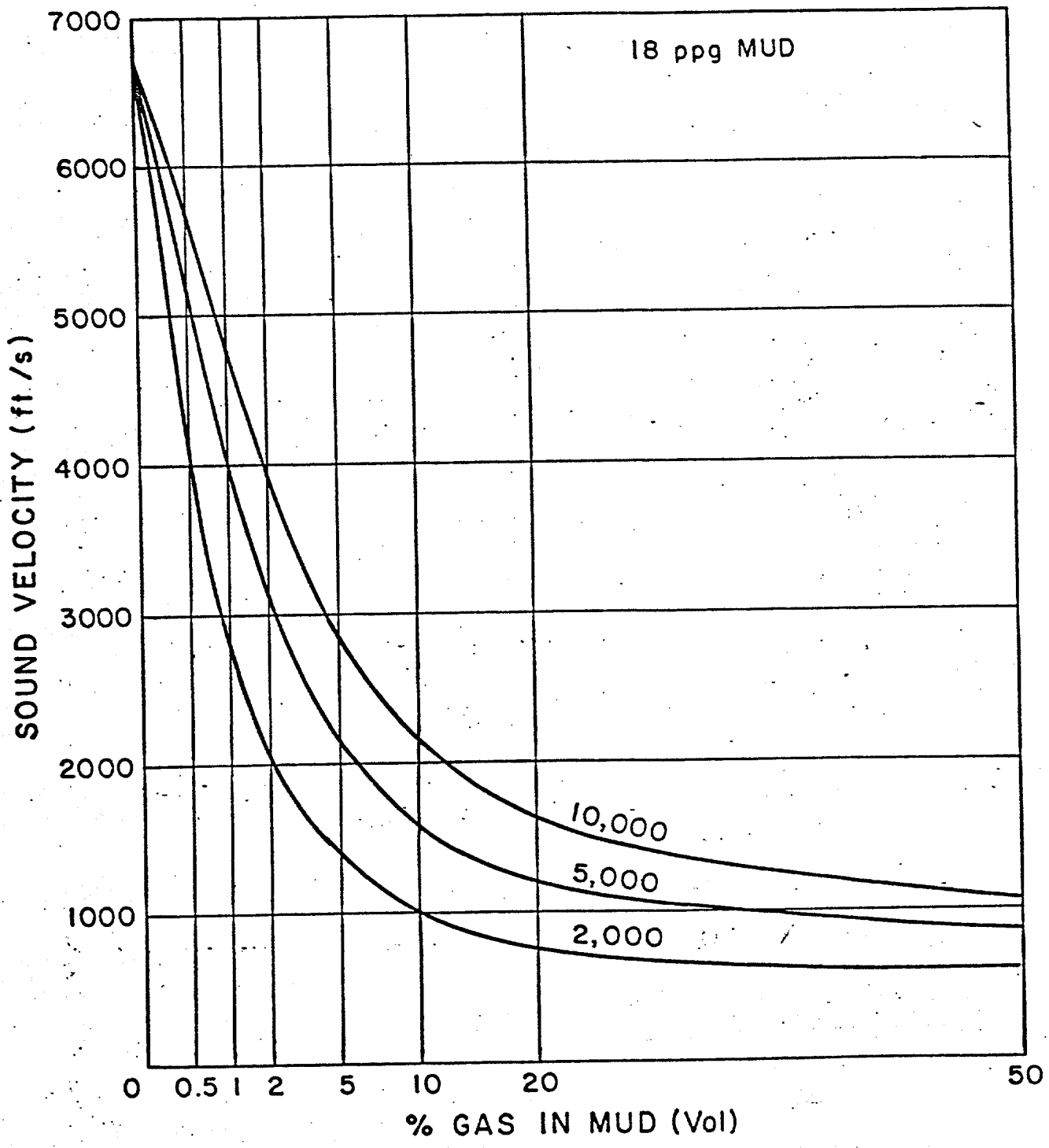

FIGURE 6.13. Elastic Wave Velocity Variation with Gas Content Calculated for Various Pressures - 18 ppg Mud

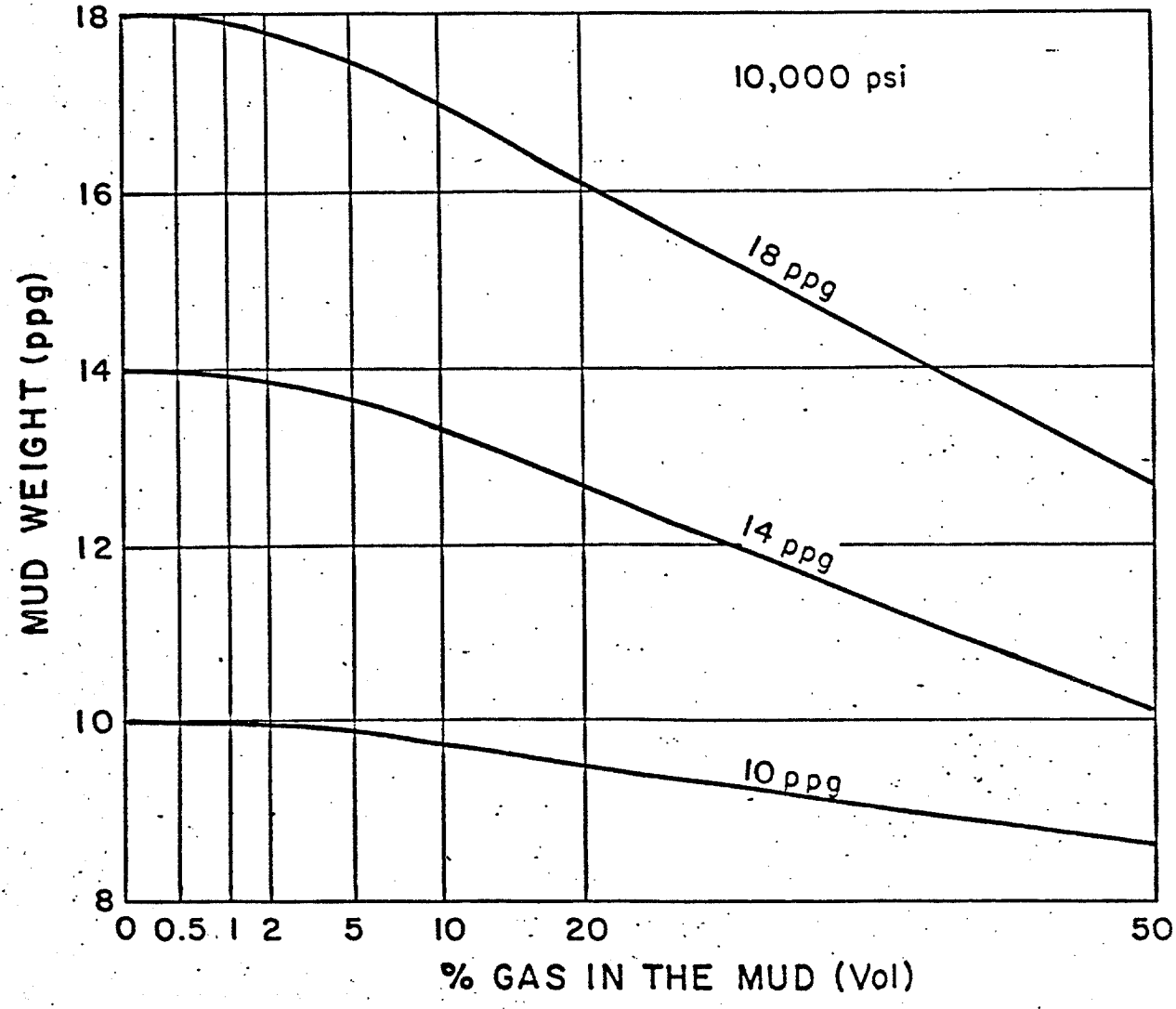

FIGURE 6.14. Mud Weight Variation with Gas Content

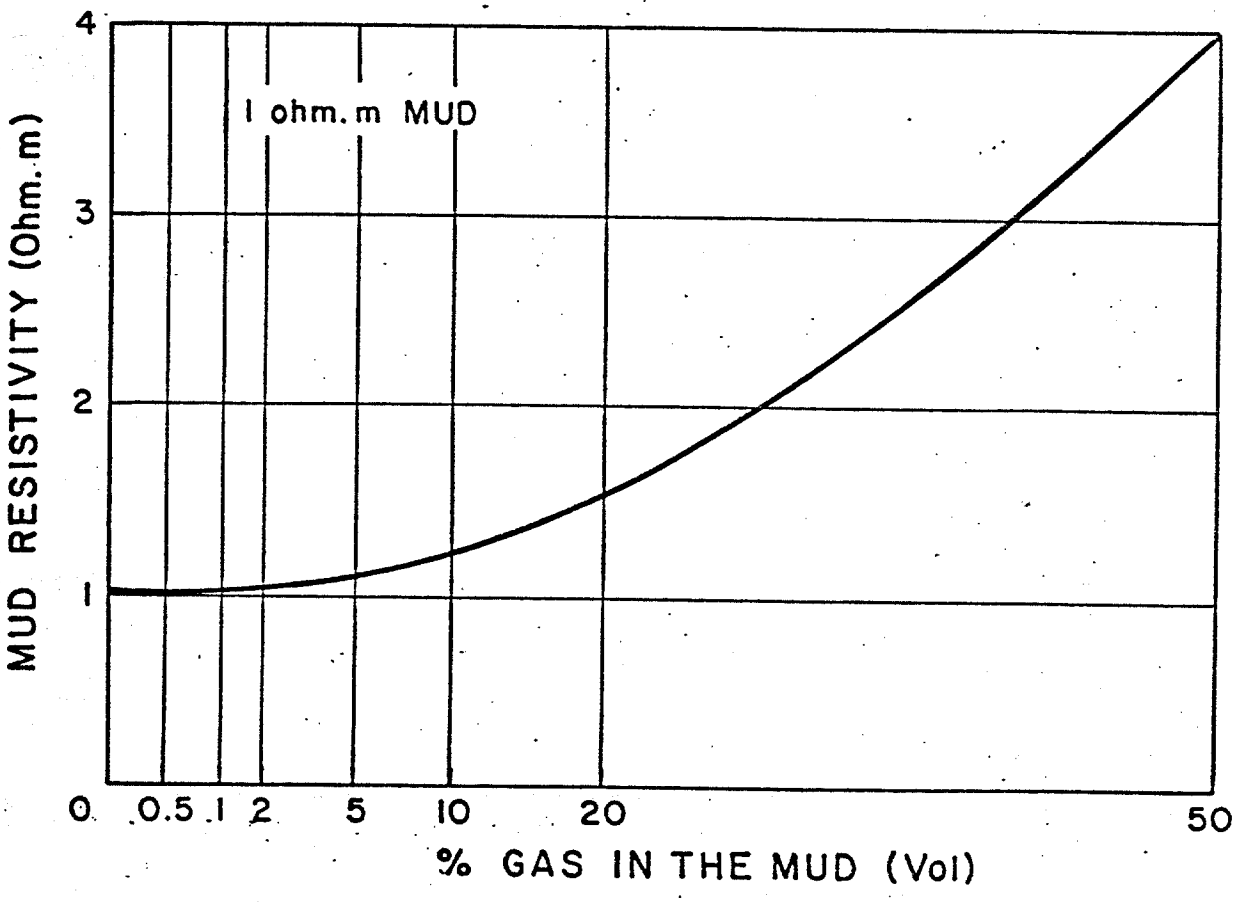

FIGURE 6.15. Mud Resistivity Variation with Gas Content

be 10 ft/sec with 10 bits, 2.5 ft/sec with 12 bits and 0.14 ft/sec with 16 bits. It seems that 10 bit data words should be adequate.

The MWD systems should be upgraded with an overriding alert mode to cut off any current transmission and start transmitting the kick data as soon as a sound velocity threshold is reached. This would require 2 words of 20 bits, 10 bits maximum for terminating the word being transmitted, and 10 bits for switching to alert mode (For Example 0000000000). A permanent measurement of the annulus mud sound velocity should be made downhole for achieving this by permanently comparing with the threshold. Each data set would require 10 bits for the pressure, 10 bits for the mud velocity and 10 bits for a synchronication word (Again 0000000000).

The alert would require a maximum of 20 bits plus a transit time of 2 sec at 10,000 ft or a total time of:

- for 0.4 bit/sec 52 sec
- for 1 bit/sec 22 sec
- for 3 bits/sec 8.33 sec
- for 5 bits/sec 6 sec

The first set of data would be available after a total time of:

- for 0.4 bit/sec	20/0.4+52	102 sec
- for 1 bit/sec	20/1+22	42 sec
- for 3 bits/sec	20/3+8.33	14.66 sec
- for 5 bits/sec	20/5+6	10 sec

The kicck data would be updated at the following time intervals:

- for 0.4 bit/sec	30/0.4	75 sec
- for 1 bit/sec	30/1	30 sec
- for 3 bits/sec	30/3	10 sec
- for 5 bits/sec	30/5	6 sec

The end of the alert mode, when the mud sound velocity is less than the threshold again, could be transmitted with a different synchronization word (For example 1111111111 instead of 0000000000) to resume normal operation.

Times shown herebefore can readily be calculated with 12 bit or 16 bit words.

A simple gas kick model has been devised for the purpose of finding the depth of the top of the gas cut mud slug when the alert signal reaches the surface. The model is as follows (see Figure 6.16):

- 10,000 ft borehole,
- 30 ft porous permeable zone,
- permeability: 500, 100, 50, 20, 10, 5, 2 mD
- reservoir pressure: 6,700 psi,
- gas density: 0.7,
- gas viscosity: 0.03 cP,
- drainage radius: 660',
- gas z factor: 0.9,
- bottomhole mud temperature: 150°F,
- surface mud temperature: 120°F,
- water base mud: 12 ppg (6,240 psi at 10,000 ft)
- mud flowrate: 500 gal/min,
- casing: 8,000', 9 5/8",
- openhole: 8 1/2",
- drill collars: 800', 6",
- drill pipe: 4 1/2",
- drilling rate: 20 ft/hr.

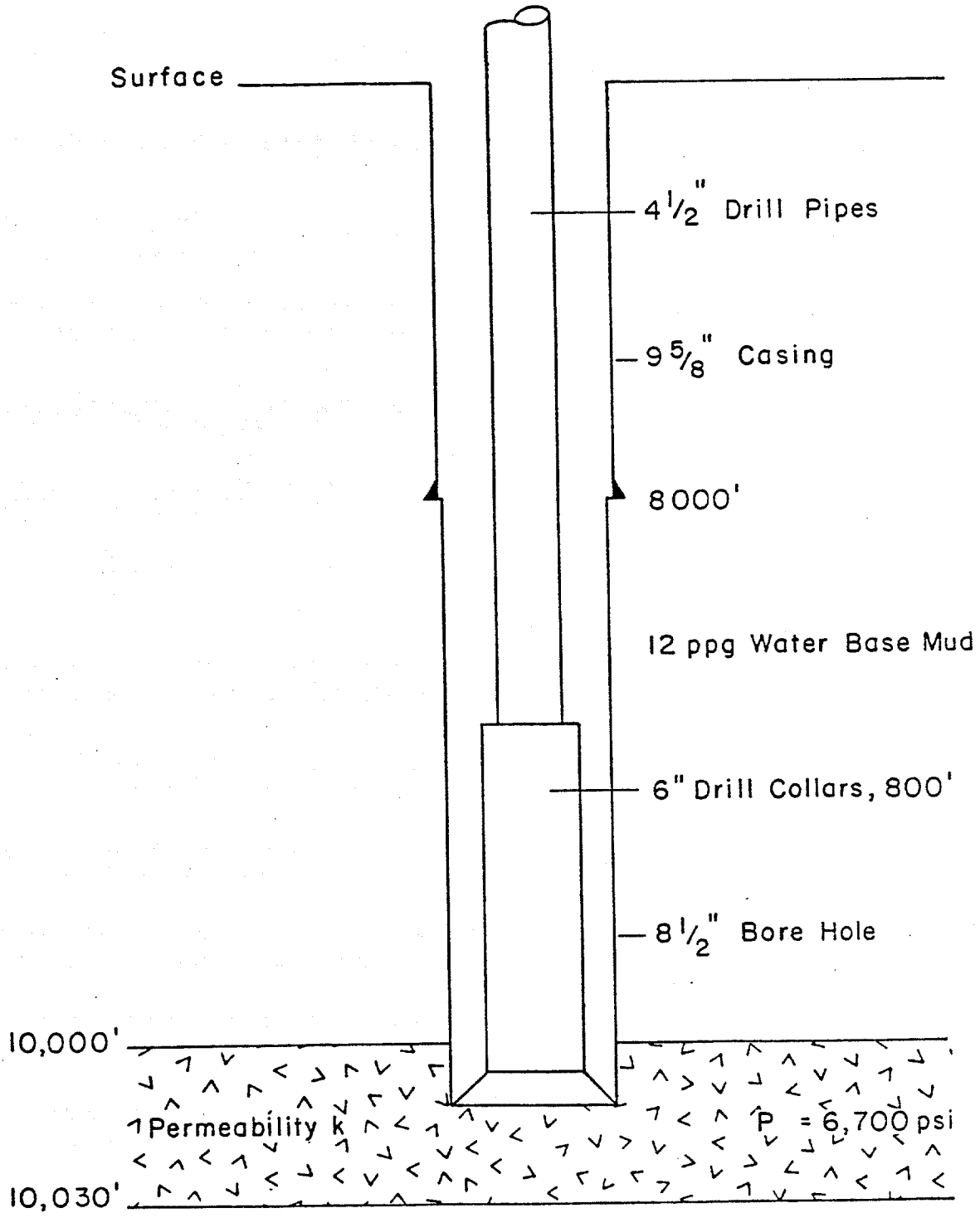

FIGURE 6.16. Mathematical Model Schematic

We assume an homogeneous gas-mud mixture, no slippage, no annular pressure loss. These effects should compensate in the first few minutes and could be added to the program readily. The gas concentration at bottom for various permeabilities versus time is given in Figure 6.17 starting when the upper boundary of the porous formation is penetrated.

The program also gives the pit gain versus time as shown in figure 6.18, the bottom hole pressure (figure 6.19), the mud weight at bottom (Figure 6.20) and the depth of the kick top (figure 6.21). The total volume of gas in the mud column at standard conditions is given in figure 6.22 versus time.

The program could be also adapted for oil base mud taking into account the dissolution of gas at bottom and the bubble point in the column. The effect of gas in solution in the oil base mud on the velocity of sound has not been examined yet, it is probably less important than with free gas. Gas kick scenarios have been made for the various tools and with two permeabilities 500 mD and 50 mD.

Figure 6.23 has been drawn for 500 mD. It shows four graphs corresponding to the four types of tools. Relying on a 10 bbl pit gain threshold for alert gives a kick depth of 9200 ft with a volume of gas in the mud column of 18 MSCF at the time of the alert and 134 MSCF when the blowout preventer is is closed 2 minutes later.

Figure 6.24 also shows that with a MWD bottomhole gas kick detection system and two minute closing time:

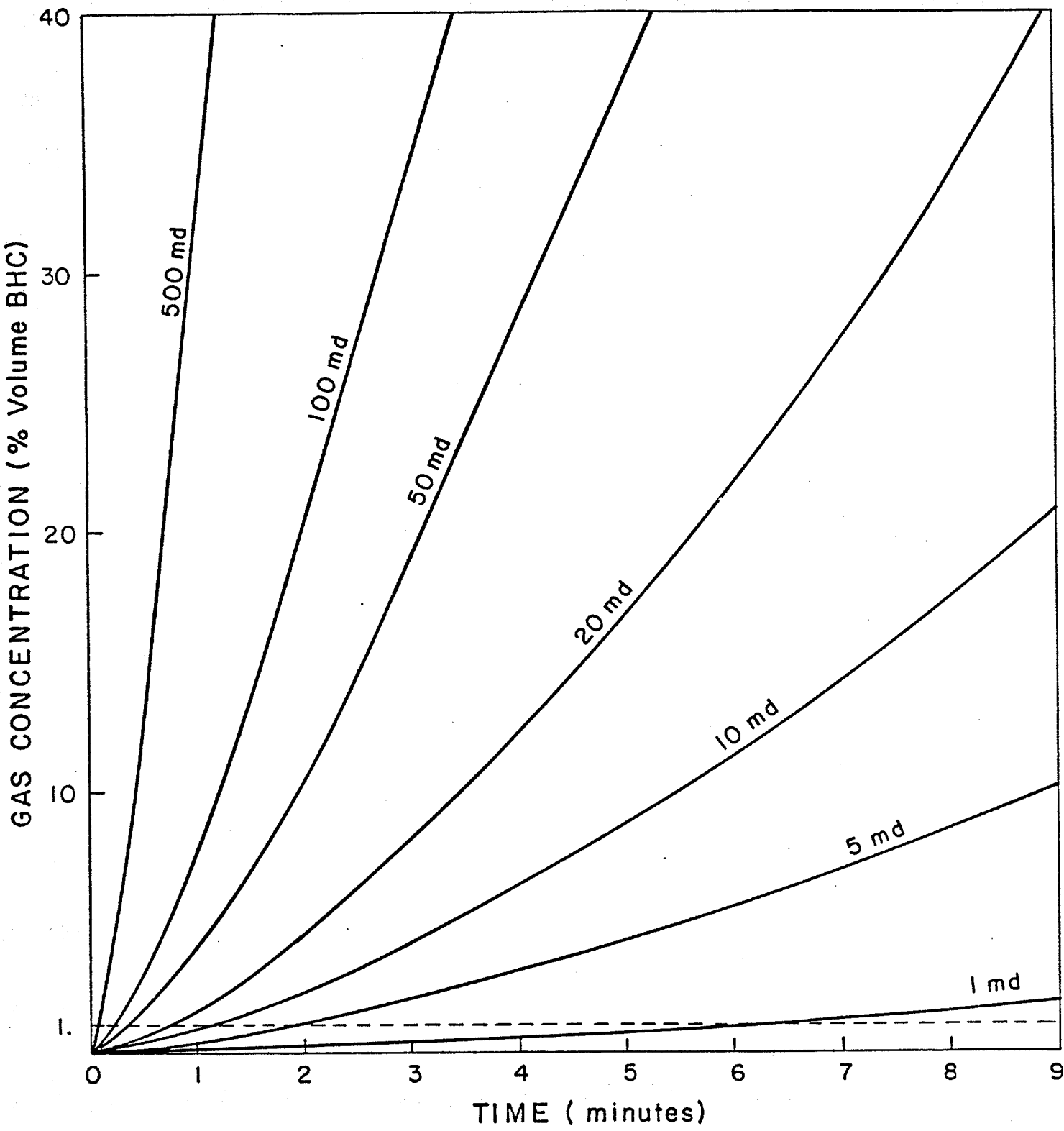

FIGURE 6.17. Volume Gas Concentration at Bottom Versus Time

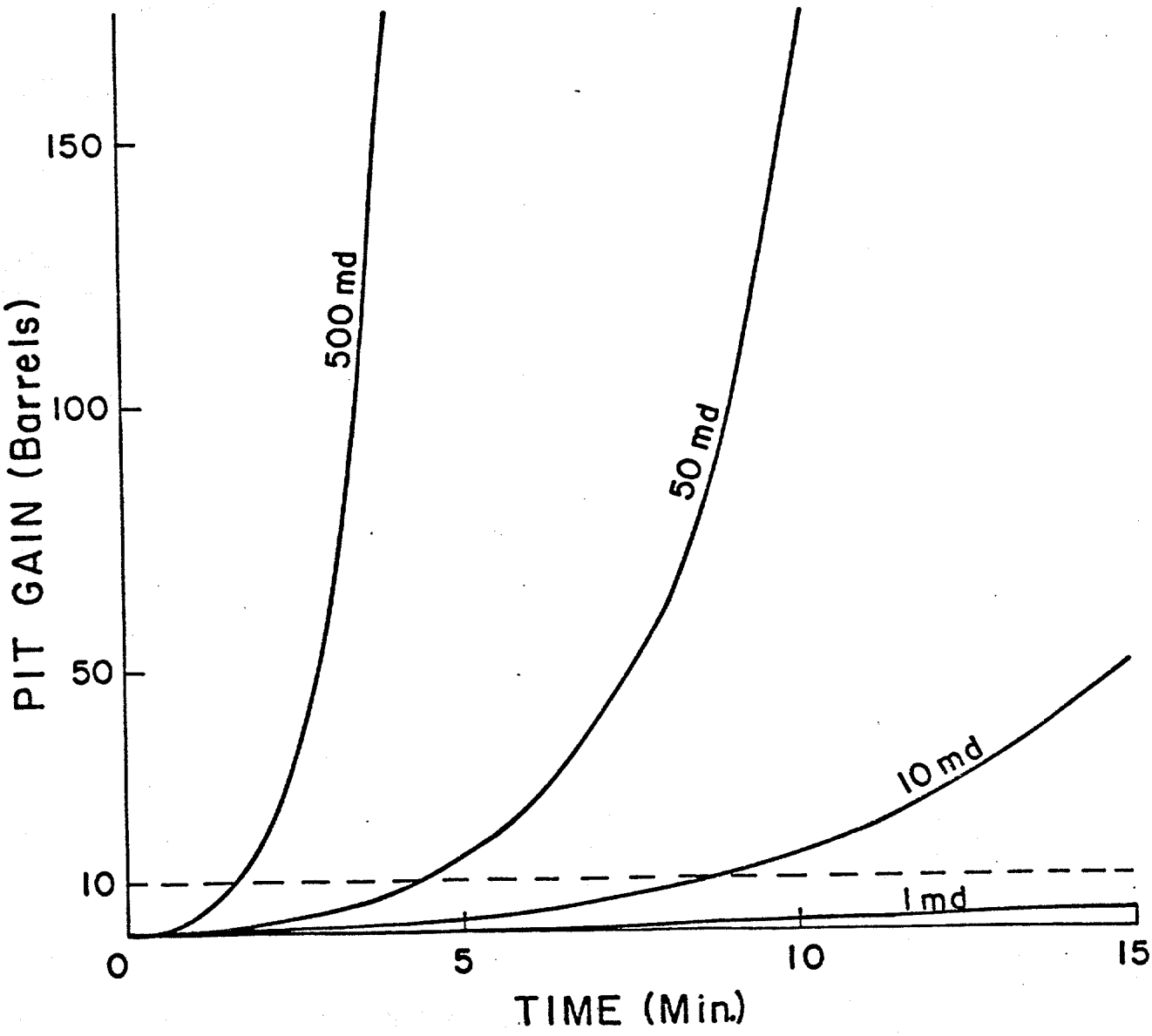

FIGURE 6.18. Pit Gain Variation with Time

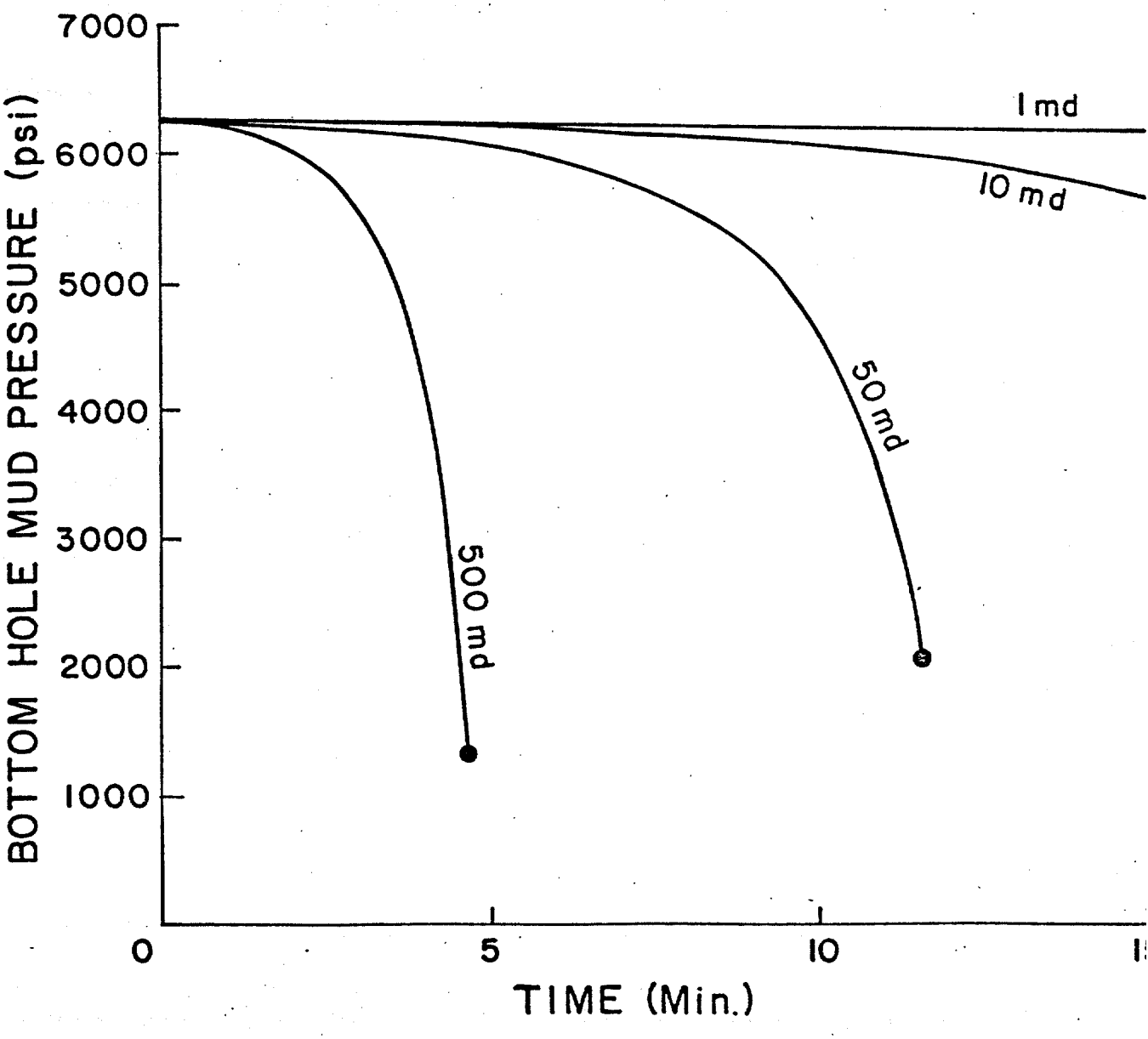

FIGURE 6.19. Bottomhole Pressure Variation with Time

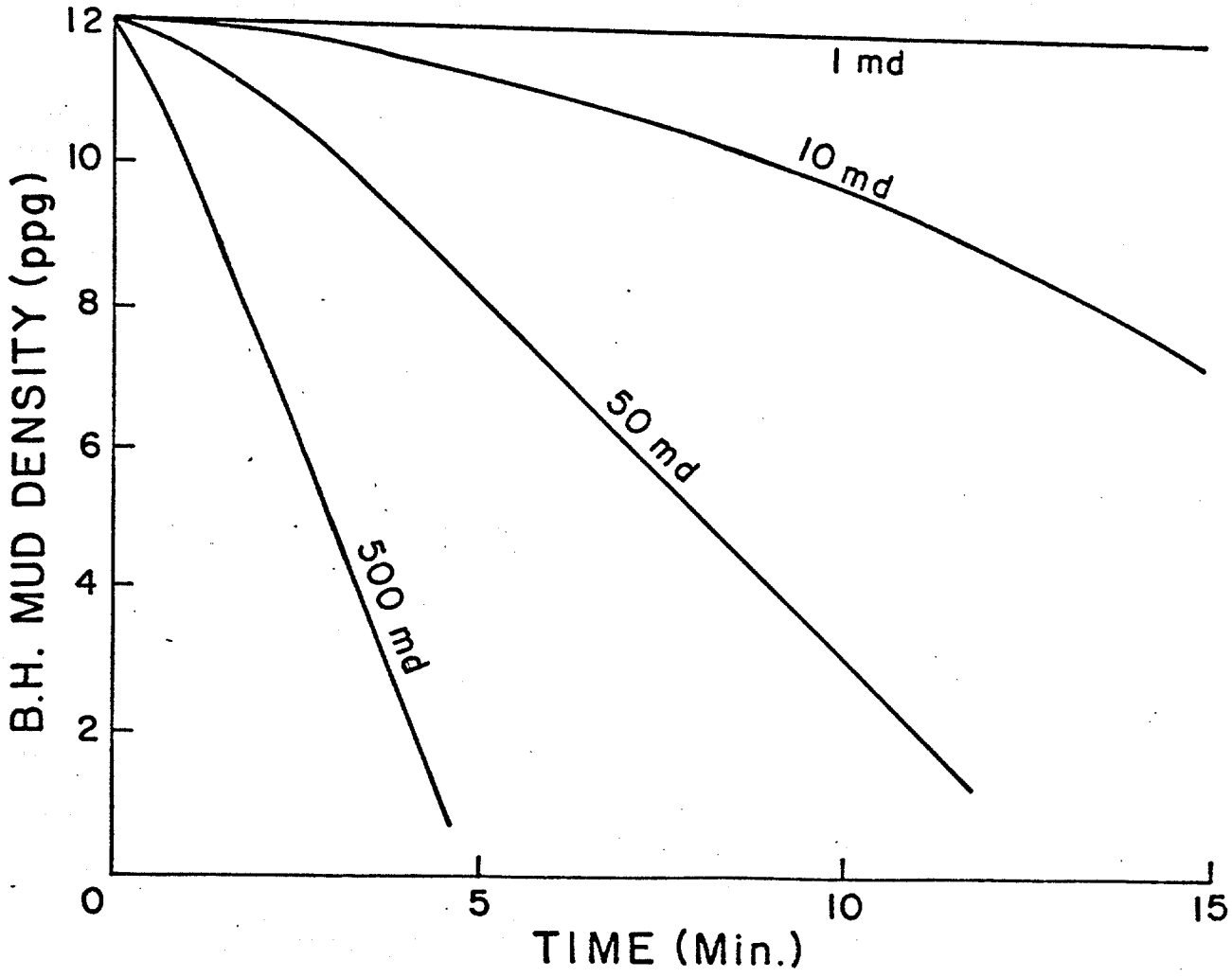

FIGURE 6.20. Bottomhole Mud Weight Variation with Time

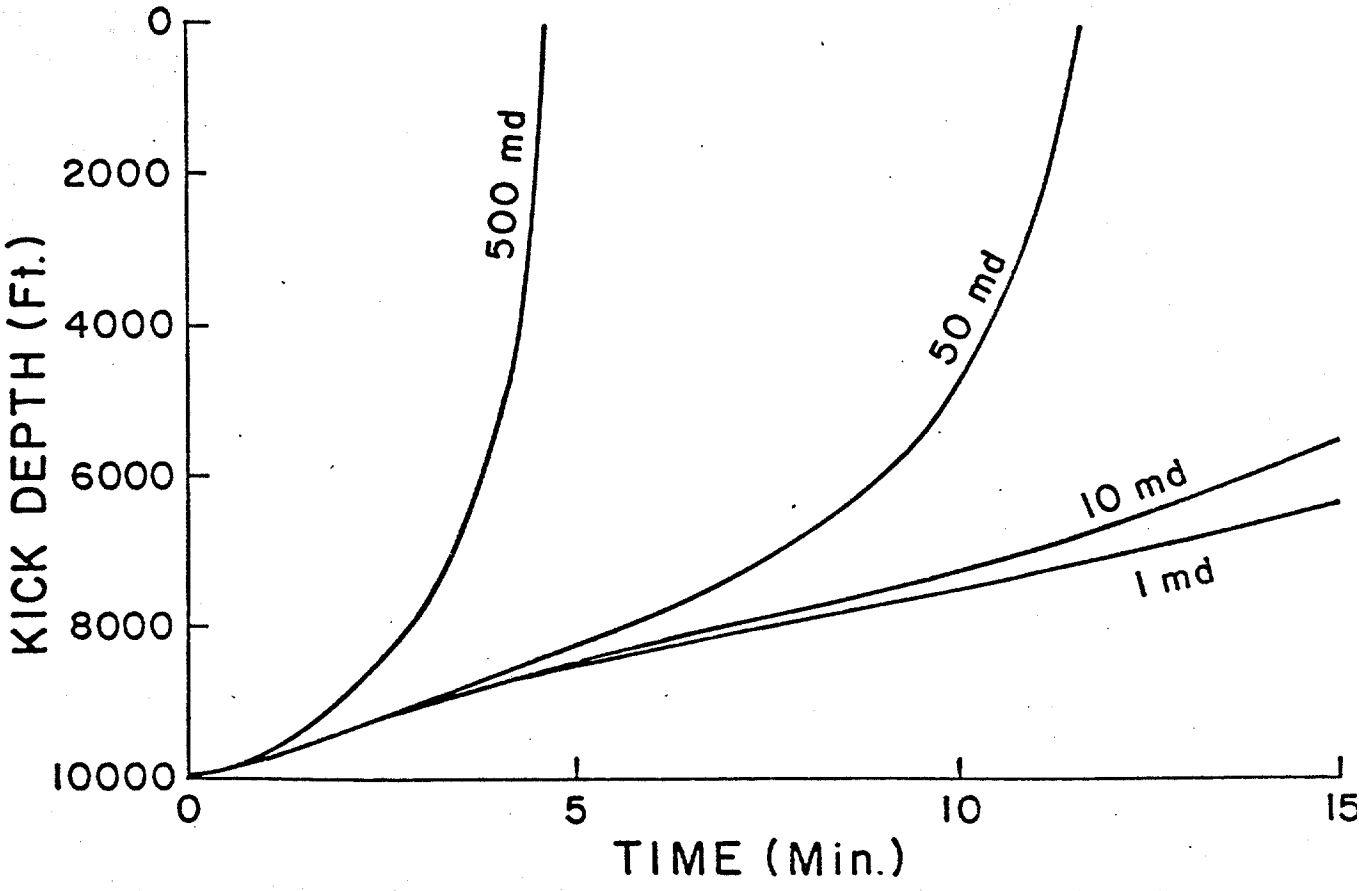

FIGURE 6.21. Top of Kick Depth Variation with Time

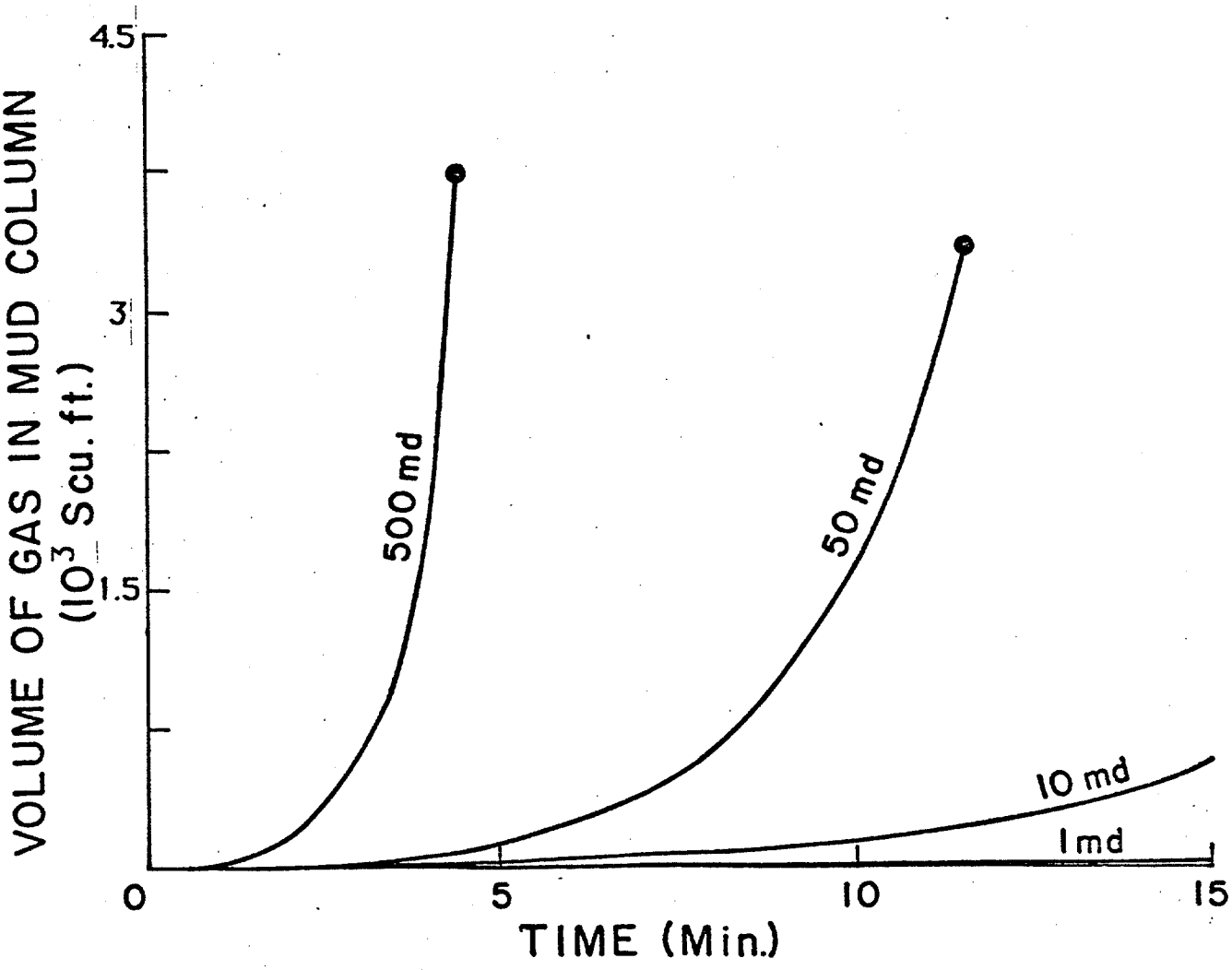

Figure 6.22. Total Volume of Gas in the Mud Column at Standard Conditions versus Time

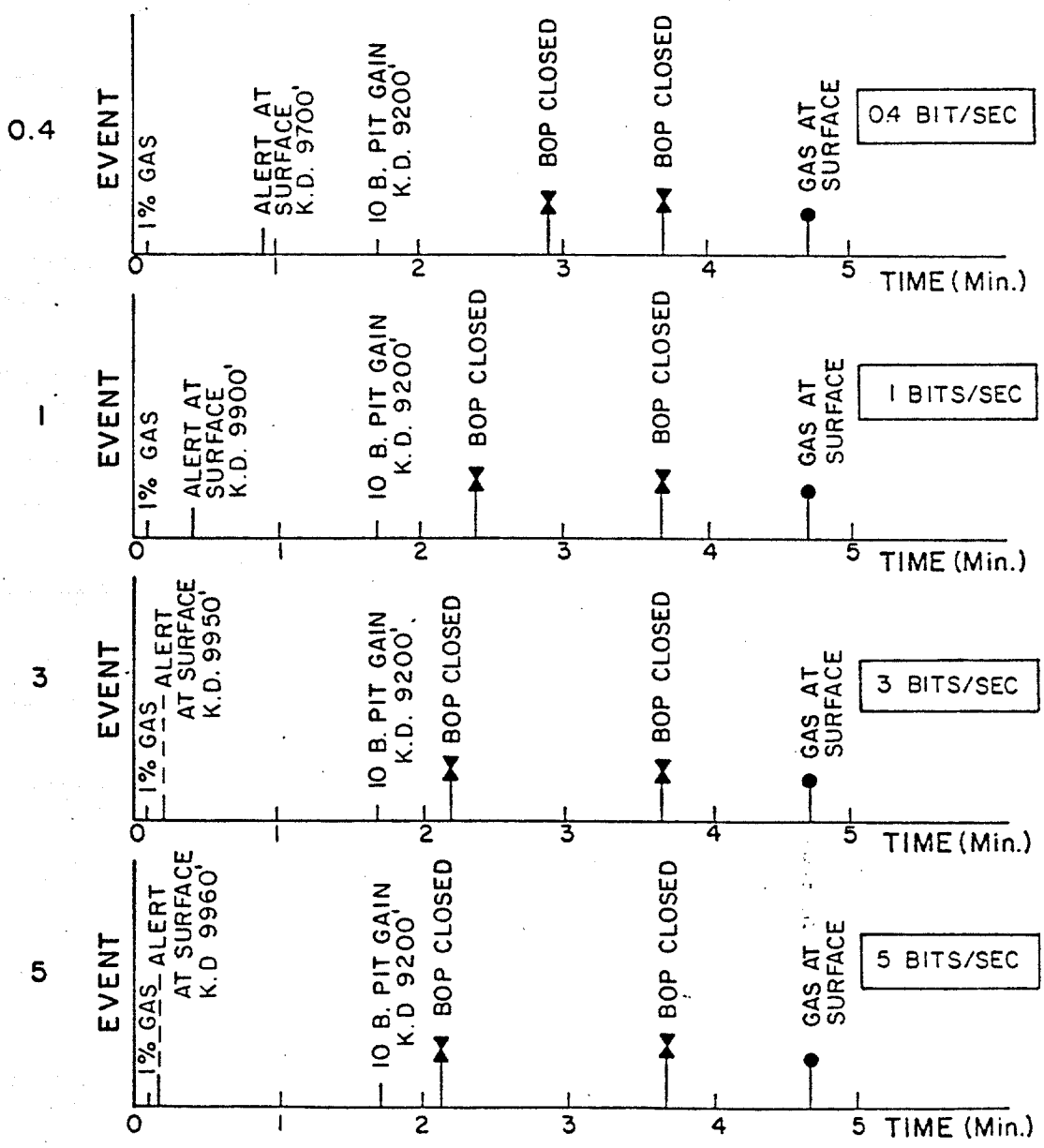

FIGURE 6.23. Gas Kick Scenarios - 10,000 ft, 500 mD, 500 psi underbalance, 20 ft/hr, 12 ppg Mud

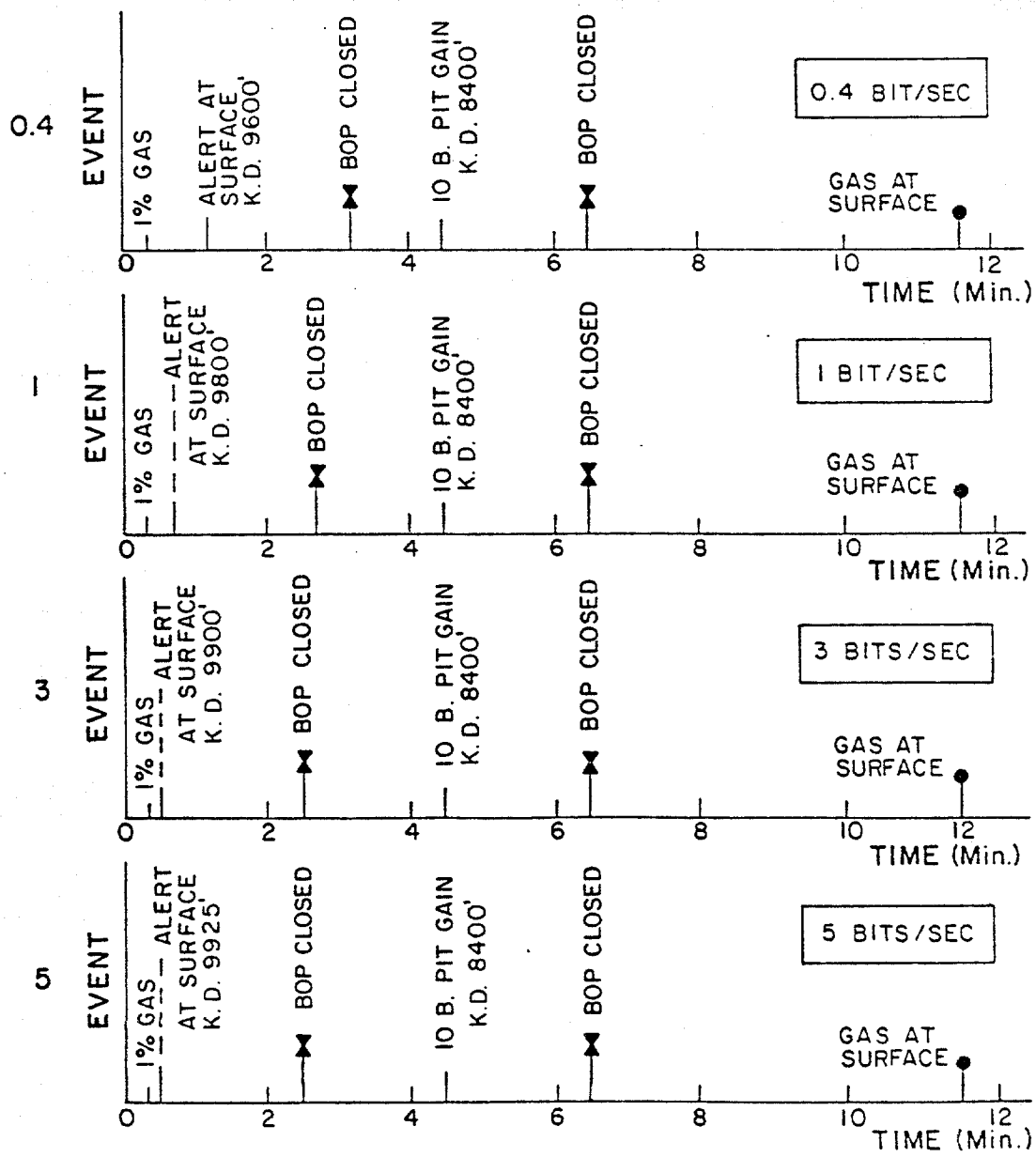

FIGURE 6.24. Gas Kick Scenarios - 10,000 ft, 50 mD, 500 psi underbalance, 20 ft/hr, 12 ppg Mud

	Surface Alert Time MSCF	Blowout Preventer closed MSCF
- with 0.4 bits/sec	10.5	102
- with 1 bit/sec	2.8	60
- with 3 bits/sec	0.9	53
- with 5 bits/sec	0.8	46

Figure 6.24 has been drawn for 50 mD. Again it shows the four graphs. Using a 10 Bbl pit gain threshold for alert the kick depth is 8400 ft with a gas volume in the mud column of 18 MSCF at the time of the alert and 34 MSCF when the blowout preventer is closed 2 minutes later. Again an MWD system and a two minute closing time would give:

	Surface Alert Time MSCF	Blowout Preventer closed MSCF
- with 0.4 bits/sec	1.5	82
- with 1 bit/sec	0.6	5.8
- with 3 bits/sec	0.4	5.4
- with 5 bits/sec	0.3	5

Thus, it can be concluded that a large decrease in the amount of gas in the mud column would be achieved by using a MWD type of gas kick alert detection and transmission. 1.3 to 4.2 times less gas would be in the annulus at the time of closing the blowout preventer with a slow system and three to seven times less with a fast system according to the permeability. The results presented herein are preliminary approximate results.

Development of Computer Controlled Choke

Two major steps in the development of a computer controlled choke include (1) the interfacing of the controllers to an easily programmed computer and (2) the development of appropriate process models and process control algorithms. This work is now about 50% complete and continued work in this area is a major portion of proposed future work.

7. EXPERIMENTAL STUDY OF NOVEL ELECTRICAL TELEMETRY METHOD

If very large increases in data transmission rates are to be achieved, a novel telemetry method will have to be developed. It appears that mud pulse telemetry will likely have a practical upper limit of about 50 hertz for most drilling applications. This will place severe limitations on the number of safety related parameters that could be transmitted at frequent time intervals from the hole bottom to the surface during well control operations. One novel technique that has been proposed for drilling data transmission is electrical telemetry using drilling fluid to conduct the electrical signal inside a partially insulated drill pipe. One major advantage of this approach is that data could be transmitted even if the well was not being circulated with the mud pumps.

The system in simplified form is shown in figure 7.1. Some form of insulation is placed on the inside surface of the drill pipe. This insulation is assumed to extend from a short distance above the drill bit to the top of the Kelly. At a distance above the insulation lower limit a transmitter is installed with electrodes contacting the mud. Similar receive electrodes are located at the lower end of the Kelly. The electrical signal passes through the mud from the transmitter to the receiver.

In the system the drill bit and the swivel assembly above the Kelly are both considered as uninsulated. Also the drill pipe insulation is also considered imperfect.

It is possible to make the following statements about the system:

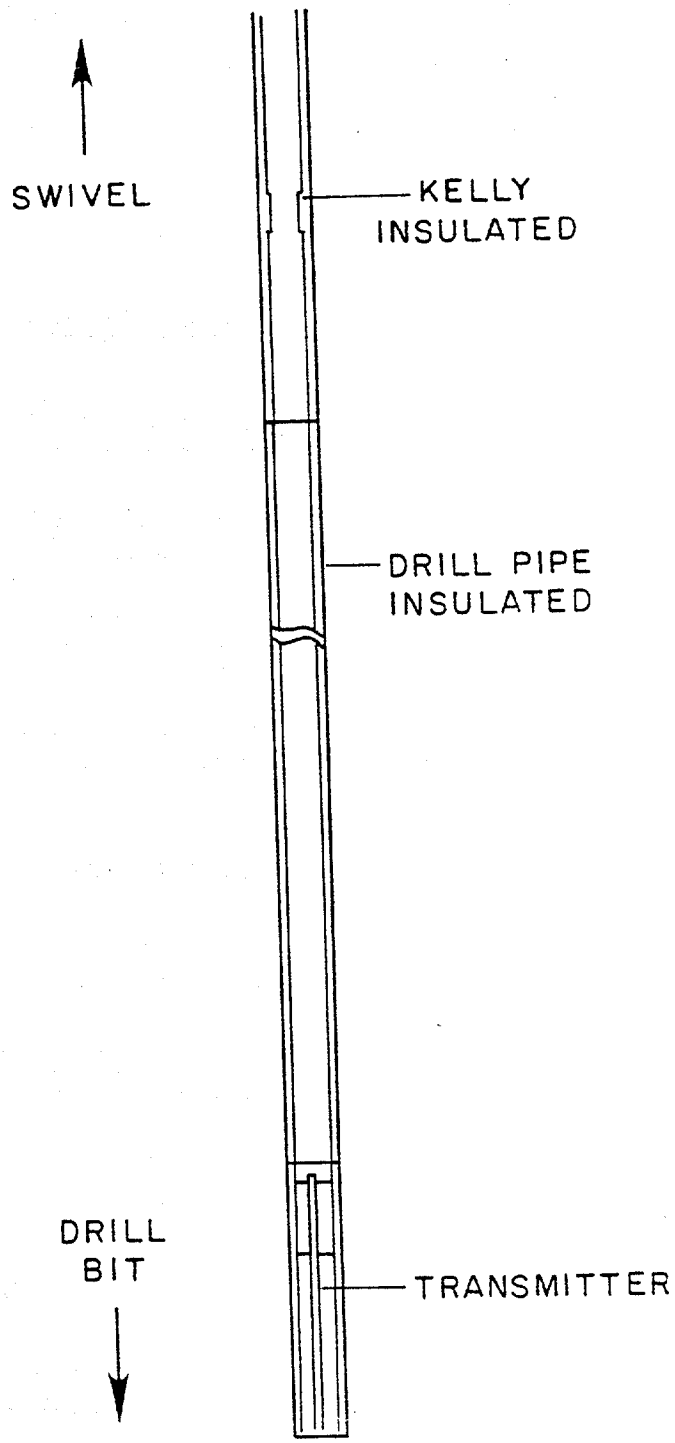

FIGURE 7.1. Simplified Drill String Arrangement

Pipe - 4 1/2 inch 3.8 inch inside dia.

Length 20,000 feet.

For the electrical propagation in such a pipe (when insulated) a simple electrical model can be devised. This is shown in figure 7.2. The resistive elements refer to the mud resistance per unit length and the capacitance is the shunt capacitance between the inner conductor, the mud, and the outer conductor, the pipe.

To calculate the attenuation these values must be known. The mud electrical conductivity can be measured using a test cell. A typical sample of mud is placed in a tube and using two outer electrodes a current is induced in the mud. The voltage across a sample is then measured using two inner electrodes. The circuit shown uses a ten turn calibrated potentiometer to balance a bridge such that if the bridge is in balance the resistance of the potentiometer is equal to the resistance of the mud sample.

The capacitance of the system can be calculated from the known geometry for different insulating materials. Material variations are not very large but the insulation thickness does strongly influence the values. Insulation thicknesses of 1/16 to 1/8 inch were calculated.

It became apparent during some early experiments that the simple model shown is not adequate. The problem lies in the electrical connection between the electrodes and the mud. If the mud is stationary (with respect to the electrode) the impedance of the electrode is relatively low but if the mud is flowing over the electrode a higher resistance value is observed and this value is frequency dependent.

To evaluate this problem a small test cell was fabricated. This cell uses a stationary electrode at the bottom of the cell and a rotating

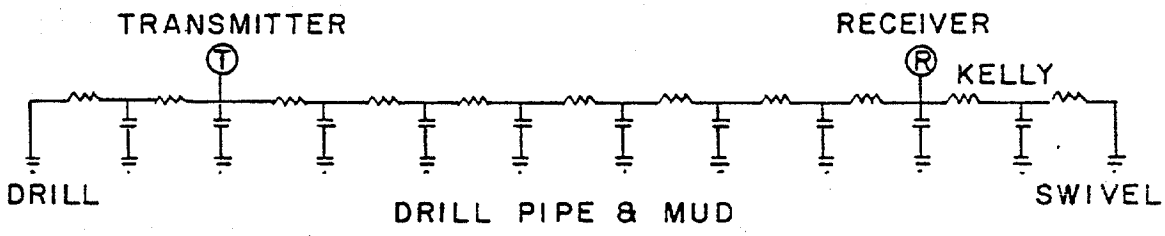

RESISTANCE IS	$\sigma L/A$
CAPACITANCE IS	$2\pi eL/\ln(D2/D1)$
ATTENUATION COEFFICIENT IS	Re ((R+iwl)(G+iwC))

NOTE.

1. For low frequencies (<100KHz) L and G insignificant
2. Attentuation is per unit length and therefore can scale problem by matching R and C per unit scale length.

FIGURE 7.2. Simple Electrical Model

plate for the upper electrode. As such there will be a small center section which is not slipping and this section is insulated. The results with a single mud sample are reasonably consistent and are shown in figure 7.3. It is possible to devise a formula for the electrode impedance. In fact the electrode can be represented closely by a capacitance and resistance in parallel with both a function of surface area.

The electrical model then appears as in figure 7.4. In addition to the electrode impedance at the transmitting and receiving electrodes the influence of leaks at the insulation joints can now be handled. These leaks will occur due to the end fits of each drill pipe section and for our purposes the area off such a leak is the unknown parameter.

Small Scale Telemetry Experiment

It is apparent from the model that it is possible to perform an experiment on mud electrical telemetry on a small scale than the full size. Since the principal parameter is the resistance then a small diameter pipe will have higher linear resistance and can be simulated by a shorter length. To simulate the 4 1/2 inch pipe of 20,000 foot length a 1/2 inch diameter pipe of 400 foot length was used. In fact PVC pipe was used and the scale (based on internal diameter) was about 50 to 1. Using a heavy wall pipe working pressures of 800 lbs. were possible allowing realistic velocities (of order 20 ft/sec) to be achieved and with Reynold's numbers well into the turbulent flow regime.

Since a thick wall PVC pipe in any configuration will have negligibly small shunt capacitance, electrodes were placed in the pipe every 10 feet to allow the electrical insertion of capacitors into the experiment.

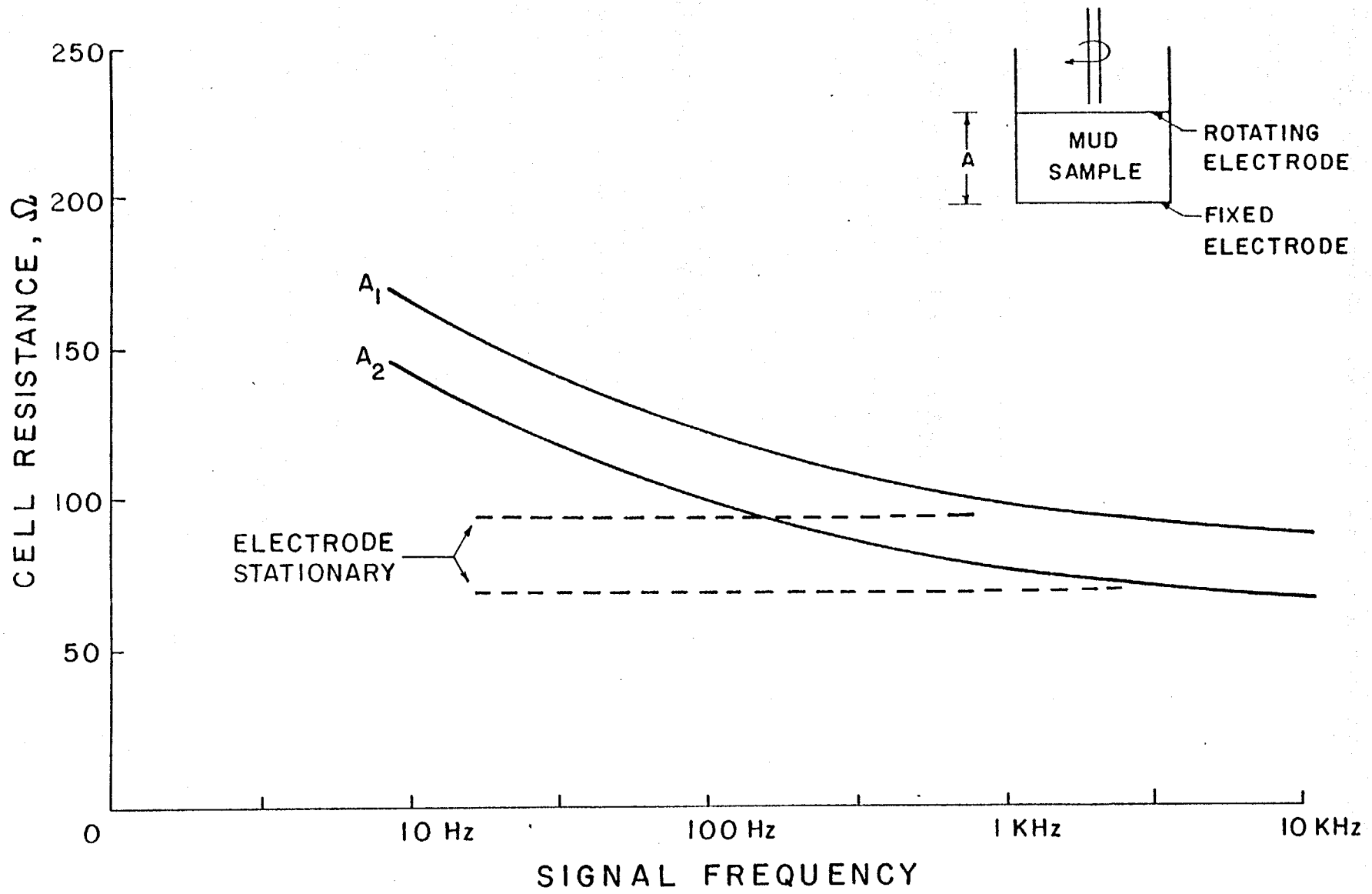

FIGURE 7.3. Effect of Slipping Electrode

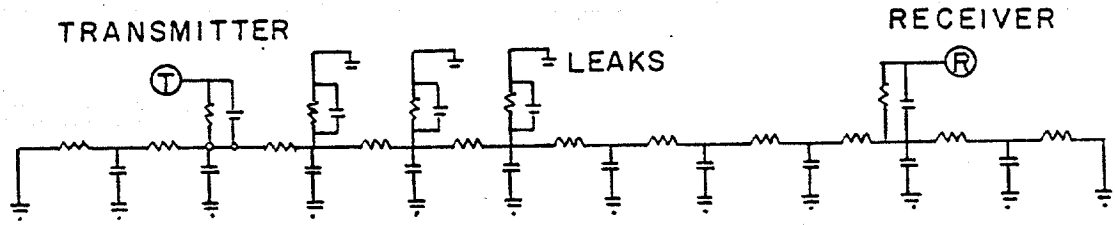

NOTE:

1 Insulation leaks at the pipe junctions become less important since they are shielded by the electrode impedance.

2 The capacitive component in the electrode impedance reduces the applied signal. This reduction can be partially overcome by adding a carrier to the signal.

FIGURE 7.4a. Improved Electrical Model

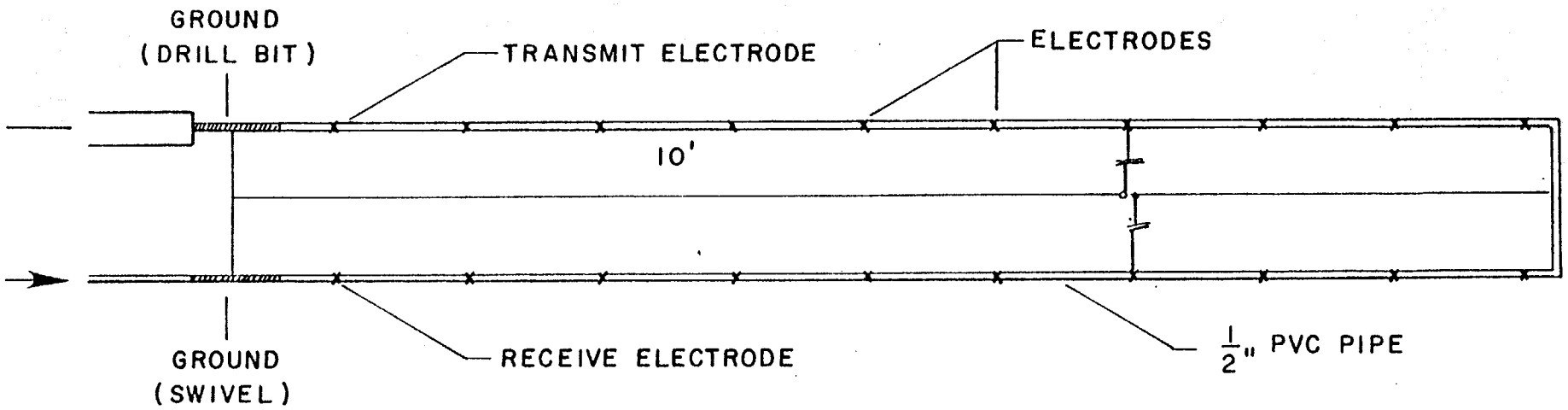

FIGURE 7.4b. Arrangement of Physical Model For Small Scale Telemetry Experiment

At the ends of the pipe sections of copper pipe were used to electrically simulate the drill bit and swivel sections. The transmitting and receiving electrodes were placed 0.6 feet from these ends to simulate a 30 foot pipe length as a typical offset. To simulate the drill pipe a length of 10 gage wire was strung along the experiment. All capacitive returns and simulated shorts were made to this wire.

Fluids for the experiment were pumped from a small mixing tank. This enabled relatively easy changes to the fluid. Initial experiments used water with salt added in stages to change the specific resistivity. Then light weight mud (8.9%) was used and salt also added to this in stages. The fluids used in the experiment are summarized in Table 2.1. The specific resistances of the mud tested were the same order as field muds. Note also that the addition of salt to the mud only made a slight change in the resistivity. The values are also shown in figure 7.5 and compared with sea water. The electrical conductivities of the experiment fluids were much lower than sea water.

A small transmitter based on a standard modem integrated circuit was fabricated. A square wave was used to simulate a typical NRZ data string. The resulting FSK signal was amplified and sent to the transmitting electrode. No attempt at impedance matching was made since power consumption was not important. Typical signals at the transmitting electrodes were 10 v p/p and 1 to 2 KHz with data modulation rates up to 325 baud.

The receiver used a two stage amplifier and combined low pass and high pass filters to provide low Q filtering of the signal. A phase locked loop squared the waveform and this was inputted to a matching demodulator.

TABLE 2.1. Electrical Properties of Drilling Fluids Used in Electrical Telemetry Experiments

	EXPERIMENT FLUIDS				
No.	Base Material	Salt Added	% Salt By St.	Specific Resistivity	Specific Conductivity
1	Water	0	?	11.7	0.08
2	Water	8	.28	2.27	0.44
3	Water	16	.56	1.21	0.83
4	Water	20	.72	0.92	1.09
5	Mud	0	0	1.49	0.67
6	Mud	12	.31	1.41	0.71
7	Mud	28	.73	1.33	0.75
		by comparison			
Sea water			3.6	0.21	4.74

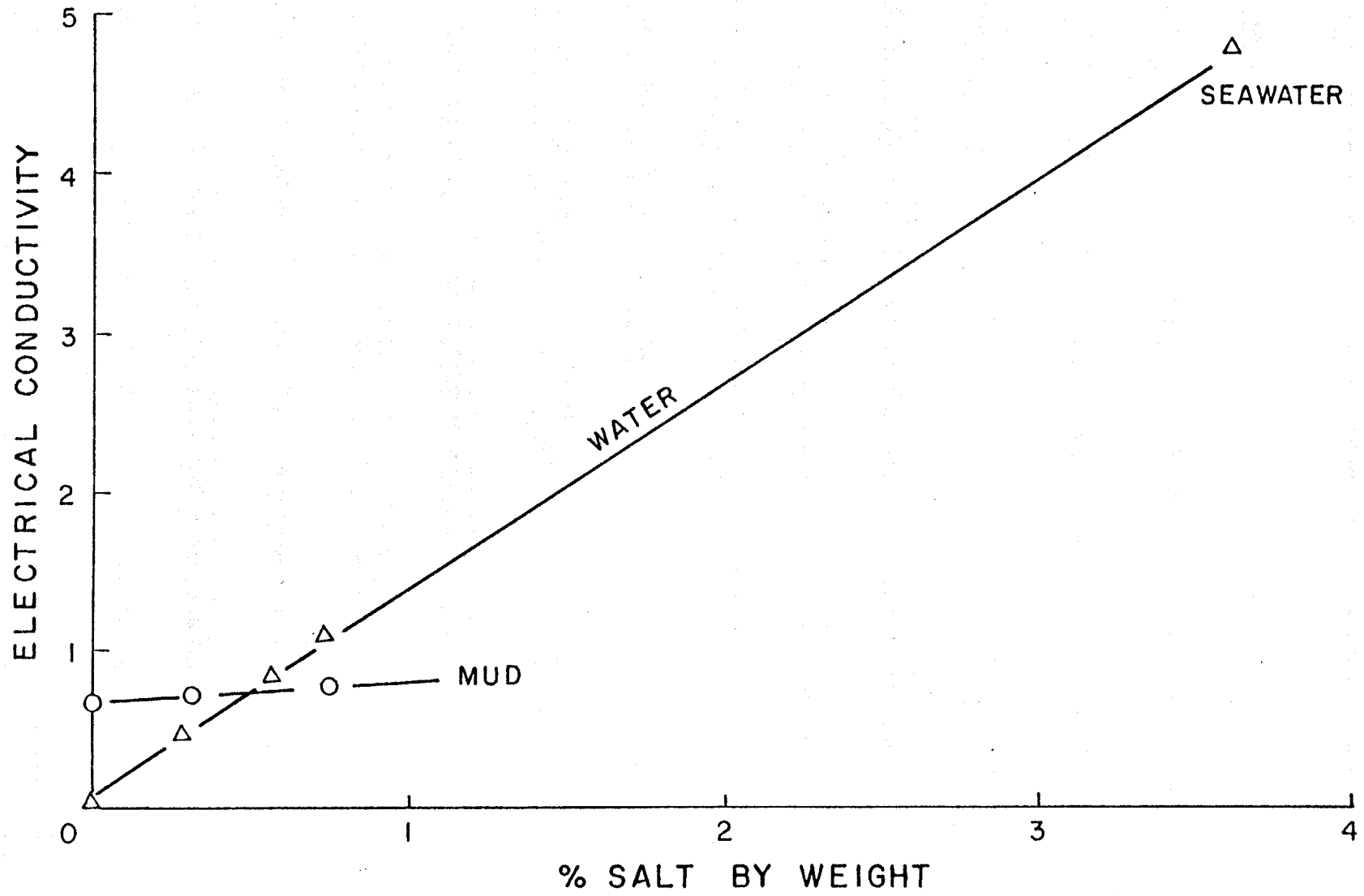

FIGURE 7.5. Variation of Electrical Conductivity In Experiment Fluids

Transmitting and receiving signals were measured and a check on the data telemetry made were pertinent. The results are shown in Table 2.2. Typical attenuation values for the simulated drill string were 70 to 100 dB which allows a satisfactory level of received signal. In even the worst case a data rate equal to a maximum for the carrier frequency was achieved. Over 300 baud was always achieved.

To test the effect of leaks (shorts) in the insulation some of the electrodes were connected directly to the "drill pipe". As each section was shorted a small additional attenuation was observed.

It is interesting to compare the calculated values for the attenuation with those observed experimentally. Figure 7.6 shows this comparison. Using the improved model values of the calculated attentuation were within a few dB of the experimental values. Note that this calculation is valid for the small scale 1/2 inch pipe as well as the full size 4 1/2 inch pipe, 20,000 ft.

For a typical full size system with suitable power matching circuitry and with low level signal detection and decoding the calculated signals are shown in figure 7.7.

The effects of leaks can also be calculated. The leak calculation will depend only on the total surface area exposed to the drill pipe. For each leak equivalent in length to a single pipe diameter the attenuation is about 1 dB. While this does not appear great it should be noted that in a pipe length of 20,000 feet there are 667 joints and if each of these has a 1/16 inch gap there would be some diameters of pipe exposed and an additional loss of 12 dB of signal. It is a measure of how good the end fits must be. The leak calculation is also shown in figure 7.7.

TABLE 2.2 - Table of Test Results

No.	Sample No.	Matl.	Flow (psi)	Elec.	Res.	Freq (KHz)	Input (V)	Output (uV)	Noise (uV)	Atten (dB)	Data Rate
1	1	Water	300	2/3	11.7	1.0	2.9	370	75	78	
2	1					2.1	2.9	150		86	
3	2	Water			2.27	1.0	0.5	150		71	
4	2	+				2.1	0.8	90		79	
5	3	Salt			1.21	1.0	4.3	700		76	
6	3					2.1	4.1	300		83	
7	4				0.92	1.0	4.3	900		74	
8	4					2.1	4.3	740		75	
10	4			1/4		2.1	1.4	150		80	
11	4					1.0	1.5	150		79	325
		Shorted #11, #28 and then both electrodes									
13	4	Water	250	1/4	0.92	2.1	3.6	370		80	
14						2.1	3.6	360		81	
15						2.1	3.6	150		88	325
				Mud tests							
16	5	Mud		1/4	1.49	2.1	3.6	150	45	88	325
17				2/4		2.1	3.6	300		82	
18				2/3		2.1	3.6	1120		70	325
		Installed capacitors in all electrode positions									
21	5	Mud		2/3	1.49	2.1	4.3	75	45	95	325
22						1.5	4.3	75		95	260
23						1.2	4.3	67		96	180
24						1.0	4.3	52		98	100
		Increase salt content of mud in stages									
25	6	Mud		2/3	1.41	2.1	4.3	82		94	
27	7	+				2.1	4.3	90		93	325
		Reverse transmitting direction									
29	7	Mud+		3/2	1.33	2.1	4.3	90		93	325
30											
				Increase flow							
31	7	Mud+	550	3/2	1.33	2.1	4.3	75	75	95	325
			Electrode #11 shorted								
32	7		550	3/2	1.33	2.1	4.3	60	75	97	325
				Shorten pipe 70							
33	7		550	3/2	1.33	2.1	4.3	300	75	825	325

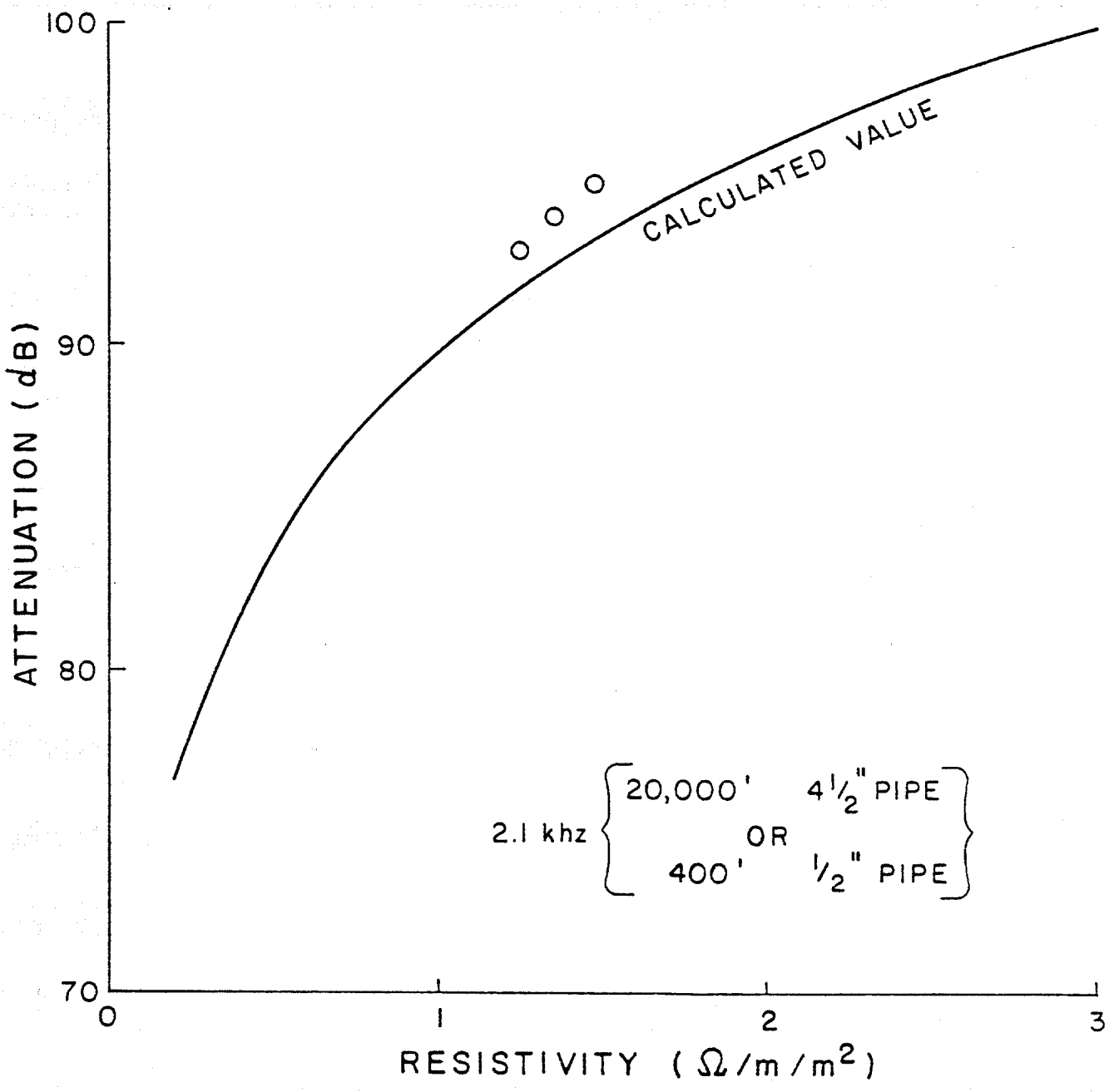

FIGURE 7.6. Comparison of Calculated and Measure Attenuations for Experiment.

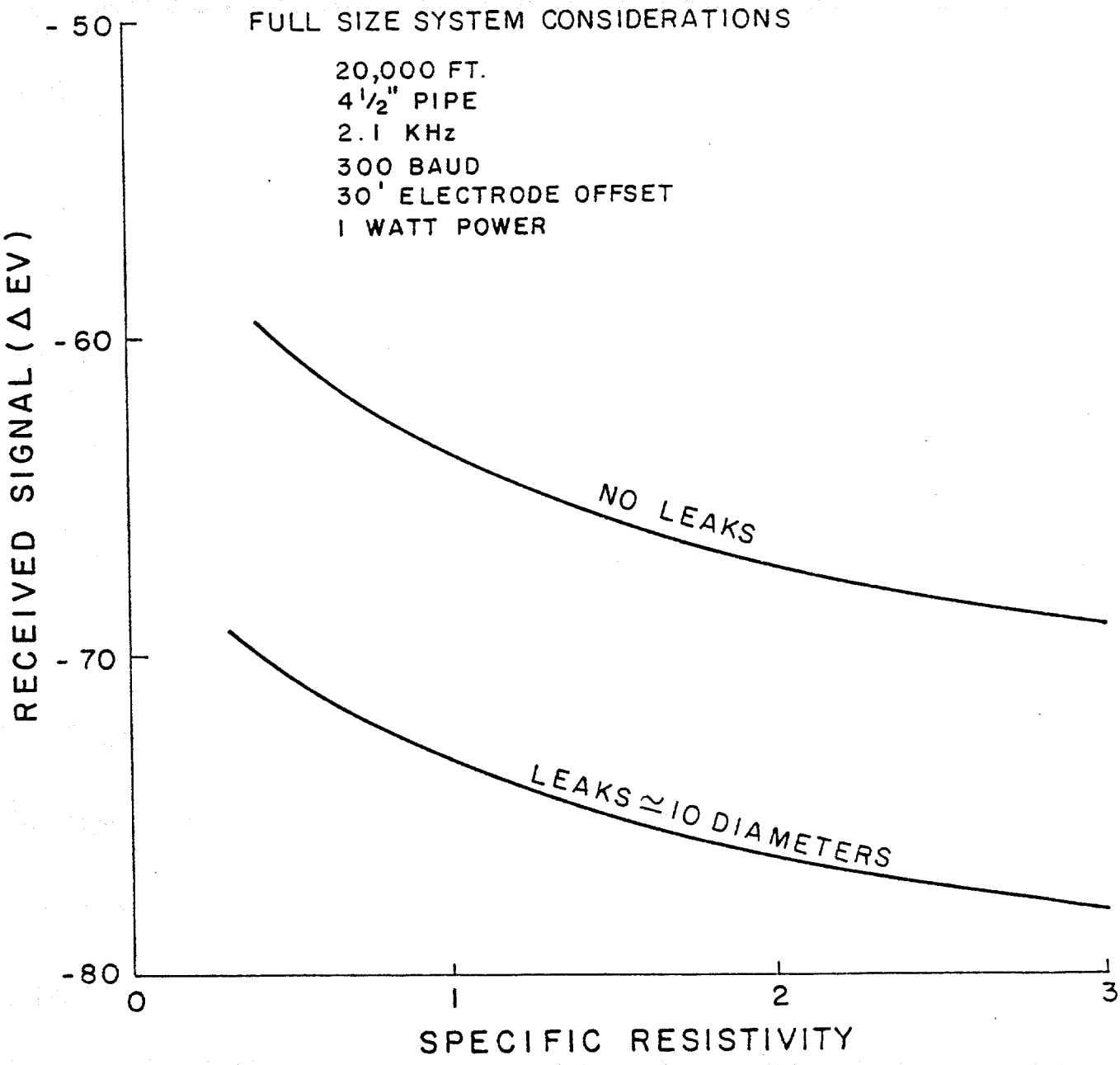

FIGURE 7.7. Typical Received Signals For Telemetry

The activity performed to date has indicated that the telemetry in the drill pipe would be expected to have measurable signal levels. The noise levels, inasmuch as they are influenced by fluid flow and pump activity would also appear to be quite reasonable. At this point several unanswered questions remain. The key questions are:

1. How to design the transmitter to maximize the signal.
    a. Design of the electrodes and coupling signals.
    b. Design of a self adjusting output coupler.
    c. Packaging of the transmitter.
2. How to design a receiver for minimum error rate.
    a. Optimum data error rate for low signal to noise.
3. How to design an insulated drill string.

SUMMARY

Although the results of the electrical telemetry experiments were promising, additional work has not yet been done because of funding limitations. The other areas of research being conducted were felt to be of higher priority, and the electrical telemetry investigation has not proceeded past the initial conceptual demonstration and verification. Major engineering problems and significant costs would be associated with the design, construction, and maintenance of the insulated drill pipe needed. Also, the technique could not be used with non-conductive oil-base muds. Since the minimum required well control parameter (Bottom Hole Pressure) could be transmitted at an acceptable time interval of about 5 seconds using an improved mud pulse telemetry system, it was felt that mud pulse telemetry offered the fastest opportunity for integration of measurement while drilling technology and well control technology.

8. AN EXPERIMENTAL STUDY OF A FLUIDIC MUD PULSER

As discussed in previous chapters, it would be extremely useful to transmit information about the borehole environment near the bit to the surface during drilling and well control operations. The best currently available technique of data transmission is by means of pressure pulses through the mud. There are presently three types of mud pulsers used for data transmission [2]. They are:

1) Negative Pulse. Pulses are generated by venting the drilling fluid from the drill string into the annulus (Figure 8.1a).
2) Positive Pulse. Positive pulses are created by a mechanical valve which restricts flow through the pipe (Figure 8.1b).
3) Continuous Wave. A pulse frequency is generated by a rotating turbine in the drill string. The data is encoded in phase shifts of this frequency (Figure 8.1c).

Although Measurement While Drilling is considered a common method of obtaining directional parameters on offshore rigs, this method of well telemetry has become much more than just a directional package. Since the introduction of MWD for commercial use in 1978 by Teleco Oilfield Services Ltd. [1], several innovations in technology have evolved. What was merely a directional package is now capable of several functions. MWD companies now offer logging sensors such as a gamma ray, spontaneous potential, and resistivity. There are also other bottom hole parameters available such as weight on bit, torque, temperature, and pressure. Information such as this is desirable to optimize drilling procedures and more important for safety of personnel.

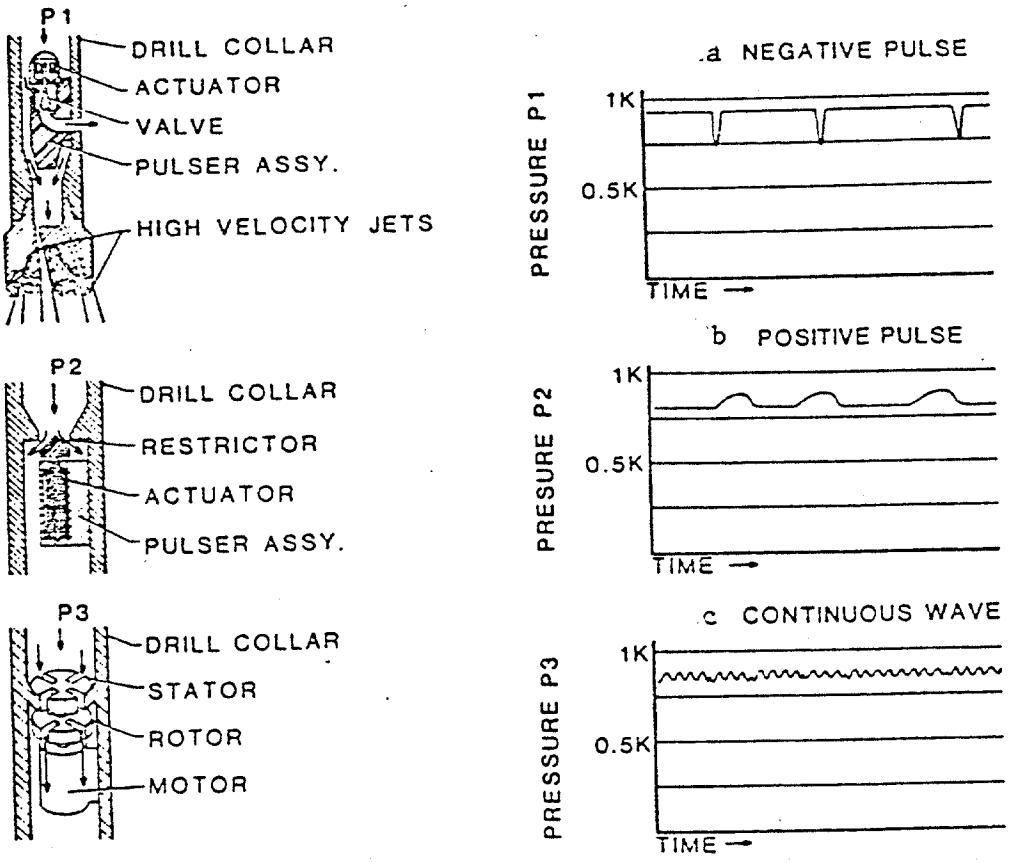

Figure 8.1. Three Types of Mud Pulsers Presently Being Used for Pressure Pulse Transmission.

However, with the increase in bottom hole data there is also an increase in the total time it takes to transmit this data to the surface. This is due to the necessity to constantly update all information concerning the formation. Some MWD tools are programmed for an update every minute on bottom hole activity. The present transmission rates are not well suited for repeatedly transmitting such large volumes of data. This inconvenience can be alleviated in two areas. First by altering the coding system of the pressure pulses, and second by increasing the pulse rate itself. It is the purpose of this research to determine if it is possible to receive signals on the surface at relatively high frequencies.

In order to accomplish this, the first objective is to establish a method to compute the sonic velocity in the drill pipe. Two approaches will be considered, each will be compared to experimentally obtained data. As a second objective of this research, hydrodynamic equations derived by Lamb [6] will be verified by experimental data. These equations were derived to compute the attenuation of pressure pulses in pipes as a function of viscosity and frequency. It is necessary to establish a relationship between frequency and pulse attenuation to determine an optimum transmission rate.

VELOCITY AND ATTENUATION THEORY

The attentuation of a pulse in a tube is a function of several factors. The first factor examined is the velocity in which the pulse travels. It is necessary to determine the pulse velocity in order to compute the attenuation. Therefore, a reliable equation must be found to calculate wave velocities. This particular value is dependent upon

the size and type of tube and also the characteristics of the fluid through which it propagates. There has been more than one approach to the calculation of wave velocities in pipes. This paper has evaluated two equations for use in drill pipe. The first of these is equation 8.1 derived by Watters[3].

$$V = 144\ g_c\left(\frac{1}{B} + \frac{1}{M}\right)^{-1/2} \quad \ldots\ldots\ldots\ldots\ldots\ldots\ldots\ldots \quad (8.1)$$

with longitudinal restraint

$$\frac{1}{M} = \frac{4b^2(1-\lambda^2) + 1(1+\lambda)(a^2-b^2)}{E(a^2-b^2)} \quad \ldots\ldots\ldots\ldots\ldots\ldots \quad (8.2)$$

where

V = Velocity (Ft/sec)

B = Bulk Modulus of Elasticity of the Fluid (psi)

E = Young's Modulus of Elasticity (psi)

a = Outer Diameter of Pipe (in.)

b = Internal Diameter of Pipe (in.)

g_c = Units conversion (32.17)

λ = Poisson's Ratio

ρ = Density (lb/ft)

M = Pipe Modulus (psi)

The pipe modulus "M" is dependent on the pipe properties and also on how the pipe is anchored. Watters has derived a pipe modulus for three different types of restraint. In case "A" above there is no longitudinal strain allowed. This is a characteristic of the system. In this experiment the pipe is buried and is expected to be restrained

from longitudinal expansion by soil friction. There are, however, equations for computing the pipe modulus for other situations. For instance consider the case where the drill string is in the borehole and on bottom, one might choose to use the equation for case "B" where:

$$\frac{1}{M} = \frac{4b^2(5/4-\lambda) + 2(1+\lambda)(a^2+b^2)}{E(a^2-b^2)} \quad \ldots\ldots\ldots\ldots\ldots\ldots \quad (8.3)$$

This equation allows for stress and strain both laterally and longitudinally. This would most likely be the case for all instances associated with drilling conditions. Watters also developed an expression for pipes with functioning expansion joints throughout their length. This configuration is not likely to be encountered in the drilling phase of the industry but will be included in the text for the benefit of the reader. This type of stress and strain condition will be referred to as case "C" and the pipe modulus is represented as

$$\frac{1}{M} = \frac{4b^2 + 2(1+\lambda)(a^2-b^2)}{E(a^2-b^2)} \quad \ldots\ldots\ldots\ldots\ldots\ldots \quad (8.4)$$

Equations 8.2, 8.3, and 8.4 are derived so that the pipe modulus for thick and thin walled pipes can be computed and plugged into equation 8.1.

The second equation studied in the experiment was derived by White [4]. The two equations are very similar in that they both were derived from the same approach. Each author chose to include the elasticity of the pipe, both longitudinal and lateral displacements. Though the equations appear different in the text of White and Watters, the only difference in the two equations is the way the pipe modulus is computed.

Therefore, through algebraic rearrangement, the equation by White can be represented as another means of calculating the pipe modulus and plugging into equation (1) to get the wave velocity. The Equation by White

$$\frac{1}{M} = \frac{2[(1+\lambda)(a^2-b^2) - 2\lambda b^2]}{E(a^2-b^2)} \quad \ldots\ldots\ldots\ldots\ldots\ldots \quad (8.5)$$

includes some work done by Lamb on radial displacement due to a pressure on the interior of a thick-walled tube. The expressions presented by White on the subject are for thick-walled pipe and low frequency waves.

Despite the two different equations the velocity calculations from the equations differed by only about 2 ft/sec for the fluids used in this experiment. This can probably be attributed to the rigidity of the drill pipe. This margin of closeness may lead one to choose either equation in the case of drill pipe. However, for the computations of this experiment the equation by Watters will be used to represent a case "A" or longitudinal restraint. It will be a goal of this work to obtain experimental data to support the theory of these equations.

Attentuation Theory

Once the wave velocity is established one can attend the aspects of pulse attentuation. There have been extensive studies performed on water hammer effects in pipes. This has led to some research on short single pulses in pipes also. Equation 8.6 represents part of the research performed by Rouleau [5] on single pulses.

$$\frac{P_{(x,t)}-\bar{P}}{P_o} = e^{0-\Upsilon_o}\,\mathrm{erfc}[1/2\Upsilon_o(\Upsilon-\Upsilon_o)^{-1/2}] \qquad (8.6)$$

$$e^{-\Upsilon_o}\,(\mathrm{erfc}[1/2\Upsilon_o(\Upsilon-\Upsilon_o)^{-1/2}] - \mathrm{erfc}[1/2\Upsilon_o(\Upsilon-\Upsilon_o-\Delta\Upsilon)^{-1/2}])$$

for

$$\Upsilon < \Upsilon_o$$

$$\Upsilon_o \leqq \Upsilon < \Upsilon_o + \Delta\Upsilon$$

$$\Upsilon \geqq \Upsilon_o + \Delta\Upsilon$$

where

$$\Upsilon = \frac{v}{b^2}t. \qquad (8.7)$$

$$\Upsilon = \frac{vx}{b^2V}. \qquad (8.8)$$

$$\Upsilon = \frac{v}{b^2}t_o \qquad (8.9)$$

$P(x,t)$ = Fluid Pressure (lb/ft^2)

$\bar{P}$ = Reservoir Pressure of Experiment (lb/ft^2)

P_o = Magnitude of Pressure Pulse (lb/ft^2)

Υ = Non-Dimensional Time

Υ_o = Non-Dimensional Time Delay

$\Delta\Upsilon$ = Non-Dimensional Duration Time of Pulse

Equation (6) will predict the amplitude of a single pulse traveling through a static fluid column at any distance x from the origin. Although this can give some insight to the dissipation of a pressure pulse over a distance, it is not applicable to Measurement While Drilling systems because in nearly all cases of MWD the data is transmitted through a series or burst of pulses in a dynamic environment. For this reason the effect of frequency must be taken into account on pulse attenuation.

Some classical work of this nature has been performed by Lamb [6]. Lamb has derived that the change in pulse amplitude traveling along a tube is given by

$$P_{(x)} = P_o e^{-x/L} \quad \ldots\ldots\ldots\ldots\ldots\ldots\ldots\ldots\ldots\ldots \quad (8.10)$$

and

$$L = \frac{bV}{2} \frac{2}{v\omega} \quad \ldots\ldots\ldots\ldots\ldots\ldots\ldots\ldots\ldots\ldots \quad (8.11)$$

where

b = Inside Diameter of Pipe (ft)

V = Pulse Velocity (ft/sec)

v = Kinematic Viscosity of Fluid (ft/sec)

ω = Angular Frequency (rad/sec)

$P_{(x)}$ = Pulse Amplitude at Distance x (psi)

P_o = Original Pulse Amplitude (psi)

L = Distance in Which Amplitude Falls to 1/e of its Original Value (ft)

The angular frequency ω can be computed by

$$\omega = 2\pi f \quad \ldots\ldots\ldots\ldots\ldots\ldots\ldots\ldots\ldots\ldots \quad (8.12)$$

where f is the pulse frequency in Hertz. The velocity computations have been discussed previously in the paper. The one problem which must be resolved now is that the equation calls for the kinematic viscosity and not the traditional plastic viscosity which is normally encountered in the Bingham plastic fluid of the oil industry. This is accomplished by substituting the absolute viscosity with the plastic viscosity and then converting over to the kinematic viscosity. The conversion can be done by using equation (13) from Marks Mechanical Engineering Handbook [7]

$$v = 2.09\ 10^{-5}\ \frac{\mu g_c}{\rho} \quad \ldots\ldots\ldots\ldots\ldots\ldots\ldots\ldots\ldots\ldots\ (8.13)$$

v = Kinematic Viscosity (ft/sec)

μ = Absolute (Plastic) Viscosity (cp)

g_c = Units Conversion

ρ = Density (lb/ft^3)

The attenuation equations were derived long ago by Lamb; however, there is little experimental data to verify the accuracy of the equations. The attenuation theory behind the derivations is based on Newtonian fluids. It will be one of the goals of this work to perform experiments with Newtonian and Non-Newtonian (Bingham Plastic) fluids and evaluate the performance of Lamb's attenuation equations. In the case of the Bingham Plastic fluids, the plastic viscosity will be substituted for the absolute viscosity and then calculations will be carried through as in the Newtonian fluid. It is expected that while the mud is in the drill pipe and in turbulent flow, the shear rate will remain so that the fluid will behave in a near Newtonian fashion.

Experimental System

A mud loop has been built to conduct the tests at the Louisiana State University Blowout School and Research Center. The conduit consists of 9,460 feet of 4.5 inch, 20 pound per foot, API drill pipe. The pipe forms two connecting loops and was buried 5 feet underground with the mid-section and both ends rising to the surface. There are concrete manholes at selected intervals to allow access to the drill pipe.

Figure 8.2 illustrates an overall view of the experimental set up. This grade of drill pipe has a 3.64 inch internal diameter and a capacity of 1.2871 barrels per 100 linear feet.

The pump connected to the loop was a Halliburton HT-400 triplex pump. The pump was equipped with 4 inch liners and has an 8 inch stroke length. This coupled with an output efficiency of 99% delivered a pump factor of approximately 1.28 gallons per stroke [8].

Due to the characteristics of a pump of this nature, it was necessary to dampen the pulsation caused by the pistons of the pump. Figure 8.3a and 8.3b illustrate the pressure surges generated by a duples and triples pump respectively [9]. It can be seen that the pressure is not steady but actually a continuous fluctuation of pressure peaking as each pump piston strikes the fluid. This fluctuation can be smoothed out considerably by interconnecting the outlet of the pump with a pocket or chamber containing a compressible fluid to act as a shock absorber. Two dampeners were used in this experiment. First a small air filled dampener was mounted directly on the pump. This particular dampener was non-chargeable and totally inadequate for experimental purposes. To reinforce the dampening, a nearby 2,000 feet well was connected 6 feet ahead of the inlet end of the drill loop. The well was equipped with an open-ended tubing. The tubing was charged with approximately 150 pounds per square inch of nitrogen. This displaced 320 feet of mud from the tubing and served as a cushion for the pump noise. Although this provided a significant amount of dampening, the proper equipment would have been a couple of 5 to 10 gallon bladder type pulsation dampeners. This has proven to work sufficiently in experiments performed by Mobil Research and Development Corporation [10].

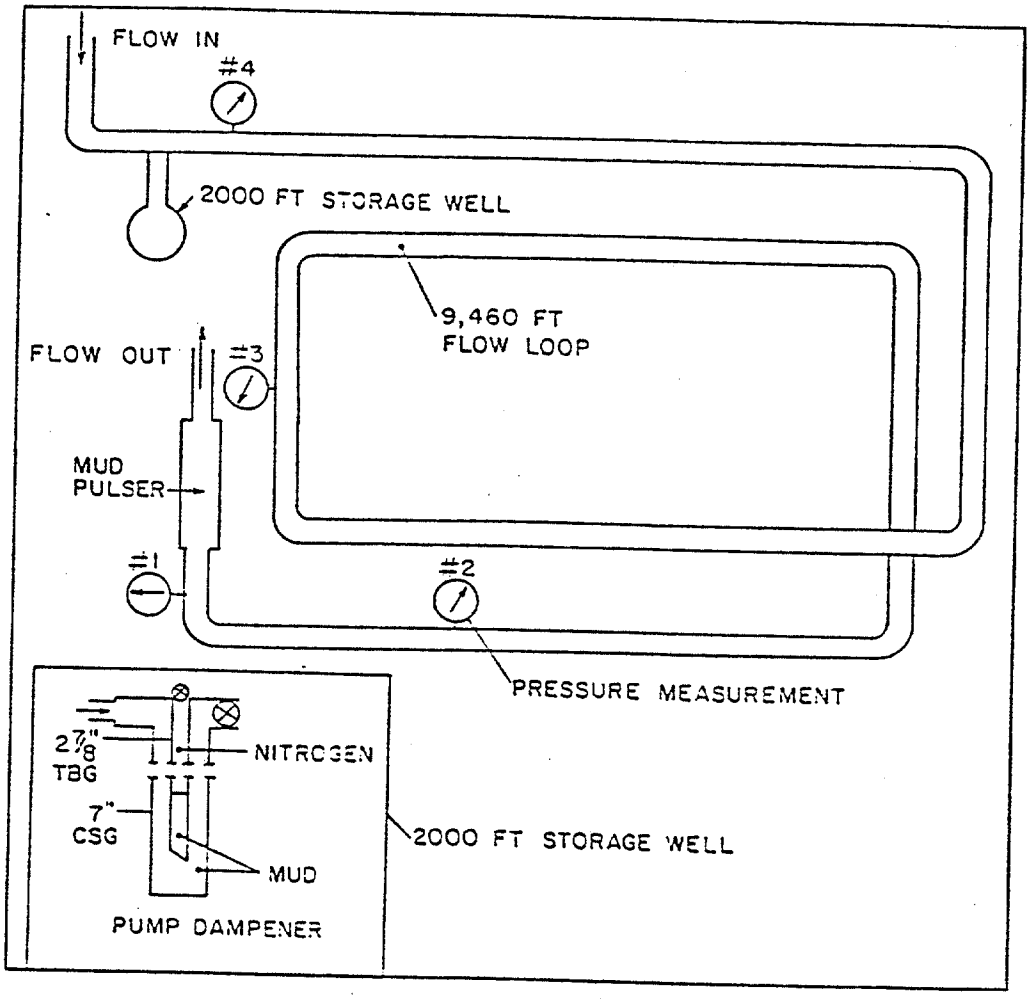

FIGURE 8.2. Flow Loop Built at the L.S.U. Research Center for Conducting Experiments.

DUPLEX DOUBLE-ACTING PUMP

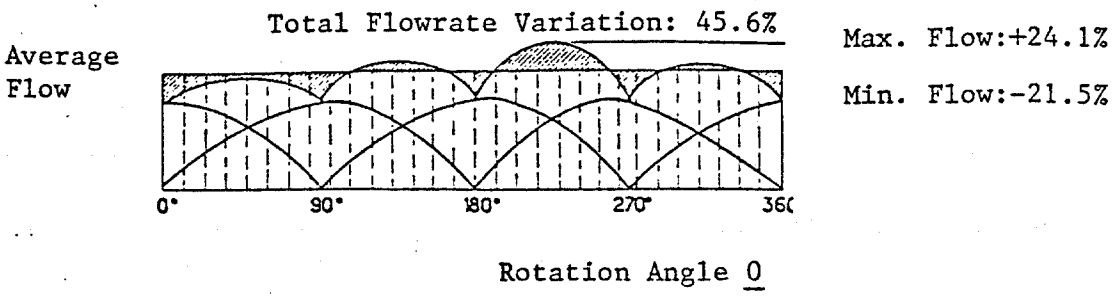

TRIPLEX SINGLE-ACTING PUMP

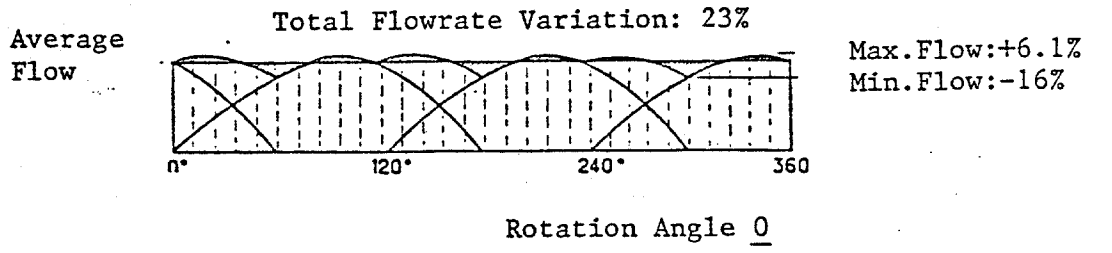

FIGURE 8.3. Diaphragm of Duplex and Triplex Pump Pressure Performance.

The pressure measurement devices consist of hydraulic pressure sensors to measure pump pressure and piezoelectric quartz transducers to monitor pressure pulses. The transducers are constructed specifically for measuring dynamic pressures. Figure 8.4 gives a cross-sectional view of a transducer. The high impedance voltage signal produced by the quartz element is fed across the input of a built-in constant current follower amplified which converts the signal to a low impedance voltage. This voltage is low enough to be fed directly into recording equipment.

The transducers are powered by AC or DC mode line power units. The power units supply excitation to transducers and also couples self-amplifying transducers to readout instrumentation. Figure 8.6 gives a schematic of the internal components of the transducer and its power supply. In the coupling process the power supply eliminates DC power bias from the output by means of a coupling capacitor or level shifter of the floating DC power supply type. The power supply generates a constant-current excitation which is adjustable from 2 mA to 20 mA. The current is factory set at about 4 mA. The current may be increased to drive longer cables or to provide more output voltage. The factory setting was sufficient to drive the 300 feet cables used in this experiment; however, due to problems of humidity seeping into the transducer connections, the current supply was stepped up to 15 mA output. The transducers are rated for 10,000 psi working pressure and 1000 psi dynamic pressure measurement. Table 8.1 and Table 8.2 give other specifications of the transducers and power supplies respectively. From Table 8.1 it is shown that the transducers have a rise time of 3 micro-seconds which is sufficient to distinguish and measure pulses at relatively high frequencies [11].

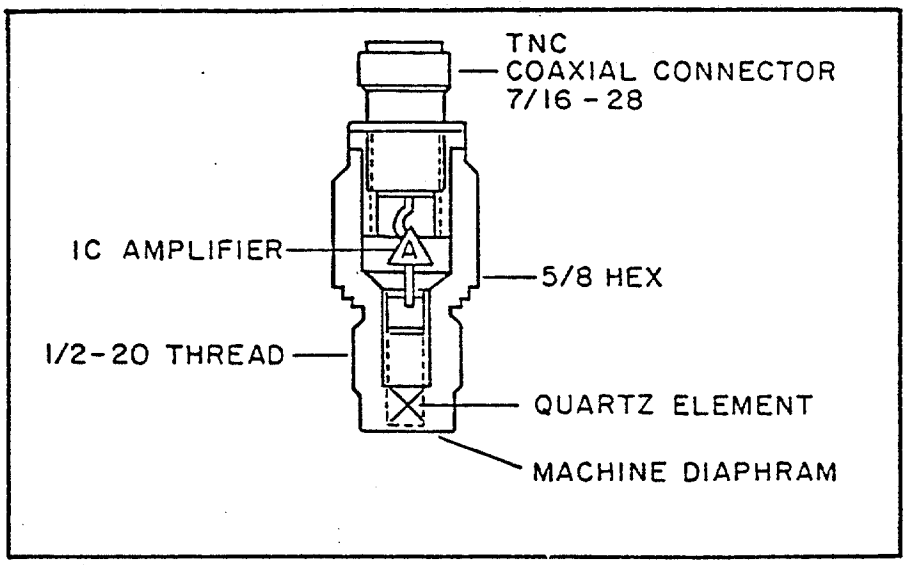

FIGURE 8.4. Cross-Sectional View of a Transducer used for Dynamic Pressure Measurement.

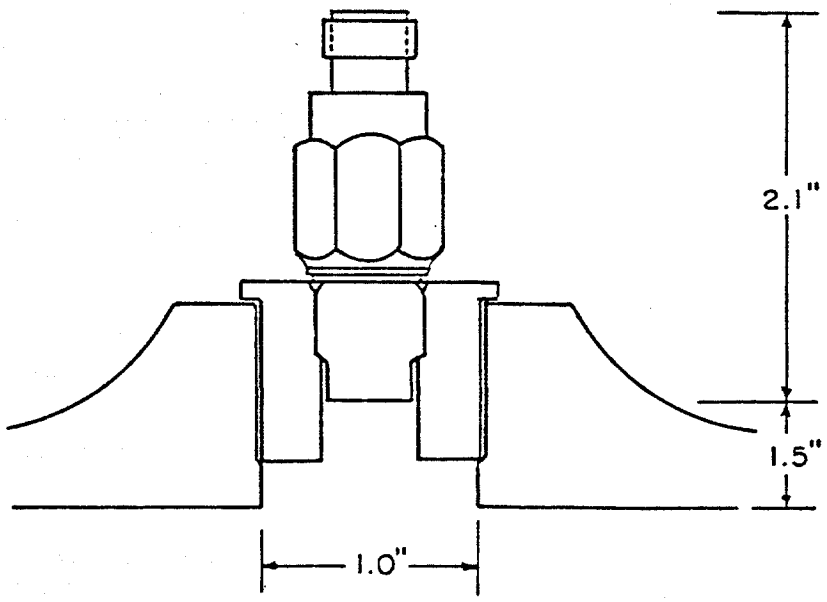

FIGURE 8.5. Mounting Technique of the Transducers.

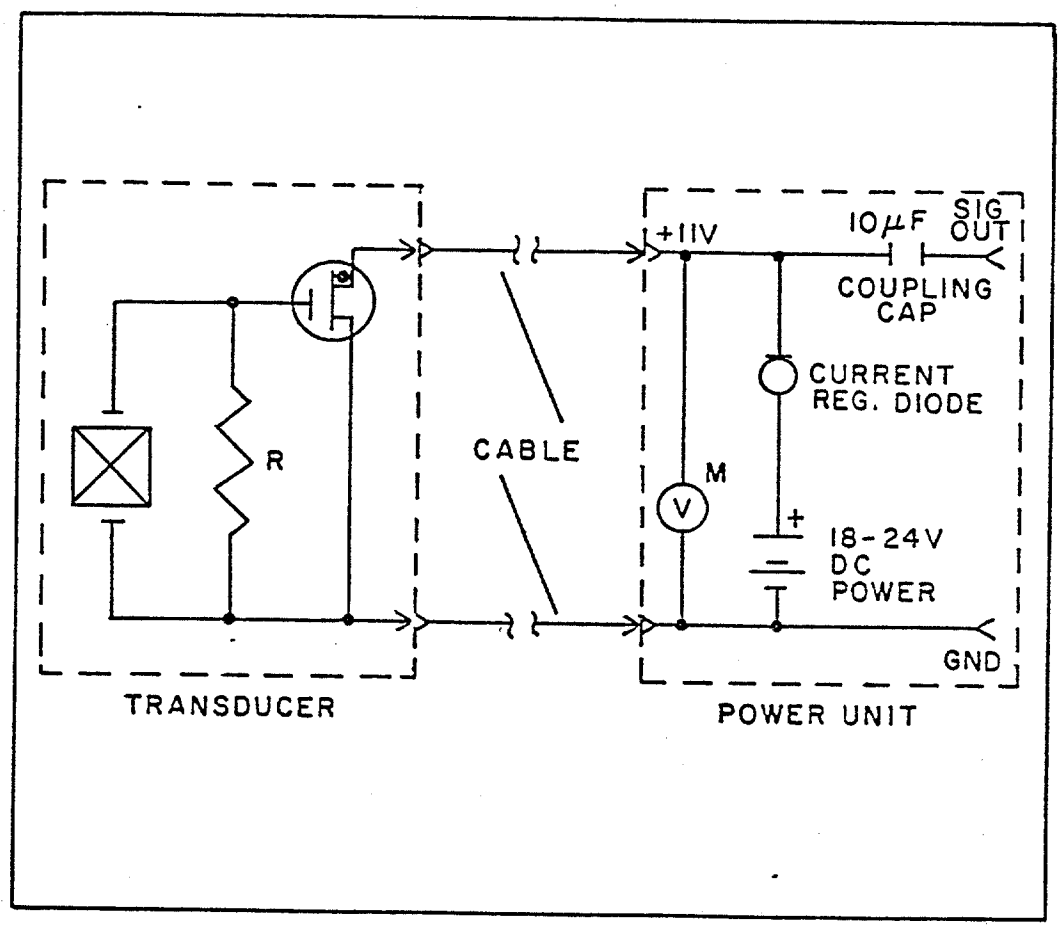

FIGURE 8.6. Schematic of the Internal Components of the Transducers and Power Supplies.

Range (5V Output)	1,000 psi
Useful Overrange (10V Output)	2,000 psi
Maximum Pressure	10,000 psi
Resolution	.005 psi
Sensitivity	5 mV/psi
Resonant Frequency	200 KHz
Rise Time	3 µS
Discharge Time	100 S
Low Frequency Response (-5%)	.5 Hz
Polarity	Positive
Output Impedence	100 Ω
Output Bias	9 to 12 V
Temperature Range	-100 to +275°F
Flash Temperature	3000°F
Vibration Shock	2,000/20,000 g
Excitation (Constant Current)	2 to 20 mA

Table 8.1. Specifications of PCB Model 121A02 Quartz Transducers.

Excitation, Constant	2 to 20 mA
Current (Set at 15)	24V DC
Voltage Gain (Non-Inverting)	1.00
Coupling Capacitor	10 µF
Coupling Time Constant (AC Mode)	10 S
Bias Elimination Range (DC Mode)	4.5 to 6.2 V
Frequency Response (±5%, DC Mode)	DC to 200 KHz
Frequency Response (±5%, AC Mode)	.05 to 200 KHz
Output Current	10 ±mA
Output Impedence	50 Ω
Noise (pk-to-pk)	600 µV

Table 8.2. Specifications of PCB Model 484M57 Constant Current Power Supply.

The transducers are located in four taps along the drill pipe. They were mounted carefully to avoid damage and as close as possible to the fluid medium to insure little or no air entrapment (figure 8.5). The transducers were located as follows:

#1 located 25 feet from the pulser

#2 located 280 feet from the pulser

#3 located 4730 feet from the pulser

#4 located 9460 feet from the pulser

The pump was connected approximately 100 feet from the last transducer. Discharge from the pulser was returned through a manifold and return line consisting of 300 feet of 2 inch heavy gauge line pipe.

The tool used to generate a pulse was a prototype developed by Harry Diamond Laboratories in Washington, D. C. The pulser is unique in its design. It is comprised of fluidic type valves which employ centrifugal forces to create a vortex flow which in turn causes an increased pressure drop in the high loss mode. A vortex valve is shown in figure 8.7. Figure 8.8 shows the two types of flow through such a valve. It can be seen that the fluid flows easily through the valve with little pressure loss before the vortex is induced (figure 8.8). When the tab is actuated to create the vortex (figure 8.8), a pressure surge is created by the centrifugal forces acting around the chamber and through the outlet [12].

The tab is mechanically driven by a small fast acting solenoid. The solenoid is isolated from the drilling fluid and operates through a bellows. The pressure between the solenoid and the drilling fluid is equalized through a rubber diaphragm. This keeps the solenoid free of mud solids and prevents it from working against needless pressure differentials.

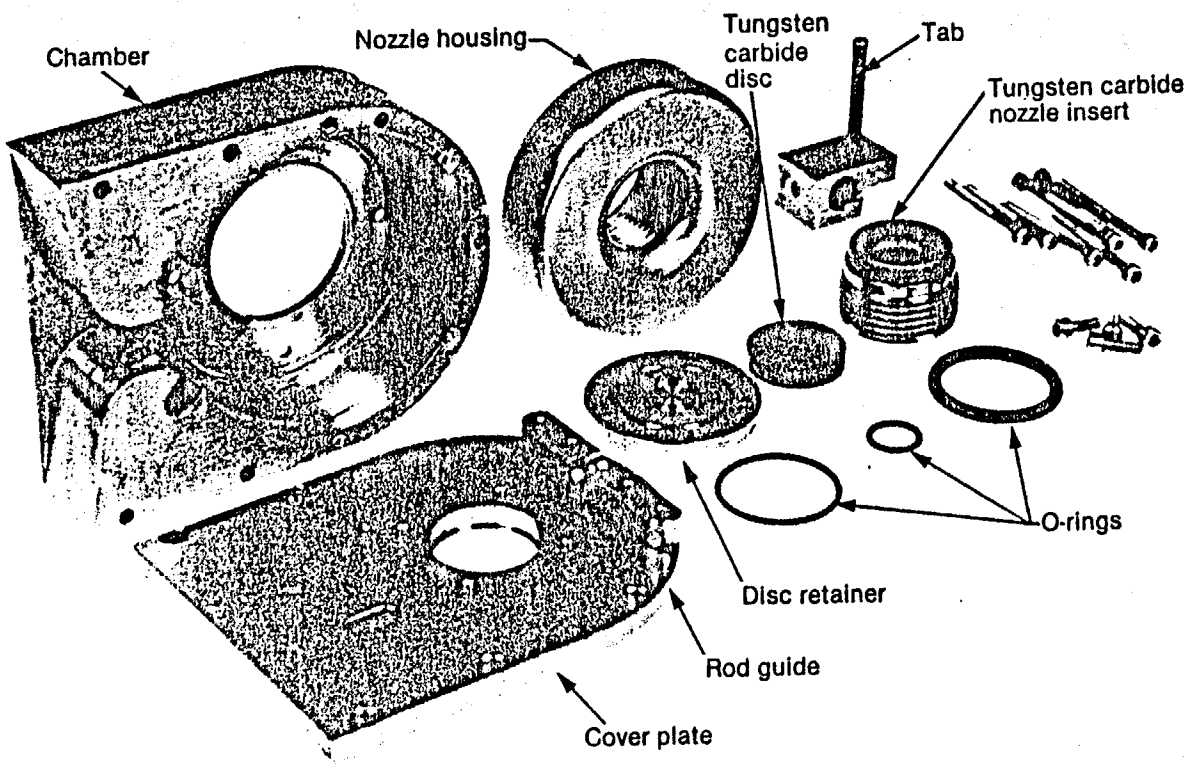

FIGURE 8.7. Tab Actuated Vortex Valve Components.

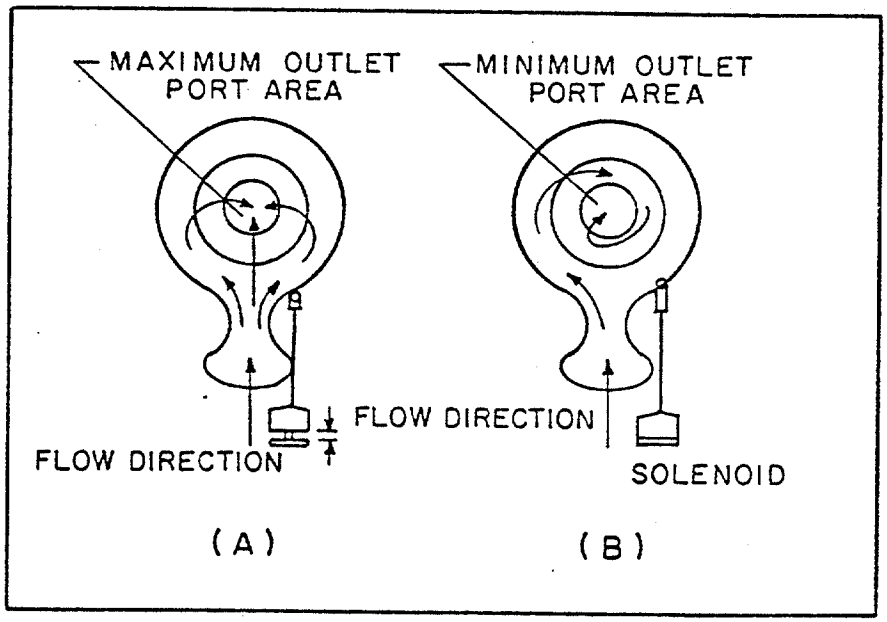

FIGURE 8.8. Flow Through a Vortex Valve. (a) Low Pressure Loss Mode. (B) High Pressure Loss Mode.

The vortex valves can be connected in parallel to adapt to high flow rates or simply blocked off or port areas reduced to handle lower flow rates. Figure 8.9 shows the entire pulser with four vortex valves in parallel. In this experiment two vortex valves were used. Only two were necessary due to a limited flow rate of 200 gallons per minute [13]. The pressure drop through the tool in the open or unactivated position was around 120 psi compared with approximately 95 psi with 4 vortex valves. This is representative of the versatility of the tool without high gains in frictional pressure loss.

Recording and Analyzing Equipment

Data was collected and stored on magnetic analog tape. The recorder was equipped to handle five tracks plus an edge track. Channels one through four contained the output from the transducers. The fifth channel on the tape recorded the signal from the signal generator which produced a square wave input to the pulser. The outside or edge track was used as an audio track to record a vocal account of various stages of the experiment.

The instrument used to analyze the data was a Wavetek Cross Channel Spectrum analyzer. This instrument had several convenient and necessary functions. It was capable of processing data at intervals and averaging data before displaying the result. The analyzer was also capable of working on communication with small computers, calculators, and printers. This provided a convenient hard copy of data for analysis and future reference. The most favorable function of the spectrum analyzer was its pre-programmed menus. The most interesting of these is its ability to perform Fast Fourier Transforms [14].

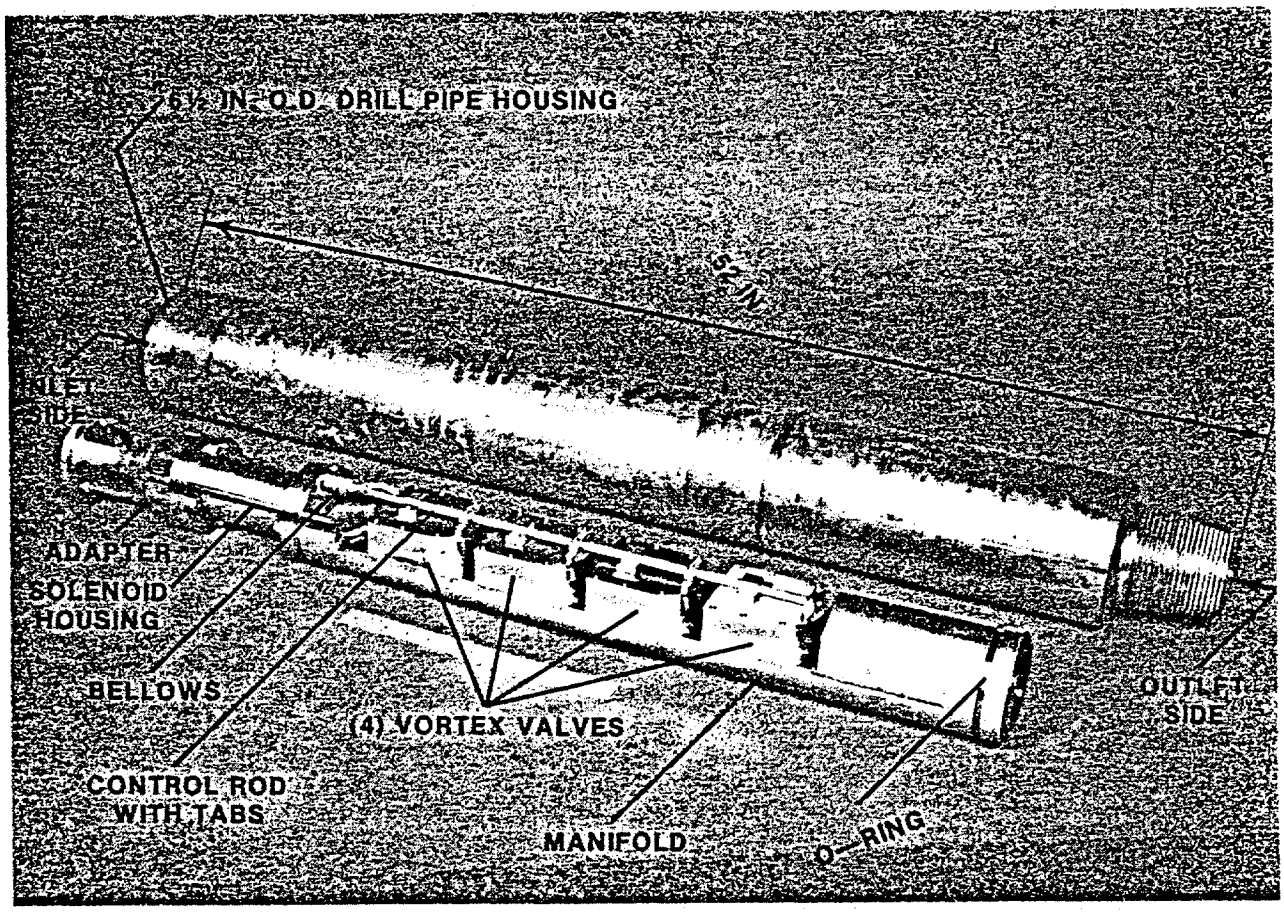

FIGURE 8.9. Fluidic Mud Pulser with Fout Tab Actuated Vortex Valves.

Fourier analysis is commonly found in engineering practices. Many complex periodic waves are mixtures of harmonic waves of several frequencies. This leads to a mathematical analysis originating with what is known as Fourier's theorem. This theorem allows any periodic function to be analyzed in terms of sines and cosines. Consider the periodic function f(t), Fourier's theorem states that this function can be written as

$$F_{(t)} = A_o + \sum_n (A_n \text{Sin } \omega_n t + B_n \text{Cos } \omega_n t) \quad \ldots\ldots\ldots\ldots (8.14)$$

where

$$\omega_n = n \frac{2\pi}{T} \quad \ldots\ldots\ldots\ldots\ldots\ldots\ldots\ldots\ldots\ldots (8.15)$$

n = Harmonic Number
ω = Frequency
T = Period

This is known as the Fourier Series of f(t). The relative values of A and B are related to the waveform. The value A + B is proportional to the intensity of the nth harmonic component of the function [15]. As part of the Fourier analysis the components A, B, and C, can be determined by the so-called Euler formulas [15]:

$$A_o = \frac{1}{2\pi} \int_{-\Pi}^{\Pi} f_{(t)} \, dt \quad \ldots\ldots\ldots\ldots\ldots\ldots\ldots\ldots (8.16)$$

$$A_n = \frac{1}{\pi} \int_{-\Pi}^{\Pi} f_{(t)} \text{ Cos } nt \, dt \quad \ldots\ldots\ldots\ldots\ldots\ldots\ldots\ldots (8.17)$$

$$B_n = \frac{1}{\pi} \int_{-\Pi}^{\Pi} f_{(t)} \text{ Sin nt dt} \quad \ldots\ldots\ldots\ldots\ldots\ldots\ldots \quad (8.18)$$

The Fourier transform is an integral expression for a Fourier series applied to an infinitely long signal. The fundamental wave and its harmonics are separated by infinitesimal increments. Fourier transform techniques are used to express a time function as a continuous function of frequency and also to synthesize a function expressed in terms of amplitude versus frequency into the function of time to which it corresponds. The mathematical expression of Fourier transform comes in two parts, one for the frequency spectrum $F(\omega)$ in terms of the time function $f(t)$ and the other for the time function in terms of the frequency spectrum. The frequency function $F(\omega)$ can be obtained by the integral [17]

$$F_{(\omega)} = \int_{-\infty}^{\infty} f_{(t)} \text{Cos } 2\pi\omega t \text{ dt} - i \int_{-\infty}^{\infty} f_{(t)} \text{Sin } 2\pi\omega t \text{ dt} \quad \ldots\ldots \quad (8.19)$$

Similarly the transform $f(t)$ can be expressed by the integral

$$f_{(t)} = \int_{-\infty}^{\infty} F_{(\omega)} \text{Cos } 2\pi\omega t \text{ d}\omega + i \int_{-\infty}^{\infty} F_{(\omega)} \text{Sin } 2\pi\omega t \text{ d}\omega \quad \ldots\ldots \quad (8.20)$$

Needless to say, it can be a difficult task to perform such mathematics without the aid of a computer. The Wavetek Spectrum Analyzer uses a network of processors to perform Fast Fourier Transform Computations. The Fast Fourier Transform is merely a digitized exponential method of performing the Fourier transform previously discussed [18].

Operational Procedure

A systematic program of steps were performed and repeated throughout the course of the experiment. The procedure began with a calibration check of the transducers. All transducers were mounted together and underwent a series of pulses to ensure that each device had been calibrated to the same output. Following the initial calibration check the transducers were spread out along the drill pipe. Once the transducers had been mounted in their proper place, a steady flow of approximately 200 gallons per minute (GPM) was established. To run at 200 GPM the pump must operate at 160 to 165 strokes per minute. At this speed the pump pistons generate a frequency around 8.25 Hz. Therefore, to obtain as pure of a pulse as possible, frequencies of 1, 2, 3, 5, 10, 13, and 20 Hz were chosen as the most adequate points to be analyzed. Figure 8.10 is a recording of the pump noise and its spectrum. It can be seen that the selected frequencies allow the experiments to be conducted with the least amount of interference from the pump pulsation. Upon completion of a set of given experiments, the transducers were again mounted together and their calibrations checked. This was found necessary from experience, to make certain that the data collected was accurate and of good quality.

The experiment consisted of running fluids most likely encountered in drilling operations. The fluids used were fresh water, water-base mud, and oil-base mud. The physical properties of the muds were altered repeatedly in order to analyze their effect on attentuation. Table 8.3 states the fluids used in the experiment.

Once the data had been collected and stored on tape, it was then possible to reproduce the data and examine carefully the velocity and

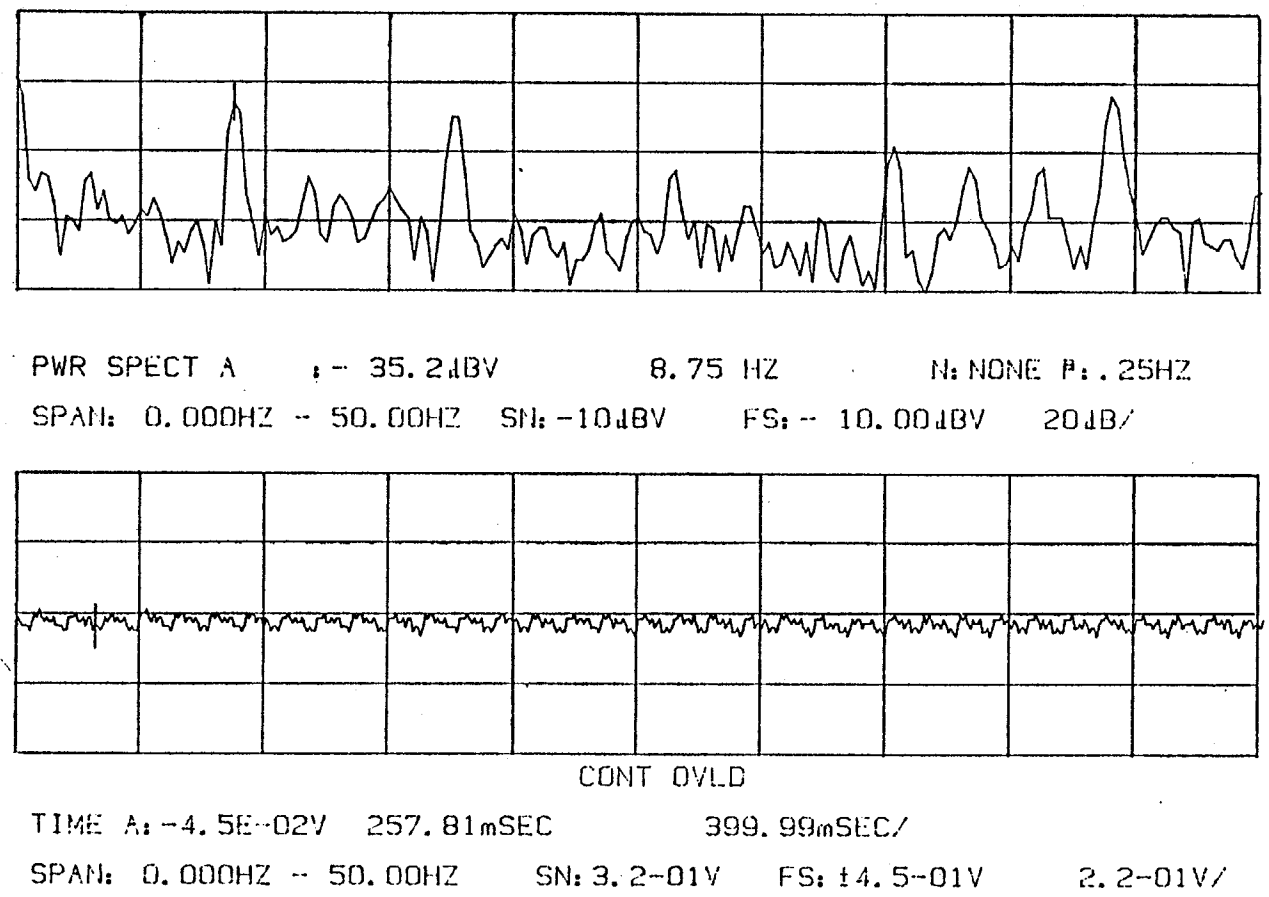

FIGURE 8.10. Recording of Pump Noise and its Fourier Transform.

PROPERTIES	WATER	WATER-BASE MUD			OIL-BASE MUD
		Mud #1	Mud #2	Mud #3	Mud #4
Density (lb/gal)	8.3	8.9	8.9	8.9	8.5
Funnel Viscosity (sec)	27	41	47	57	49
Plastic Viscosity (cp)	1	14	20	26	20
Yield Point (lb/100 ft)	---	4	7	9	4
Fan Readings	*	*	*	*	*
600 RPM	---	32	47	64	44
300 RPM	---	18	27	38	24
200 RPM	---	14	20	28	16
100 RPM	---	7	12	16	9

Table 8.3. Measured Properties of Various Fluids Used in the Experiment.

attenuation phenomena. The most promising method of interpretation seemed to be the fourier spectrum of the curves generated. The reason for this is that there are so many harmonic waves that propagate through the fluid from the pulser as well as the pump. In this method the time domain is transformed to a frequency domain through Fourier analysis. The result is a graph of fundamental and harmonic frequencies versus intensity. Figure 8.11a is representative of the Fourier transform of a 10 Hz sine wave 8.11b. This allows an easy isolation of the pulse and provides a more accurage measurement of its magnitude. As mentioned earlier, rather than solving any complicated mathematical problems, a Wavetek Spectrum Analyzer was used to perform the transform.

In the Fourier transform the intensity is proportional to the magnitude of that particular frequency. In the case of the Wavetek, the intensity is measured in decibels (db). It was found useful to establish a relationship between the intensity and actual voltage amplitude of the signal. Through a series of signal inputs, as in figure 8.11, equation 8.20 was found to give a quick conversion.

$$V_{pp} = 2 \times 10^{db/20} \quad \ldots\ldots\ldots\ldots\ldots\ldots\ldots\ldots\ldots\ldots \quad (8.21)$$

where

V_{pp} = Peak to Peak Amplitude of Wave (volts)

db = Value of Fourier Transform (decibels)

With a known transducer output of 5 millivolts per psi, this equation makes it simple to translate signal strengths into more familiar units of psi.

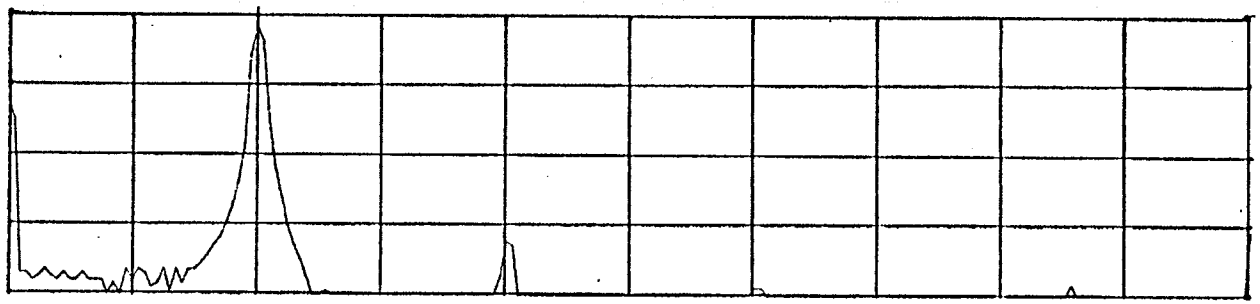

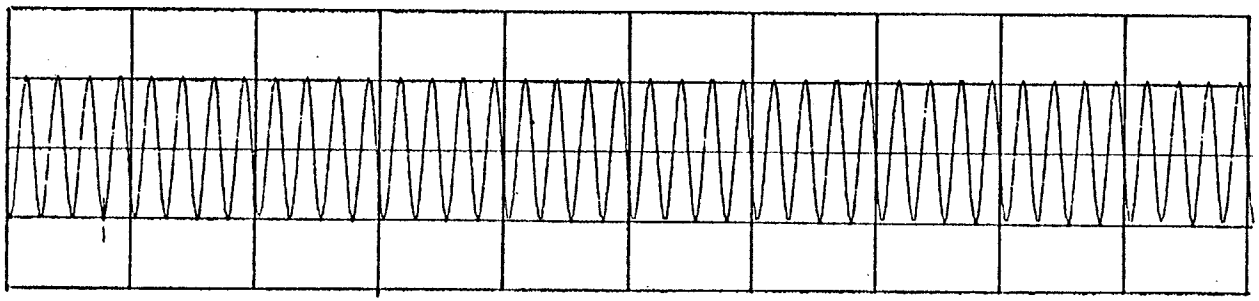

FIGURE 8.11. A Pure 10 Hertz Sine Wave From a Signal Generator. (A) The Frequency Domain of the Sine Wave. (B) The Time Domain of the Sine Wave.

EXPERIMENTAL RESULTS

The experiment began with an equipment check. The transducers were mounted on a manifold and tested for accuracy and to assure sufficient response. The manifold was packed with grease to prevent air from being trapped and in turn projecting false or misleading calibration data. During the initial stages of the experiment some moisture problems were encountered with the transducers. The quartz transducers used in the tests contained a built-in amplifier. Any dampness in or around the amplifier caused a shorting out or change in resistance within the transducer. With the cooperation of the manufacturer this problem was alleviated by sealing 6 feet of coaxial cable to the connector of the transducer. This seemed to work well and allowed the experiment to continue without interruptions.

Once environmental problems were conquered the sensitivity of the transducers was checked. The results indicated that the transducers were very closely calibrated to the same output. Figure 8.12 is representative of the calibration results. The maximum deviation by a transducer was about 3 tenths of a dB. Therefore, it was decided that 5 tenths of a dB would be an acceptable margin for transducer accuracy.

Water Results

The velocity and attenuation tests were first conducted with water. Figure 8.13 is an example of a 2 hertz wave generated by the pulser. The attenuation is difficult to see here because there is very little attenuation at this distance and frequency when water is the fluid

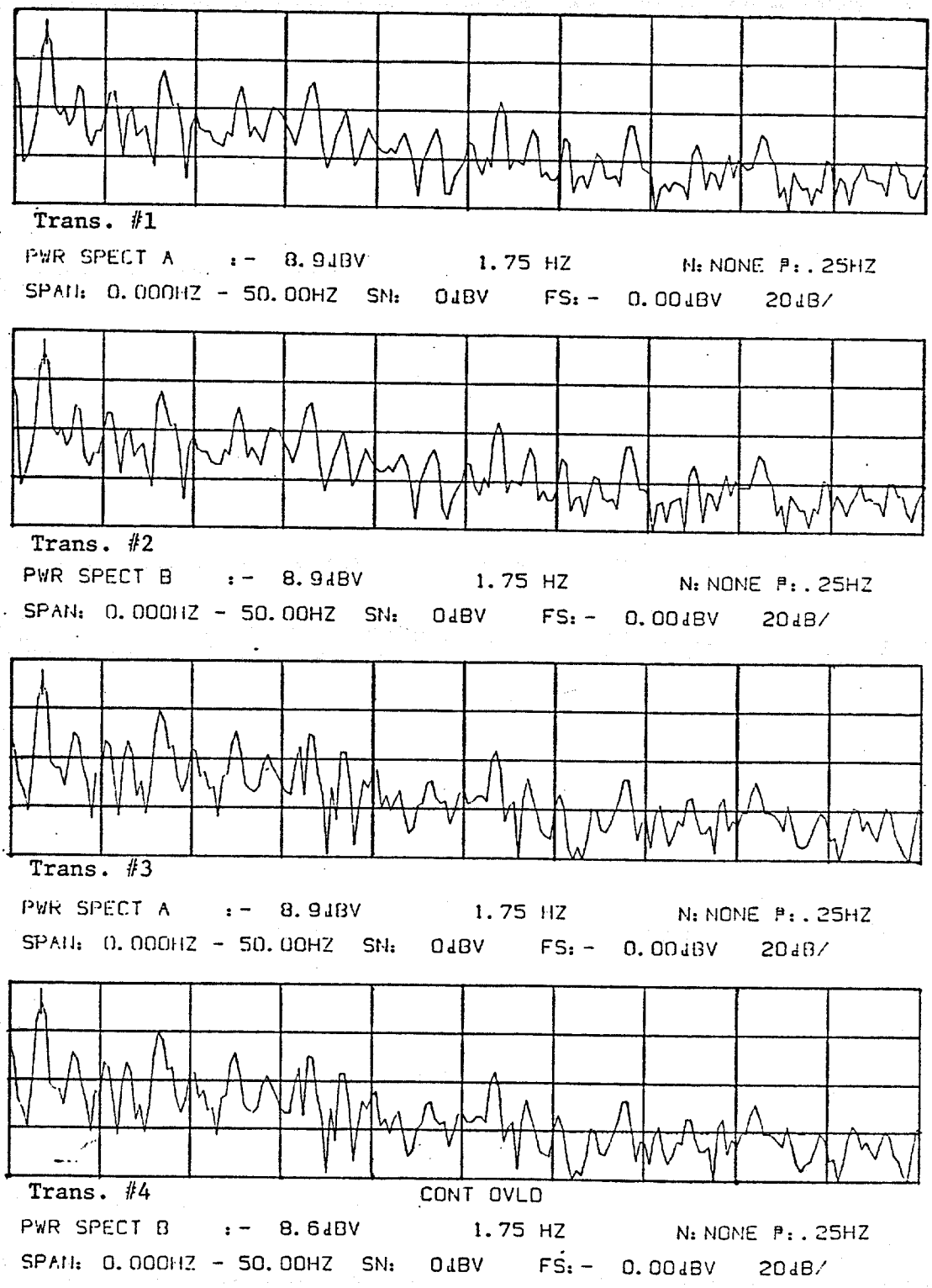

FIGURE 8.12. Typical Results of Calibration Runs on Transducers Before and Following a Set of Experiments.

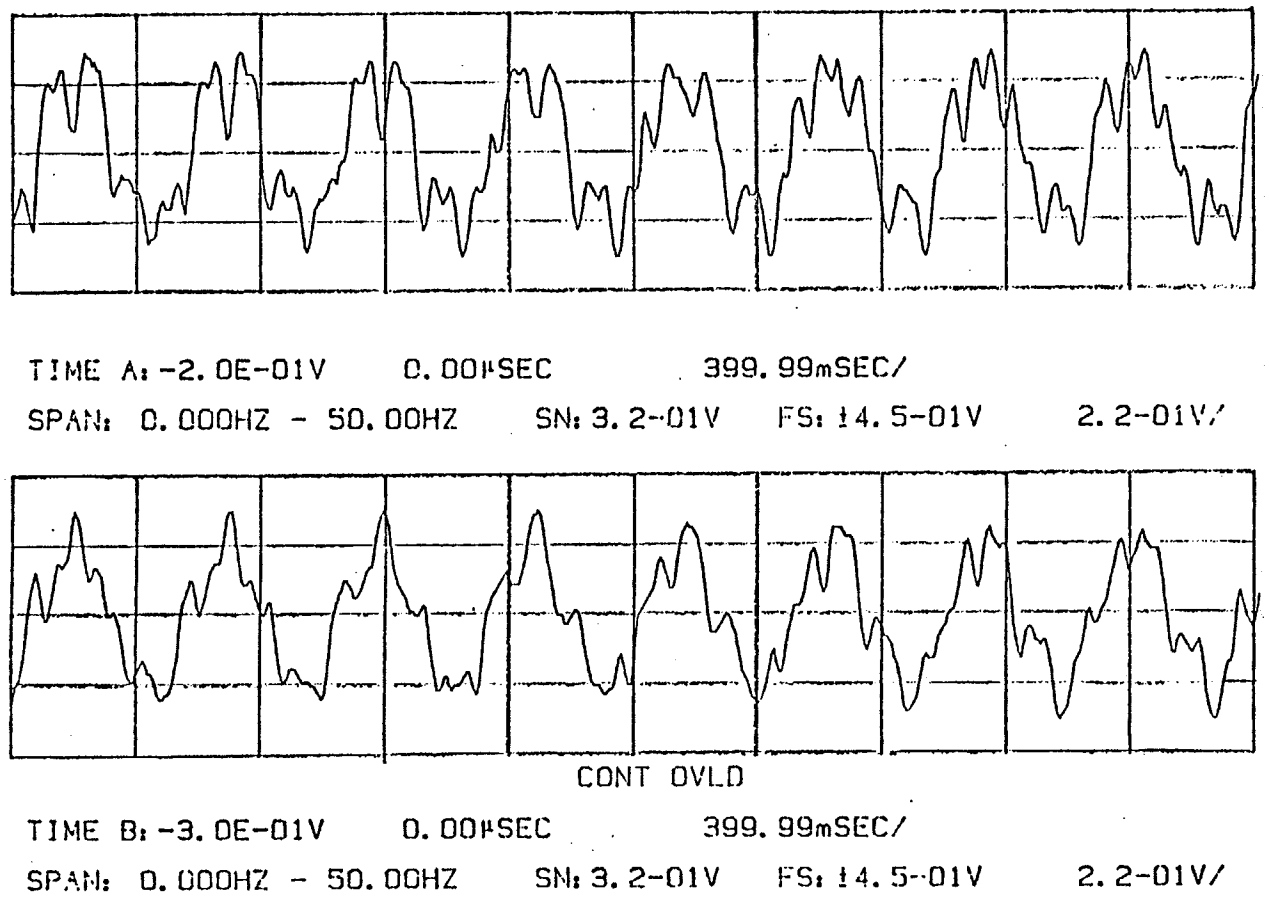

FIGURE 8.13. A 2 Hertz Pulse Generated by the Fluidic Pulser.

medium. Although Figure 8.13 was not applicable to the attenuation calculations it was very useful in calculating travel times. By producing an overlay of the signal from the first transducer, it was possible to fit the pulses over the signals produced by the other transducers. Then by measuring the time difference from the first transducer and the others the wave velocity was computed. The experimentally determined wave velocity in the water medium was about 4900-4920 feet per second.

This corresponds well to the theoretical value of 4910 feet per second which was computed usinf the equation derived by Walters [3]. Figure 8.14 is a plot of the experimental data and the theoretical value for wave velocity in water. The equation by White [4] also produces a comparable value of 4909 feet per second. However, the equation by Watters describes the present system more accurately and produces a value closest to the measured velocity.

The attenuation measurements were made using the Fourier Transform of the pulse generated. Figure 8.15 is the Fourier transform of the 2 hertz signal in Figure 8.13. The attenuation is easier to see because it is separated from the noise in the pipe. The attenuation of a wave is not linear but actually an exponential decay. By using the Fourier transform, the intensity (measured in dB) has a logarithmic relationship to the actual magnitude of pulse. Therefore, a plot of the intensity versus distance yields a straight line. Figure 8.16 gives proof of this. By constructing a plot of intensity versus distance for each frequency (figure 8.16), data was collected to form a plot of attenuation versus frequency at a distance of 9,410 feet. Figure 8.17 shows the experimental data compared with the straight line values computed by using the attenuation equation derived by Lamb [6]. It can be seen that

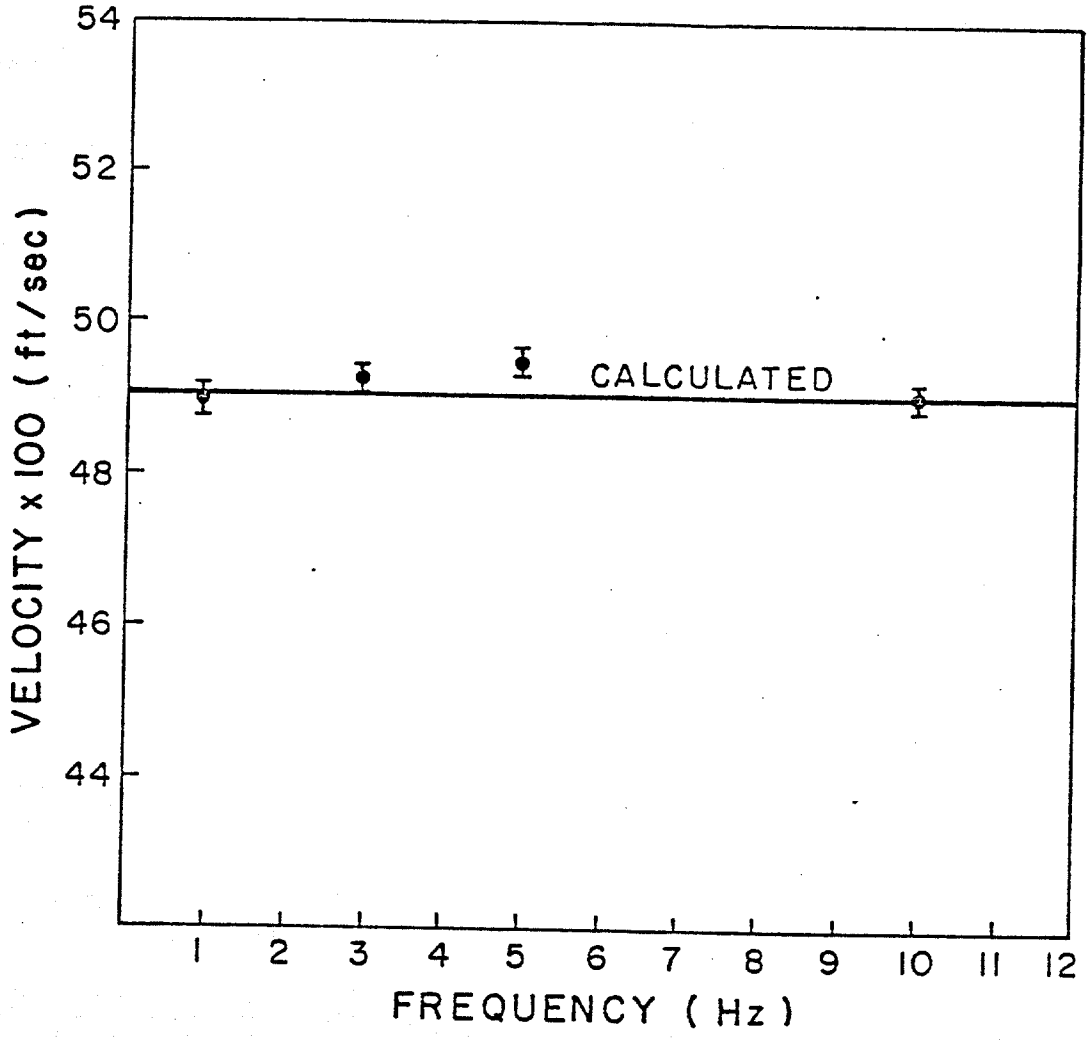

FIGURE 8.14. A Plot of the Theoretical and Experimental Velocity Measurements Conducted with Water as the Fluid Medium.

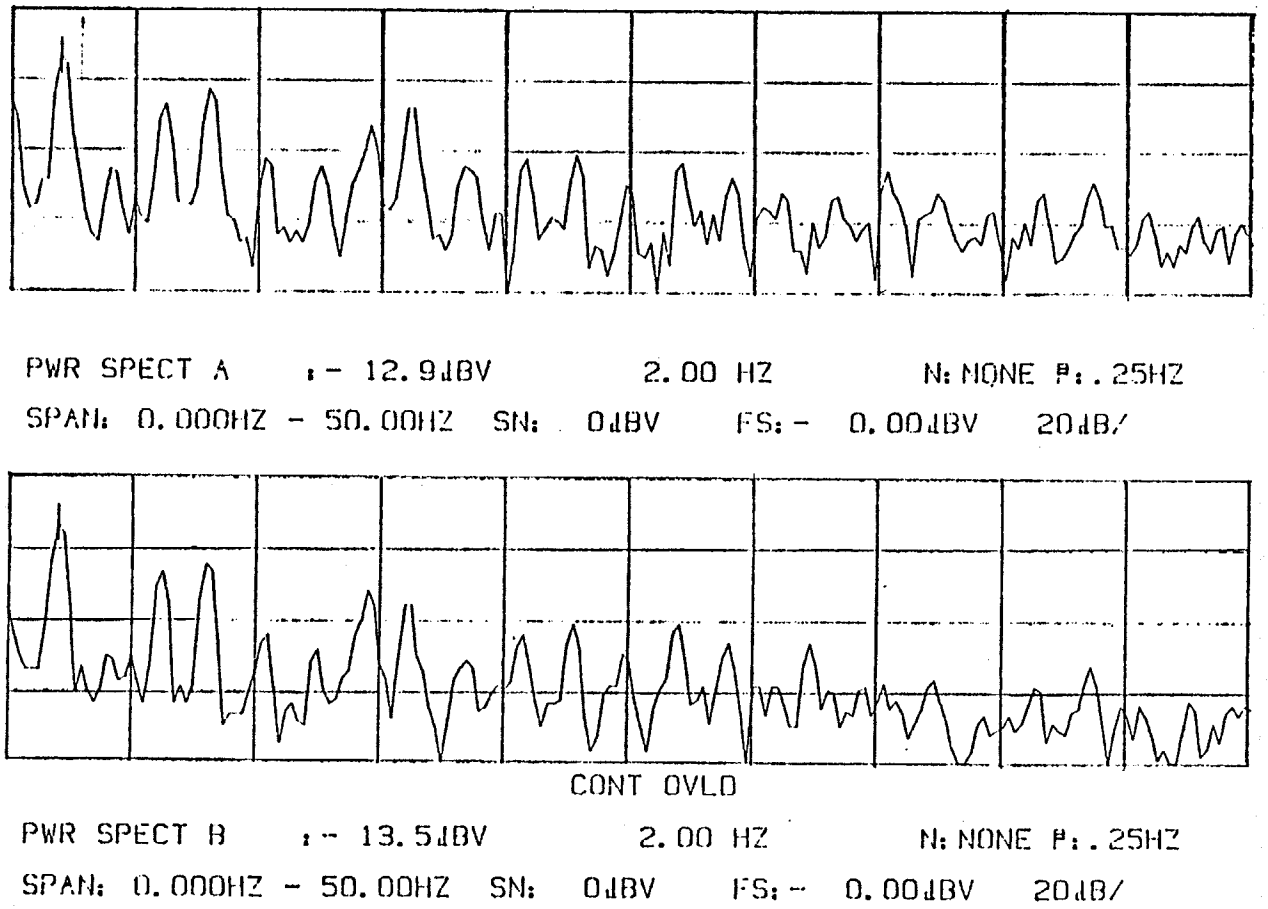

FIGURE 8.15. The Fourier Transform of the 2 Hertz Signal in Figure 8.13. Representative of the Method of Attenuation Measurements.

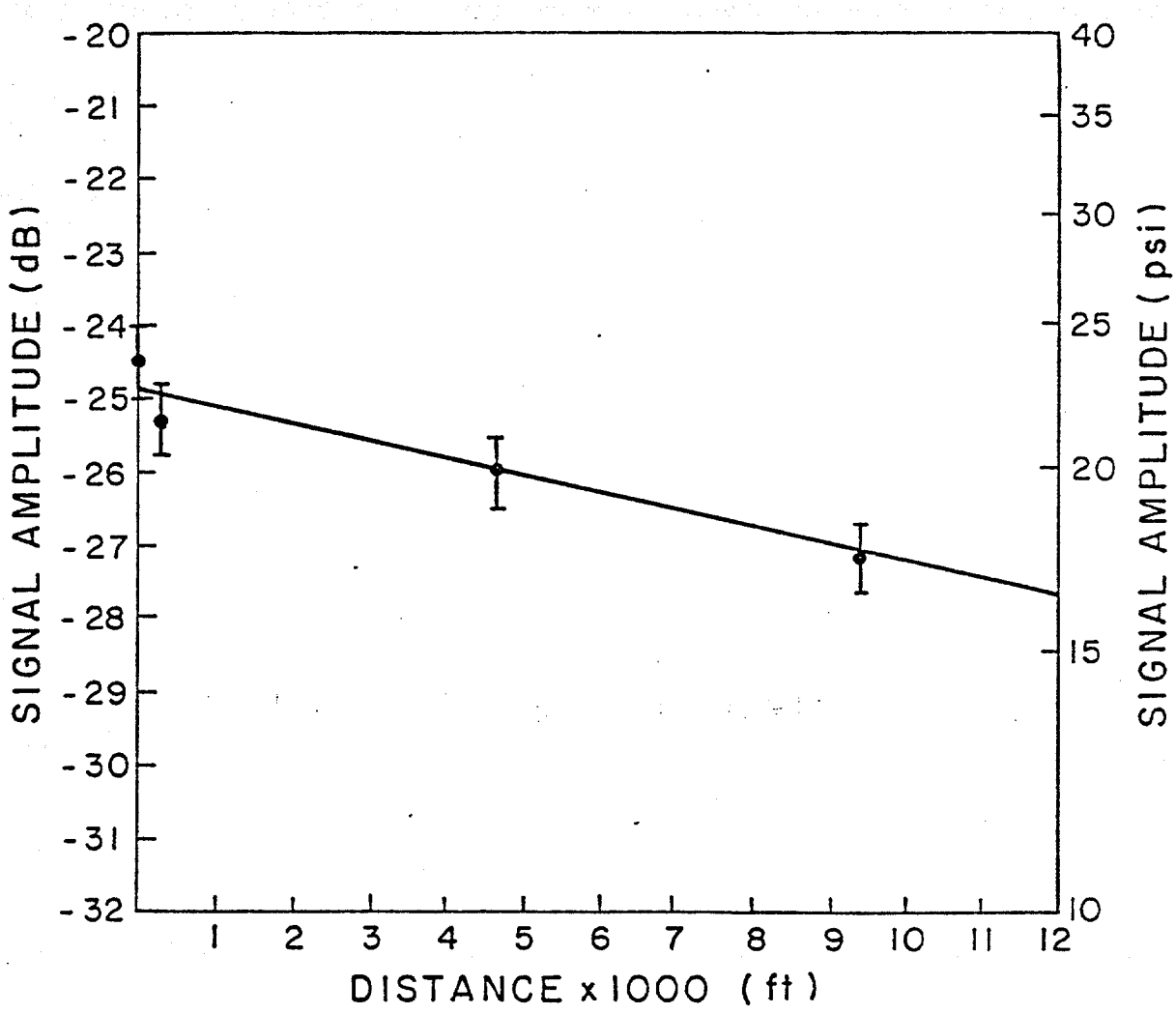

FIGURE 8.16. Plot of Signal Amplitude versus Distance of a 3 Hertz Signal in Water.

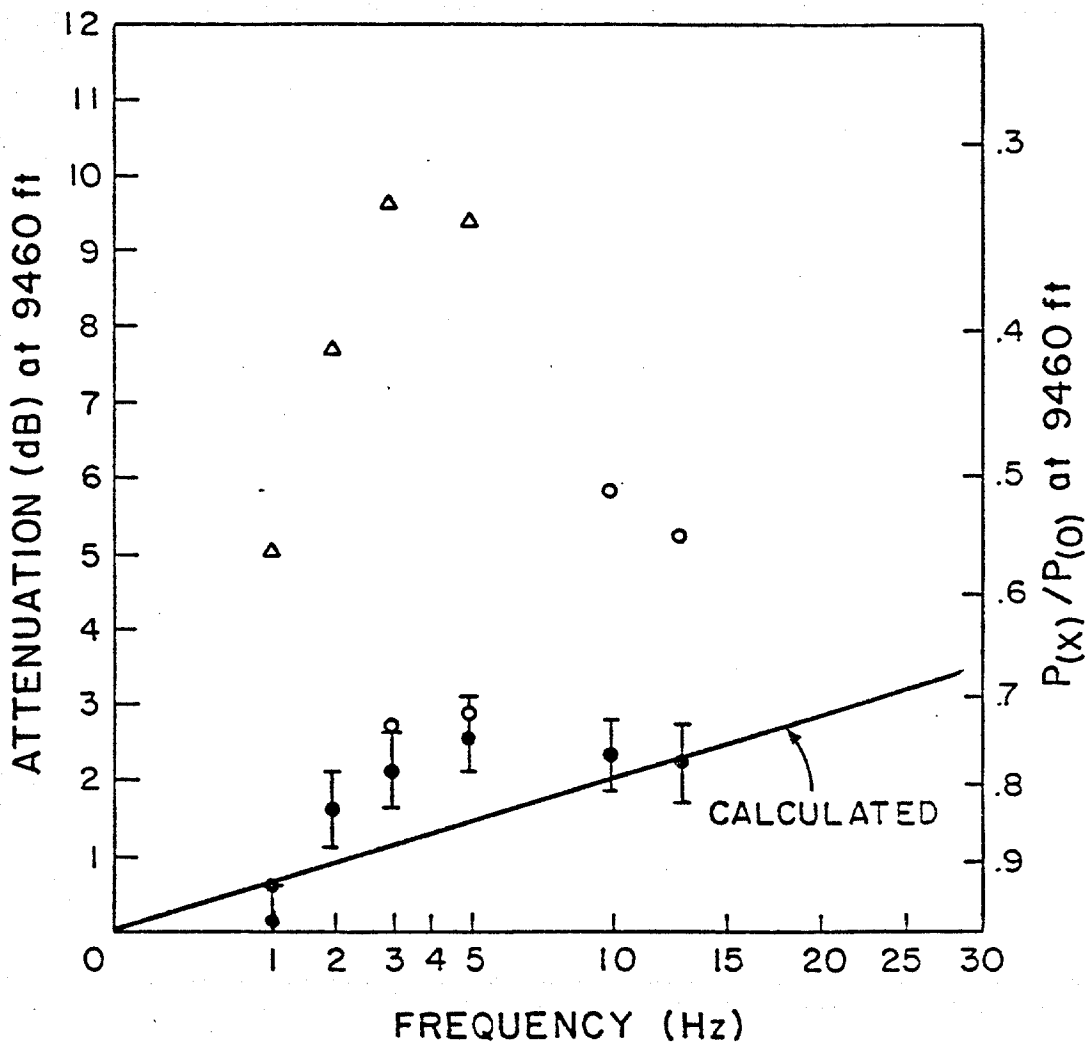

FIGURE 8.17. Graph of Resultant Attenuation Data Gathered at Various Frequencies with Water as the Fluid Medium.

that the data compares well with the theory. It can be noted that an increase in frequency does in fact cause an increase in attenuation or wave decay. Figure 8.17 also contains data of two other runs made with water. This was the result of air being trapped in the line prior to recording the data.

The air was trapped in the short section of drill pipe which rises to the surface. The impact of this small amount of air on attenuation is very large as can be seen by the upper points in figure 8.17. A centrifugal pump was used to displace the air from the flow loop. After a period of pumping the tests were repeated. The results were a reduced amount of attenuation shown by the circular points in figure 8.17 As it was clearly indicated that the problem was indeed air entrapment, a complete circulation of the flow loop was executed. In due time the tests were once again repeated and yielded the true attenuation data as shown by the shaded points of Figure 8.17.

Water-Based Mud

The second fluid used in the experiment was an unweighted water-base mud. The properties of the muds used are listed in table (3). The wave velocities in the mud were determined experimentally and theoretically in the same way as the water experiments. Wave velocity is a function of density and compressibility; therefore, a change in wave speed was expected. The compressibility of the mud cannot be found easily in correlations as in the case of water. For theoretical computations of velocity the compressibility was computed using the compressibilities of additives and their respective volumes. The measured wave speed was

around 4850-4860 feet per second. This was supported by computed velocities of 4853 feet per second (Watters) and 4852 feet per second (White). Figure 8.18 illustrates how well the theory compares with the data measured in the experiment. The fact that the viscosity varies with the mud does not affect the travel time of the pulse to any noticeable extent. This was supported by experimental results and also illustrated in figure 8.18 by plotting velocity measurements from muds #1, #2, and #3 with viscosities of 14 cp, 20 cp, and 26 cp respectively.

The attenuation of the pulse, however, was greatly affected by viscosity changes. Mud #1 was a low viscosity (14 cp) mud. A significant increase in attenuation was detected by the increase in viscosity. Figure 8.19 represents the experimental and theoretical plots of frequency versus attenuation for this mud. The experimental data corresponds very closely to the calculated response using the equation by Lamb [6]. Mud #2 which was an unweighted 20 centipoise mud was the second mud used in the experiment. Other properties were held constant as the viscosity was increased. As can be seen in figure 8.20, the increase in viscosity causes an increase in the slope of the attenuation. To provide further proof of this, the viscosity of the fluid was increased once again while holding other properties constant (mud #3, 26 cp). Figure 8.21 shows that once again there is an increase in the amount of attenuation. Throughout the course of this experiment the equations discussed have adequately described the behavior of the pulse.

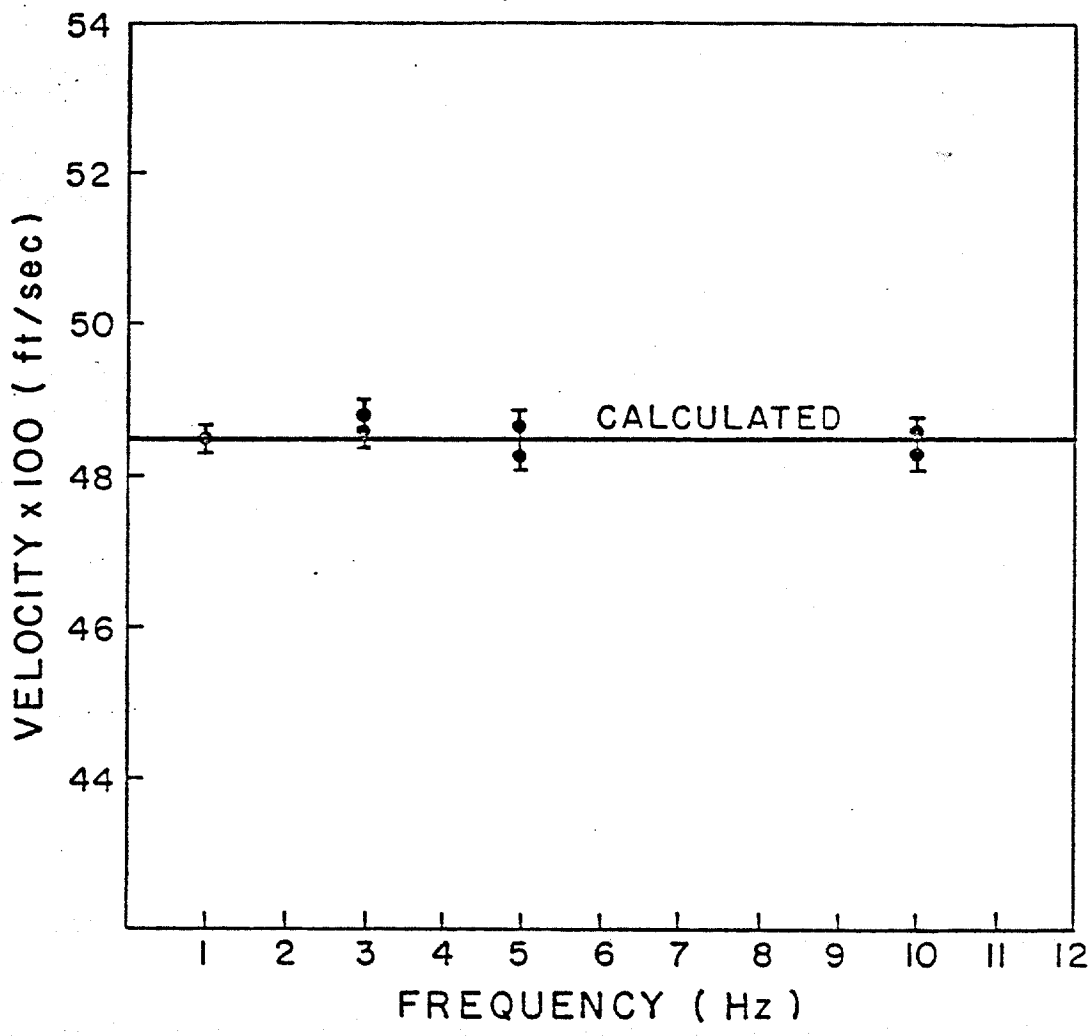

FIGURE 8.18. Theoretical and Experimental Velocity Measurements Conducted with Un-Weighted Water-Base Muds of Different Viscosities (Mud #1, #2, #3).

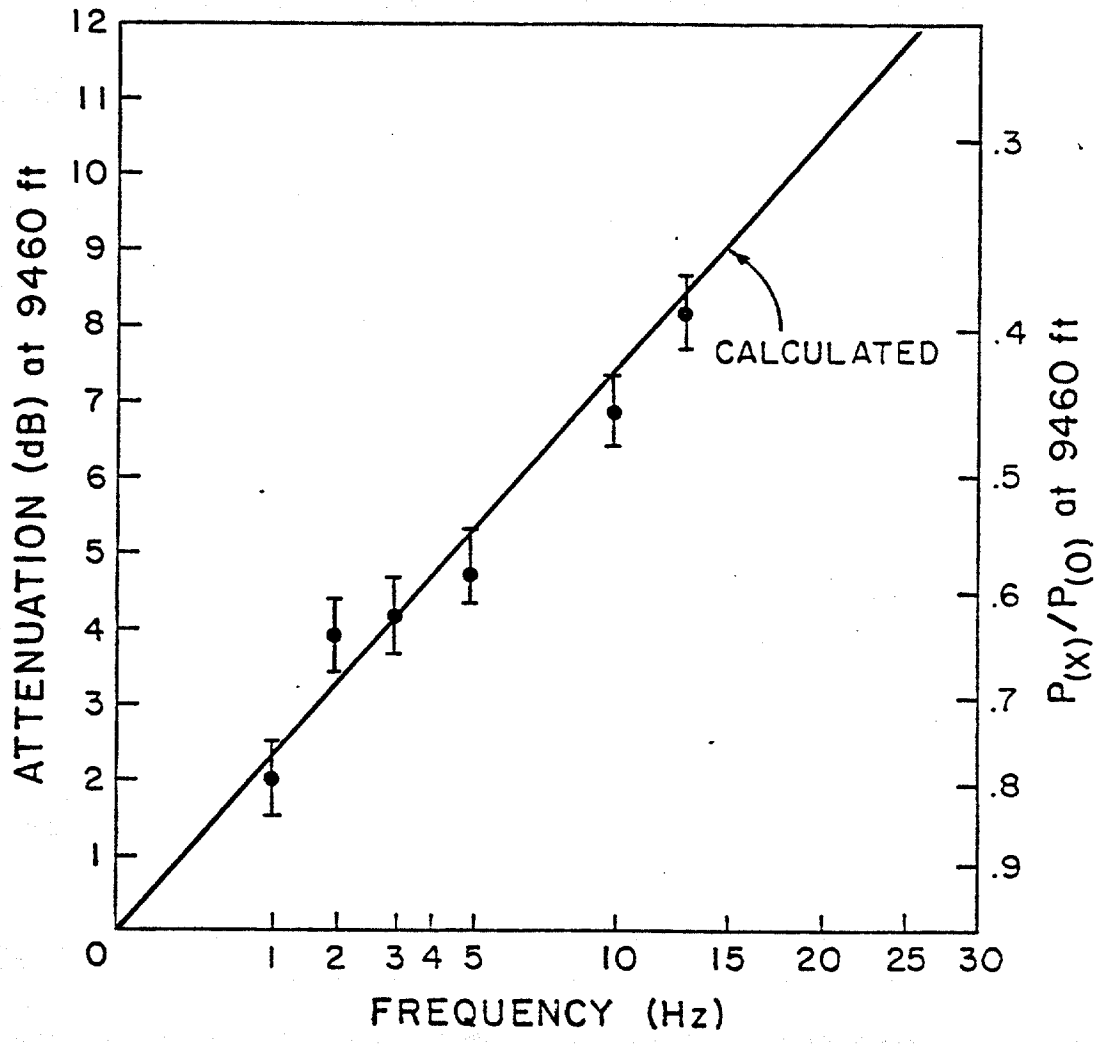

FIGURE 8.19. Graph of Attenuation Results Gathered at Various Frequencies with Mud #1 as the Fluid Medium.

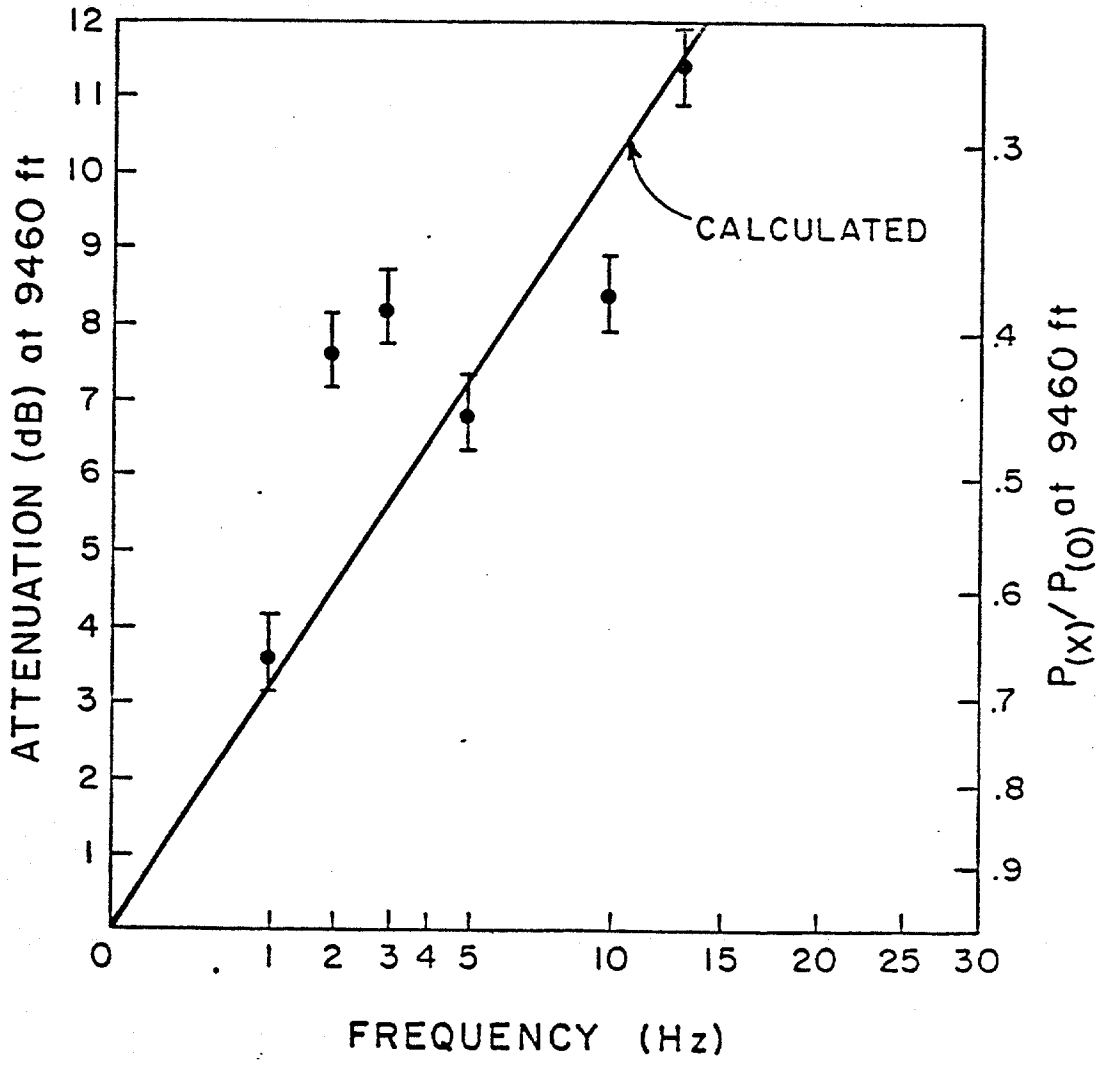

FIGURE 8.21. Graph of Attenuation Results Gathered at Various Frequencies with Mud #3 as the Fluid Medium.

Oil-Base Mud

Oil muds are much more compressible than water base muds. Thus it was desirable to test the pulser in an oil base system. The mud used consisted of a 84/16 oil-water ratio. It also was an unweighted mud of 8.5 pounds per gallon. Other properties of the oil-base mud are stated in table 8.3 under mud #4. Frequencies as high as 25 hertz were reached and analyzed. Figure 8.22 is an example of a 13 hertz signal generated by the pulser.

The velocity measurements were measured using transparent overlays as in the previous cases. The velocity was experimentally measured to be 4545-4553 feet per second. This again compared well with the calculated data as shown in figure 8.23. The calculated velocity was 4550 feet per second using the equation by Watters [3]. The computations using the equation by White [4] were again very close to that of Watters with 4548 feet per second. The velocity equations appear to be a valid means of evaluating pressure wave velocities in drill pipe containing a fluid of known density and compressibility.

The attenuation as before was computed for each frequency. Figure 8.24 also shows that the pulse still maintains an exponential decline as it travels over a distance. The amount of attenuation was measured and plotted against frequency in figure 8.25. Although the attenuation was much greater when the oil-base mud was the fluid medium, the experimental data remained very close to the calculated trend using the equations by Lamb [6]. The experiment was concluded with the usual calibration check following a run. The equipment checked out very well and supported the accuracy of the data collected.

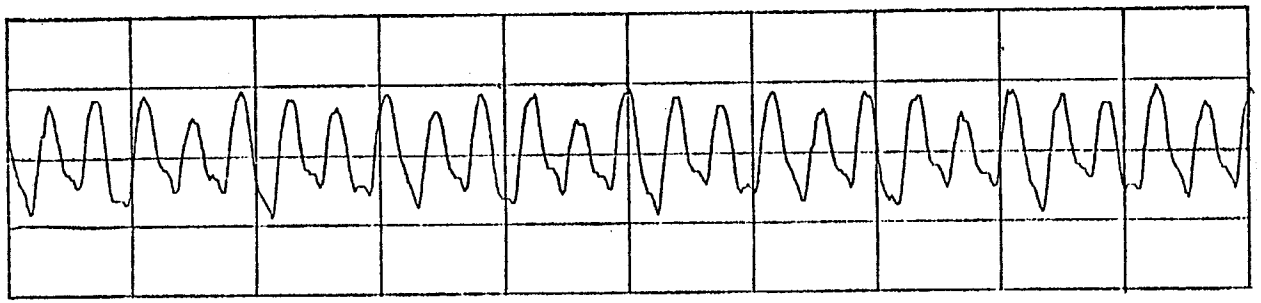

TIME A: 2.1E-01V 1.99SEC 200.00mSEC/
SPAN: 0.000HZ -100.00HZ SN: 3.6-01V FS: 15.0-01V 2.5-01V/

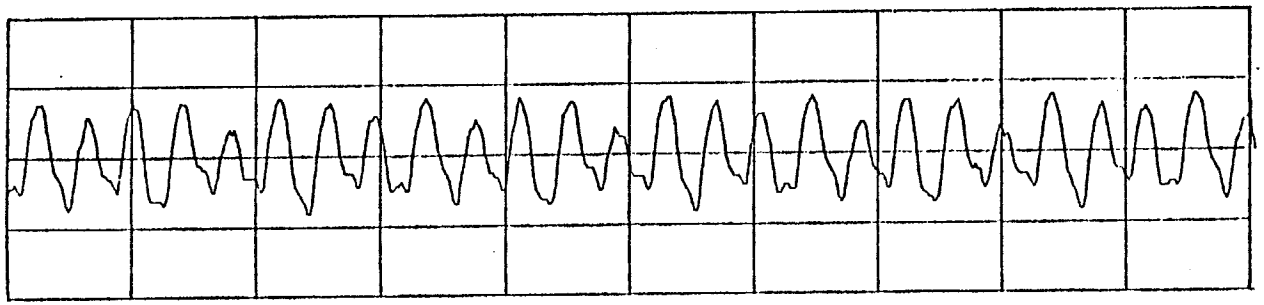

TIME B: 9.4E-02V 1.99SEC 200.00mSEC/
SPAN: 0.000HZ -100.00HZ SN: 3.6-01V FS: 15.0-01V 2.5-01V/

FIGURE 8.22. A 13 Hertz Pulse Generated by the Fluidic Pulser.

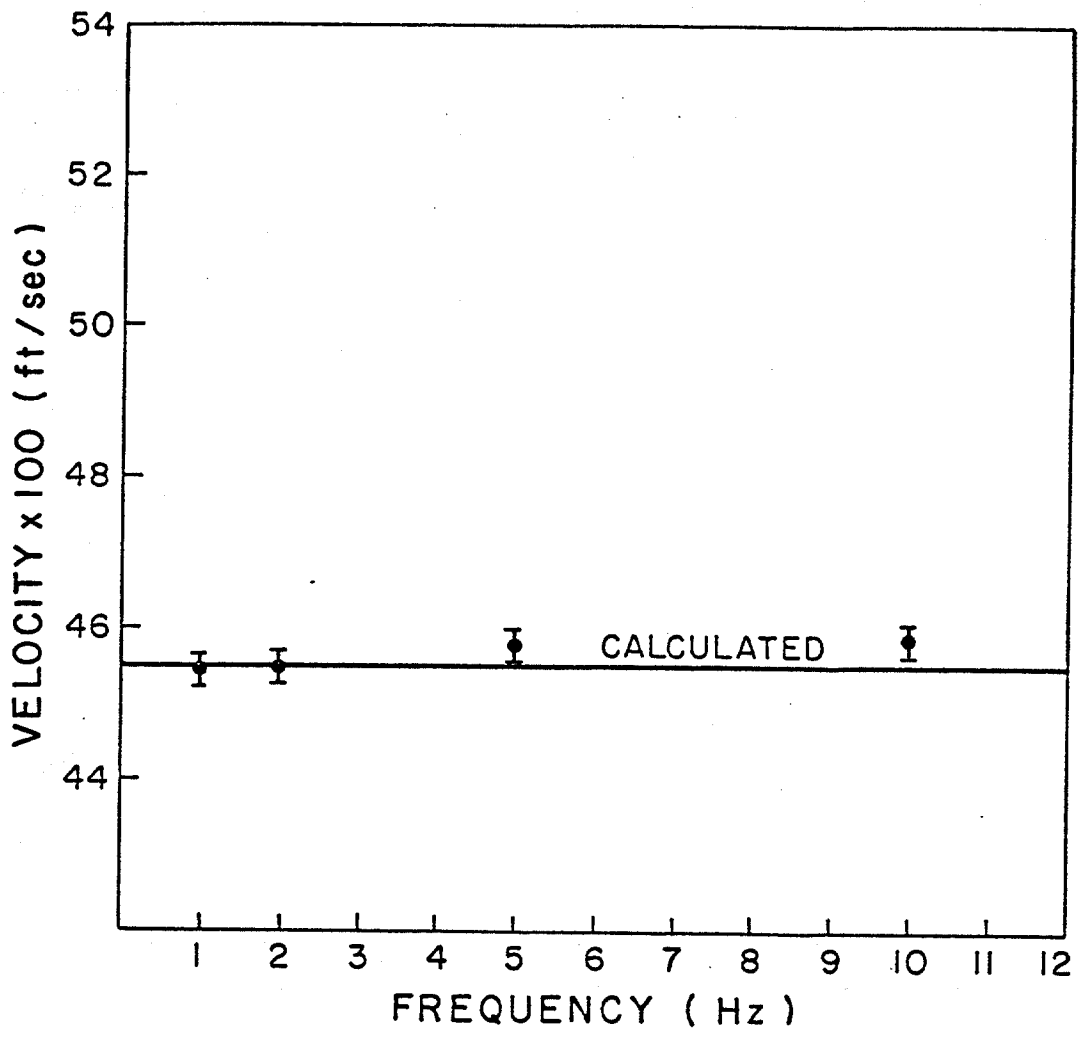

FIGURE 8.23. Theoretical and Experimental Velocity Measurements Conducted with an Un-Weighted Oil-Base Mud (Mud #4).

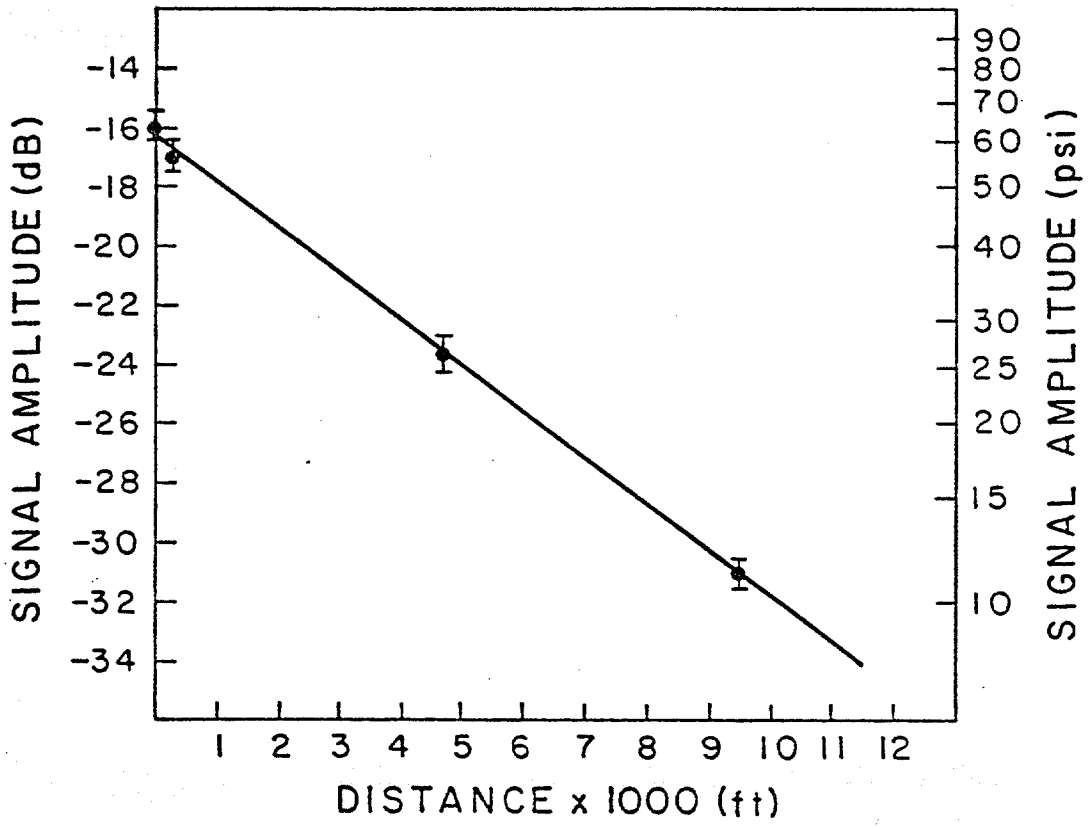

FIGURE 8.24. Plot of Signal Amplitude Versus Distance for a 13 Hertz Signal with Oil-Base Mud (Mud #4) as the Fluid Medium.

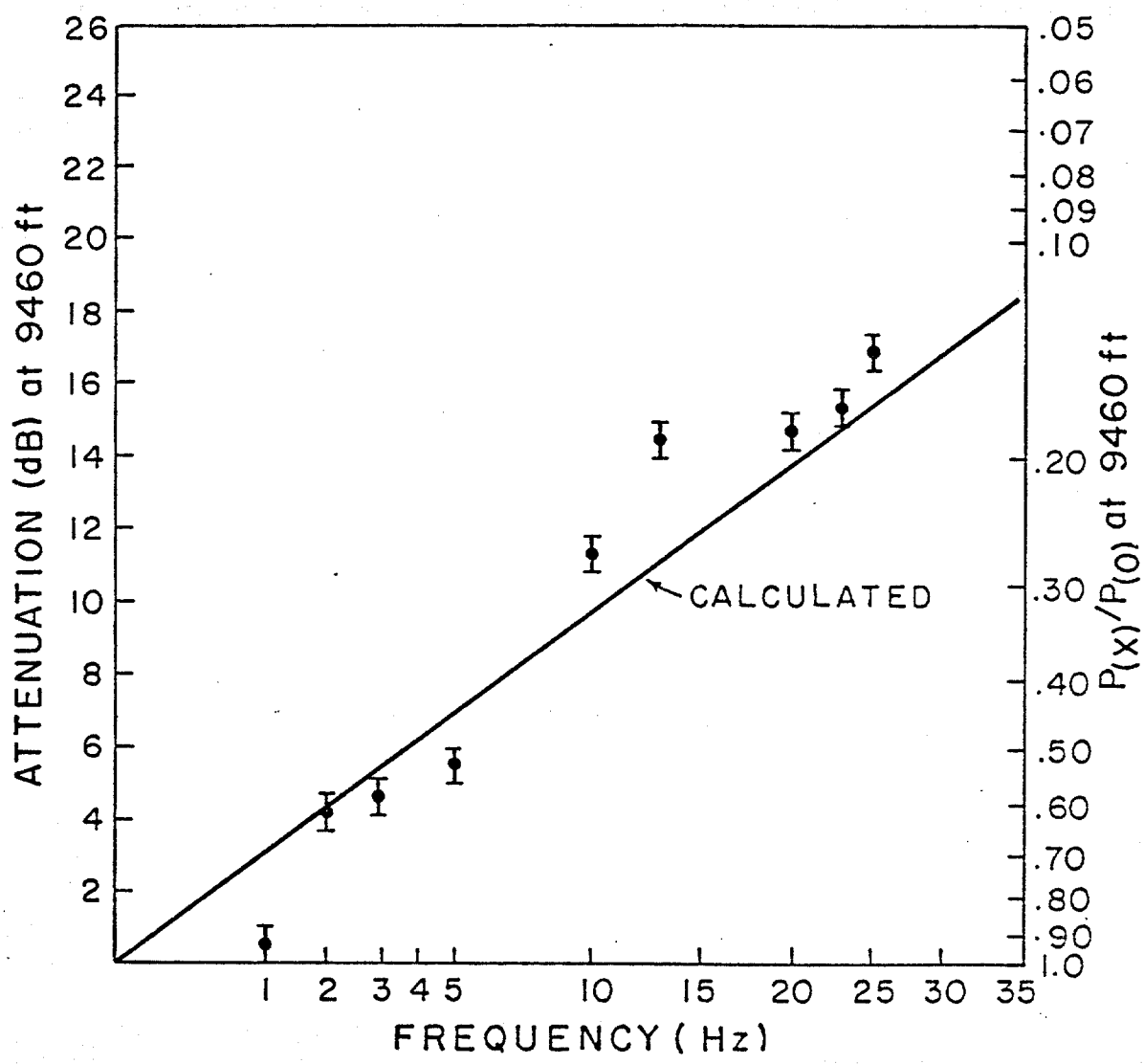

FIGURE 8.25. Graph of Attenuation Results Gathered at Various Frequencies with Mud #4 as the Fluid Medium.

Discussion

The data collected during the course of the experiment appears to be of good quality. The velocity measurements correlate well with the theory of White and Watters. The error bars were included in the plots of the experimental data to show the range of variation seen in the measurement. The method of velocity measurement was repeated using the same data. The difference between the two measurements of velocity was used as an indication of error. The time differences measured from one transducer to another were less than a second and measured in milliseconds. The influence of 10 to 20 milliseconds over a few thousand feet reflects the indicated error. The difference of the measured and calculated velocities amounted to less than 1 percent. With this accuracy one can safely use the theory derived by White and Watters to predict pressure wave velocities in drill pipe.

The attenuation data, however, followed the trend of the theory by Lamb, but showed slight scattering as the viscosity was increased. This could possibly be a result of one or a combination of pump noise effects and the fact that the equations were derived for a Newtonian fluid. As the plastic viscosity is increased, the fluid would tend to go further from a Newtonian towards a Bingham Plastic state.

CONCLUSIONS AND RECOMMENDATIONS

1) The velocity of a pressure pulse in drill pipe has been studied and found to be dependent on the density and compressibility of the fluid medium.

2) The equations by White [3] and Watters [4] have been proven to predict the pressure wave velocities very accurately. Properties that must be known to use these equations are:

Pipe - Young's Modulus, Outside diameter, Inside diameter, and Poisson's ratio.

Fluid - Compressibility and density.

3) Pressure wave attenuation was analyzed and indeed found to be of an exponential decay over distance.

4) Attenuation of a pulse was also found to be very sensitive to viscosity, compressibility, and frequency at which the pulse was transmitted. The equations by Lamb [6] on this subject were supported by experimental data to be useful in estimating the magnitude of a pulse after having traveled a distance from its point of origination.

5) It was also verified that very small volumes of gas could have a detrimental effect on the attenuation of a wave. This could come into effect when air is trapped in the drillstring while making connections during standard drilling operations. Directional data is often transmitted to the surface following a connection.

6) It has been proven that signals can be detected at higher frequencies than in present use. It would be of further interest to determine if it is possible to encode data at the higher frequencies through the use of the popular binary coding system.

REFERENCES

1. Andrew Roberts, Robert Newton, Frederick Stone: "MWD Field Use and Results in the Gulf of Mexico," Teleco Oilfield Services Ltd., SPE 11226 57th Annual Fall Technical Conference, September, 1982.

2. Martin Gearhart, Kelly A. Siemer, Orien Monroe Knight: "LMud Pulse MWD (Measurement-While-Drilling) Systems Report," Gearhard Industries, SPE 10053 Annual Fall Technical Conference, October, 1981.

3. Gary Z. Watters, Modern Analysis and Control of Unsteady Flow in Pipelines, Ann Arbor Science, Ann Arbor, Michigan, pp 29-39, 1980.

4. James Edward White, Seismic Waves: Radiation, Transmission and Attenuation, Marathon Oil Co., McGraw Hill, pp 148-158, 1965.

5. E. L. Holmboe, W. T.. Rouleau, "The Effect of Viscous Shear on Transients in Liquid Lines," Carnegie Institute of Technology, Paper No. 66-WA/FE-11, 1966.

6. Horace Lamb, Hydrodynamics, Dover, New York, NY, 1945.

7. Aurthor T. Ippen, Marks Mechanical Engineers' Handbook, McGraw Hill, New York, 1951.

8. "Halliburton Cementing Tables", Halliburton Services, 1981.

9. "Le Forage aujourd'hui" (Drilling Today) Vol. 1, Technip Editions, Paris, 1970.

10. B. J. Patton, W. Gravely, J. K. Godbey, J. H. Sexton, D. E. Hawk, V. R. Slover, J. N. Harrell, "Development and Successful Testing of a Continuous-wave Logging-While-Drilling Telemetry System" Mobil

Research and Development Corp., Journal of Petroleum Technology, pp. 1215-1221, October, 1977.

11. "Quartz Sensors," PCB Piezotronics, Inc., 1984.

12. Allen B. Holmes, "The Fluidic Approach to Mud Pulser Valve Design for Measurement-While-Drilling Systems," HDL Technical Report, U.S. Army, October 4, 1984.

13. Allen B. Holmes, "Fluidic Mud Pulse Telemetry," Harry Diamond Laboratories, U.S. Army, 1983.

14. "Operating Manual Model 5820A Cross Channel Spectrum Analyses," Wavetek Rockland, Inc., 2nd Edition, 1983.

15. Paul A. Tipler, "Harmonic Analysis and Synthesis," Tipler Physics, Worth Publishers, Inc., New York, pp. 552-56, 1976.

16. Erwin Kreyszig, "Fourier Series and Integrals," Advanced Engineering Mathematics, John Wiley & Sons, New York, Fourth Edition, pp. 468-508, 1979.

17. Milton B. Dobrin, "Enhancement of Seismic Reflection Data in Processing Centers," Introduction to Geophysical Prospecting, McGraw Hill, Third Edition, pp. 157-165, 1976.

18. J. W. Codez, P. A. W. Lewis, P. D. Welch, "The Fast Fourier Transform Algorithm: Programming Considerations in the Calculation of Sine, Cosine, and Laplace Transforms," IBM Corp., August 22, 1969.

APPENDIX A

EXPERIMENTAL DATA FOR DIVERTER EROSION STUDY

The flow loop described in the chapter entitled EXPERIMENTAL APPARATUS was used to test 4 different cast fittings. The short radius ell was tested first, followed by the plugged tee, then the long radius ell, and, finally, the Vortice-Ell. This Appendix lists the data recorded while testing each fitting, including the dimensions of each fitting, their weights before and after testing, their pipe wall thicknesses before and after testing, the locations of the thickness measurement points, and the flow loop data. Flow loop data includes the following: flowline pressure, differential pressure across the fitting, temperatures upstream and downstream of the fitting, pump flowrate, sand content of the mud/sand slurry, sand sieve analysis, and mud density, viscosity, and yield point. The results of the welded fitting runs are presented at the end of this Appendix. The experimental data for these fittings are not provided since it was often incomplete or not very representative.

DATA COMMON TO ALL TEST RUNS

Drilling mud composition - mixture of Magobar bentonite clay (Magogel), caustic soda, and fresh water.

TABLE A1

NUMBER TWO BLASTING SAND INITIAL GRAIN SIZE DISTRIBUTION
SAMPLE NUMBER ONE

US sieve number	sieve opening (mm/in)	weight retained (gm)	weight %	cumulative weight %
10	2.000/0.0787	19.60	2.52	2.52
16	1.180/0.0469	119.46	15.37	17.89
30	0.590/0.0232	237.04	30.51	48.40
40	0.420/0.0165	200.01	25.74	74.14
50	0.297/0.0116	165.92	21.35	95.49
80	0.177/0.0070	34.35	4.42	99.91
100	0.149/0.0059	0.30	0.04	99.95
200	0.074/0.0029	0.26	0.03	99.98
tray	-	0.05	0.01	99.99
		766.99	100.00	

TABLE A2

NUMBER TWO BLASTING SAND INITIAL GRAIN SIZE DISTRIBUTION
SAMPLE NUMBER TWO

US sieve number	sieve opening (mm/in)	weight retained (gm)	weight %	cumulative weight %
10	2.000/0.0787	19.80	2.82	2.82
16	1.180/0.0469	96.28	13.73	16.55
30	0.590/0.0232	200.51	28.60	45.15
40	0.420/0.0165	185.37	26.44	71.59
50	0.297/0.0116	146.17	20.85	92.43
80	0.177/0.0070	52.30	7.46	99.89
100	0.149/0.0059	0.58	0.08	99.97
200	0.074/0.0029	0.13	0.02	99.99
tray	-	0.05	0.01	100.00
		701.19	100.00	

Figure A1 is a plot of the initial grain size distribution.

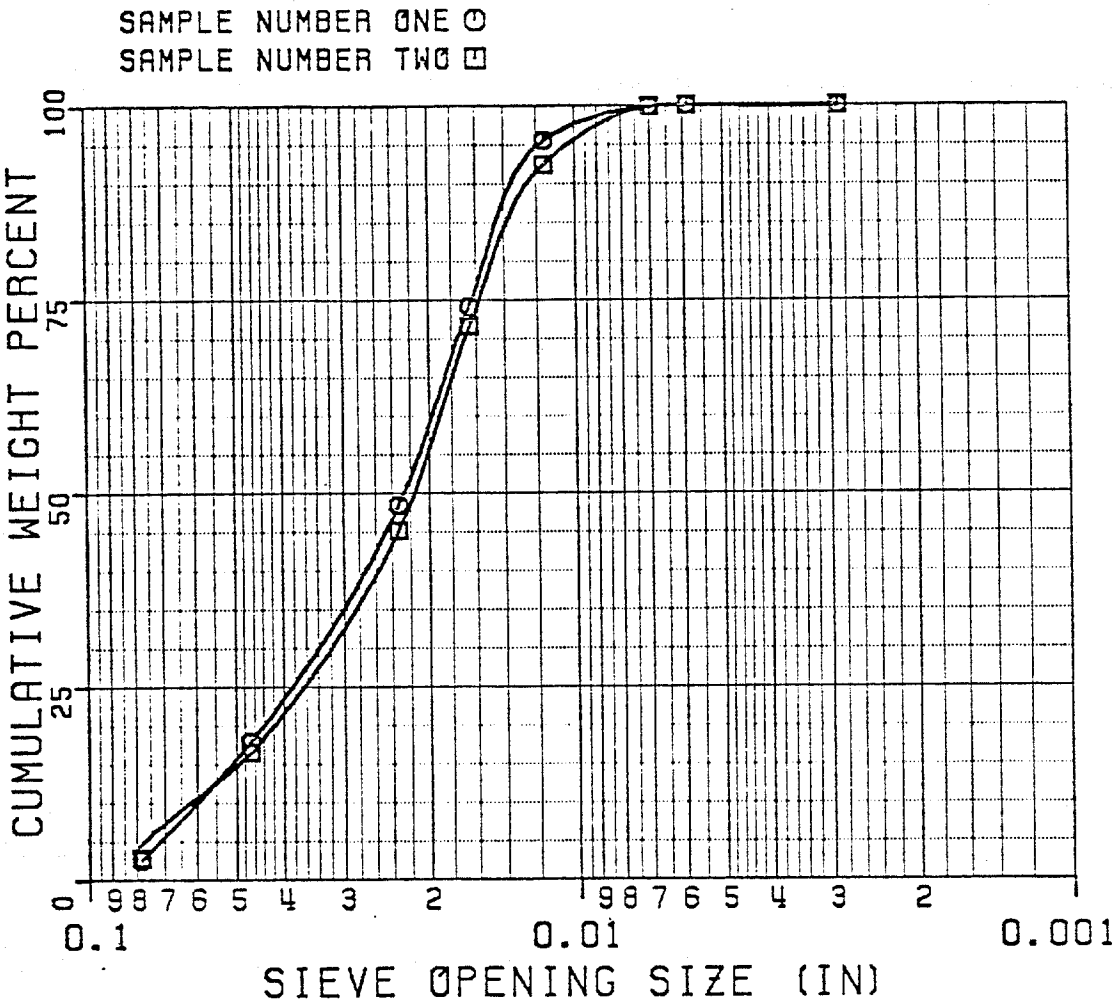

Figure A1. Grain size distribution of the initial number 2 blasting sand.

EXPERIMENTAL DATA

SHORT RADIUS ELL

radius of curvature = 5.73 inches

radius/diameter = 2.86

total run time = 90.0 hours

initial fitting weight = 26.10 pounds

final fitting weight = 25.46 pounds

total weight loss = 0.64 pounds

weight loss/exposed surface area = 0.0136 psi

$$\text{percent change in weight} = \frac{26.10 - 25.46}{26.10} \times 100 = 2.45\%$$

initial mud properties:

density = 8.9 pounds/gallon

absolute viscosity = 6 centipoise

yield point = 3 pounds/100 square feet

Figure A2 is a plot of the sand grain size distribution after 90 hours of run time.

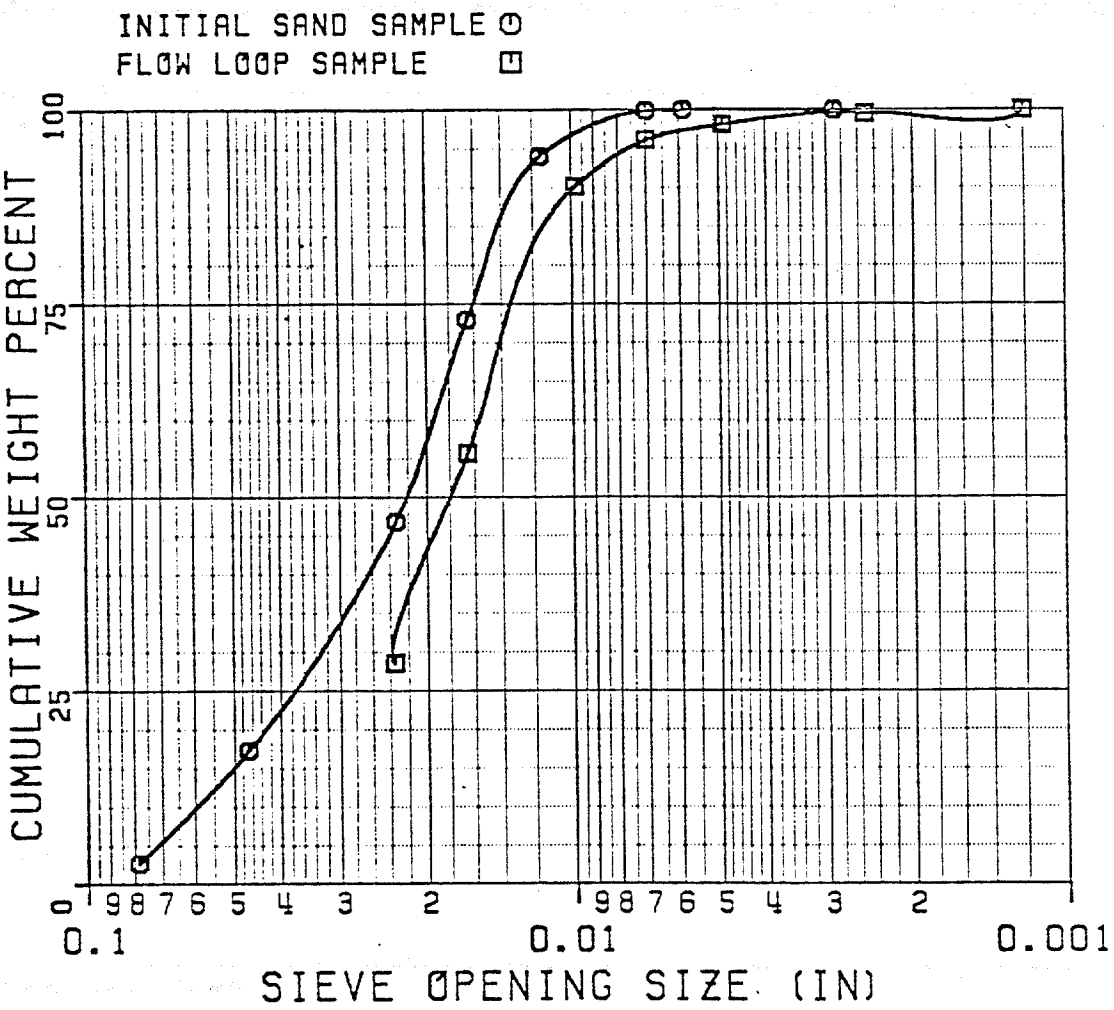

Figure A2. Grain size distribution of the sand after 90 hours of run time (all samples combined).

TABLE A3

FLOW LOOP DATA FOR THE
SHORT RADIUS ELL

elapsed time (hr)	flowline pressure (psig)	differential pressure (psig)	flowrate (bbl/min)	sand content (%)
0.0	58.5	3.11	8.6	8
17.5	55.0	2.57	8.6	6
41.0	54.9	2.50	9.1	6
65.5	55.3	2.35	-	8
90.0	54.9	2.40	8.9	2
averages	55.7	2.59	8.8	6

average slurry velocity (calculated) = 37.7 feet/second

elapsed time (hr)	upstream temperature (F)	downstream temperature (F)	average temperature (F)
0.0	108.3	107.4	107.8
17.5	172.0	170.7	171.3
41.0	175.7	174.4	175.0
65.5	181.7	180.3	181.0
90.0	160.3	158.6	159.4
averages	159.6	158.3	158.9

TABLE A4

THICKNESS MEASUREMENT LOCATIONS (INCHES)
SHORT RADIUS ELL

OUTSIDE RADIUS (A TO B)

measure point number	1	2	3	4	5
distance from flange face A	1/4	1	1 7/8	2 7/8	3 3/4

measure point number	6	7	8	9	10
distance from flange face A	4 7/8	5 7/8	6 7/8	7 7/8	8 7/8

INSIDE RADIUS (A TO B)

measure point number	1	2	3	4
distance from flange face A	1/2	1 1/2	2 3/4	3 3/4

TABLE A5

ULTRASONIC THICKNESS MEASUREMENT DATA
SHORT RADIUS ELL

BEFORE TESTING/AFTER TESTING (THOUSANDTHS OF AN INCH)

OUTSIDE RADIUS (A TO B)

point number	1	2	3	4	5
top row	620/600	620/600	620/600	620/620	590/580
middle row	630/630	625/620	605/600	590/580	580/555
bottom row	660/645	640/640	620/605	585/570	585/560

point number	6	7	8	9	10
top row	585/580	600/580	605/570	580/545	570/545
middle row	590/560	600/560	605/570	590/545	600/560
bottom row	600/565	620/580	600/570	585/540	580/540

INSIDE RADIUS (A TO B)

point number	1	2	3	4
middle row	585/565	600/570	640/620	600/580

EXPERIMENTAL DATA

PLUGGED TEE

radius of curvature = N/A

radius/diameter = N/A

total run time = 90.0 hours

initial fitting weight = 42.86 pounds

final fitting weight = 41.29 pounds

total weight loss = 1.57 pounds

weight loss/exposed surface area = 0.0222 psi

$$\text{percent change in weight} = \frac{42.86 - 41.29}{42.86} \times 100 = 3.66\%$$

initial mud properties:

density = 9.4 pounds/gallon

absolute viscosity = 2 centipoise

gel strength = 5 pounds/100 square feet

Figure A3 is a plot of the sand grain size distribution after 90 hours of run time.

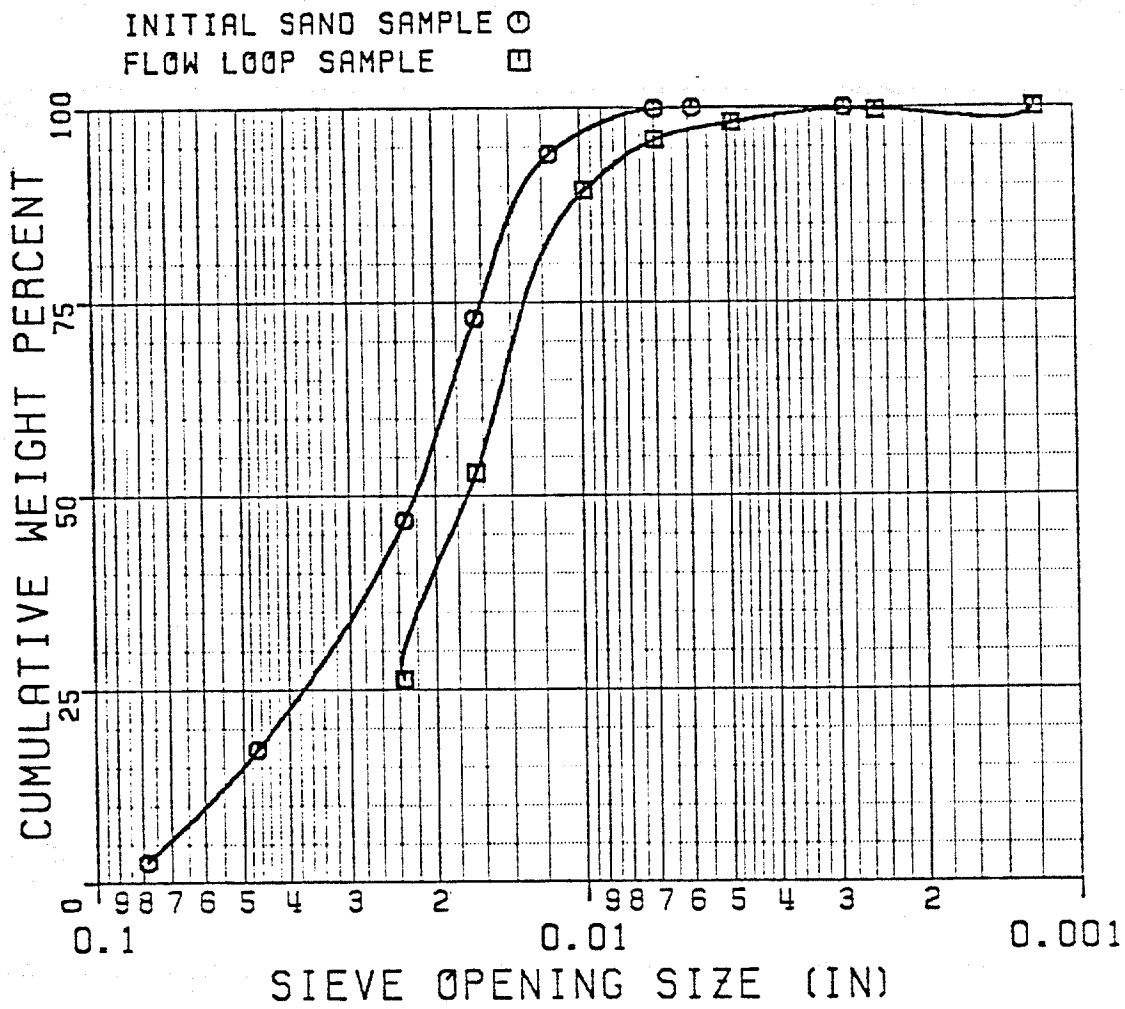

Figure A3. Grain size distribution of the sand after 90 hours of run time (all samples combined).

TABLE A6

FLOW LOOP DATA FOR THE PLUGGED TEE

elapsed time (hr)	flowline pressure (psig)	differential pressure (psig)	flowrate (bbl/min)	sand content (%)
0.0	55.2	6.80	8.9	18
22.5	51.1	6.33	9.8	16
47.0	52.0	7.26	-	1
66.0	51.7	7.39	10.3	3
73.5	52.7	7.34	10.0	3
90.0	50.2	7.34	-	5
averages	51.5	6.78	9.8	8

average slurry velocity (calculated) = 41.9 feet/second

elapsed time (hr)	upstream temperature (F)	downstream temperature (F)	average temperature (F)
0.0	133.8	132.4	133.1
22.5	155.6	153.8	154.7
47.0	95.0	93.5	94.3
66.0	152.8	151.4	152.1
73.5	154.9	153.2	154.0
90.0	201.8	199.7	200.8
averages	149.0	147.3	148.2

TABLE A7

THICKNESS MEASUREMENT LOCATIONS (INCHES)
PLUGGED TEE

OUTSIDE RADIUS (A TO B)

measure point number	1	2	3	4	5
distance from flange face A	1/4	1	2	3	4

measure point number	6	7	8	9
distance from flange face A	5	6	7	8

INSIDE RADIUS (A TO C)

measure point number	1	2	3	4
distance from flange face A	3/8	1 1/2	3 1/4	4

INSIDE RADIUS (B TO C)

measure point number	1	2	3	4
distance from flange face B	3/4	2	3 1/4	4 1/4

TABLE A8

ULTRASONIC THICKNESS MEASUREMENT DATA
PLUGGED TEE

BEFORE TESTING/AFTER TESTING (THOUSANDTHS OF AN INCH)

OUTSIDE (A TO B)

point number	1	2	3	4	5
top row	665/620	640/625	640/620	645/640	680/625
middle row	640/600	600/600	590/580	600/580	600/585
bottom row	580/560	580/565	580/580	585/565	600/580

point number	6	7	8	9
top row	685/650	645/630	640/620	640/620
middle row	605/605	685/680	585/570	620/600
bottom row	585/570	580/560	580/560	580/560

INSIDE RADIUS (A TO C)

point number	1	2	3	4
top row	600/570	640/580	620/520	600/440
middle row	620/585	620/620	620/420	605/435
bottom row	585/580	600/600	695/385	660/420

INSIDE RADIUS (B TO C)

point number	1	2	3	4
top row	620/570	640/660	700/480	620/495
middle row	650/600	610/600	680/460	640/490
bottom row	600/600	610/600	640/400	600/495

EXPERIMENTAL DATA

LONG RADIUS ELL

radius of curvature = 7.00 inches

radius/ diameter = 3.50

total run time = 90.0 hours

initial fitting weight = 22.59 pounds

final fitting weight = 21.13 pounds

total weight loss = 1.46 pounds

weight loss/exposed surface area = 0.0258 psi

$$\text{percent change in weight} = \frac{22.59 - 21.13}{22.59} \times 100 = 6.46\%$$

initial mud properties:

density = 9.0 pounds/gallon

absolute viscosity = 5 centipoise

yield point = 4 pounds/100 square feet

Figure A4 is a plot of the sand grain size distribution after 90 hours of run time.

TABLE A9

FLOW LOOP DATA FOR THE
LONG RADIUS ELL

elapsed time (hr)	flowline pressure (psig)	differential pressure (psig)	flowrate (bbl/min)	sand content (%)
0.0	46.0	1.27	11.2	3
6.0	43.9	1.18	-	5
30.0	40.3	1.13	11.4	5
39.5	42.2	1.13	-	-
64.0	42.8	1.14	11.1	2
90.0	43.5	1.18	10.9	1
averages	43.1	1.17	11.2	3

average slurry velocity (calculated) = 47.8 feet/second

elapsed time (hr)	upstream temperature (F)	downstream temperature (F)	average temperature (F)
0.0	107.9	106.4	107.2
6.0	171.3	170.3	170.8
30.0	180.7	179.6	180.2
39.5	122.7	121.1	121.9
64.0	116.5	114.1	115.3
90.0	207.1	206.2	206.6
averages	151.0	149.6	150.3

TABLE A10

THICKNESS MEASUREMENT LOCATIONS (INCHES)
LONG RADIUS ELL

OUTSIDE RADIUS (A TO B)

measure point number	1	2	3	4
distance from flange face A	1/4	7/8	1 7/8	2 7/8

measure point number	5	6	7	8
distance from flange face A	3 7/8	4 7/8	5 3/8	6 7/8

measure point number	9	10	11	12
distance from flange face A	7 7/8	8 7/8	9 7/8	10 1/2

INSIDE RADIUS (A TO B)

measure point number	1	2	3
distance from flange face A	3/4	1 3/4	2 3/4

measure point number	4	5	6
distance from flange face A	3 3/4	4 3/4	5 5/8

TABLE A11

ULTRASONIC THICKNESS MEASUREMENT DATA
LONG RADIUS ELL

BEFORE TESTING/AFTER TESTING (THOUSANDTHS OF AN INCH)

OUTSIDE RADIUS (A TO B)

point number	1	2	3	4
top row	460/420	450/405	440/380	435/340
middle row	480/440	460/400	460/360	445/320
bottom row	480/460	480/420	480/385	480/325

point number	5	6	7	8
top row	430/305	445/300	440/270	460/260
middle row	445/300	440/250	420/220	440/205
bottom row	455/325	440/260	440/245	425/220

point number	9	10	11	12
top row	480/245	485/305	500/240	490/240
middle row	440/160	440/210	440/160	480/140
bottom row	420/180	420/180	435/150	430/120

TABLE A11-CONTINUED

INSIDE RADIUS (A TO B)

point number	1	2	3
top row	545/540	585/560	565/550
middle row	540/505	530/500	545/525
bottom row	490/480	520/520	540/500

point number	4	5	6
top row	565/540	540/505	500/480
middle row	565/540	540/505	500/480
bottom row	560/500	560/535	520/500

EXPERIMENTAL DATA

VORTICE-ELL

radius of curvature = 4.66 inches

radius/diameter = 2.33

total run time = 90.0 hours

initial fitting weight = 61.85 pounds

final fitting weight = 59.96 pounds

total weight loss = 1.89 pounds

weight loss/exposed surface area = 0.0222 psi

$$\text{percent change in weight} = \frac{61.85 - 59.96}{61.85} \times 100 = 3.06\%$$

initial mud properties:

density = 10.0 pounds/gallon

absolute viscosity = 6 centipoise

yield point = 3 pounds/100 square feet

Figure A4 is a plot of the sand grain size distribution after 90 hours of run time.

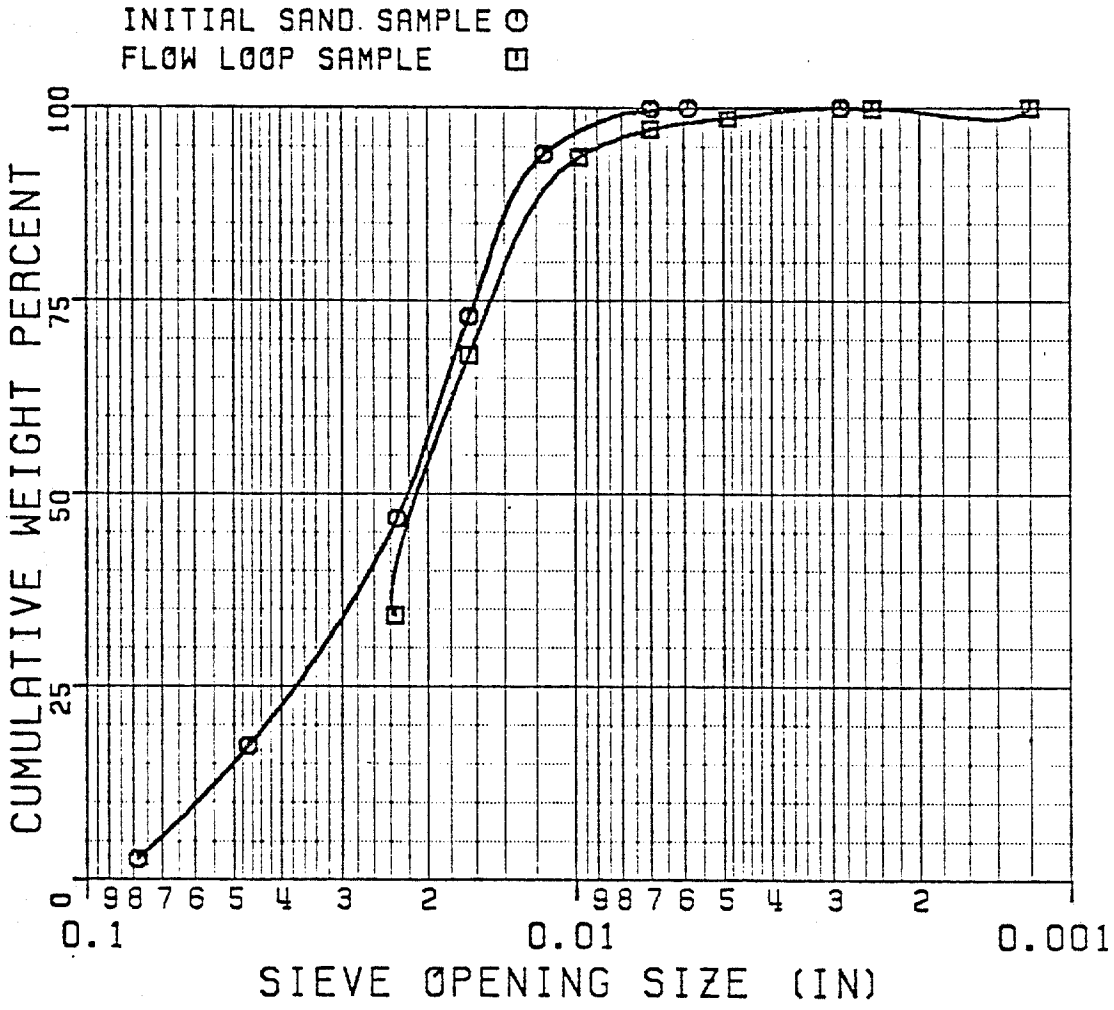

GRAIN SIZE DISTRIBUTION

Figure A4. Grain size distribution of the sand after 90 hours of run time (all samples combined).

TABLE A12

FLOW LOOP DATA FOR THE VORTICE-ELL

elapsed time (hr)	flowline pressure (psig)	differential pressure (psig)	flowrate (bbl/min)	sand content (%)
0.0	51.8	8.34	11.1	20
19.0	48.6	7.32	10.4	5
44.0	50.0	7.56	10.5	13
67.0	47.0	8.54	10.8	6
90.0	51.2	7.90	10.8	-
averages	49.7	7.93	10.7	11

average slurry velocity (calculated) = 45.9 feet/second

elapsed time (hr)	upstream temperature (F)	downstream temperature (F)	average temperature (F)
0.0	134.9	133.3	134.1
19.0	206.2	205.4	205.8
44.0	178.8	177.8	178.3
67.0	190.6	189.5	190.1
90.0	193.6	192.7	193.2
90.0	193.6	192.7	193.2
averages	180.8	179.7	180.3

TABLE A13

THICKNESS MEASUREMENT LOCATIONS (INCHES)
VORTICE-ELL

OUTSIDE RADIUS (A TO B)

measure point number	1	2	3	4	5
distance from flange face A	3/4	1 3/4	4 7/8	5 7/8	6 7/8

measure point number	6	7	8	9	10
distance from flange face A	7 7/8	9	10	11	12 1/8

measure point number	11	12	13	14	15
distance from flange face A	13 1/8	14 1/8	15 1/8	16 1/8	16 7/8

INSIDE RADIUS (A TO B)

measure point number	1	2	3
distance from flange face A	1/2	1 1/2	2 1/2

measure point number	4	5	6
distance from flange face A	3 1/2	4 1/2	5

TABLE A14

ULTRASONIC THICKNESS MEASUREMENT DATA
VORTICE-ELL

BEFORE TESTING/AFTER TESTING (THOUSANDTHS OF AN INCH)

OUTSIDE RADIUS (A TO B)

point number	1	2	3	4	5
top row	645/620	640/620	660/660	640/600	620/540
middle row	660/540	580/540	700/680	630/590	620/500
bottom row	665/560	585/560	640/610	585/540	580/520

point number	6	7	8	9	10
top row	650/600	645/600	680/600	645/545	640/560
middle row	605/540	605/545	690/580	700/560	620/540
bottom row	605/550	600/540	600/585	620/550	620/540

point number	11	12	13	14	15
top row	620/545	620/540	720/440	605/235	625/425
middle row	620/540	620/560	620/380	605/300	600/360
bottom row	600/540	660/600	585/345	575/300	560/360

TABLE A14-CONTINUED

INSIDE RADIUS (A TO B)

point number	1	2	3
top row	580/565	580/540	545/440
middle row	600/580	560/560	580/480
bottom row	580/560	580/560	580/480

point number	4	5	6
top row	545/400	540/425	575/460
middle row	580/440	560/445	575/460
bottom row	565/460	565/465	560/450

Figure A5. WELDED SHORT RADIUS ELL

Erosion Patterns

OUTSIDE RADIUS

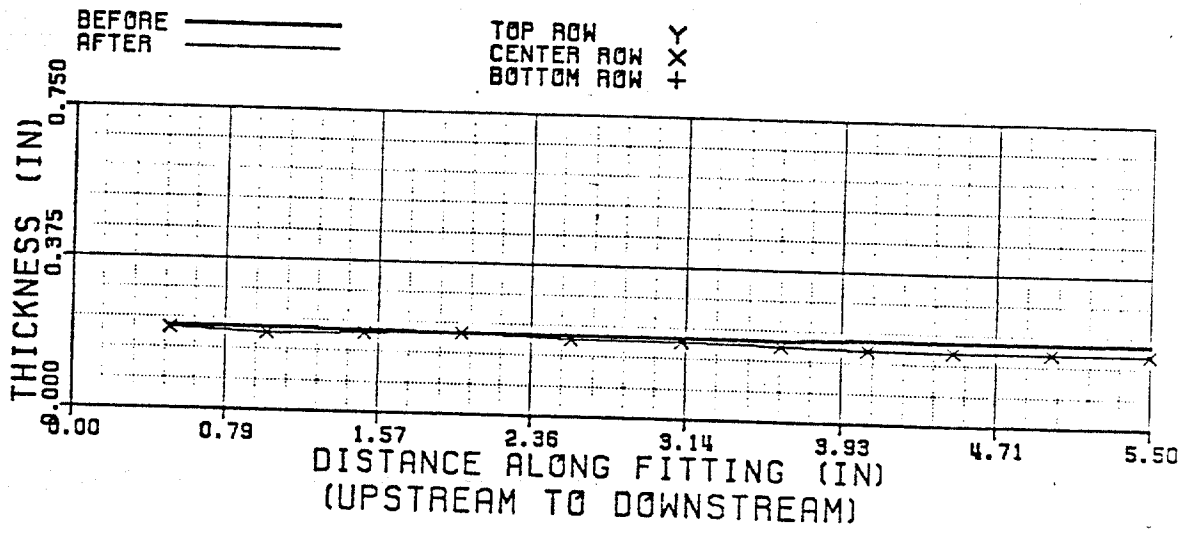

WELDED SHORT RADIUS ELL
OUTSIDE (A TO B)

Figure A6. WELDED SHORT RADIUS ELL

(SECOND RUN)

Erosion Patterns

OUTSIDE RADIUS

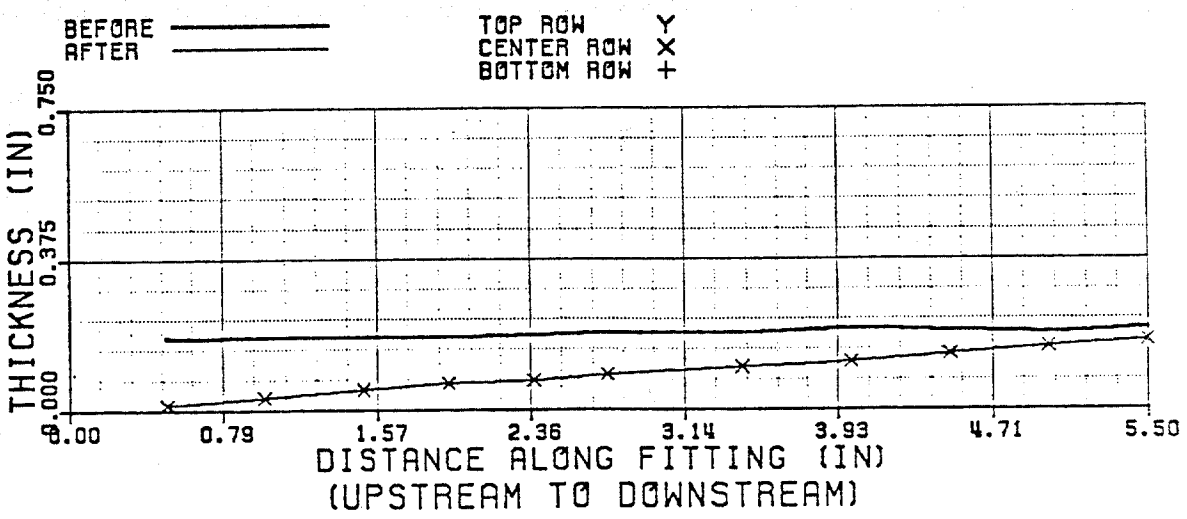

WELDED SHORT RADIUS ELL
OUTSIDE (A TO B)
(SECOND RUN)

Figure A7. WELDED PLUGGED TEE

Erosion Patterns

INSIDE RADIUS

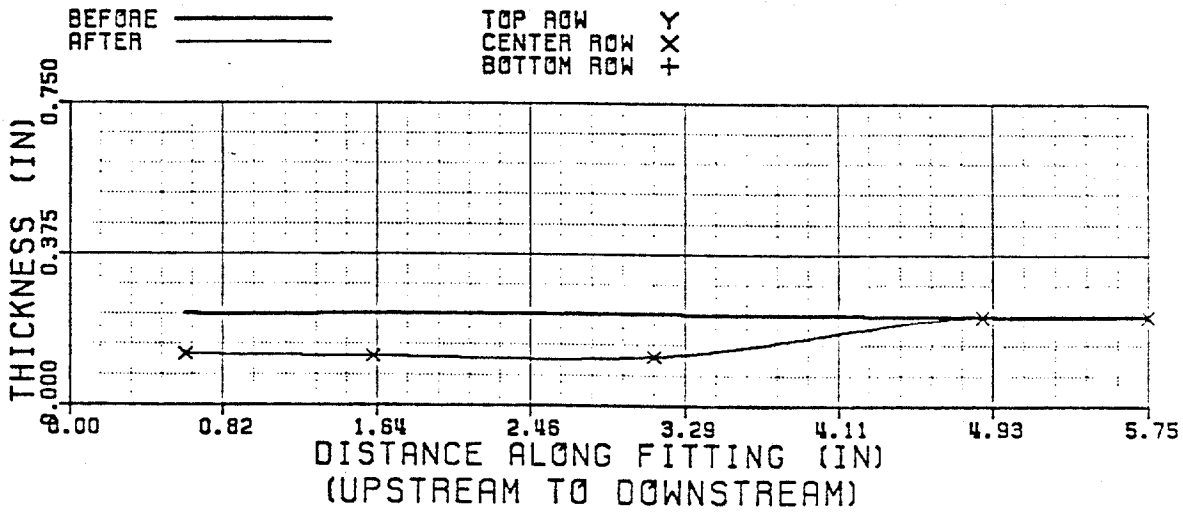

WELDED PLUGGED TEE
INSIDE (A TO C)

INSIDE RADIUS

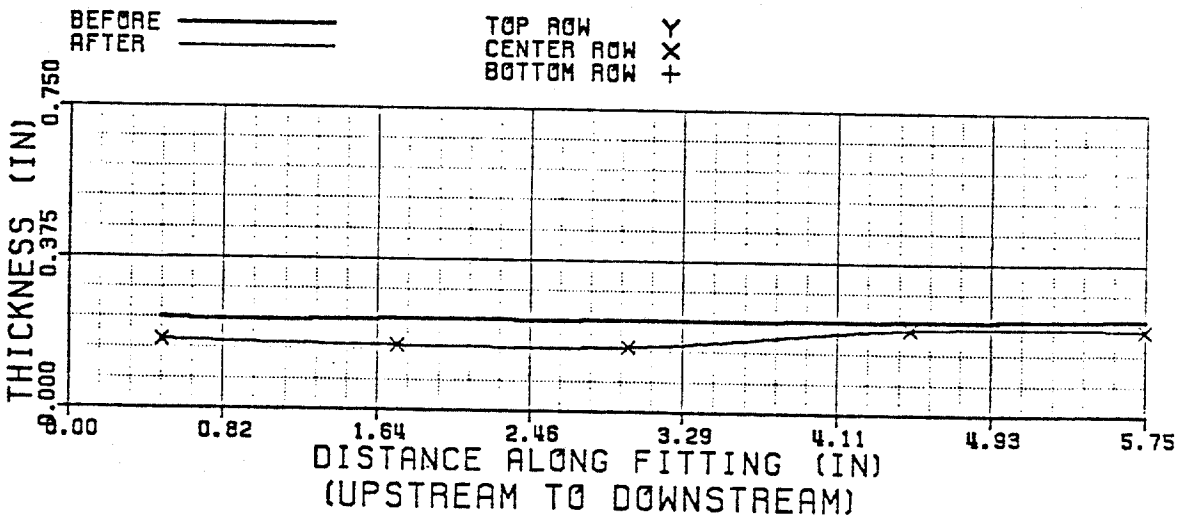

WELDED PLUGGED TEE
INSIDE (B TO C)

Figure A7-Continued

OUTSIDE RADIUS

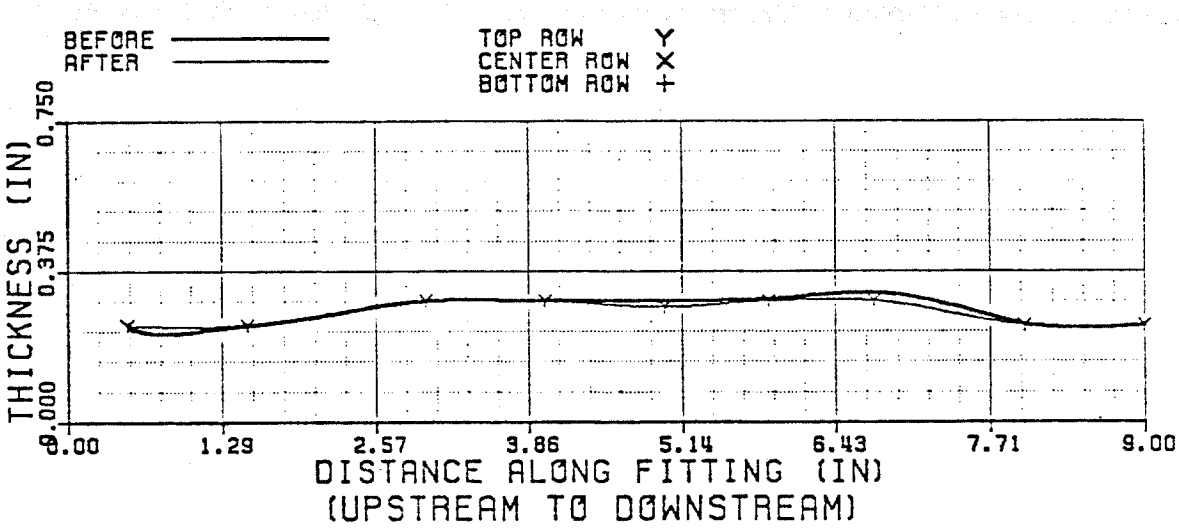

WELDED PLUGGED TEE
OUTSIDE (A TO B)

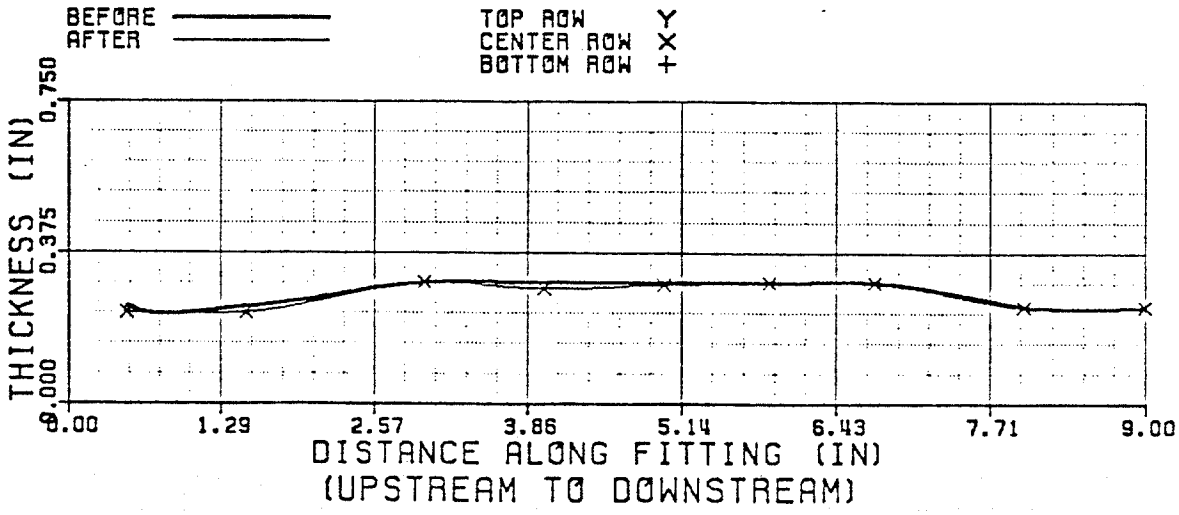

WELDED PLUGGED TEE
OUTSIDE (A TO B)

Figure A7-Continued

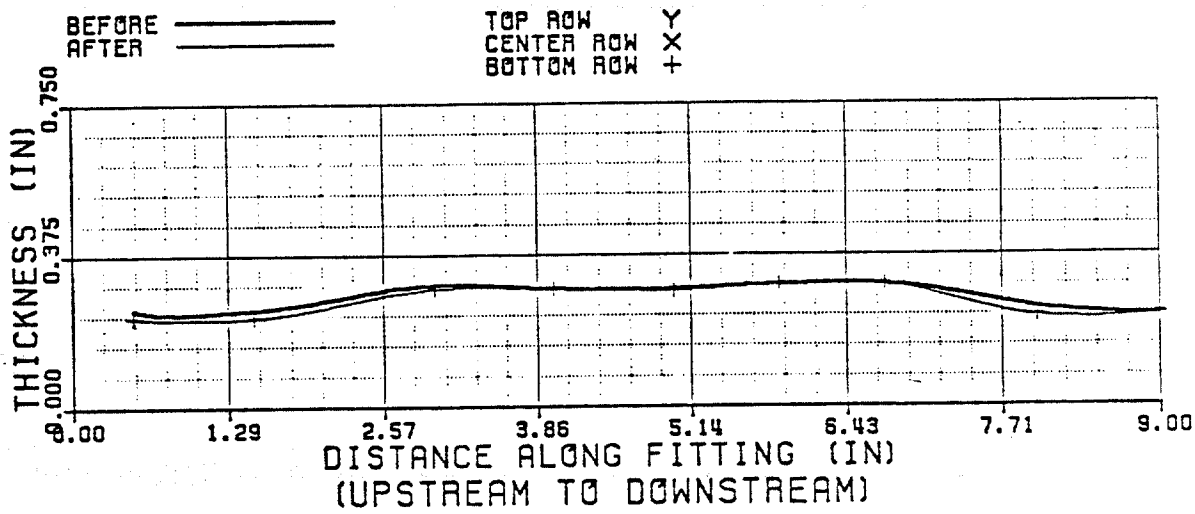

WELDED PLUGGED TEE
OUTSIDE (A TO B)

Figure A7-Continued

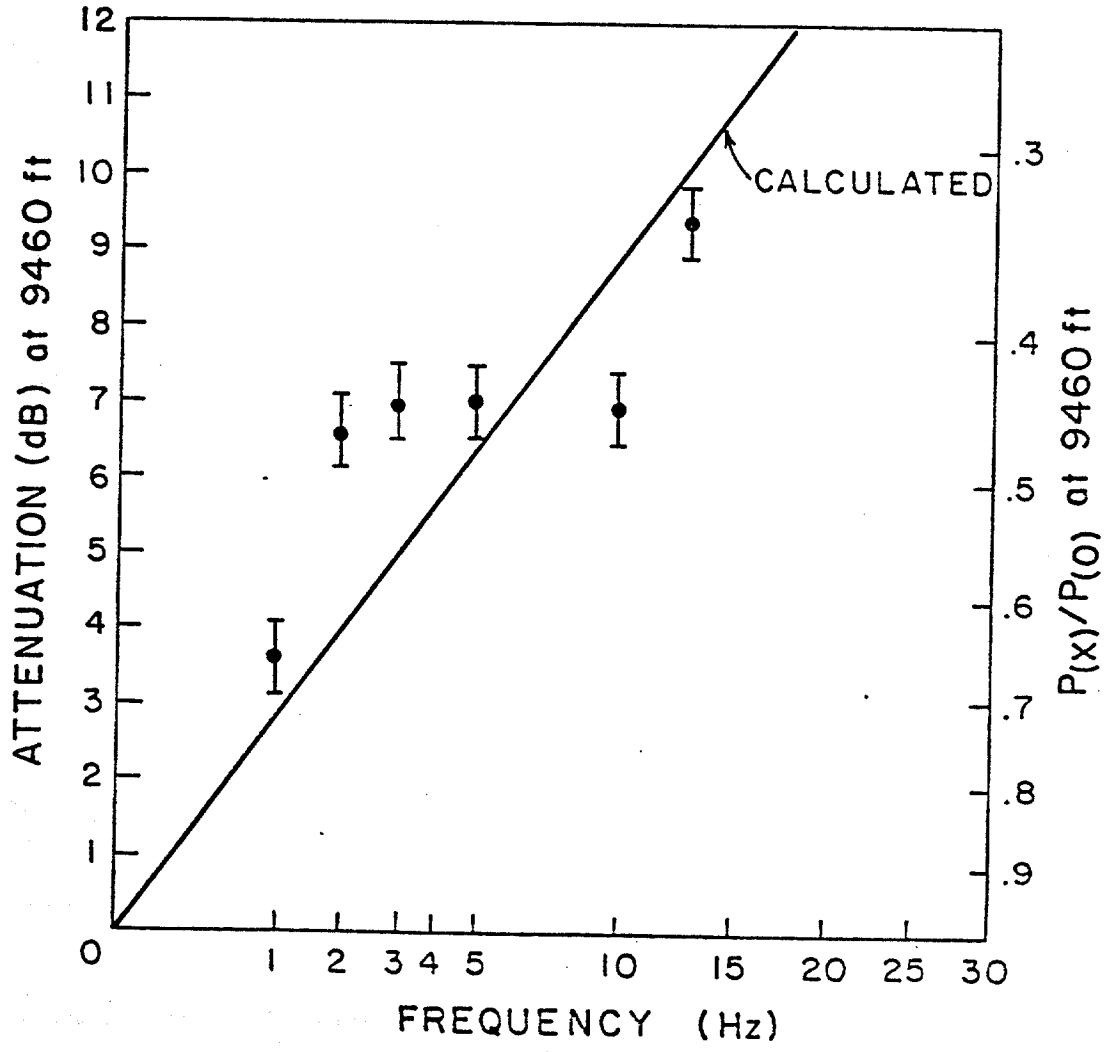

FIGURE 8.20. Graph of Attenuation Results Gathered at Various Frequencies with Mud #2 as the Fluid Medium.